Dissertation zur Erlangung des Doktorgrades
der Fakultät für Chemie und Pharmazie
der Ludwig-Maximilians-Universität München

Assembly and optimization of a super-resolution STORM microscope for nanoscopic imaging of biological structures

Jens Prescher

aus

München, Deutschland

2016

Erklärung

Diese Dissertation wurde im Sinne von §7 der Promotionsordnung vom 28. November 2011 von Herrn Prof. Don C. Lamb, PhD betreut.

Eidesstattliche Versicherung

Diese Dissertation wurde eigenständig und ohne unerlaubte Hilfe erarbeitet.

München, den 13. Januar 2016

. . . .

Dissertation eingereicht am	15. Januar 2016
1. Gutachter	Prof. Don C. Lamb, PhD
2. Gutachter	Prof. Dr. Christoph Bräuchle
Mündliche Prüfung am	18. Februar 2016

Contents

Abstract

Fluorescence microscopy is a widely used technique for imaging of biological structures due to its noninvasiveness although resolution of conventional fluorescence microscopes is limited to about 200–300 nm due to the diffraction limit of light. Super-resolution fluorescence microscopy offers an extension of the original method that allows optical imaging below the diffraction limit. In this thesis, a microscope for localization-based super-resolution fluorescence microscopy techniques such as Stochastic Optical Reconstruction Microscopy (STORM) or Photoactivated Localization Microscopy (PALM) was established. An epifluorescence microscope was built for this purpose that provides both widefield and Total Internal Reflection Fluorescence (TIRF) excitation modalities and focus was put on the special requirements of localization-based super-resolution methods. This included a high mechanical and optical stability realized by a compact design and implementation of a home-built perfect focus system. The setup was further designed to allow both two- and three-dimensional imaging. The work also included both the development of a setup control software and a software for the analysis of the required data. Different analysis methods and parameters were tested on simulated data before the performance of the microscope was demonstrated in two and three dimensions at appropriate test samples such as the cellular microtubule network. These experiments showed the capability of super-resolution microscopy to reveal underlying structures that cannot be resolved by conventional fluorescence microscopy. Resolutions could be achieved down to approximately 30 nm in the lateral and 115 nm in the axial dimension.

Subsequently, the established method was applied to two biological systems. The first is a study of the budding of the human immunodeficiency virus type 1 (HIV-1) from the host cell. In this step of the viral reproduction cycle, the virus hijacks the cellular endosomal sorting complex required for transport (ESCRT) machinery to achieve membrane fission. ESCRT consists of the subcomplexes ESCRT-0, -I, -II and -III and additional related proteins, from which HIV-1 recruits certain components. The fission process is initiated by the HIV-1 Gag protein, which recruits the ESCRT-I protein Tsg101 and the ESCRT-related protein ALIX to the virus assembly site. Subsequently, ESCRT-III proteins CHMP4 and CHMP2 form transient lattices at the membrane, which are actively involved in membrane fission. However, the actual geometry of the ESCRT machinery assembling at the HIV-1 budding site that is driving the fission process is still not fully understood. Different models proposed either constriction of the budding neck by lattices surrounding the neck, by ESCRT structures within the neck or within the bud itself. A problematic aspect in previous studies was the usage of modified, tagged versions of the involved proteins for visualization. In this study, super-resolution microscopy was therefore applied to endogenous Tsg101, ALIX and CHMP2 isoform CHMP2A and to a version of CHMP4 isoform CHMP4B with a small HA-tag to elucidate the size and the distribution of the structure relative to the HIV-1 assembly sites. ESCRT structures colocalizing with HIV-1 exhibited closed, circular structures with an average size restricted to 45 and 60 nm in diameter. This size was significantly smaller than found for HIV-1 assembly sites and the constriction of the size, which was not observed for non-colocalizing ESCRT structures at the cell membrane, ruled out an external restriction model. Super-resolution imaging of ALIX often revealed an additional cloud-like structure of individual molecules surrounding the central clusters. This was attributed to ALIX molecules incorporated into the nascent HIV-1 Gag shell. Together with experiments that confirmed the non-physiological behavior of tagged Tsg101 and a relative orientation of ESCRT clusters towards the edge of the assembly site, the results strongly point toward a within-neck model.

A second project focused on the influence of external constriction on cell migration. The latter plays an important role in various processes in the human body ranging from wound healing to metastasis formation by cancer cells. Migration is driven by the lamellipodium, which is a meshwork of fine actin filaments that drive membrane protrusion. Endothelial cells were grown on micropatterns that confined the freedom of movement of the cells. Three-dimensional super-resolution imaging revealed that the lamellipodia of these cells showed a much broader axial extension than was the case for control cells that grew without confinement of migration. The different organization of the actin filament network showed a clear effect of environmental conditions on cellular migration.

Overall, it was possible to build a super-resolution fluorescence microscope over the course of this study and establish the required analysis methods to allow STORM and PALM imaging below the diffraction limit of light. Two applications further showed that these tools are capable of answering currently discussed questions in the biological sciences.

Chapter 1

Introduction

In order to understand how a mechanism works, it is necessary to be able to observe all the components that form its entirety. This includes especially biological organisms, which are highly complex systems with an uncountable number of connected and interacting processes that all contribute to life in its versatility. Many of these processes can be studied by eye but other things remain hidden as objects that are smaller than approximately 0.1 mm are no longer resolvable by the human eye. Often, it is only feasible to observe the macroscopic effect of a process but not the process itself. This means that it might, for example, be possible to see how blood flows in its vessels but not to distinguish its components. It might further be possible to see the effects a sickness but not the pathogen that caused that disease and how it interacts with the body. For these reasons, tools are required that allow to go beyond the constraints imposed by the eye. Although the magnifying effect of glass lenses had been known since antiquity, the quality of the lenses and therefore also their impact on the study of biology remained limited for a long time. The foundation for modern microscopy was not laid until the end of the 16th century when Hans and Matthias Janssen claimed to have constructed the first microscope [1]. Several years later, Robert Hooke discovered, using a compound microscope, that large and complex organisms are built up of small subunits he named 'cells' [2]. This work has to be seen in close context with that of Antoni van Leeuwenhoek who provided substantial improvement of both fabrication and quality of optical lenses. Magnifying glasses built out of these improved lenses allowed him to observe organisms that only consist of one single cell [3]. These inventions and discoveries marked a turning point opening a new world for the biological sciences: from the discovery of cells and microorganisms research soon advanced further to the intracellular level revealing structures and functions of cellular subcomponents. The benefits of this gain of knowledge have been undeniable: now, reasons for diseases and other impairments of the body could be identified and effectively counteracted in combination with newly developed chemical and biochemical analysis methods. The essential contribution that optical microscopy has made to this progress can be especially attributed to its high compatibility with biological samples. Its non-invasiveness and relatively mild demands on sample preparation even allow the study of living organisms. Since its invention, the method has been further improved. Especially the combination with fluorescence has emerged to be highly effective: a certain biological structure is specifically labeled with a fluorescent dye for this purpose and the emitted fluorescence is detected. This eliminates the difficulty to identify a certain structure among many others in a larger organism by maintaining the assets of conventional light microscopy. With the development of efficient light sources such as lasers and highly sensitive detectors, fluorescence microscopy has become an indispensable tool for the biological sciences.

Still, although the method allows the study of many processes inside a cell, the capacity of conventional optical microscopes has nevertheless a restriction. Due to refraction of the light at the aperture of the microscope, its resolution is limited to approximately 200 nm as it was described in the famous works of Ernst Abbe [4] and John William Strutt better known as Lord Rayleigh [5]. The resolution limit implies that many smaller structures cannot be studied with optical microscopy. This includes, for example, not only subunits of larger structures within a cell but also viruses. These are small infectious particles, which have to use organisms to replicate and are responsible for a huge number of infections.

In order to circumvent the resolution limit, non-optical methods such as Scanning Electron Microscopy (SEM) or Transmission Electron Microscopy (TEM) were developed. SEM and TEM, however, provide only a very limited compatibility with organic and living material. Furthermore, optical microscopy cannot only be applied to surfaces (like SEM) or very thin structures (like TEM) but also to larger volumes allowing imaging of entire cells. However, the diffraction limit in optical microscopy was regarded as a barrier that could not be penetrated for a long time. Although theoretical works by Stefan Hell and Eric Betzig discussed options how to circumvent this limit [6, 7], technical realization was not achieved until methods like Stimulated Emission Depletion (STED, [8]), Photoactivated Localization Microscopy (PALM, [9]), Stochastic Optical Reconstruction Microscopy (STORM, [10]) and other related approaches were presented. Today, all these methods are summarized by the term super-resolution fluorescence microscopy. Stefan Hell and Eric Betzig were awarded with the Nobel Prize in Chemistry in 2014 for their pathbreaking work on this field together with William E. Moerner who was the first to perform single-molecule spectroscopy [11]. The latter was an indispensable fundament for the development of the various super-resolution techniques. Methods such as STORM and PALM, which were used in this work, are able to provide resolutions down to 10 nm in the lateral and 20 nm in the axial dimension making them an ideal tool to study cellular processes on the nanoscale.

The scope of this thesis comprised the construction and tuning of a super-resolution fluorescence microscope for PALM and STORM applications that allows imaging in both two and three dimensions. This included not only the assembly of the microscope but also the development of analysis software that allows the rendering of super-resolution images from the acquired data with the required high accuracy. Simulations were performed to find optimal analysis settings and imaging of test samples such as the cellular microtubule network demonstrated the performance of the microscope in two as well as in three dimensions.

The established method was subsequently applied on the study of the human immunodeficiency virus type 1 (HIV-1). HIV-1 is the virus responsible for the acquired immunodeficiency syndrome (AIDS), which is regarded to be one of the four pandemic diseases claiming the highest number of victims worldwide (together with tuberculosis, hepatitis and malaria) where HIV-1 alone caused more than one million deaths in 2013 alone [12]. Its fatality is based on the fact that HIV-1 attacks cells that are an integral part of the human immune system and thus critically weakens the defense of the body. Although HIV-1 is maybe the best studied virus overall and though antiviral medication now exists, a vaccination or a cure is still not available as many details of its replication cycle are still not fully understood. Furthermore, the HIV-1 genome features a high mutation rate, allowing the virus to rapidly develop resistances against existing medications making continuous research even more important. This thesis focuses on the viral budding of HIV-1, which is a relatively late step in the viral reproduction cycle when a newly formed virus particle is released from the host cell. In this context, HIV-1 depends on recruitment and exploitation of the cellular endosomal sorting complex required For transport (ESCRT) to achieve complete fission from the host cell. ESCRT forms oligomeric protein complexes that drive membrane fission. However, the underlying mechanism and geometric organization of these oligomeric structures are still not fully understood. As all these processes occur below the diffraction limit of light, PALM and STORM are good methods to give answers to this question.

Infection of cells by viruses or other pathogens as well as mechanical injuries of the body require effective defense and repair mechanisms. For this purpose, many cells that are involved in these processes need the ability to move actively. Migration of cells, for example, plays a crucial role in tissue formation, which also includes wound healing processes. Migration is furthermore essential for the organization of the immune response. These are, however, only some of the most prominent examples that involve cell migration. In order to achieve directed motion, a number of concerted processes is needed to generate the required propulsion. Disruptions of these processes can effect critical damages. One prominent example is the formation of metastases, which arise from cancer cells that are migrating uncontrolled through the respective organism. A key step during cell migration is pushing the cellular membrane in the direction of motion. The mechanical force for this process is generated by a very fine network of actin filaments. Actin is a major component of the cytoskeleton and forms in this case two-dimensional networks within the protrusions of migrating cells, which are called lamellipodia. These networks grow in the direction of migration and thereby drive locomotion. Contraction of additional actin filaments in the rear part of the moving cell further provides the required energy to allow the rest of the cell body to follow the protrusions. Controlled migration further requires the ability to react to external triggers or signals, which, for example, can be chemical or mechanical forces. In this context, the question arises whether and how external stress put on cells changes the organization of the lamellipodia network. For this purpose, endothelial cells were grown on one-dimensionsl microstructures that allowed growth only in a specific direction. 3D super-resolution imaging was used to gain insight into the fine structure of the actin filament network and to reveal differences in its organization compared to cells with unrestricted two-dimensional migration.

Overall, the experiments that were performed to build and tune the super-resolution microscope along with the applications shown in this thesis demonstrate the high performance potential of super-resolution fluorescence microscopy. The obtained results emphasize the capability of the microscope to provide answers to relevant open questions in biology that cannot be obtained by other techniques making it a versatile and highly promising tool for the nanoscopic sciences.

Chapter 2

Theory of super-resolution fluorescence microscopy

Super-resolution microscopy methods such as STORM and PALM seek to circumvent the resolution limit of conventional fluorescence microscopy by exploiting certain properties of fluorescent dyes. In particular, fluorophores are needed that can undergo a spectral shift as it will be discussed in detail in this chapter. Further, understanding of the fundamental principles of the used fluorescence microscope plays a vital role for achieving good image quality and resolution. This starts at the fundamental operation mode of the microscope and reaches to additional extensions that allow even three-dimensional imaging.

2.1 Principles of fluorescence

STORM and PALM are super-resolution fluorescence microscopy methods that are based on the switching of fluorescent dyes between dark and bright, fluorescent states. In order to understand this process, which is often referred to as blinking, and the conditions that contribute to it, some basic information about the physical background regarding fluorescence is required.

Fluorescence is essentially a consequence of the interaction of electromagnetic waves with matter. An electromagnetic wave can be absorbed by matter as a result of the interaction with the electromagnetic field of the respective material. As a consequence, the energy of the absorbed photons is taken up by the atom or molecule, which can thus be excited to higher rotational, vibrational or electronic states. These excited states are typically metastable and after a certain period of time, the system will relax back to the energetic ground state releasing the excess of energy to the environment. In many cases, this occurs in the form of heat but it is also possible that a photon is emitted. Processes that include light emission after absorption of a photon by matter can be summarized under the term photoluminescence. Fluorescence and phosphorescence, which will be discussed in detail below, are two special cases of photoluminescence.

As depicted in Figure 2.1, absorption of a photon will initially excite an electron from the vibrational ground state of the lowest electronic singlet state S_0 to a higher electronic state (S_1, S_2, etc.). However, light from the visible part of the electromagnetic spectrum does not provide enough energy to reach higher electronic states than S_1. The probability for the transition from S_0 to S_1 can be found in the number of electrons N_0 occupying S_0 and the power density ρ of the incoming light at frequency ν by means of

$$\frac{\mathrm{d}N_0}{\mathrm{d}t} = -B_{01} N_0 \rho(\nu) \tag{2.1}$$

where B_{01} the Einstein-coefficient for absorption, which depends on the transition dipole moment. A more general description of the transition probability was provided by Dirac [13] who stated that the latter is proportional to the density of the final states and to the magnitude of the matrix element of the transition between the final and initial states (also known as Fermi's Golden Rule). Excitation takes place in the range of femtoseconds. The Born-Oppenheimer approximation [14] states that the much slower movement of the atomic nuclei is negligible during the excitation process although the equilibrium position of the nucleus depends on the electronic configuration. As a spatial overlap of the wave functions of the initial and the final state is required for a transition and the position of the nucleus cannot change, the vibrational state that is reached by excitation does not necessarily correspond to the vibrational ground state but one that is compatible to the nuclear position of the initial state. This observation is described by the Franck-Condon-Principle [15, 16]), which is graphically depicted in Figure 2.1. The excited system will relax within picoseconds to the vibrational ground state of the respective electronic state releasing the excess of energy in the form of heat. As a consequence, the amount of energy that can be released during a following relaxation back to S_0 is lower than the energy that was absorbed for excitation. This means, in the case of photoluminescence, that an emitted photon will have a higher wavelength than the one that was absorbed before resulting in a spectral shift between both of them that is known as Stokes shift [17]. The lifetime, τ, of the excited electron in the ground state of S_1 lies in the range of nanoseconds before the system relaxes to S_0, where the rules of Born-Oppenheimer approximation and the Franck-Condon-Principle apply analogously to excitation.

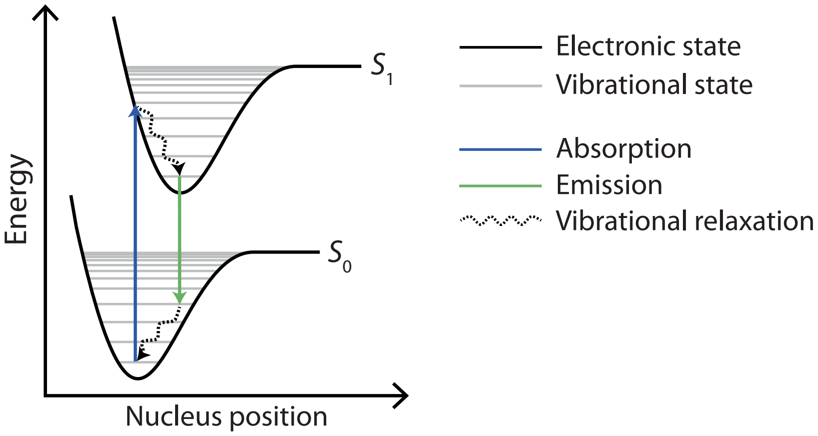

Figure 2.1: Franck-Condon-Principle. Energetic potentials for electronic ground and first excited state illustrate the Franck-Condon-Principle.

A Jablonski diagram [18], as shown in Figure 2.2, can be used to further explain the processes contributing to photoluminescence in detail. As explained before, absorption of a photon (blue arrows) will excite a molecule to a higher electronic state from where it will relax almost immediately to the vibrational ground state of the respective electronic state (brown arrows). From electronic states higher than S_1, non-radiative relaxation to S_1 is possible. Such non-radiative processes are called internal conversion (black dashed arrows). From the vibrational ground state of S_1, further relaxation back to S_0 will occur. This can either take place by internal conversion or under the (spontaneous) emission of a photon. Such a photoluminescent process is called fluorescence (green arrows) and its dynamics can be described by a similar equation as was given in Eq. 2.1 for absorption:

$$\frac{\mathrm{d}N_1}{\mathrm{d}t} = -N_1 A_{10} \tag{2.2}$$

In Eq. 2.2, N_1 is the number of electrons in S_1 and A_{10} the Einstein-coefficient for sponta-

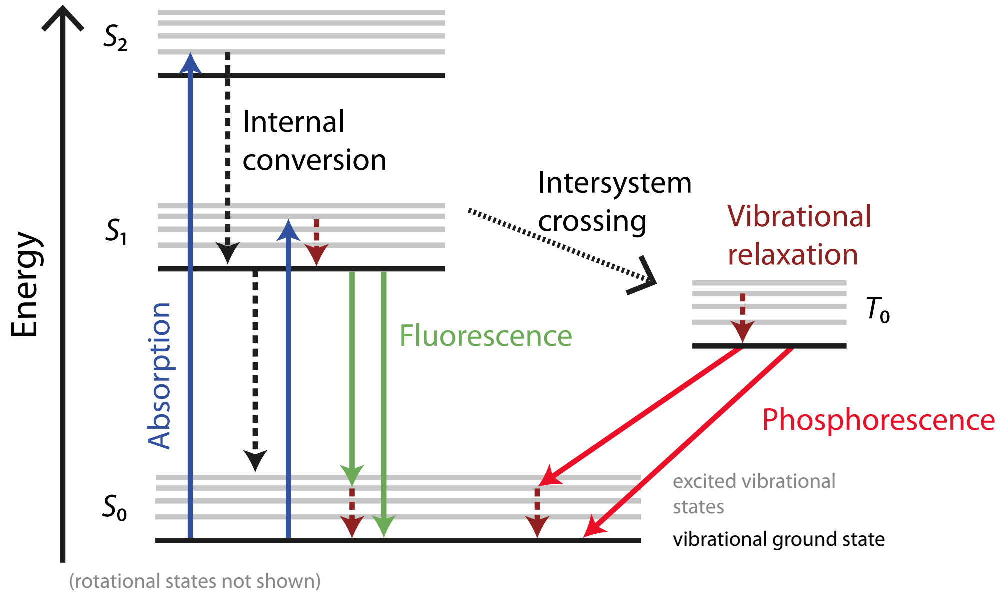

Figure 2.2: Jablonski diagram. A Jablonski diagram describes the electronic and vibrational transitions that lead to photon emission in form of fluorescence (green) or phosphorescence (red) after absorption of light by matter (blue). Radiative processes are represented by solid lines, non-radiative transitions by dotted or dashed lines (S_n, T_n: n$^{\text{th}}$ singlet or triplet state).

neous emission. After emission of the photon, vibrational and rotational relaxation back to the vibrational ground state of S_0 occurs.

This means that both excitation and relaxation occur most likely from the lowest vibrational state. Together with the fact that the densities of the vibrational states are approximately similar in S_0 and S_1, this leads to an approximate mirror symmetry between the absorption and emission spectra of fluorescent dyes as it is shown in Figure 2.3 at the example of the cyanine dye Cy5. The example also illustrates the Stokes shift between the absorption maximum at 647 nm and the emission maximum at 665 nm.

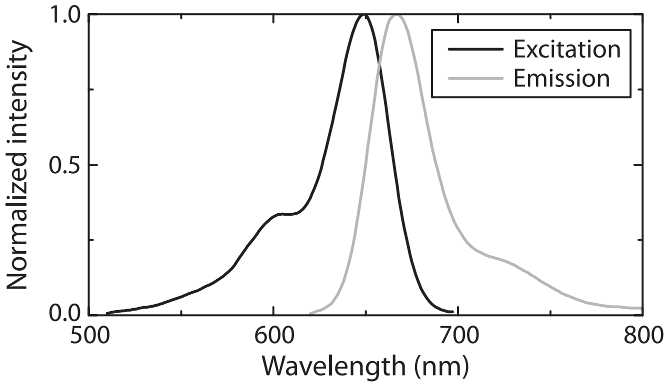

Figure 2.3: Absorption and emission spectra of fluorescent dye Cy5. The Stokes shift between the absorption (black) and the fluorescence emission spectrum (gray) of Cy5 is visible as well as the mirror symmetry between both spectra.

Emission can also be stimulated by another incoming photon with a wavelength matching the energy gap between S_1 and S_0. If this photon hits the excited molecule before spontaneous emission can occur, the system relaxes to the electronic ground state by emitting a photon with the same energy, direction of movement and phase as the stimulating photon. In contrast to spontaneous emission, the dynamics of stimulated emission given by Eq. 2.3 depend on $\rho(\nu)$ and on the Einstein-coefficient for stimulated emission B_{10}:

$$\frac{\mathrm{d}N_1}{\mathrm{d}t} = -N_1 B_{10} \rho(\nu) \tag{2.3}$$

Apart from fluorescence, there is a second form of photoluminescence, which is called phosphorescence. In this case, the excited electron in S_1 does not relax to the ground state immediately but undergoes intersystem crossing (Figure 2.2, black dotted arrow), where the spin of the excited electron is flipped and the triplet state T_0 is reached. This conversion is, in theory, quantum-mechanically forbidden but due to interaction of spin and orbital momentum, there is still a certain probability for this process to occur. For the same reason, the probability for the relaxation from T_0 back to S_0 is also small. As a consequence, the electron is trapped in the triplet state for a relatively long period of time that can lie in the range of milliseconds up to seconds. During this time, the molecule will appear dark to the observer until it finally relaxes back to S_0 under emission of a photon (Figure 2.2, red arrows). Only after this happened, the molecule can be excited once more and fluorescence can occur again.

Intersystem crossing to a triplet state is one example for a process where a fluorophore is trapped in a non-fluorescent state for a certain period of time. The latter can, however, also be caused by quenching [19]. Fluorescence can be quenched e.g. by the presence of an acceptor molecule to which the excited fluorophore can transfer the excess of energy radiationless. There are several ways how this transfer can occur, Fluorescence Resonance Energy Transfer or Dexter transfer [20] are only two examples to name. Quenching can be transient when it is controlled only by the diffusion of the molecules but it can also be stable when the dye and the quenching molecule form stable complexes.

Repeated excitation and relaxation of a fluorophore is reversible. There is, however, a certain probability during each excitation cycle that the imparted energy leads to an irreversible change of the chemical structure of the fluorophore by e.g. breaking of chemical bonds. This can irreversibly destroy the fluorescence of the molecule. This process is described by the term photobleaching and has to be distinguished from quenching. Nevertheless, both mechanisms can be used to achieve switching of fluorescent molecules between dark and bright states although different experimental settings might be necessary, as will be explained in Section 2.3.

2.2 Fluorescence microscopy and optical resolution

Many biological processes occur on the micro- or nanometer scale and cannot be observed by the human eye. Microscopy and especially optical microscopy have been proven to be valuable tools in order to study these systems. However, optical microscopy requires light to illuminate the sample or light that is emitted by the sample itself. Fluorescence microscopy combines both approaches by studying structures that are specifically labeled with fluorophores allowing the observation of emitted fluorescence upon excitation with light. Along with technological advance, fluorescence microscopy has developed from its early beginnings [21] to an indispensable tool especially for the biological sciences.

2.2.1 Principle of fluorescence microscopy

In general, two different basic approaches can be distinguished for fluorescence microscopy. The first one can be summarized under the term of epifluorescence or widefield microscopy, where a larger field of view within the sample is illuminated with a broad collimated beam and the image obtained from the field of view is collected with a camera. The second approach is called confocal fluorescence microscopy [22], where only a small volume is illuminated at a time and the complete image is only obtained by scanning of the sample. In comparison to confocal microscopy, an epifluorescence microscope provides in general a higher photon detection efficiency, which is favorable for STORM and PALM as will be explained in detail in Section 2.3. For this reason, this work exclusively focuses on epifluorescence microscopy and the following description of fluorescence microscopy will therefore also be based on this type of microscope.

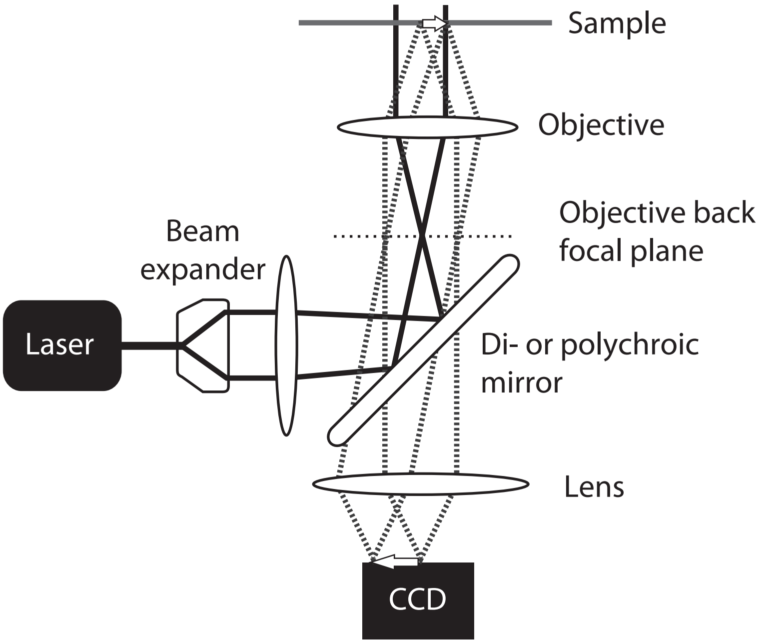

Figure 2.4: Scheme of a widefield fluorescence microscope. A laser beam (black solid lines) is expanded and focused on the back focal plane of the objective creating a collimated beam for illumination and excitation of the sample here indicated by the white arrow. The emitted fluorescence (dashed gray lines) is collected by the objective and separated from excitation light by a di- or polychroic mirror and eventually focused on a CCD camera obtaining the image of the original object.

Figure 2.4 shows the scheme of a basic epifluorescence microscope. Typically, lasers are used as monochromatic, collimated and coherent light sources. The light beam is focused onto the back focal plane of the objective lens. As a consequence, a collimated beam will leave the objective illuminating the sample exciting fluorophores within the illuminated area of the sample. A beam expander, which, for example, can consist of a set of two lenses, optionally allows an expansion of the excitation beam in order to increase the diameter of this area. The fluorescence emitted by the sample is usually collected by the same objective resulting in a collimated beam that is separated from the excitation light by a di- or polychroic mirror. These mirrors are able to reflect well-defined parts of the electromagnetic spectrum and let pass other parts [23]. As the fluorescence has a longer wavelength than the excitation beam due to the Stokes shift, such a mirror is an ideal tool to separate excitation and detection beams. Emission filters, which block all light that is not coming from a specific region of the spectrum, can be used to further filter out remaining light that is not part of the actual fluorescent signal (e.g. stray light, Raman scattering or fluorescence originating from other dyes that can be excited by the same wavelength but have a shifted emission spectrum).

Another lens finally focuses the collimated beam onto the respective detector. Typically, charge-coupled devices (CCD) are chosen for this purpose, which can be characterized by their low readout noise and high quantum efficiencies (up to 90%) [24]. Electron-multiplying CCDs (EMCCD) offer additional amplification of the signal, which, however, comes along with an additional noise factor of $\sqrt{2}$ [25]. Complementary metal-oxide semiconductor (CMOS) detectors might be an alternative, especially when very fast data acquisition is required. However, noise of CMOS cameras is pixel-dependent in contrast to CCDs and a more complex noise treatment is required [26].

In recent years, fluorescence microscopy has found various applications especially for biological applications. Beside the relatively low technical effort and costs compared to other methods such as electron microscopy techniques, it is particularly appreciated for its non-invasiveness and its moderate operating conditions that allow the study of living organisms: Light microscopy can be performed at room temperature and normal pressure. Additionally, energy and power of the light source can be chosen in a biocompatible way. Imaging is also not restricted to small parts of the sample as it is, for example, the case for SEM that can only provide images of the surface.

As mentioned above, fluorescence imaging requires the presence of a fluorescent structure or of a fluorescent label attached to the structure of interest. Certainly, the need to modify the respective sample with fluorescent molecules might be regarded as a drawback of the method as it is possible that the modification of the sample changes its structure or properties. But in this context, it is also important to note that sample modification is also required for many other microscopy techniques and is often more invasive than it is for fluorescence microscopy such as metallic coating that is required for SEM. Fluorescent labeling further provides a convenient way to distinguish between different structures, for example in a cell, by labeling them specifically with differently colored fluorophores. This approach offers the possibility for simultaneous imaging of the respective structures, which is much more difficult to realize with non-optical methods.

2.2.2 Resolution in optical microscopy

Despite the numerous advantages of optical fluorescence microscopy, one major limitation of the method is the confinement of the achievable resolution to about 200–300 nm. In general, resolution defines the smallest distance in which two objects can still be distinguished. The reason for this confinement in optical microscopy is based on the diffraction of the light on the objective and condenser lenses of the microscope. George Airy observed already in 1835 [27] that the image of a round, condensed beam of light that is diffracted on circular apertures such as optical lenses shows a pattern where a central intensity maximum is surrounded by rings whose intensities decline with the distance from the center of the structure. Ernst von Abbe recognized the connection between Airy's observation and the resolution power of light microscopes. Starting with his groundbreaking work [4], he focused on the influence of the optical properties of the objective lens on image resolution and coined, in this context, the term numerical aperture (NA), which is defined as

$$NA = n \cdot \sin\alpha \tag{2.4}$$

with n being the refractive index of the surrounding medium and α the half of the angle of the aperture of the objective. Abbe found that the numerical aperture is, together with the wavelength of light λ, related to the distance Δx in which two objects can still be resolved:

$$\Delta x = \frac{\lambda}{2NA} \tag{2.5}$$

Lord Rayleigh later combined Abbe's observation with the ring structure Airy had observed [5] and could refine Eq. 2.5 defining Δx as the distance between the global maximum in the center of the diffraction pattern and its first minimum. This condition, which can be expressed by Eq. 2.6, is also known as Rayleigh limit or Rayleigh criterion:

$$\Delta x = 0.61 \frac{\lambda}{NA} \tag{2.6}$$

The effect of diffraction can also be described by means of the image of a theoretically point-shaped (zero-dimensional) object. The observed diffraction pattern – or in other words the probability to detect the respective object at a certain point of the image plane – is called point spread function (PSF). In the case of a set of ideal lenses, the PSF perpendicular to the optical axis is also called the Airy Disk and the signal intensity $I(r)$ at position r given by

$$I(r) = I_0 \cdot \left[\frac{2J_1(2\pi r NA/\lambda)}{2\pi r NA/\lambda} \right]^2 \tag{2.7}$$

where I_0 is the maximum intensity of the distribution and J_1 the Bessel function of the first kind of order 1 [28]. Calculation of the first minimum of Eq. 2.7 yields the factor of 0.61 in Eq. 2.6. Analogously to Eq. 2.7, the intensity distribution $I(z)$ along the optical axis is given by:

$$I(z) = I_0 \cdot \left[\frac{\sin\left[(z\pi NA^2)/(2\lambda n)\right]}{(z\pi NA^2)/(2\lambda n)} \right]^2 \tag{2.8}$$

To be precise, these rules apply only for far-field imaging. In contrast to the near-field, the far-field defines a region, where the propagation of an electromagnetic wave does not depend on the distance from the radiation source. For a propagating Gaussian light beam, this is true for distances larger than the so called Rayleigh length, which must not be mixed with the Rayleigh criterion.

For most applications, the actual Airy disk, shown in Figure 2.5A, can be approximated by a two-dimensional Gaussian function (Figure 2.5B). In Cartesian coordinates, its intensity distribution $I(x, y)$ is given by the following equation, which provides a good estimate for the central peak of the original function despite negligence of the side maxima as demonstrated in Figure 2.5C:

$$I(x, y) = I_0 \cdot \mathrm{e}^{-\frac{(x-x_0)^2}{2\sigma_x^2} - \frac{(y-y_0)^2}{2\sigma_y^2}} \tag{2.9}$$

Again, I_0 represents the maximum intensity of the distribution, whereas x_0 and y_0 are the coordinates of the centroid position of the Gaussian distribution and σ_x and σ_y its standard deviations in x- and y-direction, respectively.

Figure 2.5D illustrates the effect of diffraction-limited imaging at the example of a 40 nm sized polystyrene bead labeled with Cy5 dye: obviously, the image lets the bead appear much larger than it actually is. Mathematically, the final image can be described as a convolution of the actual structure with the PSF. If one assumes that the original object can be treated as a Gaussian distribution and the PSF is approximated as a Gaussian distribution as well,

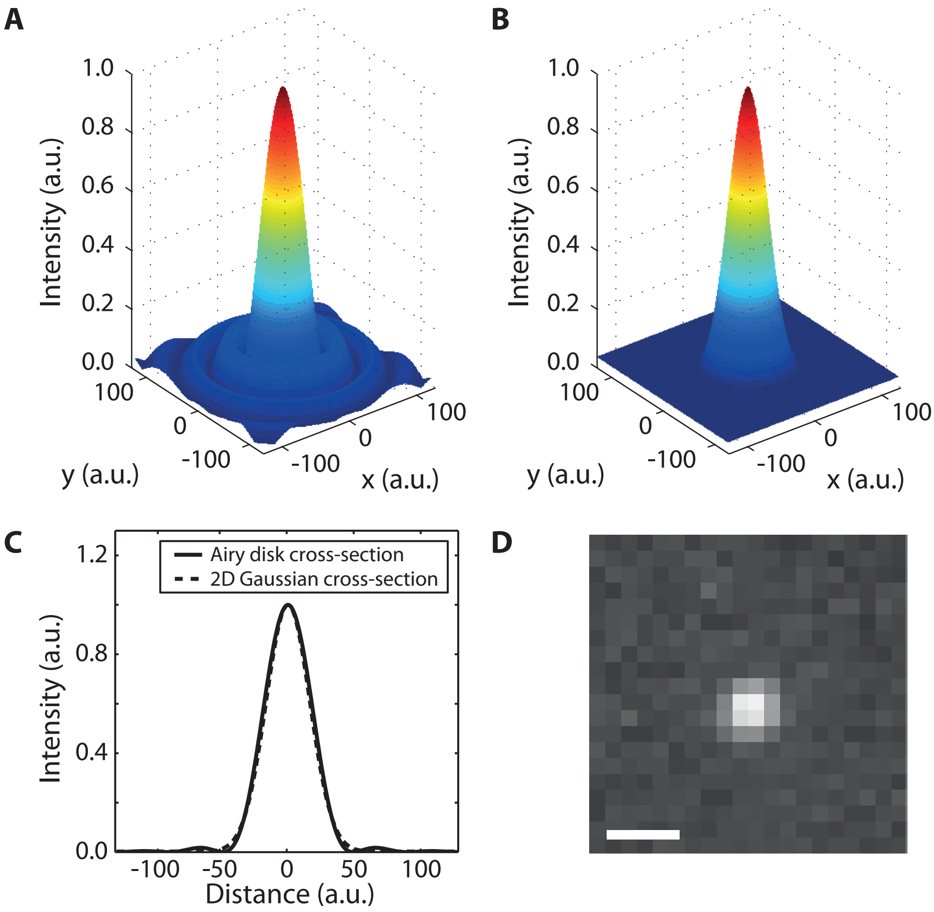

Figure 2.5: Approximation of the Airy disk with a 2D Gaussian distribution. (A) 3D representation of the Airy Disk as a Bessel Function of the first kind of order 1. (B) Gaussian approximation of the Airy disk in A. (C) Cross-sections through the centers of A and B. (D) Diffraction-limited image of a 40 nm sized polystyrene bead. Scale bar: 500 nm.

the squared standard deviation of the observed signal σ^2_{total} is given by the sum of the squared standard deviations of the PSF and the structure:

$$\sigma^2_{total} = \sigma^2_{object} + \sigma^2_{PSF} \tag{2.10}$$

A visualization of the resolution criterion as Abbe and Rayleigh defined it by Eq. 2.6 is shown in Figure 2.6A: two objects that are in a closer distance than Δx are considered as non-distinguishable. Although this definition gives reasonable values for optical resolution in general, using the first local minimum of the Bessel function as resolution criterion might seem quite arbitrary. Considering the original definition of resolution as the smallest distance in which two objects can still be distinguished, other factors apart from the mere wave-optical approach have an impact on spatial resolution as well. On the one hand, resolution is limited by the sampling rate. According to the Nyquist-Shannon criterion, a signal with a frequency f has to be scanned with a scan frequency f_{scan} that is at least twice of f in order to be resolved [29]:

$$f_{scan} > 2 \cdot f \tag{2.11}$$

In the case of imaging with a CCD camera, f_{scan} is given by the respective pixel size that therefore sets a limit for resolution in optical imaging. On the other hand, resolution is also influenced by the obtained signal-to-noise ratio. For this reason, it is under certain conditions

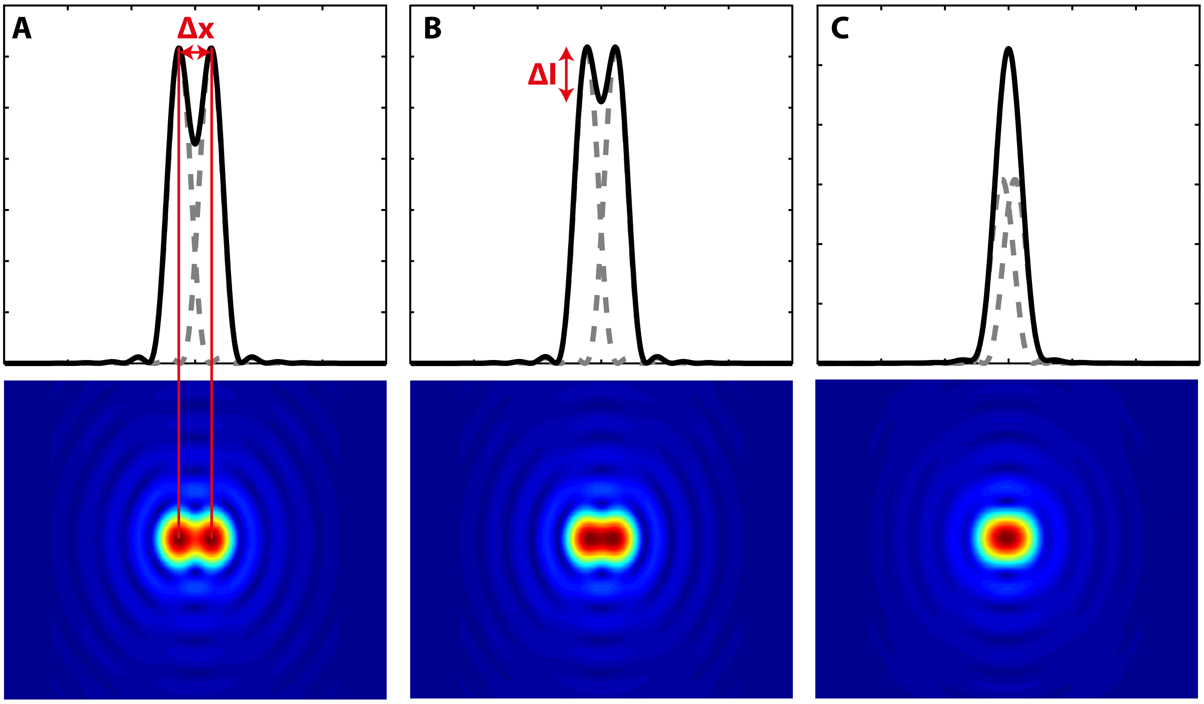

Figure 2.6: Different criteria for optical resolution. The upper panels are cross-sections through the respective lower panel showing two PSFs with distances declining from left to right. In the cross-sections, dashed lines represent the single PSFs and solid lines the merged signals. (A) Rayleigh criterion. The maximum of the second PSF is at the position of the first minimum of the first PSF. (B) Sparrow criterion. The intensity dip at the merged PSF is still visible although the distance between both PSF is smaller than in A. (C) Two PSFs are shown that cannot be distinguished neither by Rayleigh's nor by Sparrow's resolution criterion.

possible to distinguish the signals of two distinct point sources whose distance is smaller than the Rayleigh limit. This is, for example, the case when the intensity dip ΔI at the center of the merged PSFs can still be detected as shown in Figure 2.6B in contrast to the counterexample in Figure 2.6C depicting two unresolvable PSFs. Astrophysicist C.M. Sparrow therefore presented a new definition of the resolution limit based on ΔI [30]. Assuming a one-dimensional case with two objects with equal intensities at a distance a and an intensity of the merged signals I with respect to coordinate x, the achievable resolution a_0 can be found by setting the second derivate of I to 0 and solving the result for a:

$$\frac{\delta^2 I}{\delta x^2} = 0 \tag{2.12}$$

The detectability of ΔI largely depends on the given photon count rates pointing out the importance of an effective photon detection. For this reason, factors like the quality of the respective sample including image contrast, signal-to-noise ratio and the properties of the fluorescent emitters play a key role in fluorescence microscopy for the achievable resolution as well as the technical equipment that is used.

2.2.3 Total Internal Reflection Fluorescence Microscopy

Image background and Raman scattering are two of the most significant factors that may reduce image contrast and therefore as well the achievable resolution according to Sparrow's criterion as described in the previous section. Some sources of image background such as e.g. fluorescence of the used medium can be relatively easily avoided but especially when biological samples are investigated, there are sources of noise that can hardly be eliminated. One prominent example here is the autofluorescence observed when imaging cells. This phenomenon arises e.g. from absorption of light by aromatic amino acids or other aromatic compounds in the cell and can often easily overlay the fluorescence of the actual fluorescent label.

There are several methods to cut out background signals amongst which confocal microscopy [22] is one of the most prominent. Briefly, a pinhole is inserted into the optical beampath in order to block out-of-focus excitation and detection light. Thus, only a small volume at a defined position of the sample is imaged at a time and the probe has to be scanned to acquire the entire image. This approach has proven to be a powerful tool for fluorescence microscopy and spectroscopy. Nevertheless, it comes along with some disadvantages especially in combination with STORM and PALM: the most important point is that the need of a pinhole with a size small enough to effectively block out-of-focus fluorescence, inevitably leads to a loss of detected photons as well. As will be explained later in detail (Section 2.3), STORM and PALM rely on localization of single fluorescent emitters and the accuracy of this localization strongly depends on the number of detected photons (Section 2.3.2). Furthermore, image acquisition time depends on the scanning speed, which – if too slow – might result in missing fast dynamics of the fluorescence intensity of blinking single emitters.

Total Internal Reflection Fluorescence (TIRF) Microscopy, which was first presented by Ambrose [31] and further developed by Axelrod *et al.* [32, 33], offers a promising way to reduce background noise detection without losing signal intensity: total internal reflection of the incoming light on the phase interface between the glass microscope slide and the aqueous medium of the sample generates an evanescent wave penetrating into the aqueous medium (Figure 2.7A). In contrast to propagating waves, whose spatial expansion can be mathematically described by sine functions, evanescent waves show an exponential decay resulting in very short ranges ($< 200\,\mathrm{nm}$). Therefore, only objects close to the interface (e.g. structures on the cell membrane) are detected while cutting out the background. Although the restricted penetration depth approach does not allow the imaging of thick samples, it is an ideal tool for *in vitro* as well as for *in vivo* experiments when studying objects that are close to the microscope slide. Whereas evanescent waves are used for excitation, the emitted fluorescence is detected in the form of propagating waves according to the same principle, which is depicted in Figure 2.4. For this reason, the resulting image is still diffraction-limited. Improvement of image quality and resolution in TIRF compared to conventional widefield microscopy is therefore only a result of an improved image contrast according to the Sparrow criterion.

Figure 2.7B illustrates the refraction of a beam $\vec{k_1}$ at the interface of two Phases I and II with their respective refraction indices n_1 and n_2. In general, an incoming beam under the angle θ_1 will be split into a beam that is reflected at the interface ($\vec{k}_{2;reflected}$) and a refracted beam that penetrates into Phase II ($\vec{k}_{2;refracted}$). As the frequency of the wave does not change when passing the interface in contrast to the wavelength, a change of direction is necessary to maintain the continuity of the phase of the wave across the interface [34]. The connection between θ_1 and the new angle of the refracted beam, θ_2, follows Snell's law:

$$n_1 \sin\theta_1 = n_2 \sin\theta_2 \tag{2.13}$$

When $n_1 > n_2$, the refracted beam will therefore always have a larger angle from the perpen-

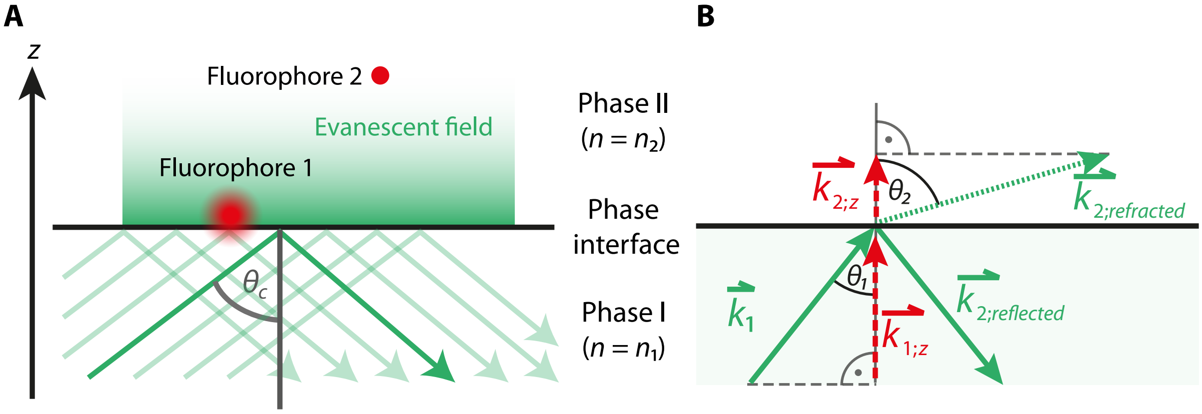

Figure 2.7: Principle of TIRF microscopy. (A) Incoming light with an incident angle equal or larger θ_C is totally refracted on the phase interface between two media with refraction indices n_1 and n_2 ($n_1 > n_2$) generating an evanescent wave whose low penetration depth allows only excitation of fluorophores in close distance to the interface. (B) A vector diagram illustrates the processes involved in refraction and total internal reflection. A propagating wave $\vec{k_1}$ incoming under angle θ_1 is refracted at the interface of Phases I and II returning a reflected ($\vec{k}_{2;reflected}$) and a refracted beam ($\vec{k}_{2;refracted}$). The latter, which has an angle θ_2 from the perpendicular axis, is not observed in the case of total internal reflection. $\vec{k_{1z}}$ and $\vec{k_{2z}}$ represent the z-components of $\vec{k_1}$ and $\vec{k}_{2;refracted}$, respectively.

dicular axis than the incoming beam. When θ_1 is gradually increased, θ_2 will eventually reach 90° whereupon Eq. 2.13 can be transformed into

$$\sin\theta_1 = \frac{n_2}{n_1} \tag{2.14}$$

where $\theta_1 = \theta_c$ is defined as the critical angle. For all $\theta_1 \geq \theta_c$, the incoming beam is totally reflected at the phase interface and no refracted propagating beam in Phase II can be observed. For example, at the interface between a glass cover slide with $n_1 = 1.52$ and an aqueous solution with $n_2 = 1.33$, θ_c would be 61.0°.

According to Figure 2.7B, the magnitude of the refracted wave propagating in z-direction $\vec{k_{2z}}$ is connected to θ_2 and the magnitude of $\vec{k}_{2;refracted}$ by the following equation:

$$\cos\theta_2 = \frac{k_{2z}}{k_{2;refracted}} \text{ or } k_{2z} = k_{2;refracted}\cos\theta_2 = k_{2;refracted}\sqrt{1-\sin^2\theta_2} \tag{2.15}$$

Using Eq. 2.13, this expression can be transformed to:

$$k_{2z} = k_{2;refracted}\sqrt{1-(n_1^2/n_2^2)\sin^2\theta_1} \tag{2.16}$$

In the case of total internal reflection, which is given when $\theta_1 \geq \theta_c$, k_{2z} will be imaginary. This result seems plausible as it proves the absence of a propagating wave penetrating into Phase II under the given conditions. In order to understand why there is still an evanescent electromagnetic field that is able to overcome the interface, it is necessary to focus on the distinction between propagating and evanescent waves, which is a result of the general wave equation describing the electromagnetic field $\vec{E}$ at time t and spatial coordinate $\vec{r}$ as:

$$\vec{E}(\vec{r},t) = \vec{E_0}[\mathrm{e}^{i(\vec{k}\cdot\vec{r}-\omega t)} + \mathrm{e}^{-i(\vec{k}\cdot\vec{r}-\omega t)}] \tag{2.17}$$

The connection between spatial and temporal frequencies, $\vec{k}$ and ω, is $|\vec{k}| = \frac{\omega}{c} = \frac{2\pi}{\lambda}$ where c is the speed and λ the wavelength of light. If the spatial term in Eq. 2.17 is real, the resulting wave will propagate in the form of a sine wave whereas an imaginary term will result in an evanescent wave with a mean decaying length of $1/|\vec{k}|$

As k^2 can also be expressed by the sum of its squared contributions for the different spatial directions as well as r^2 ($k^2 = k_x^2 + k_y^2 + k_z^2$ and $r^2 = r_x^2 + r_y^2 + r_z^2$), Eq. 2.17 can also be written as:

$$\vec{E}(\vec{r}, t) = \vec{E_0}[\mathrm{e}^{-i\omega t}\mathrm{e}^{ik_x r_x + ik_y r_y + ik_z r_z} + \mathrm{e}^{i\omega t}\mathrm{e}^{-ik_x r_x - ik_y r_y - ik_z r_z}] \tag{2.18}$$

When an imaginary value of k_{2z}, which is obtained by Eq. 2.16 in the case of total internal reflection, is inserted into the term of Eq. 2.18 describing the propagation of the wave in z-direction, the corresponding expression $e^{-k_z r_z}$ will now describe a wave in z-direction, $\vec{E_z}$, with an exponential decay. As the amount of absorption of light by bound electrons is proportional to $|\vec{E}|^2$, the penetration depth d of an evanescent wave is usually defined as the depth where $|\vec{E_z}|^2$ has declined to 1/e. Using Eq. 2.16 and $|\vec{k}| = \frac{2\pi}{\lambda}$, d can also be expressed on the base of the respective refraction indices, the wavelength of light and the angle of the incoming light:

$$d = \frac{\lambda}{4\pi\sqrt{n_1^2 \sin^2\theta_1 - n_2^2}} \tag{2.19}$$

For instance, a penetration depth d of approximately 200 nm would be obtained by Eq. 2.19 using the values from the previous example with $n_1 = 1.52$ and $n_2 = 1.33$ assuming an angle of incident of 63.0° and a wavelength of light of 642 nm.

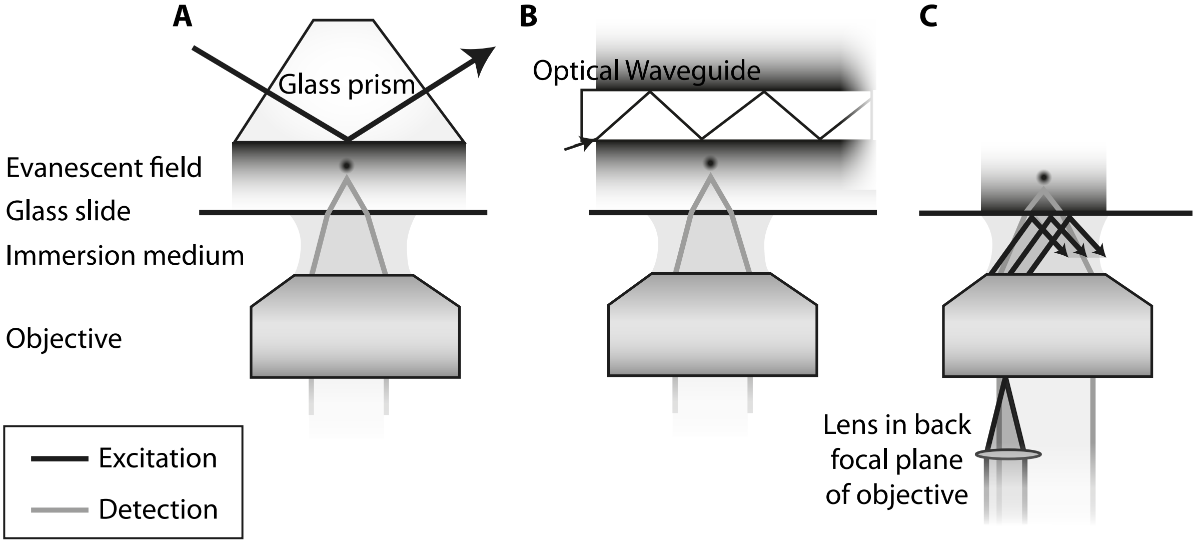

Figure 2.8: Different realization approaches for TIRF microscopy. Excitation (dark gray) and detection pathways (light gray) are shown for (A) prism-, (B) waveguide- and (C) objective-type TIRF microscopy.

There are three major approaches for technical realization of TIRF microscopy (TIRFM), which are depicted in Figure 2.8. In the first approach (Figure 2.8A), the excitation beam is directed into a glass prism at an angle large enough for total internal reflection at one of the outer surfaces. Hence, it is possible to generate e.g. an evanescent field at the bottom side of the prism. The sample has to be placed below this prism in the range of the evanescent field and the emitted fluorescence can be detected with the help of an objective that is placed on the other side of the slide. Although this setup is quite intuitive and offers various applications in the field of single-molecule and *in vitro* studies, the required sample configuration can be disadvantageous. Particularly, imaging of cells is technically challenging as it is difficult to place a sample chamber containing the cells and the imaging buffer or growing medium under the prism while maintaining the cells in the evanescent field. The second approach, waveguide TIRFM (Figure 2.8B) [35], faces the same problem despite a different approach for the generation of the evanescent field. Here, the exciting beam is coupled into an optical waveguide and undergoes total internal reflection at the outer surfaces of the waveguide thereby generating an evanescent field.

In order to make TIRF accessible for imaging of cells, objective-type TIRFM was developed as an alternative [36]. As depicted in Figure 2.8C, a collimated laser beam is focused on the back focal plane of the objective. The set of lenses that form the objective as a consequence generates another collimated beam that leaves the objective under an angle that increases with the displacement of the excitation beam from the center of the objective. When this displacement gets large enough and θ_c is reached, total internal reflection occurs at the interface between the glass slide and the sample medium. In order to reach these high angles, objectives for objective-type TIRFM must provide a high NA. For example, when using glass slides and aqueous buffers for microscopy, a NA larger than 1.4 is typically required. This value can only be obtained by using oil as immersion medium. While increased background noise due to autofluorescence of the oil is no longer a problem with modern objectives, partial detection of the total reflected laser beam might still be a drawback compared to waveguide- or prism-type TIRFM. Implementation of an appropriate set of emission filters, however, can cut off the scattering light effectively and make objective-type TIRFM a powerful and widely-used tool to study the structures and dynamics of biological systems.

2.3 Super-resolution fluorescence microscopy

For a long time, the diffraction limit was believed to be the utmost barrier for further improvement of the resolution capability of far-field light microscopes. It was assumed that the way towards better images could only lead over techniques like confocal microscopy [22] or TIRFM that principally increase resolution by enhancement of image contrast according to Sparrow's resolution criterion (cf. Sections 2.2.2 and 2.2.3). However, many biological processes on the cellular level occur on a much smaller scale making it impossible to resolve them simply by contrast enhancement. For these applications, methods providing a higher resolution than the diffraction limit are required, which can be summarized under the term of super-resolution microscopy.

One way to evade the diffraction limit of light is near-field scanning optical microscopy, which had already been proposed in the 1920's [37] and was technically realized about sixty years later [38, 39]: it aims at using the optical near-field that is not subject to the far-field diffraction limit. However, near-field microscopy is still technically highly challenging compared to far-field microscopy. Furthermore, imaging is limited to the low penetration depth of the near-field of $\sim 200\,\text{nm}$ that allows only surface imaging similar to TIRFM. Near-field scanning microscopy further requires scanning of the sample with either a tip or an aperture, which can both serve as near-field sources and which have to be brought in close proximity to the sample.

When looking for other options to increase optical resolution as defined by the Rayleigh criterion, an approach to increase the resolution Δx obtained by Eq. 2.6 would be to reduce the excitation wavelength. For example, the use of X-ray beams would provide excitation wavelengths smaller than 200 nm, allowing Δx to be smaller than 100 nm. Recent developments showed that is possible to achieve resolutions down to approximately 10 nm with X-ray microscopy [40]. Another option would be the use of non-optical techniques, where electron microscopy methods are the most prominent examples. With SEM, a resolution down to 3 nm is obtainable [41] and TEM is able to go even further to resolutions below 1 nm [42]. However, all these techniques come along with a number of drawbacks compared to light microscopy especially for imaging of biological samples where the invasiveness caused by the use of X-ray or electron beams is evidently one of the most critical ones. Both are highly energetic and can easily damage a sensitive structure. As a consequence, this allows only imaging of fixed samples and thereby also rules out any form of live cell or *in vivo* experiments. Special demands regarding sample preparation have to be considered as well: for example, the surface of samples for SEM has to be conducting. This requires metal coating in case of biological samples, which obviously means a massive modification of the sample. Furthermore, optical microscopy makes it much easier to differentiate between different structures as it is possible to label diverse structures specifically with differently colored dyes. Due to all these reasons, it would be beneficial to combine the advantages of optical microscopy as described in Section 2.2.1 with increased resolution. This would provide an eminently suited method to obtain so far unknown details of structures and processes on the nanoscale without the limitations of non-optical methods.

2.3.1 Localization-based super-resolution microscopy

In Section 2.2.2, it was shown that the constraint in separating two fluorescent emitters in close proximity is based on the merging of their respective PSFs. Therefore, it seems obvious that this problem does not occur if only one fluorescent emitter is present in a diffraction-limited area. If this is the case, the position of the single fluorophore can be detected with very high precision by fitting the PSF signal to an appropriate model function. This can either be the exact Bessel function or, to a good approximation, a two-dimensional Gaussian function as e.g. given by Eq. 2.9. The centroid position of the Gaussian corresponds to the position of the original molecule, which can thus be localized with a very high accuracy [43]. Today, localization precisions below 10 nm can be reached in the lateral dimensions [44, 45]. When the PSF can be approximated by a 2D Gaussian function and all sources of noise except of shot noise [46], which is a result of the particle character of light (see Section 3.1.3), can be neglected, the localization accuracy Δx is inversely proportional to the square root of the number of photons N that were collected. However, other sources of noise can increase Δx (see also Section 2.3.2), which is then given by

$$\Delta x \geq \frac{\sigma_x}{\sqrt{N}} \tag{2.20}$$

where σ_x is the PSF standard deviation in the respective dimension.

Due to limited technical capacities in the past, imaging of single molecules was considered to be only hypothetical or as Erwin Schrödinger said it in 1952 [47]: "(...) we never experiment with just one electron or atom or (small) molecule. In thought-experiments we sometimes assume that we do (...)". However, it was not possible to foresee the rapid development of highly advanced techniques such as extremely sensitive detectors that finally proved Schrödinger wrong in this case. William E. Moerner was the first to measure the absorption spectra of a single molecule embedded into a host crystal at cryogenic temperatures [11]. Based on this first breakthrough, the technique was subsequently extended to fluorescence imaging in solution first at cryogenic [48] and later also at biologically relevant temperatures [49].

Localization of single fluorophores alone, however, does not allow the visualization of a complex structure with high resolution. These structures have to be marked with many fluorophores in order to avoid undersampling and to fulfill the Nyquist-Shannon criterion as given by Eq. 2.11 [29]. When this statement is transfered to the problem of labeling density, this means that the resolution cannot be better than twice the distance between the distinct labels. For this reason, a high labeling density is required, what inevitably leads again to a situation where the distance between two fluorophores is smaller than the diffraction limit.

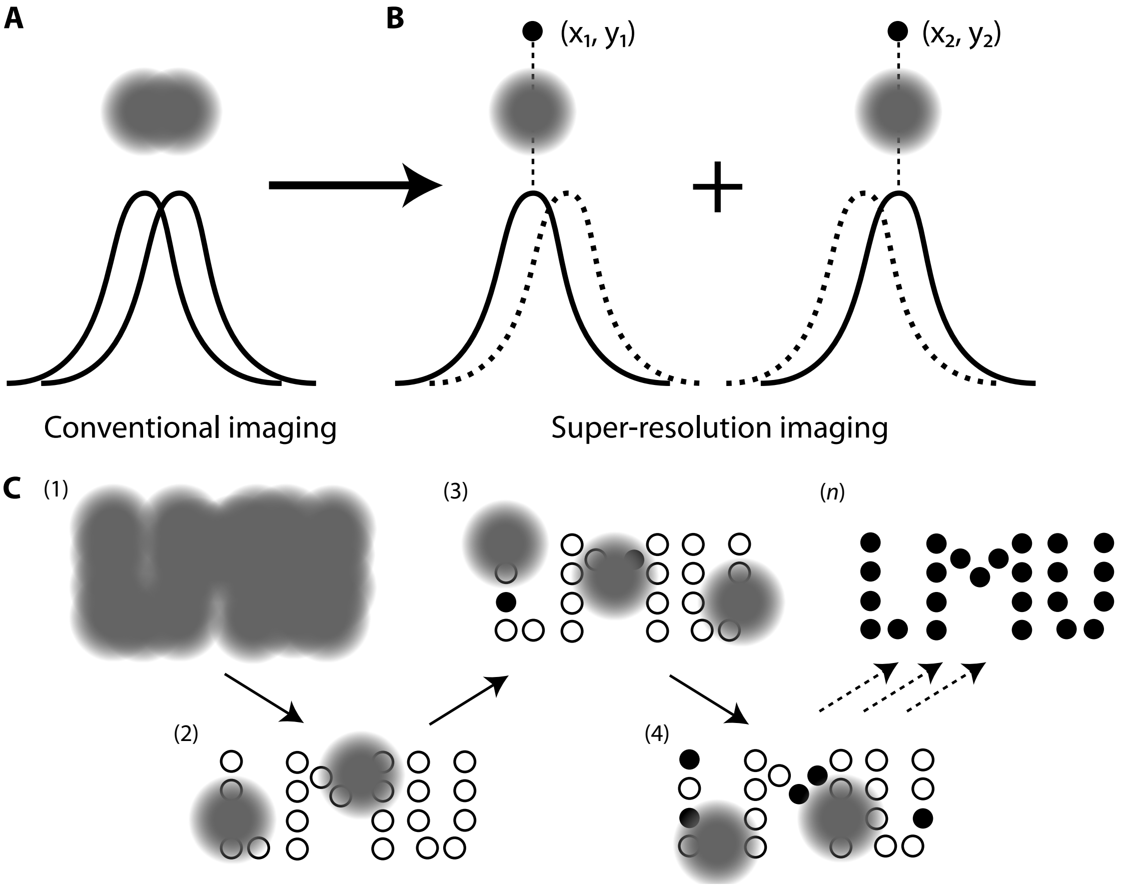

Figure 2.9: Principle of localization-based super-resolution methods. (A) A conventional, diffraction-limited image cannot separate the merging PSFs of two adjacent fluorescent emitters. (B) The fluorophores are successively activated (solid lines) and deactivated (dotted lines) and the centroid positions of the detected PSFs are determined with high accuracy. (C) Demonstration of the method on a hypothetical arrangement of fluorophores. The structure cannot be resolved in the conventional image (step 1), but stochastic activation and deactivation of single fluorophores (steps 2-4) gradually reveals the underlying pattern by summing up the position of all localized emitters (step n) (large gray circles: activated fluorophores, filled black circles: localized fluorophores, empty circles: fluorophores still to be localized).

In 1994, Eric Betzig presented an idea [7] how this problem could be overcome, which is visualized in Figure 2.9A and B: He suggested to label the respective structures with fluorophores that can be switched between a dark and a bright state in a way that only one fluorophore is emitting photons in a diffraction-limited spot at a time. For example, two fluorophores within a distance smaller than the diffraction limit as depicted in Figure 2.9A cannot be distinguished when both are in an active, fluorescing state. In Figure 2.9B, the two emitters are imaged sequentially using the ability of the dyes to switch between dark and bright states. By this means, it can be achieved that only one of them is active in each step of data acquisition whereas the other is in a dark state. The positions of the fluorophores can now be sequentially localized independently of each other and the calculated positions can be used afterwards to render a high-resolution image. Typically, the activation and deactivation process is stochastic and only the average switching rate can be influenced.

Figure 2.9C shows how this principle can be applied to a more complex hypothetical sample: the underlying structure cannot be resolved when all fluorophores are active at the same time (Figure 2.9C, step 1). As a result, a situation has to be reached, where only so many fluorophores are active that their PSFs do not interfere with each other (Figure 2.9C, step 2). It is important to emphasize that the number of stochastically activated molecules in each activation step has to be low to keep the probability of activating more than one fluorophore in a diffraction-limited area low. It is obvious that this would have a considerably negative impact on resolution and quality of the respective image. In summary, it can be stated that best results can be achieved when the probability for activation is low whereas the probability for deactivation is high. In the following steps (Figure 2.9C, step 3 and 4), all active fluorophores are deactivated and others are activated stochastically. The cycles of activation and deactivation are subsequently repeated n times until it can be assumed that all fluorophores have been activated and imaged at least once. Depending on the number of fluorophores and sample size, a high number of cycles might be required to obtain the complete image. The localization of the fluorophores can be carried out either immediately after registration of the respective event, or – what is more common – after data acquisition concludes. After data acquisition and particle localization, the combined localizations finally lead to a super-resolution image (Figure 2.9C, step n), which reveals the actual structure of the sample.

There are several ways how to experimentally realize the required stochastic switching of fluorophores, which are summarized in Table 2.1 and will be discussed in detail below. Depending on the fluorescent label, different names for localization-based super-resolution methods have been coined although all of them follow the principle as it is described in Figure 2.9. Independently of the respective dye, imaging is typically performed on a conventional widefield or TIRF microscope as described above. Apart from the straightforward approach for this kind of microscope, it allows fast data acquisition combined with a sufficient photon detection efficiency, which is required to achieve a high localization accuracy (Eq. 2.20 and Section 2.3.2) and image resolution.

Table 2.1: Overview of different localization-based super-resolution methods using stochastic activation and deactivation of fluorophores

Methods	**Fluorophore**	**Activation step**		**Deactivation step**	
STORM	photo-switchable organic dyes	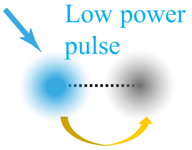	**triplet → singlet** conversion induced by **energy transfer**	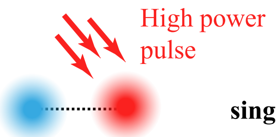	**singlet → triplet** conversion induced by **high laser power**
dSTORM		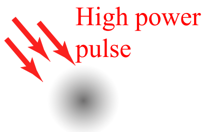	**triplet → singlet** conversion induced by **high laser power**	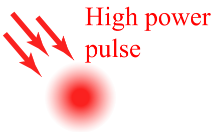	
PALM/ fPALM	photo-switchable fluorescent proteins	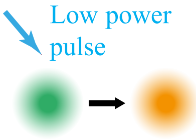	**conformational change**	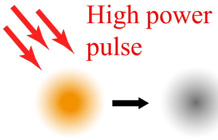	**photobleaching** or **conformational change**

2.3.1.1 Photoactivated Localization Microscopy (PALM)

Photoactivated Localization Microscopy (PALM), which is based on photoinduced activation or spectral shifts of fluorescent proteins, was the first localization-based super-resolution microscopy method, which was published [9]. In 2006, Betzig *et al.* succeeded to present the experimental realization of the method Betzig had proposed earlier [7] although it has to be mentioned that Hess *et al.* independently developed a very similar method shortly afterwards that they called Fluorescence Photoactivation Localization Microscopy (fPALM) [50]. Eric Betzig received the Nobel Prize in Chemistry for this achievement in 2014 together with Stefan Hell, the inventor of Stimulated Emission Deletion Microscopy (STED, Section 2.3.4) and William E. Moerner, who – apart from his work on single molecule fluorescence detection – was the first to discover a fluorescent protein showing photoconversion. This class of proteins shows an emission that can switch between dark and bright states or between different colors due to conformational changes that can be effectuated by irradiation with light of a certain energy.

Although the Green Fluorescent Protein (GFP) was already discovered in 1962 by Shimomura *et al.* [51], it was Moerner who found a version of GFP that would go to a dark, non-fluorescent state upon irradiation with blue light at 488 nm as a result of light induced conformational changes of the protein structure. Upon irradiation at 405 nm, it can be converted back to a fluorescent state with an absorption maximum at approximately 500 nm and an emission maximum at 535 nm [52]. These properties can be used for super-resolution imaging according to the principles described above: The photoswitchable protein is tagged to the structure of interest and the sample is exposed to activation-deactivation cycles: First, a laser pulse at a wavelength of 405 nm is used for activation. The power is kept low in order to keep the probability for photoconversion low as it has to be ensured that only one fluorescent emitter is activated within a diffraction-limited area. After activation, the converted, fluorescent state can be imaged by excitation at 488 nm and the detected fluorophores can be localized. The same wavelength will also eventually convert the molecules back to the non-fluorescent state. A high laser power (in this case at 488 nm) increases the probability of conversion to the dark state and therefore accelerates the data acquisition process, which is essential for the study of dynamic processes.

In the case of the described GFP version, the protein switches from a dark to a bright state and back in a reversible process and many switching cycles of a single molecule can be observed until it is eventually photobleached. However, there are also many examples of fluorescent proteins where photoconversion is irreversible. Here, only photobleaching can be used to switch of fluorophores once they were activated. Additionally, switching is not only possible between dark and bright states but emission wavelengths of fluorescent protein can also switch between two different colors of the visible spectrum. An example for a fluorescent protein that is switched both irreversibly and from one visible color to another, is the mEos protein, which is the monomeric form of tetrameric EosFP. The protein was originally isolated from stone coral *Lobophyllia hemprichii* [53] and has its absorption and emission maximum in the green part of the electromagnetic spectrum (506 nm and 516 nm, respectively). Irradiation with UV light induces conformational changes that result in red-shifted absorption and emission maxima at 571 nm and 581 nm, respectively. As mentioned before, the process is irreversible, which means that the red state is monitored after activation until the molecule is photobleached.

An advantage of PALM compared to other super-resolution techniques is its compatibility with living systems. It is, for example, possible to make a cell express a DNA construct that encodes a mutant of the protein of interest that is fused to a fluorescent protein. This overcomes the need of procedures such as sample fixation or membrane permeabilization that cannot be brought in accordance with living systems. There is also no requirement of a special imaging buffer as for other methods (see below). However, this approach also brings a significant drawback: tagging fluorescent proteins to other proteins is always risky as the tag can change the behavior of the original protein sometimes even to a point where it is no longer functional. Furthermore, the number of photons emitted by fluorescent proteins is typically lower than for e.g. organic fluorescent dyes, which, according to Eq. 2.20, results in a loss of localization accuracy. Therefore, despite their advantages, it would be desirable for super-resolution microscopy to utilize further classes of suitable fluorophores without the disadvantages of fluorescent proteins.

2.3.1.2 Stochastic Optical Reconstruction Microscopy (STORM)

One alternative though closely related method to PALM is called Stochastic Optical Reconstruction Microscopy (STORM), which was published by Rust *et al.* [10] in the same period of time as PALM and fPALM. The main difference to PALM is the class of fluorophores that is used: instead of photoconvertible fluorescent proteins, organic fluorescent dyes are used here. In fact, many organic dyes provide the required ability to switch between two different fluorescent states. However, in order to be suitable for super-resolution microscopy, they ideally need to have three further characteristics in order to be able to provide good results [54]: First, they should emit a high number of photons in order to achieve a high localization accuracy (see Eq. 2.20 and Section 2.3.2). For the same reason, it is secondly favorable to obtain as many switching cycles as possible before photobleaching occurs. Finally, the average time the dyes spends in the 'on'-state, which is the state that is used for imaging, should be short compared to the time in the dark state in order to keep the probability of multiple activations as low as possible.

Among various potential dye classes such as photochromic rhodamines [55] and caged dyes [9, 56], fluorescent dyes that can be switched to a metastable dark state like a triplet-state [57, 58] have been proved to fulfill these conditions best. Especially the cyanine dyes Cy5, Alexa Fluor 647 and, to a certain extent, also Cy3 stand out in optimal switching properties for STORM [54]. The underlying photophysical mechanism has not been fully understood, although there is some evidence for the involvement of a triplet state: it is indicative that blinking only occurs in the absence of any kind of triplet quencher such as oxygen. This means that STORM experiments require an oxygen scavenger buffer (e.g. based on glucose oxidase [54]), which removes all oxygen from the surrounding medium. Switching of cyanine dyes further depends on the presence of a reducing agent like thiol agents (e.g. β-mercaptoethylamine or β-mercaptoethanol), which were found to build covalent conjugates with the dye [58]. The pathway of this reaction is assumed to lead over a triplet state as well. This was confirmed by van de Linde *et al.* [59] who could provide evidence for the formation of a metastable radical ion in the case of rhodamine dyes in the presence of thiol regents. Switching of cyanine dyes therefore consists of activation-deactivation cycles, where the deactivation corresponds to a reduction and the activation to an oxidation reaction.

As depicted in Table 2.1, the reduction causing deactivation by conversion of the molecule from singlet to triplet state can be triggered by excitation with high laser powers. Irradiation at the same wavelength and power can also be used to facilitate the required oxidation reaction that will eventually lead to a conversion from the dark triplet back to the fluorescent singlet state. This activation can be enhanced when a second dye (activator dye) with an absorption maximum lower than the actual monitored dye (reporter dye) is found in very close proximity to the reporter (distance $< 10\,\mathrm{nm}$) [60]. Excitation of the activator dye then triggers the conversion of the reporter dye from the dark to the bright state. It is assumed that an energy transfer from the activator dye to the dark state of the reporter dye is responsible for this phenomenon [61]. The observed distance dependence appears to be steeper than for Fluorescence Resonance Energy Transfer [20] but the details of the mechanism have so far remained unknown.

Regardless of the photophysical aspect, the combination of activator and reporter dyes is an ideal tool for multi-color super-resolution imaging, which would allow the imaging of two distinct structures simultaneously in super-resolution. There are two different possibilities to combine activator and reporter dyes for this purpose [60]: On the one hand, the same reporter dye can be used for all structures and combined with different activator dyes for each of them to specifically activate only one of them at a time. On the other hand, different reporter dyes can be used for the distinct target structures and all of them are simultaneously activated by the same activator dye. The second approach requires a very accurate alignment of the detection channels for the respective colors on the nanoscale. Furthermore, chromatic aberrations and different switching kinetics of the various reporter dyes might cause problems. For example, different photon yields can lead to deviating optical resolutions. Therefore, the first approach is usually preferred although activation crosstalk might occur, which must be corrected [60]. This is, for example, the case when the excitation spectra of the respective activator dyes overlap and are to a certain extent excitable with more than one of the used activation wavelengths. Furthermore, there is also a certain probability that activation of cyanine dyes through oxidation occurs spontaneously in addition to activation.

2.3.1.3 Direct Stochastic Optical Reconstruction Microscopy (dSTORM)

As mentioned before, the presence of an activator dye is actually not essential for the switching of the cyanine dyes. Heilemann *et al.* [62] developed a modification of STORM in 2008 that they called 'direct STORM' or dSTORM, which uses only the reporter dye. One option to realize dSTORM is to exploit the fact that activation and deactivation can be achieved with the same wavelength when the power is high enough. Although high laser powers are desirable for imaging of the reporter dye in STORM as well to obtain fast switching cycles, it is an absolutely indispensable requirement for dSTORM. It is also possible, despite the absence of an activator dye, to use two separate wavelengths in dSTORM for both steps although higher laser powers are required for activation than is the case in STORM. It has not been clarified how this mechanism works in detail although it was shown [59] that the metastable triplet states formed in the presence of thiol regents show absorption peaks in a spectral range between 350 and 550 nm, which are wavelengths that are typically used for activation in STORM (e.g. 488 nm for activation of Cy5). Another technique that is based on the same observation and used the switch of photochromic rhodamines, was presented by Fölling *et al.* [55, 57] and called ground-state depletion and single-molecule return (GSDIM).

dSTORM has the clear advantage compared to STORM that it is no longer necessary to occupy labeling positions on the target structure with a dye that is not actually imaged. When all positions can be used for the reporter dye, the apparent labeling density increases and therefore also the achievable resolution according to the Nyquist-Shannon criterion becomes better. Furthermore, sample labeling for dSTORM is less challenging as the condition is omitted to bring two different dyes in a distance close enough to allow the required energy transfer for STORM. On the contrary, STORM has proven to be superior in multi-color applications as the use of specific activator dyes for different structures allows specific activation of those reporter dyes that are attached to these structures and separate them from each other. The only option for multi-color dSTORM imaging is the use of multiple reporter dyes. However, deviating switching kinetics for the different dyes might be unfavorable, which might result in the same problems as for STORM with different reporter dyes.

2.3.2 Determination of resolution in STORM and PALM

In order to be able to evaluate the quality of STORM and PALM images, it is mandatory to find a comparable way to define and calculate the resolution of the reconstructed high-resolution images. The latter can be limited by two factors: the first is based on the accuracy with which a single fluorescent emitter can be localized whereas the second, called structural resolution, is given by the fact that the actual sample and the attached label (like e.g. antibodies, fluorescent proteins) have a finite size. The original structure will therefore be increased by the size of all molecules the label consists of. In the case of immunostaining, when both primary and an additional secondary antibody binding to the primary antibody are used, the size of the structure can increase by more than 50 nm as will be demonstrated later (Section 3.5). This again involves the Nyquist-Shannon criterion, which states that the structural resolution of an image can never be higher than two times the distance between the respective labels. This means that if the distance between the labels gets larger just because of the intrinsic size of the label, the ultimate limit for the best achievable resolution will get worse. In this context, it is also important to achieve a good labeling density. If the latter is low, the structural resolution decreases as well.

Whereas the structural resolution represents the lowest limit for resolution in super-resolution microscopy, this value can be compromised by the localization accuracy Δx. For a single fluorophore, Δx can be statistically described by the standard error of the mean (see also Eq. 2.20)

$$\left\langle (\Delta x)^2 \right\rangle \approx \frac{\sigma^2}{N} \tag{2.21}$$

where σ is the standard deviation of the PSF of the detected fluorescence signal and N the number of collected photons. However, this formula only considers photon noise and ignores other error sources such as pixelation noise caused by the finite size of each pixel a and background noise b. For this purpose, Eq. 2.21 can be extended as shown by Thompson *et al.* [43] finally obtaining the following expression:

$$\left\langle (\Delta x)^2 \right\rangle = \frac{\sigma^2 + a^2/12}{N} + \frac{4\sqrt{\pi}\sigma^3 b^2}{aN^2} \tag{2.22}$$

An effect that is not addressed by Eq. 2.22 is the influence of fluorescence anisotropy on localization accuracy. When a fluorescent molecule is not able to rotate freely, the respective dipole orientation has a significant effect on the shape of the observed PSF. For particles with a fixed dipole orientation at the interface between a glass slide and an aqueous imaging medium, an additional localization error up to 10 nm can occur [63], which can increase up to 40 nm in the presence of optical aberrations [64]. However, when the emitters are able to rotate freely, these effects are negligible, which is for example the case when dye molecules are linked to the respective structure by an aliphatic chain.

The theoretical minimum of localization precision is given by the Cramér-Rao lower bound (CRLB) that calculates the smallest variance achievable for any parameter set p using the model function $f_p(x,y,z)$ (e.g. a Gaussian approximation). For example, the CRLB σ_x^2, for the localization precision in x is given by the following expression where N is the number of collected photons [65, 66]:

$$\sigma_x^2 \geq \frac{1}{N \int\int\int_{-\infty}^{+\infty} \frac{1}{f_p(x,y,z)} \left(\frac{\partial f_p(x,y,z)}{\partial x} \right)^2 \mathrm{d}x\mathrm{d}y\mathrm{d}z} \tag{2.23}$$

It is important to point out in this context the difference between localization accuracy and the actual resolution. Whereas the first simply defines the accuracy with which the centroid of the PSF of a single fluorescent emitter can be localized, resolution is limited by the smallest distance of two fluorescent emitters that can be still distinguished as defined by the Sparrow criterion (cf. Section 2.2.2). This means that although localization accuracy gives a quite reasonable estimate for super-resolution image quality, the actual resolution may be worse as the occurrence of multiple activations cannot always be excluded or identified. It is obvious that the centroid position of a merged signal originating from two or more emitters in close proximity can still be calculated fairly accurately depending on photon statistics whereas resolution clearly decreases. In these cases, advanced analysis algorithms such as DAOSTORM [67] can help to provide a good high-resolution image nevertheless.

Typically, resolutions down to 20 nm are achievable with STORM although certain modifications allow even better results. Xu *et al.* [68] combined STORM with the concept of 4Pi microscopy that was developed by Hell *et al.* [69] before. Two objectives are placed on both sides of the sample allowing the detection of twice the amount of photons as with a conventional setup. Applied to a STORM experiment, it will as a consequence increase localization accuracy according to Eqs. 2.21 and 2.22. With this approach, which is called dualObjective STORM, resolutions down to 9 nm were reached. This value is close to the size of a single dye molecule, beyond which no further increase of resolution is possible with PALM, STORM or dSTORM without violating the Nyquist-Shannon criterion (Eq. 2.11).

2.3.3 Three-dimensional localization-based super-resolution imaging

STORM, dSTORM and also PALM have proven to be valuable methods to explore the world of nanoscopy. However, biology happens in the third dimension. Therefore, it would be beneficial to extend this method to localize the axial coordinates of the fluorophores as well. The challenge here is to extract this information from a two-dimensional image.

One approach was developed by Shtengel *et al.* [70]. Instead of using the raw shape of the PSF, they collected the emitted fluorescence with two objectives similar to 4Pi microscopy [69]. If the fluorophore is not exactly in the middle between both objectives, this results in two detection pathways with different lengths. If these two beams are recombined, the emitted photon will interfere with itself. The interference pattern depends on the different pathway lengths, which can be used to deduce the position of the emitter. This approach has provided the highest achievable axial resolutions compared too all other super-resolution techniques (Table 2.2). However, it is technically highly challenging as it depends on most accurate alignment of the system to generate the required interference pattern.

Table 2.2: Lateral and axial resolutions achievable with different 3D localization-based super-resolution methods

Method	**Resolution**	
	lateral	**axial**
iPALM [70]	23 nm	9.8 nm
Biplane fPALM [71]	30 nm	75 nm
Astigmatism [72, 73]	20 nm	50 nm
Dual-objective astigmatism [68]	9 nm	19 nm

A more straightforward method deduces the axial position of a fluorescent emitter from the PSF shape. Even in a conventional widefield microscope without any modification, some –

though limited – information about the axial position is provided. The left part of Figure 2.10A shows the detection pathway of a conventional widefield microscope. The objective lens transforms light emitted by the fluorophore into a collimated beam and another lens subsequently focuses it onto the detector. If the object is significantly smaller than the diffraction limit, its observed image will then correspond to the PSF of the system (cf. Section 2.2.2). Depending on the position of the imaged object relative to the focal plane, the size of the PSF will change. When the emitter is in focus, it will appear the smallest and become larger in size with increasing distance of the emitter from the focal plane. Thus, the axial distance form the focal plane of a single, diffraction-limited fluorescent emitter can be deduced from the size of the detected PSF. However, this method is not able to differentiate whether the fluorophore is above or below the focal plane.

In order to make these two sites distinguishable, Juette *et al.* [71] presented an approach named Biplane fPALM. They suggested to split the detected fluorescence signal into two parts after passing the lens that focuses the beam onto the detector with the condition that the pathway of one of the two beams to the detector is longer than the other. As a consequence, only one of them is in focus. From the difference between the focused and the defocused image, the axial position can be calculated. A slight drawback of this method is the fact that the imaging region of the CCD detector has to be split into two regions, which reduces the available field of view. Alternatively, two separate detectors can be used to perform 3D imaging.

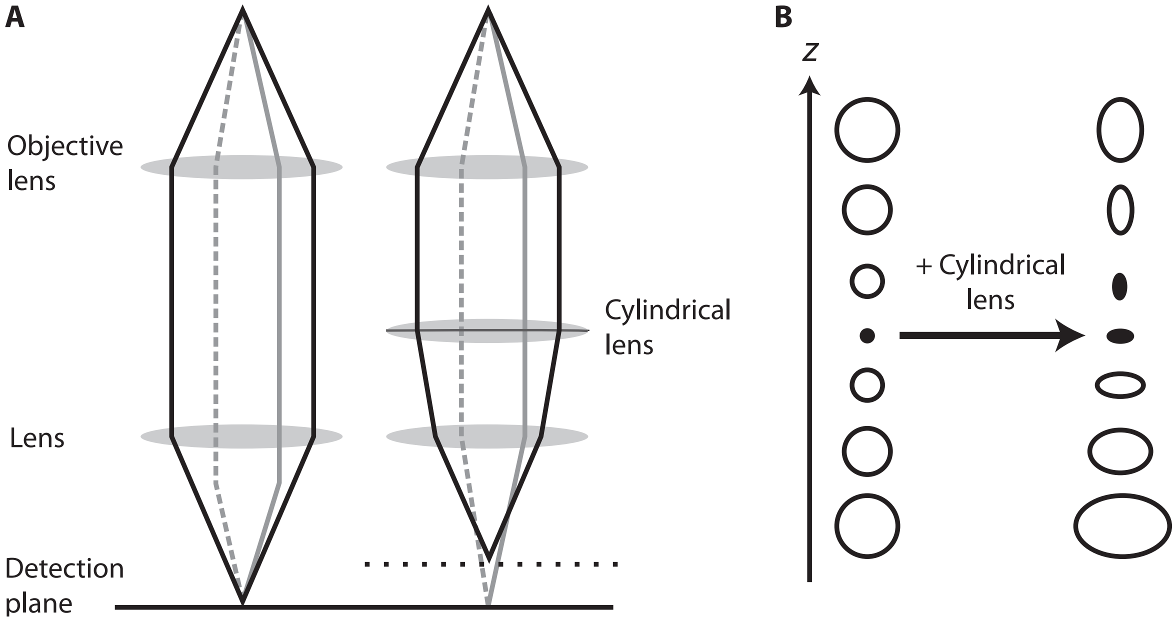

Figure 2.10: 3D super-resolution microscopy using optical astigmatism. (A) The focal plane of one optical direction is shifted upon introduction of a weak cylindrical lens into the detection pathway of an optical microscope resulting in an astigmatism of the detected PSF (B).

Another approach, which was used in this thesis and which is based on the same idea, requires even less modifications of the detection pathway. An idea was transferred to STORM that had already been applied to single particle tracking [74]: a weak cylindrical lens is introduced into the detection pathway of the microscope as depicted in the right part of Figure 2.10A. A cylindrical lens focuses the light in only one direction, which results in a focal line instead of a focal point that one would obtain for a normal lens. If the focal length of the cylindrical lens is relatively long (here typically in the range of 1 up to 10 m), it will only introduce an astigmatism to the PSF. As indicated by the dotted line in Figure 2.10A, the focal plane for one direction will be slightly shifted whereas the other remains unchanged. The effect on the PSF can be seen in the right part of Figure 2.10B: now, a unique, elliptic PSF shape can be assigned to each respective axial position. Huang *et al.* demonstrated that after taking a calibration measurement, it is possible to apply this principle on STORM [72, 73]. Typically, resolutions down to 50 nm in axial directions can be obtained with this approach. It provides slightly better axial resolution than Biplane fPALM and is comparable with both Biplane fPALM and iPALM regarding lateral resolution (Table 2.2). Although iPALM delivers a higher resolution, astigmatism-based 3D super-resolution imaging stands out by the small modifications of the microscope that are necessary to switch between 2D and 3D imaging. It has to be pointed out that the risk of introducing artifacts generated e.g. by optical aberrations increases with the number of optical elements. A method that only requires the insertion of a single lens doubtlessly reduces this risk significantly.

DualObjective STORM [68], which allows to increase the axial resolution beyond the limit given in Table 2.2 uses the configuration of a 4Pi microscope for imaging as described before. By this means, the number of collected photons can be doubled, which does not only increase lateral resolution by a factor of $\sqrt{2}$ according to Eq. 2.21 but also axial resolution to a value of approximately 20 nm. This gain in resolution, however, comes along with significantly increased technical effort.

2.3.4 Overview over other optical super-resolution methods

This thesis focuses on the establishment of STORM and PALM. However, there are also other approaches to super-resolution microscopy, which come along with certain advantages and disadvantages compared to STORM and PALM. In general, these techniques can be divided into stochastic-based methods, which include also STORM and PALM, and approaches where active modeling of the PSF shape brings gain in resolution.

One stochastic method that is closely related to STORM and PALM is Super-Resolution Optical Fluctuation Imaging (SOFI), which was developed by Dertinger *et al.* [75]. It exploits the stochastic blinking behavior of fluorescence dyes but instead of performing a localization of the centroid, SOFI is based on pixel-wise temporal correlation of the intensity of a fluorophore. For a correlation of order n, the nominal resolution would be increased by a factor $\sqrt{n}$. However, SOFI is very sensitive to photobleaching of dyes during imaging, which results in correlation of fluorescence with background noise. Compared to fluorophores that do not bleach, this leads to brightness artifacts in the super-resolution image, which decrease image quality for correlation orders higher than ~ 4 [76]. SOFI is expendable for 3D imaging although it requires scanning at different axial image planes and SOFI has to be applied to each of these planes separately [75, 77].

Another localization-based approach focuses more on improvement of sample preparation and labeling efficiency. Point Accumulation for Imaging in Nanoscale Topography (PAINT) was first developed by Sharonov *et al.* [78] and exploits reversible electrostatic or hydrophobic interactions between a fluorescent dye and the sample. When the dye binds only for a short period of time before detaching again in a way that only one dye attaches in a diffraction-limited area at a time, this dye can localized with high accuracy as it is the case in STORM and PALM. For example, it is possible to use dyes with a high affinity to lipid membranes for specific labeling [78]. However, the field of application of this method is limited to the availability of specific dyes for a specific structure. For this reason, PAINT was developed further by Jungmann *et al.* with the modifications DNA-PAINT [79] and Exchange-PAINT [80]. The principle of DNA-PAINT is to attach the respective fluorescent label to a DNA strand ('imager strand'), which will bind to a complementary DNA strand that is bound to the sample ('docking strand'). As DNA pair binding is highly specific, the risk of unspecific labeling decreases significantly. A limitation of this method in cellular experiments is, however, that this specificity can be limited by the specificity with which the docking strand is bound to the respective structure. If the docking strand is, for example, attached to an antibody, which in turn will bind to a specific protein, the specificity of the antibody has to be evaluated carefully. Exchange-PAINT further enhances the method for multi-color imaging. All structures of interest are labeled with docking strands orthogonal to each other. Imager strands for one of the structures are then added in a first step and washed away after imaging before proceeding with the next structure. By this means, the entire sample can be imaged by using only one fluorophore therefore avoiding any kind of chromatic aberrations or crosstalk.

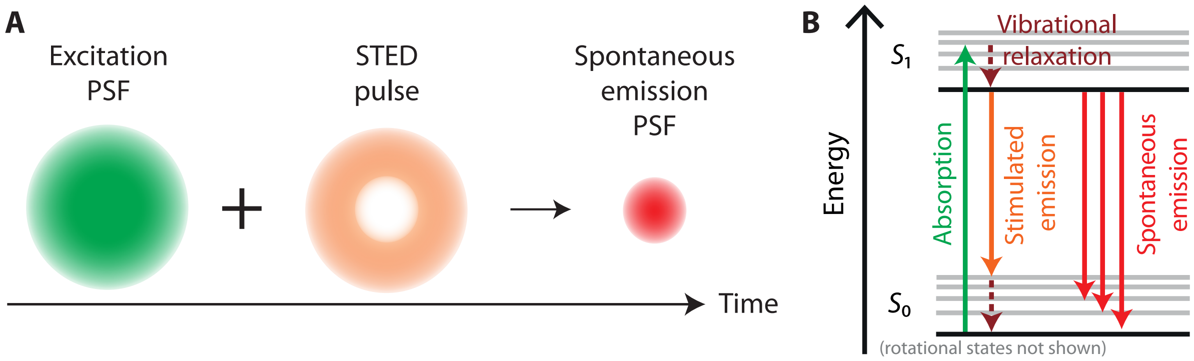

Figure 2.11: Principle of STED. (A) A doughnut-shaped STED pulse (orange) is applied picoseconds after the excitation pulse (green) forcing relaxation of all excited states except for the middle area, therefore reducing the size of the PSF of the observed signal from spontaneous emission (red) below the diffraction limit. (B) A simplified Jablonski diagram illustrates absorption (green), stimulated (orange) and spontaneous emission (red) and vibrational relaxation (brown) processes involved in STED.

In contrast to the methods described so far, Stimulated Emission Depletion (STED), which was first theoretically described by Hell [6] before realized [8], does not rely on stochastic blinking but seeks to model the PSF actively: as depicted in Figure 2.11A, several picoseconds after the excitation pulse, a doughnut-shaped pulse is applied, which stimulates emission in the outer area and spontaneous fluorescence is only observed from the smaller spot in the middle. As a photon emitted by stimulated emission has the same wavelength as the triggering photon, the wavelength of the stimulated emission signal can be therefore be chosen to match the smallest possible transition energy between S_1 and S_0 as depicted in Figure 2.11B. In this case, spontaneous emission signal with longer wavelengths can easily be separated from stimulated emission. In theory, the achievable resolution of a STED microscope therefore depends on how small the minimum in the middle of the doughnut-shaped pulse can be made. Typically, STED achieves resolutions in the range between 30 and 70 nm in the lateral dimension, although resolutions below 20 nm have been reported [81]. The method can further be extended to the third dimension [82]. Whereas STED data acquisition time is considerably faster than for STORM and PALM, the higher technical effort for a STED microscope compared to a STORM or PALM microscope has to be considered as well as a lower suitability of STED for living samples compared to PALM as the high laser powers are often incompatible with living organisms.

Chapter 3

Experimental setup and analysis methods for STORM

3.1 Experimental setup

In order to perform super-resolution microscopy imaging, a microscope setup was assembled. Overall, the system was designed as a combined widefield and objective-type TIRF microscope allowing both kinds of illumination modalities. Special focus was put on high mechanical stability including a home-built perfect focus system in order to allow nanometer-precise measurements required for localization-based super-resolution microscopy.

3.1.1 Instrumentation of the STORM setup

A schematic of the built STORM setup is shown in Figure 3.1. All optical elements incorporated into the microscope are mounted on a vibration isolated optical table (KNS Series, Newport, Irvine, CA, USA) to absorb potential percussions without affecting the optical settings. Mirrors shown in the setup scheme correspond to broadband dielectric mirrors (BB1-E02 or BB2-E02, Thorlabs, Dachau, Germany).

Excitation is based on continuous wave (cw) lasers with emission wavelengths of 405 nm (LuxX 405-120, Omicron Laserage, Rodgau, Germany), 488 nm (LuxX 488-60, Omicron Laserage, Rodgau, Germany), 561 nm (CL561-025, CrystaLaser, Reno, NV, USA, later replaced by Cobolt Jive 300, Cobolt, Solna, Sweden) and 642 nm (PhoxX 642, Omicron Laserage, Rodgau, Germany). For laser beam alignment, beam displacers (custom product, PicoQuant, Berlin, Germany) are placed in front of every laser, which allow the direction of the beam to be changed in both the horizontal and vertical directions. The 561 nm laser is reflected by a mirror and aligned with the other laser lines by appropriate dichroic mirrors (F48-502, F73-611 and F38-M01, AHF Analysentechnik, Tübingen, Germany). Another mirror then directs the aligned beams onto an acousto-optical tunable filter (AOTF, TF525-250-6-3-GH18A, Gooch & Housego, Ilminster, UK), which allows the selection of individual laser lines and power by tuning frequency and power of the oscillating wave coupled to the AOTF.

Behind the AOTF, a set of two consecutive achromatic lenses with focal lengths $f = 10\,\mathrm{mm}$ (AC254-010-A, Thorlabs, Dachau, Germany) and $f = 75\,\mathrm{mm}$ (AC254-075-A, Thorlabs, Dachau, Germany), respectively, expand the excitation beam in order to increase the field of illumination. In order to improve the shape of the beam profile, which is distorted by the AOTF, a pinhole with an opening size of 10 µm (P10S, Thorlabs, Dachau, Germany) is placed in the back focal plane of the first lens. An achromatic lens with a focal length of $f = 300\,\mathrm{mm}$ (AC254-300-A, Thorlabs, Dachau, Germany) focuses the expanded beam on the back focal plane of the microscope objective (SR Apo TIRF 100x/1.49 oil objective, Nikon, Tokyo, Japan), which results in

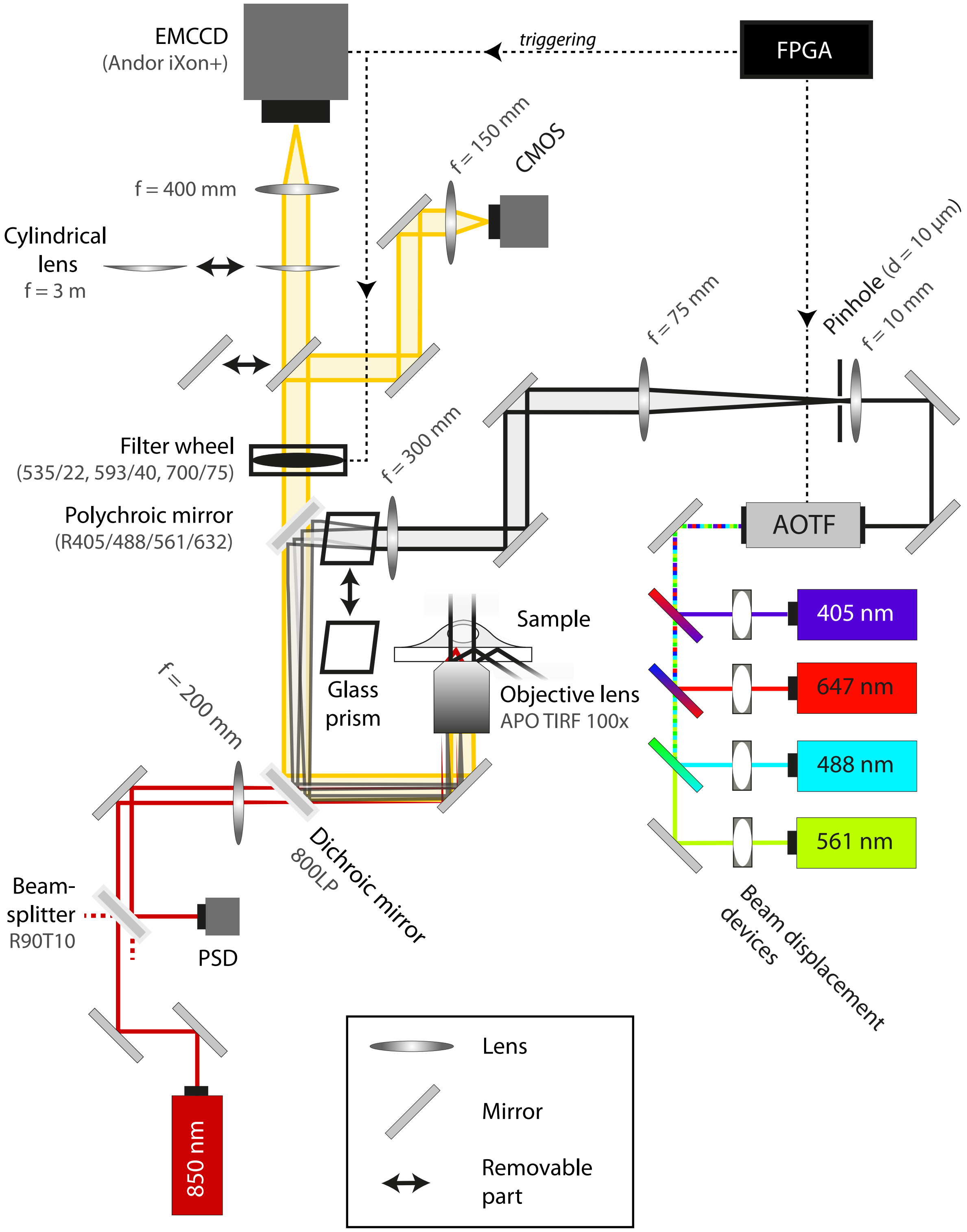

Figure 3.1: Microscope setup scheme. A scheme of the built microscope with all incorporated optical elements is shown. It offers both widefield and TIRF excitation modalities (black) and detection of sample fluorescence (yellow) for 2D and 3D super-resolution microscopy. The system includes a perfect focus system (dark red) for increased stability.

a collimated beam leaving the objective.

A polychroic mirror (Di01-R405/488/561/635-25x36, Semrock, Rochester, NY, USA) reflects the excitation beam and separates it from fluorescence emission. A 800 nm longpass dichroic beamsplitter (F43-800, AHF Analysentechnik, Tübingen, Germany) further couples in an infrared beam required for the implemented perfect focus system, which will be described in detail in the following section. The objective is mounted on a home-built microscope stage, which is shown in Figure 3.2. Integral parts of the stage are made out of Invar, which is a nickel–iron alloy that is known for its low thermal expansion coefficient [83]. This reduces thermal drift, which, together with the compact design of the stage, increases the mechanical stability. Two linear actuators (NSA12 in combination with NSC200 and NSC-SB controller, Newport, Irvine, CA, USA) allow lateral movement of the sample holder while the objective remains fixed. Coarse movement of the holder in the axial direction is driven by a high-resolution actuator (PZA12, Newport, Irvine, CA, USA) whereas fine adjustment is performed by a piezoelectric objective scanner (PD72Z1CA0, Physik Instrumente, Karlsruhe, Germany).

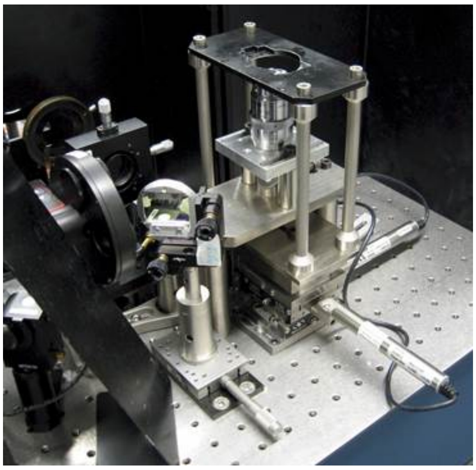

Figure 3.2: Microscope stage

The excitation mode (widefield or TIRF) depends on the angle under which the collimated beam leaves the objective. This angle can be controlled by the displacement of the excitation beam from the center of the objective. When this off-axis-distance of the focused beam is zero, a collimated beam will leave the objective along the optical axis resulting in widefield excitation. The emission angle of the collimated beam can be increased with the off-axis-distance of the incoming beam. This will result in TIRF excitation when the angle exceeds the critical angle for total internal reflection (cf. Section 2.2.3). Two options were implemented into the setup to adjust the emission angle. First, the polychroic mirror that separates excitation and fluorescence emission is mounted on a linear stage (M-UMR5.25, Newport, Irvine, CA, USA) that allows the displacement of the excitation beam to be changed from the center of the objective to one edge. Second, a glass prism (WG11050-A, Thorlabs, Dachau, Germany), which is mounted on a motorized flip mount (MFF101/M, Thorlabs, Dachau, Germany), can be inserted into the beam path after the focusing lens. Depending on the tilt angle of the prism, the beam is shifted by a certain distance, which allows convenient switching between TIRF and widefield excitation modes.

The fluorescence signal collected by the objective is a collimated beam and after separation from perfect focus and excitation beam paths by the respective di- and polychroic mirrors, it passes a set of band pass filters mounted on a motorized filter wheel (FW102C, Thorlabs, Dachau, Germany) allowing the selection of distinct detection wavelengths. The system contains a 593/40 (FF01-593/40-25, Semrock, Rochester, NY, USA), a 700/75 (F47-700, AHF Analysentechnik, Tübingen, Germany) and a 535/22 (FF01-535/22-25, Semrock, Rochester, NY, USA) bandpass filter. The selected detection wavelength is then focused by an achromatic lens with $f = 400\,\mathrm{mm}$ (AC254-400-A, Thorlabs, Dachau, Germany) onto an EMCCD camera (DU860D-CS0-BV, Andor, Belfast, UK), which is controlled by Andor Solis software (version 4.19.3, Andor, Belfast, UK). The long focal length of the focusing lens was chosen due to the relatively small imaging area of the EMCCD camera with a dimension of 128 × 128 pixel. The physical size of each pixel is 24 × 24 µm. On the one hand, magnification has to be chosen high enough to avoid that all detected photons of a PSF are collected by the same pixel, which would hinder accurate fitting of the PSF. On the other hand, the field of view should be large enough to allow efficient imaging. The use of a lens with $f = 400\,\mathrm{mm}$ results in a pixel size of 120 nm and therefore represents a good compromise for this setup. A cylindrical lens with a focal length of 3 m (1-PCL-1-D300, Altechna, Vilnius, Lithuania) can further be implemented between the focusing lens and the camera in order to perform 3D super-resolution imaging (cf. Section 2.3.3).

In order to facilitate the selection of appropriate imaging regions, the emitted fluorescence can also be detected by a CMOS camera (DCC1545M, Thorlabs, Dachau, Germany) with a larger imaging area of 1280 × 1024 pixel but lower sensitivity. A flip mirror (MFF101/M, Thorlabs, Dachau, Germany), which is placed directly behind the filter wheel, allows switching between both detection channels. An achromatic lens with $f = 150\,\mathrm{mm}$ (AC150-400-A, Thorlabs, Dachau, Germany) is used to focus the beam onto the CMOS camera.

A field-programmable gate array (FPGA) mounted on a real-time controller (NI cRIO-9073, National Instruments, Austin, TX, USA), which is controlled by a home-written software created with LabView 2013 (National Instruments, Austin, TX, USA), triggers the EMCCD camera as well as the AOTF in order to synchronize the AOTF pulses with data acquisition. The software further allows programming of pulse sequences with changing laser lines in order to realize activation and deactivation cycles required for STORM and PALM as they were described in Section 2.3. The filter wheel is either triggered by the same software or is manually accessed by an additional program also written in LabView 2013. The second program further allows control of both NSA12 actuators for lateral movement of the sample holder as well as the PZA12 motor for axial movement.

3.1.2 Implementation and tuning of a perfect focus system for increased focus stability

Super-resolution techniques such as STORM and PALM often require long imaging times in order to collect the position of all stochastically switchable fluorophores. It is therefore crucial to ensure that the position of the optical focus does not change over the course of data acquisition. In order to increase focus stability, a home-built perfect focus system was implemented into the microscope setup. The system is based on an infrared (IR) 850 nm cw laser (DL852-100, CrystaLaser, Reno, NV, USA), which is focused on the back focal plane of the objective by an achromatic lens with $f = 200\,\mathrm{mm}$ (AC200-400-A, Thorlabs, Dachau, Germany). The off-axis-distance of the incoming beam to the center of the objective has be large enough to ensure total internal reflection. A 90:10 beam splitter (BSX11R, Thorlabs, Dachau, Germany) directs the larger part of the totally reflected beam onto a position sensitive detector (DUM-SPOTANA-9-USB-H, Duma Optronics, Nesher, Israel). As depicted in Figure 3.3A, a change in the focal plane caused by e.g. axial drift results in a shift of the reflected IR beam, which can be detected and measured by the position sensitive detector (PSD). An inevitable side effect of this design

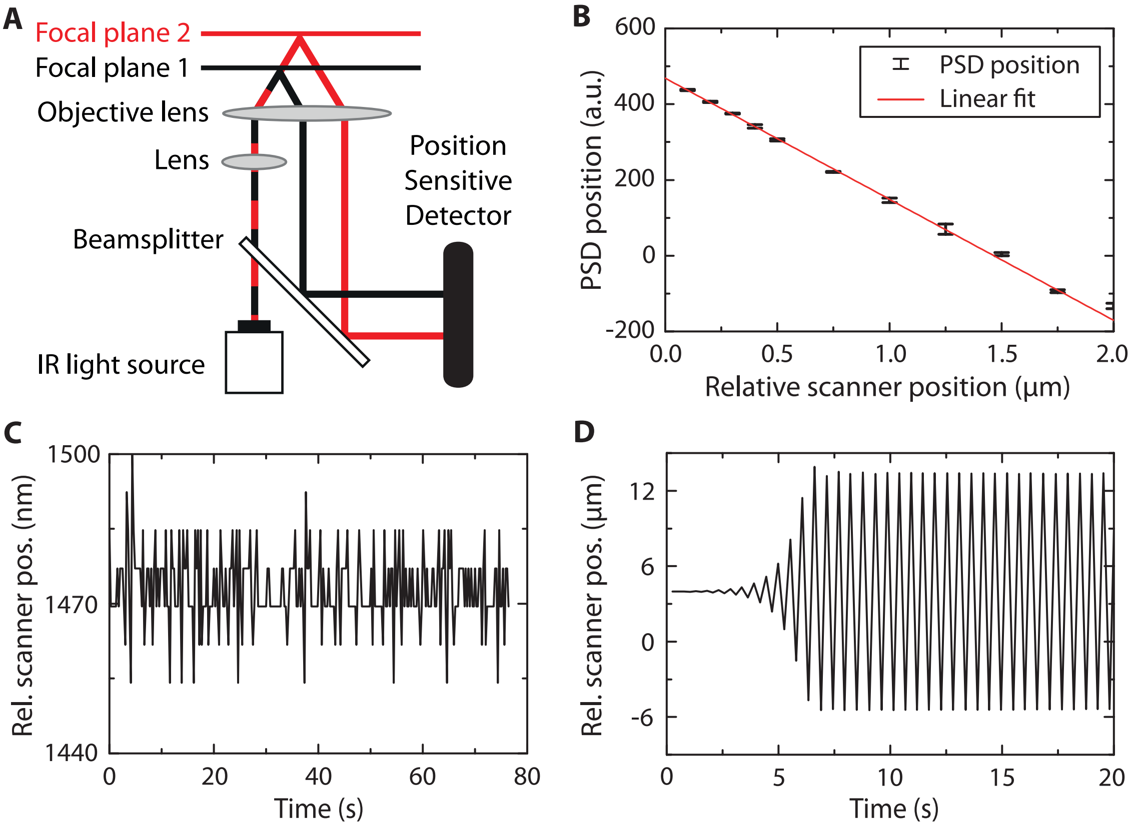

Figure 3.3: Principle and characterization of the implemented perfect focus system. (A) A scheme of the perfect focus system illustrates the change of detected IR beam position on the PSD upon axial movement of the sample from focal plane 1 (black) to focal plane 2 (red). (B) A calibration curve was measured for quantitative conversion of axial movement of the sample into shift of the IR beam position on the PSD. (C) Stability measurement with full PID provides a stable objective position with a standard deviation of 7.4 nm. (D) Feedback turns instable as a result of a too high proportional correction gain factor (without integral and derivative feedback).

is the fact that a considerable part of the incoming beam is lost at the 90:10 beam splitter. However, as the PSD only requires a minimal input power of 1 µW and the initial output of the IR laser is 100 mW, the remaining power reaching the detector (approximately 180 µW) is still high enough to achieve accurate measurements.

In order to analyze changes of the IR beam position on the PSD due to movement of the focal plane and to correct the axial position of the sample stage dynamically during data acquisition, a proportional-integral-derivative (PID) feedback mechanism [84–86] was implemented into the stage control software (cf. Section 3.1.1). A calibration measurement was performed to determine the magnitude of the shift of the IR on the PSD for a corresponding movement of the focal plane. For this purpose, the change of the IR beam position on the PSD was measured for varying movements of the piezoelectric scanner as shown in Figure 3.3B. A linear fit of the obtained values revealed that a movement of 1.0 µm on the detector corresponds to a 3.134 nm movement of the objective scanner. It has to be noted, however, that this calibration strongly depends on the current alignment of the system and may change slightly upon possible realignment.

As the term PID suggests, correction based on this mechanism is a sum of three different correction terms that yields the response to an occurring error. The proportional term is based on the offset D at a time t, which is the difference between the current and the initial position of the IR beam on the PSD. The response for this proportional term R_P is then obtained by adjustment of factor G_P, which is called proportional gain constant:

$$R_P = G_P \cdot D(t) \tag{3.1}$$

Proportional correction alone is, however, not capable to correct the offset perfectly. Small errors remain and will accumulate over time. An additional integral correction term sums up all those errors and returns an additional integral response R_I, which is adjusted by the associated integral gain constant G_I:

$$R_I = G_I \cdot \int_0^t D(t)\mathrm{d}t \tag{3.2}$$

In order to counteract potential overshooting by too large correction steps caused by the proportional and integral term, derivative feedback can be introduced as a third correction term R_D. If the corresponding derivative gain constant G_D is correctly adjusted, it acts as a damping factor against overshooting:

$$R_D = G_D \cdot \frac{\mathrm{d}}{\mathrm{d}t} D(t) \tag{3.3}$$

The total response R is subsequently obtained by the sum of all three terms and the piezoelectric scanner is moved according to this value:

$$R = R_P + R_I + R_D \tag{3.4}$$

PID based feedback control depends on careful selection of the parameters G_P, G_I and G_D in order to ensure effective and fast correction of occurring errors to keep the focus position stable as depicted in Figure 3.3C. At the same time, overshooting due to too fast correction has to be avoided. In this case, a situation might occur where a large correction step in one direction triggers another large correction step in the opposite direction, which will result in an oscillation as demonstrated in Figure 3.3D, where only the proportional term was used to visualize this effect. A method for effective calculation of the feedback parameters was described by Ziegler and Nichols [85]: first, all gains are set to zero before G_P is set as high as possible without the system starting to oscillate. Based on this critical gain $G_{P;crit}$, the other parameters can be calculated using the following equations where t_S is the time between two correction steps (50 ms in this case):

$$G_P = 0.6 \cdot G_{P;crit} \tag{3.5}$$

$$G_I = (2 \cdot G_P)/t_S \tag{3.6}$$

$$G_D = (G_P \cdot t_S)/8 \tag{3.7}$$

Figure 3.3C shows the signal fluctuations on the PSD with activated perfect focus applying the parameters calculated by Eqs. 3.5 - 3.7. It can be stated that the system offers a high degree of stability with a standard deviation of the signal of 7.4 nm. This value even lies below the size of typical dye molecules and therefore below the Nyquist-Shannon criterion (Eq. 2.11). This means that distortion of measurements through axial drift could be effectively eliminated and the focus position kept stable. Apart from its general significance for super-resolution imaging, this is an indispensable precondition especially for three-dimensional imaging as any axial drift would make accurate determination of axial positions highly inaccurate.

3.1.3 EMCCD camera characterization and mapping

EMCCD cameras offer many advantages such as high photon detection efficiencies and signal-to-noise ratios. For these reasons, they are widely used as detectors for fluorescence microscopy, including this thesis. However, two additional calibration steps are necessary for an accurate analysis of the obtained images. This comprises conversion of camera counts into photons and alignment of images of different detection colors.

3.1.3.1 Count to photon conversion for EMCCD cameras

Data acquired by EMCCD cameras is usually not displayed by the respective software directly in the number of collected photons per pixel but in form of image counts, which include information about noise that is generated during data processing. However, the actual number of photons is required for quantitative comparison of data with data obtained on other systems as well as for reliable calculation of image resolution or localization accuracy by means of Eqs. 2.21 and 2.22. For this reason, the conversion factor between both values has to be determined, which requires some information about the working principle of an EMCCD detector.

The first point that one has to consider is the fact that although the average number of photons arriving at the detector per time is constant in the case of continuous wave laser sources, it is nevertheless subject to a Poisson distribution as a consequence of the particle character of light. This effect is called shot noise [46] and means that the mean number of detected photons N_P is equal to its variance σ_P^2:

$$\frac{\sigma_P^2}{N_P} = 1 \tag{3.8}$$

The counts displayed in the final output image, however, do not follow a Poisson distribution. Error and noise sources, which arise form the operation mode of EMCCD cameras, influence the distribution and lead to the introduction of a correction factor C into Eq. 3.8 with N_C being the mean number of output counts and σ_C^2 the corresponding variance:

$$\frac{\sigma_C^2}{N_C} = \frac{\sigma_P^2}{N_P} \cdot C \tag{3.9}$$

As $\sigma_P^2/N_P = 1$ as stated by Eq. 3.8, C is given by:

$$\frac{\sigma_C^2}{N_C} = C \quad \text{or} \quad \sigma_C^2 = C \cdot N_C \tag{3.10}$$

Noise contributing to C is generated at various steps during data processing, starting with the initial detection of photons by an array of photodiodes, which is illustrated by the white area in Figure 3.4. Upon impingement of a photon on one of these diodes, which has a finite size and represents one pixel, an electron-hole pair is generated. However, due to thermal energy of the environment, there is a certain probability for additionally electron-hole pairs to be created that are called dark current. The latter can be effectively reduced by cooling the detector down. For example, for the model used in this thesis, only 0.002 additional electrons are generated in average by dark current per pixel and per second at a temperature of −85 °C and can therefore be neglected. After exposure, the electrons are shifted to an opaque storage area of the array, which is shielded against photon impingement (illustrated by the gray area in Figure 3.4). This frame transfer process allows faster frame rates by parallelization of data acquisition and readout. The stored charges are subsequently read out row by row by serial shifting to a readout register, which sequentially shifts each row of the image to the output node, where charges are converted into voltage, which is finally visualized in the form of camera counts.

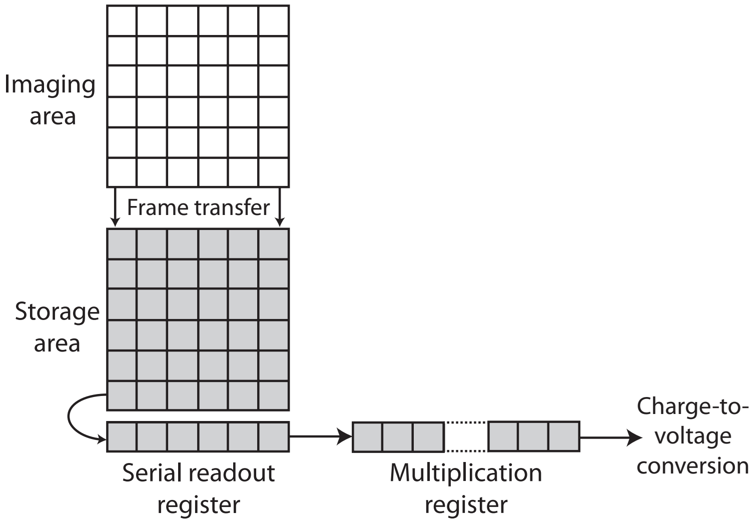

Figure 3.4: Working principle of an EMCCD detector. Impingement of photons onto the photodiodes of the imaging area (white area) generates electron-hole pairs that are subsequently shifted to a storage area (gray area), from where they can be read out serially. In order to reduce noise generated by this readout process, the obtained charges can be multiplied in a multiplication register before they are converted to voltage, which are finally displayed in form of digital counts.

During this charge transfer process, it is possible that the original charge induces additional charges by impact ionizations. The number of these clock induced charges can be reduced to very small values (approximately 1 event per line) in modern EMCCD detectors but cannot be totally avoided.

Further noise is generated during charge-to-voltage conversion, which is called readout noise. In conventional CCD cameras, readout noise is usually about 45 electrons per pixel. In an EMCCD, however, an extended multiplication register is placed before the charge-to-voltage converter is performed that amplifies the original charge to a multiple in a serial array of multiplication steps before reading. The resulting amplification factor is called Gain M. As a consequence, the readout noise is reduced by a factor of $\sim 1/M$. As clock induced charges and dark counts are usually negligible at low temperatures, this readout noise remains as the most prominent noise source and its reduction is the main advantage of EMCCDs compared to normal CCDs. Nevertheless, noise cannot be suppressed completely, which is expressed by the video chain gain factor A, which is sometimes also referred to as the analogue-to-digital conversion factor [87]. Charge multiplying introduces an additional multiplication noise factor F that is generated by the multiplication register. It has been shown [25] that F converges to $\sqrt{2}$ when the number of multiplication steps is larger than 100, which is true for almost all modern EMCCD cameras.

As shown in [25], σ_C^2 can be calculated from σ_P^2 by Eq. 3.11 by means of A, M and F and the variances of the readout noise, σ_R^2, and the dark counts, σ_D^2:

$$\sigma_C^2 = A^2 M^2 F^2 (\sigma_P^2 + \sigma_D^2) + A^2 \sigma_R^2 \tag{3.11}$$

In contrast, N_C is given as:

$$N_C = AM(N_P + N_D) \tag{3.12}$$

where N_D is the mean number of dark count photons. Combining Eq. 3.11 and Eq. 3.12 leads to the following expression with the assumptions that dark counts and the additional term for the readout noise, $A^2\sigma_R^2$, are negligible when M is large:

$$\frac{\sigma_C^2}{N_C} = \frac{A^2M^2F^2(\sigma_P^2 + \sigma_D^2) + A^2\sigma_R^2}{AM(N_P + N_D)} \approx \frac{A^2M^2F^2}{AM} \cdot \frac{\sigma_P^2}{N_P} \tag{3.13}$$

The last factor is 1 as stated by Eq. 3.8 and Eq. 3.13 therefore simplifies to the following expression, which can be used to calculate the correction factor C from Eq. 3.10:

$$\frac{\sigma_C^2}{N_C} = \frac{A^2M^2F^2}{AM} = AMF^2 = C \tag{3.14}$$

This expression states a linear relationship between σ_C^2 and N_C with a slope $C = AMF^2$ when σ_C^2 is plotted against N_C. The factor AM, which is needed in Eq. 3.12 to convert photons into camera counts, can easily be calculated as C/F^2 and N_P can then be determined in the absence of dark counts as:

$$N_P = \frac{F^2}{C} N_C \tag{3.15}$$

In order to use Eq. 3.15 to determine the conversion factor from counts to photons for the camera implemented into the described microscope setup, a calibration measurement was performed. Auto-fluorescent plastic slides excitable at 561 nm (#92001, Chroma, Bellows Falls, VT, USA) were used as a sample to ensure homogeneous count rates over the entire field of view. Movie stacks with 1000 frames each at an exposure time of 50 ms and $M = 50$ were recorded at varying laser powers and N_C and σ_C^2 determined for each measurement. In Figure 3.5, σ_C^2 is plotted against N_C revealing a linear curve between mean count values of 5000 and 15 000. Above this value, saturation effects cause a deviation from linearity. The deviation at low count rates, in contrast, might be explained by inhomogeneities or stray light that distorted the measured values. A fit of the linear region gave a slope of $C = 5.789$, which according to Eq. 3.15 corresponds to a conversion factor of 0.35 photons/count when F^2 is assumed to be 2 when the number of multiplication steps is high [25].

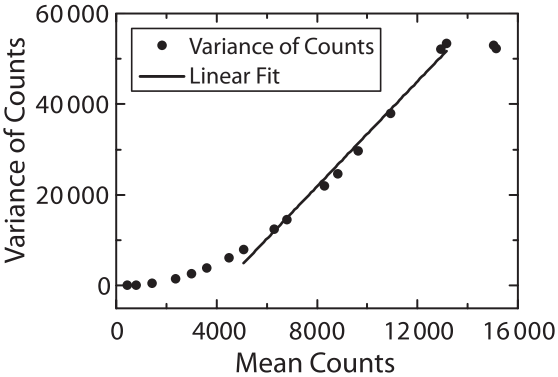

Figure 3.5: EMCCD camera calibration. The variance of the displayed camera count intensity is plotted against the mean number of counts resulting in a linear slope of 5.789, which corresponds to a conversion factor of 0.35 photons/count.

3.1.3.2 Camera mapping

The predominant majority of EMCCD cameras measure intensity and are not able to distinguish different photon wavelengths. Separation of multiple colors must therefore be realized by optical elements in combination with the knowledge about the fluorescent labels attached to the sample. For example, a set of emission filters can be used to allow only the fluorescence of a specific wavelength range to reach the detector. Thus, fluorescence of different wavelengths are distinguished by consecutive imaging with different filters. Simultaneous multi-color imaging, in contrast, requires two or more detectors, where the detection beam path is split up by dichroic mirrors and different parts of the spectrum are directed onto different detectors. Especially the latter approach comes along with the need of very accurate alignment of the respective channels. Misalignments in combination with spherical and chromatic aberrations can lead to distortions between the images acquired by the different channels, which are difficult to eliminate completely by optical alignment.

When only one detection path is available for all colors, shifts due to channel misalignment do not occur. However, chromatic aberrations of the optical elements can still lead to shifts and distortions between images of different colors. These deviations are certainly smaller than in the case of two separate detectors and might not be a critical problem for diffraction-limited widefield imaging as the resulting shifts mostly lie in a sub-pixel range. This is shown in Figure 3.6A. Two images of 100 nm sized TetraSpeck Microspheres (#T-7279, Thermo Fisher Scientific, Waltham, MA, USA) were measured at excitation wavelengths of 642 nm and 561 nm, respectively. But although the overlap is visible, multi-color super-resolution imaging requires alignment on the nanometer scale. Chromatic aberrations therefore are a factor that must be accounted for.

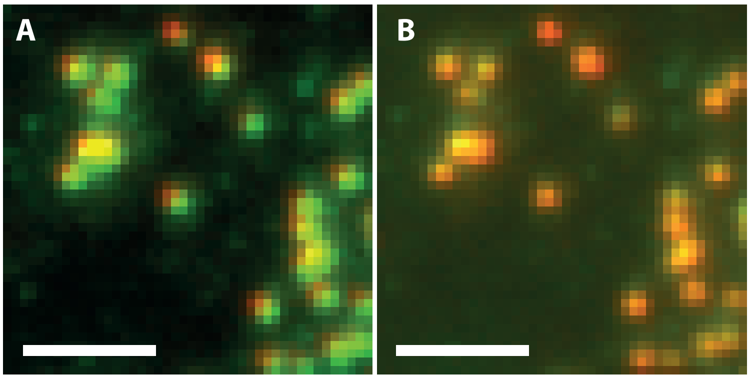

Figure 3.6: EMCCD camera mapping. (A) The uncorrected image of TetraSpeck Microspheres on a glass slide is shown. (B) A third-order polynomial map was applied to A to correct for chromatic aberrations (red: excitation at 642 nm, green: excitation at 561 nm). Scale bars: 2 µm.

For this reason, mapping of the respective channels has to be performed. In this process, pixel coordinates from the image of the first channel are projected onto the corresponding coordinates in the second channel by an appropriate transformation matrix. A software was written for this purpose using MatLab R2014b (The Mathworks, Natick, Massachusetts, USA) and tested with the bead sample described above. As a first step, this program allows manual assignment of the signals in the different channels that originate from the same bead. In order to obtain a nanometer-precise mapping, the obtained coordinates from both channels are fitted to a two-dimensional Gaussian function according to Eq. 2.9. The centroids of the PSF are determined as exact as possible. The program then applies a third order polynomial transformation matrix

$$\begin{pmatrix} u \\ v \end{pmatrix} = \begin{pmatrix} 1 & x^2 & y^2 & yx^2 & xy^2 & x^3 & y^3 \end{pmatrix} \cdot T_{inv} \tag{3.16}$$

that images the coordinates x, y of a base image on the corresponding coordinates u, v of an input image. The obtained transformation matrix T_{inv} subsequently can be used to map any input image onto the respective base. T_{inv} is a $10 \cdot 2$ matrix that requires 10 reference points to obtain a solvable equation system. In order to test the mapping algorithm, the obtained matrix was applied on the example shown in Figure 3.6A yielding the mapped image Figure 3.6B where the green coordinates were projected onto the red coordinates demonstrating successful high-resolution mapping.

3.2 STORM data acquisition and analysis protocol

The acquisition of data for super-resolution images and the subsequent processing that leads to the final high-resolution image consists of several steps, which will be presented in the following section. The first part will discuss the selected parameters and settings for data acquisition and the second section will focus on data analysis, which consists of two major steps: First, detected fluorescent emitters have to be localized with an accuracy as high as possible before a super-resolution image can be rendered based on the data obtained in the localization step including optional correction steps (for example for sample drift). Focus must be kept on a localization accuracy as high as possible but also the evaluation speed plays a role to achieve an efficient evaluation. Whereas data acquisition was performed by the software described in previous sections, a software for STORM data analysis was written with MATLAB 2014b (The Mathworks, Natick, Massachusetts, USA).

3.2.1 Test systems

For testing of the performance of the data evaluation methods, simulated data was generated and analyzed by these methods accordingly. For this purpose, images with a background noise of $A = 500$ counts were simulated. Gaussian signals in these images were defined by the following equation:

$$I(x,y) = A + I_0 \cdot \mathrm{e}^{\frac{1}{2}\left[-\left(\frac{x-x_0}{\sigma_G}\right)^2-\left(\frac{y-y_0}{\sigma_G}\right)^2\right]} \tag{3.17}$$

Each pixel in the obtained image follows a Poisson distribution to simulate measurement noise and all parameters could be freely chosen depending on the requirements for the respective test. The Gaussian standard deviation, σ_G, was assumed to be equal in the x- and y-directions. Different signal-to-noise ratios (SNR) were simulated by changing the amplitude of the Gaussian, I_0, while leaving the background amplitude A constant. The SNR was defined as SNR $= I_0/\mathrm{mean}(A)$ and the respective deviation between the original centroid position (x_0, y_0) or standard deviation (σ_G) and the value obtained by the localization algorithm gave the error of the respective simulation.

In order to get a realistic impression about the performance of the system, 200 nm sized polystyrene beads labeled with Cy5 were used as a simple test system. The detailed sample preparation protocol can be found in the materials and methods section.

3.2.2 Data acquisition

Efficient and accurate data acquisition for localization-based super-resolution microscopy depends on keeping the number of activated fluorophores low enough in each acquisition step to avoid detection of overlapping PSF in a diffraction-limited area. This is achieved by a number of parameters, which comprise, among others, the imaging buffer composition as well as effective excitation and detection.

The composition of the imaging buffer depends on the respective method. In the case of STORM or dSTORM, the buffer has to support the switching of the dye molecules. The switching of cyanine dyes, for example, which are preferentially used for these methods, depends considerably on the environmental conditions. As described in the theoretical section, switching of the cyanine dyes to the dark state is a reduction reaction leading over a triplet intermediate. An oxygen-free medium is therefore required in order to suppress quenching of the triplet state. For this reason, STORM and dSTORM imaging was carried out in an oxygen scavenger system based on glucose oxidase and catalase [54]. Oxygen is used up in this case by the glucose oxidase-mediated oxidation of glucose. Hydrogen peroxide, which is the other product of this reaction, has to be removed subsequently to prevent chemical bleaching of the organic dyes. This is achieved by a catalase-mediated degradation.

Furthermore, a reducing agent has to be added to the imaging buffer to enable the reduction reaction. Different agents are suitable for this purpose, where β-mercaptoethylamine and β-mercaptoethanol are the most prominent. The decision, which agent should be preferably used, depends on the respective dye as shown in [54]. For Cy5, a 100 mM β-mercaptoethylamine buffer was used in this work. Due to the addition of the amine agent, the buffer has a pH of ~ 9, which additionally accelerates switching as high pH values have emerged to be favorable for the reduction reaction [88].

In contrast to STORM and dSTORM, buffer conditions are not as critical for PALM, where switching is often based on light-induced conformational changes or photobleaching. In this context, oxygen scavenger buffers that reduce photobleaching are in fact counterproductive. PALM experiments were therefore usually carried out in a conventional phosphate buffered saline solution.

For data acquisition, efficient detection of photons from activated fluorophores is important as this effectiveness determines the resolution of the final super-resolution image. On the one hand, the exposure time of the EMCCD must be high enough to get reasonable photon statistics in every frame. On the other hand, the exposure time must not be set too high in order to avoid averaging of signals of adjacent emitters or of signals with background noise. This can occur when the switching rate of the dyes is significantly faster than the imaging rate. In order to achieve a good compromise between both positions, a frame rate of 20 Hz was chosen and the EMCCD gain set to 50 in order to achieve a good signal-to-noise ratio.

Switching kinetics of cyanine are further determined by the power of the respective exciting laser. This dependency is shown in Figure 3.7A: here, a bead sample was imaged at different laser powers for 100 seconds in each case and the number of detectable events was calculated for each measurement. In this context, an event is defined as a detected fluorophore that remained in the bright state for more than one frame in order to exclude unspecific blinking, which might, for example, arise from freely diffusing dyes. The power values were measured directly before the objective, which means that an additional loss of about 15% has to be accounted for the actual excitation power. It was found that the number of detected events decreased significantly when the laser power sank below a power of approximately 10 mW. Above this threshold, the value remained constant until a second threshold was reached at about 60 mW. It is plausible that higher laser powers favor activation as this step corresponds to an oxidation in the case

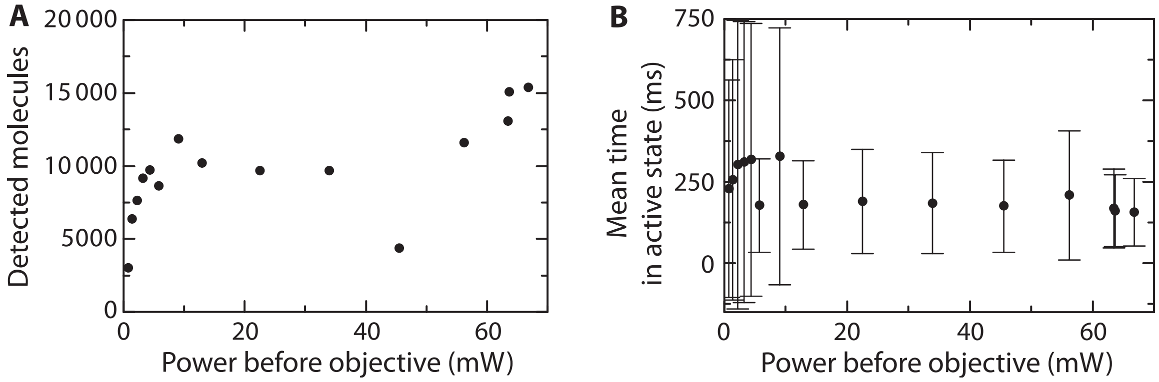

Figure 3.7: Influence of excitation power on cyanine dye switching. (A) A Cy5-labeled bead sample was imaged for 100 s under STORM conditions with varying laser powers and the number of detected molecules was determined for each setting. (B) The average time over which a molecule is active was calculated for the same data set as shown in A.

of cyanine dyes, which were used here. Although the thresholds depend on the nature of the respective fluorophore, these considerations can be transferred to other fluorophores and to PALM, where fast deactivation through photobleaching is analogously enhanced by high laser powers. In contrast, Figure 3.7B depicts the average time a molecule is active upon activation before going back into the dark state. Apparently, this value does not depend on the laser power but remains constant for laser powers above 10 mW. This implies that the excitation power does not have as much impact on the deactivation process, which is a reduction, as on activation.

STORM imaging is, in general, possible at laser powers higher than 10 mW where the average time of a molecule in the active state stabilizes between 150 and 200 ms. This corresponds to 3 and 4 frames at a sampling rate of 20 Hz, (Figure 3.7B). In addition, the number of detectable events reaches its first threshold above 10 mW (Figure 3.7A). Whereas the latter value can be increased by additional activation in STORM, dSTORM imaging that does not use additional activation requires a much higher blinking rate. Therefore, excitation powers higher than 60 mW, which corresponds to the second threshold visible in Figure 3.7A, are necessary for successful dSTORM imaging.

Another setting that is connected to the achievable blinking rate is the total number of frames that has to be acquired for one super-resolution measurement. In order to obtain a complete reproduction of the sample and high structural resolution according to the Nyquist-Shannon criterion, as many fluorophores as possible should be stochastically activated and imaged at least once during data acquisition.

Figure 3.8A illustrates the effect of data acquisition time on the dSTORM image of a 200 nm sized bead measured at a frame rate of 20 Hz: while the number of detected molecules increases as shown in Figure 3.8B, the image of the bead gradually emerges from the background noise. In the first images of the series, the latter appears to be more prominent than the actual structure. Only after approximately 5000 to 10 000 frames, the image of the bead clearly dominates the picture. The difference between the images taken after 10 000 frames and after 15 000 frames, respectively, is less prominent. Therefore, the acquisition of 10 000 frames at the mentioned frame rate appears to be a reasonable compromise between good molecule statistics and acquisition time. The character of the respective sample may require deviations. When, for example, all dyes are photobleached before the 10 000 frames are reached, one can desist from further data acquisition whereas a longer imaging time might also be necessary in some cases, for example, when a sample does not tolerate high laser powers.

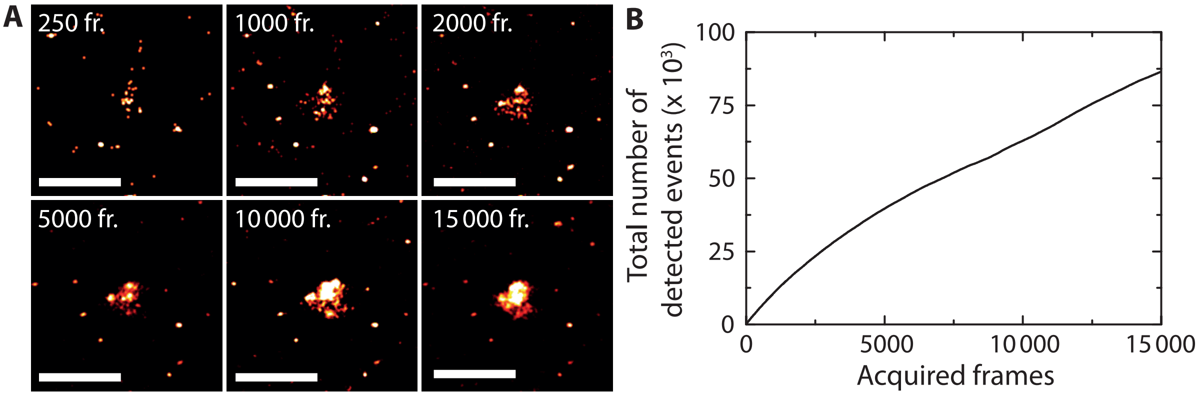

Figure 3.8: Effect of STORM data acquisition time on image quality. (A) The state of a STORM image of a 200 nm sized bead is shown after 250, 1000, 2000, 5000, 10 000 and 15 000 acquired frames at a sampling rate of 20 Hz. Scale bars: 500 nm (B) The number of detected events increased with data acquisition time.

In the case of STORM and PALM, data acquisition consists of activation cycles of one activation frame followed by a number of imaging frames. The number of imaging frames depends on how fast the activated fluorophores can be switched off again. However, considering the mean time of a cyanine dye in the active state (Figure 3.7B), five imaging frames at a sampling rate of 20 Hz are usually a reasonable number. But again, these values depend on the respective imaging conditions and have to be adjusted if necessary.

Whereas laser power at the output of the objective was set as high as possible for imaging, a lower power was set for activation in order to reduce the probability of multiple activations of adjacent fluorophores. At the beginning of the data acquisition, the power of the activation laser was therefore set to the lowest power where activation was still observable, which corresponded to approximately 0.5 µW for STORM and 5 µW for PALM. These values were chosen for the examples of Alexa Fluor 488 as STORM activator dye and for mEosFP as photoconvertible protein and might vary slightly when other fluorophores are used. Over the course of data acquisition, power was successively increased in both cases in order to compensate for photobleaching and to maintain a constant rate of blinking. For dSTORM imaging, no additional activation was used at the beginning of the measurement. When the blinking rate decreased due to photobleaching over the course of data acquisition, activation was used according to the same principle as for STORM.

3.2.3 Fluorescent emitter localization

Different methods have been proposed to obtain the centroid position and other characteristics of the PSF of a single fluorescent emitter with nanometer-precise accuracy. The most important criterion for the quality of all these algorithms is the localization accuracy but also the evaluation speed plays a role. The most common method is to fit the PSF to a two-dimensional Gaussian function, which is a good approximation to the real shape of the Airy disk as shown in Section 2.2.2. However, it is also possible to use numerical algorithms for particle localization such as center-of-mass based methods [89], centroid localization over a triangulation approach [90, 91] or radial symmetry [92]. Sage *et al.* performed an evaluation of different localization methods [93] and found that non-fitting algorithms such as triangulation and center-of-mass are among the fastest but do not offer the accuracy that is achievable with algorithms based on Gaussian fitting, which can either be carried out by a least squares fit or by maximum likelihood estimation. Although a Gaussian function is only an approximation of the true PSF, it was further shown that this model is sufficient to deliver accurate results as long as the density of signals per frame is low and the assumption that no overlapping PSF exist is still valid. If this is not the case, advanced localization algorithms have to be applied that allow localization of these events in two [67] as well as in three dimensions [94].

The average number of fluorophores that are stochastically activated can be controlled by data acquisition settings, which keeps the probability to observe overlapping PSFs in a diffraction-limited area to a minimum. For this reason, the condition for accurate Gaussian fitting is given and fitting was performed using either a nonlinear least squares fit or a maximum likelihood estimation. The latter offers the advantage that it is possible to use an actually measured PSF for optimization and hence avoid approximation by models. However, if the shape of the PSF is not known or varying PSF shapes are observed during measurements. For example, the PSF shape depends on the axial position of the respective fluorescent in the case of astigmatism-based 3D imaging. Here, Gaussian least squares fitting is often more suitable.

3.2.3.1 Gaussian least squares fitting

In order to identify fluorescent molecules in the acquired raw data image stacks, each frame of the respective stack was in a first step scanned for local maxima that surpass an intensity and signal-to-noise-threshold set individually for each measurement in order to ensure that only actual PSF signals are analyzed and not background noise. For each event that was selected in this way, a fit window was created covering an area of 9 × 9 pixel with the respective brightest pixel in the center. The event was subsequently fitted to a two-dimensional Gaussian function whose intensity I at coordinates x and y is given by

$$I(x,y) = A + I_0 \cdot \mathrm{e}^{\frac{1}{2}\left[-\left(\frac{(x-x_0)\cos\theta-(y-y_0)\sin\theta}{\sigma_x}\right)^2-\left(\frac{(x-x_0)\sin\theta-(y-y_0)\cos\theta}{\sigma_y}\right)^2\right]} \tag{3.18}$$

where x_0 and y_0 are the coordinates of the centroid of the Gaussian, I_0 the signal amplitude, A the intensity of the fluorescent background, σ_x and σ_y the standard deviations in x- and y-direction, respectively, and θ the tilt angle of the intensity distribution relative to the pixel edges.

Analysis was performed by a least squares fit using the Levenberg-Marquardt algorithm [95, 96]. Briefly, the algorithm seeks to minimize the squared error χ^2 for a set of parameters p, where y_i are N observed data points that are obtained by function f depending on p and variable x_i:

$$\chi^2(p) = \sum_{i=1}^{N}[y_i - f(x_i,p)]^2 \tag{3.19}$$

The Levenberg-Marquardt algorithm now seeks to solve this equation for nonlinear functions f by a linearization of f through a Taylor series expansion. The result is a solvable linear equation, which allows minimization of χ^2 in an iterative process, where an initial guess of the unknown parameters is optimized in each step. A more detailed description of the algorithm can be found in Section A.4.

It is essential to carefully select start parameters that lie as close as possible to the actual solution. Otherwise, the optimization algorithm might converge at a side minimum of $\chi^2(p)$ instead of the global minimum. The selection of the start parameters for the fit of the detected PSFs is illustrated in Figure 3.9.

The coordinates of the brightest pixel within the respective fit region were chosen as start values for x_0 and y_0, the intensity of the brightest pixel for I_0 and a fixed value of 0 for θ. For

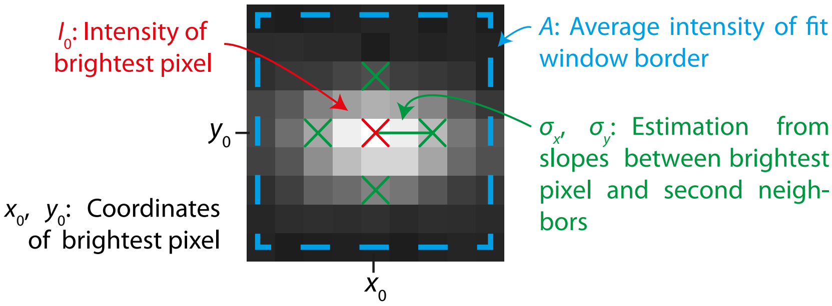

Figure 3.9: Calculation of start parameters for Gaussian least squares fit

the background intensity, A, the mean intensity of all pixels forming the border of the respective fit window was taken. The start values for the standard deviations σ_x and σ_y were estimated by calculation of the slope of the intensity distribution of the PSF using the brightest pixel and the respective second-next pixels as reference points as demonstrated in Figure 3.9. By means of the slope, it is possible to estimate the position of the full width at half maximum (FWHM) for the x- and y-direction, respectively. The estimates for the standard deviations in x and y are then given by $\sigma = \frac{\text{FWHM}}{2\sqrt{2\ln 2}}$.

The maximal fitting accuracy was set to an absolute value of 0.01 in the respective units, which e.g. corresponds to a value of 0.01 px or 1.2 nm for the centroid position and the standard deviations. This value was chosen as it is usually not practical to localize the centroid position of a single PSF with an accuracy higher than 1 nm considering the typically achievable sample labeling density. The latter sets a lower limit to the resolution achievable with STORM and PALM that cannot be circumvented (cf. Section 2.3.2).

The number of maximal iteration steps, which are allowed for the fit algorithm to converge, was set to 40. This number was chosen in order to ensure that the bulk of the calculations converges without investing too much calculation time on fits unlikely to converge at all. In the example shown in Figure 3.10, an evaluation with a total number of 668 908 localizations was performed, from which 57 226 (8.6 %) did not converge after 40 iterations and from which again 5135 (0.77 %) did not converge even after 3000 iterations (Figure 3.10A).

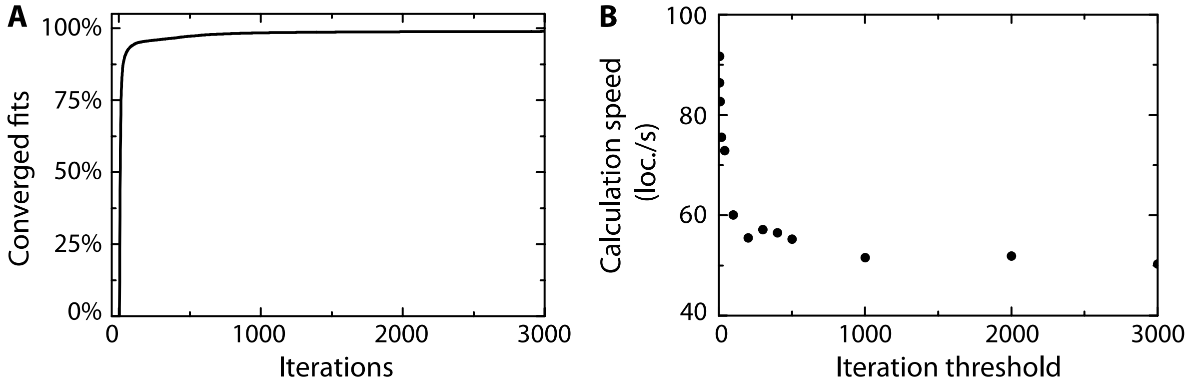

Figure 3.10: Convergence of Gaussian least squares fit. (A) Percentage of converged localizations depending on the number of performed fit iterations using a maximal fitting accuracy of 0.01. (B) Average number of localizations per second for varying thresholds for the maximum number of allowed iteration cycles.

At the same time, the calculation speed, using a computer system with two 2.0 GHz Intel Xeon CPU E5-2620 processors, slowed down considerably when the maximum number of allowed iterations was raised (Figure 3.10B). This resulted in calculation times of almost two hours for the example shown here. For this reason, the threshold was in general kept relatively low but could nevertheless be raised in cases where statistics did not allow the discarding of slowly converging fits.

Although this method promises a high fitting accuracy, data evaluation was still relatively slow compared with other super-resolution software such as rapidSTORM by Wolter *et al.* [97]. Using the computer system described above, a calculation speed of only approximately 30 localizations per second (loc./s) could be achieved as shown in Table 3.1. This included utilization of parallel computing where localizations were distributed on all available CPU cores using the distributed computing extension for MATLAB provided by MathWorks.

Table 3.1: Performance of Gaussian least squares fit depending on the the treatment of the Gaussian standard deviation σ and on localization algorithm implementation

Method	**Localizations/second**
MATLAB based fit	
σ free fit parameter	69.1
σ estimated	114.7
Java based fit	
σ free fit parameter	237.0
σ estimated	295.4

Apart from using a different localization algorithm, as discussed in the next section, least squares Gaussian fitting can be speeded up by reducing the number of free fit parameters, which is seven according to Eq. 3.18. In a first step, the tilt angle θ was set to 0, as Gaussian ellipticity should be small in 2D imaging as events with a high ellipticity will be excluded from evaluation as will be explained in detail in Section 3.2.4. For astigmatism-based 3D imaging, the tilt angle can be controlled by the alignment of the cylindrical lens (cf. Section 3.6). With $\theta = 0$, Eq. 3.18 can be transformed into the following term:

$$I(x, y) = A + I_0 \cdot \mathrm{e}^{\frac{1}{2}\left[-\left(\frac{x-x_0}{\sigma_x}\right)^2-\left(\frac{y-y_0}{\sigma_y}\right)^2\right]} \tag{3.20}$$

Considering the other fit parameters, it is obvious that the centroid position has to be a free fit parameter as well as the signal intensity I_0, which is required to calculate localization accuracy and image resolution (cf. Sections 3.3 and 2.2.2). The Gaussian standard deviations, σ_x and σ_y, have to be free fit parameters when astigmatism-based 3D imaging is performed. Otherwise, the values that were chosen as start parameters for the least squares fit can be used as estimates. This is also possible for the background intensity A.

Simulated data with varying SNR (cf. Section 3.2.1) was fitted using A, σ and θ either as free parameters or the respective fixed (for θ) or estimated values (for A and σ). As described in Section 3.2.1, the standard deviation is assumed to be equal in x- and y-direction. The effect of the reduction of the number of free fit parameters on the accuracy of the fit regarding the centroid position and the standard deviation of the Gaussian was evaluated. Figure 3.11A shows the accuracy of Gaussian centroid determination depending on the choice of free fit parameters. Analysis of simulated data revealed that a reduction of free fit parameters did not lead to a detectable loss of localization accuracy.

Even in a case when the fit was performed with only three free parameters (Figure 3.11A, green points), the difference was negligible. Only at very low SNR, the accuracy was higher for

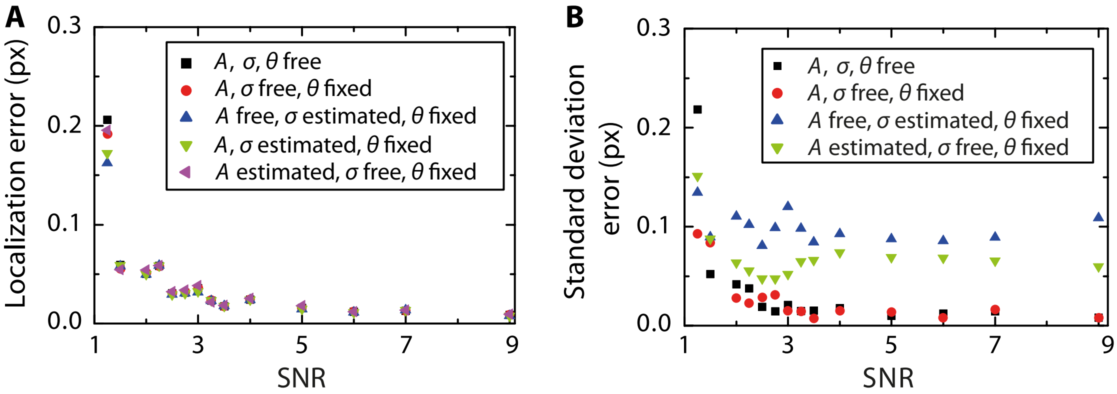

Figure 3.11: Accuracy of Gaussian least squares fit depending on the choice of free fit parameters was tested on simulated data for (A) localization of the centroid position and (B) determination of the standard deviation.

a larger number of free fit parameters. The error of the calculated standard deviations, which is depicted in Figure 3.11B, however, gave a different result: when all fit parameters were free (Figure 3.11B, black points), localization accuracy showed a similar dependence on the SNR as observed for the determination of the centroid position. A fixed value for θ (red points) did not have a significant impact on the fit performance, whereas replacing the fitted values for σ by their estimates led to a significant loss of accuracy (Figure 3.11B, blue points). This result seems plausible as the estimate of σ by means of the intensity slope (Figure 3.9) cannot compete with the result of a fit. Interestingly, an estimated background intensity combined with a fixed θ and σ as free fit parameter (Figure 3.11B, green points) brought a similar decline in accuracy.

For these reasons, Gaussian least squares optimizations were carried out using $\theta = 0$ and keeping all other parameters as free fit parameters. The written software nevertheless allows one to use the estimate for the standard deviations if desired. The gain in calculation speed achieved by this approach was, however, less than a factor of 2 (cf. Table 3.1).

Another reason for the relatively low calculation speed can be found in the way that MATLAB handles the data. It is optimized for handling large data matrices and is, on the contrary, slow at processing iterative algorithms such as the Levenberg-Marquardt algorithm. For this reason, a Java-based implementation of the algorithm was integrated into the original MATLAB software. The code is based on the LMA-package by Holopainen [98] and was adapted for this study. In particular, Levenberg-Marquardt requires the calculation of the Jacobi-Matrix J for each iteration step, which contains the partial derivatives for all parameters. As it follows from the chain rule of derivation

$$\frac{\mathrm{d}f(g(x))}{\mathrm{d}x} = \frac{\mathrm{d}f(g(x))}{\mathrm{d}g(x)} \cdot \frac{\mathrm{d}g(x)}{\mathrm{d}x} \tag{3.21}$$

all derivatives of Eq. 3.20, with the exception of $\mathrm{d}I/\mathrm{d}A$, are composed of the exponential term of the original function multiplied by an additional factor. Hence, although calculating the exponential term only once per iteration step will save only little time in each step, accumulation over the entire process leads to a noticeable reduction of computation time [97].

Table 3.1 summarizes the effects of different variations of the fit routine on the calculation speed. The following values were again obtained at a computer system with two 2.0 GHz Intel Xeon CPU E5-2620 processors. As it can be seen in Table 3.1, the Java based fit implementation brought an increase of calculation speed of about a factor of 3.4 for σ as a free fit parameter and a factor of 2.6 for estimated σ.

3.2.3.2 Maximum likelihood estimation

Maximum likelihood estimation (MLE) is an alternative to least squares fitting in order to fit a model function to measured data. In contrast to a least squares fit, the parameters of the model function are not calculated directly. Instead, a likelihood function $\mathcal{L}$ is used that yields the probability for the respective set of parameters to fit to the respective model. Subsequently, the set of parameters for which the likelihood function is maximized is determined.

The likelihood function of a certain distribution is based on the underlying probability density function, $f(y|\theta)$, whose integral

$$P = \int_b^a f(y|\theta)\mathrm{d}y \tag{3.22}$$

yields the probability P that the value y under the condition of the parameter set θ lies between a and b. For N observed values $(y_1, y_2, ..., y_n)$ (e.g. N pixels of an image), the joint density distribution $\mathcal{L}$, which in this case is also called likelihood, is then:

$$\mathcal{L}(\theta|y) = \prod_i^N f_i(y_i; \theta) \tag{3.23}$$

For practical reasons, the logarithmized function $l = \ln \mathcal{L}$ is often used instead of the original likelihood function as l in many cases easier to solve and as the maximum of $\ln \mathcal{L}$ lies at the same position as the maximum of $\mathcal{L}$:

$$l = \ln \mathcal{L}(\theta|y) = \sum_i^N \ln f_i(y_i; \theta) \tag{3.24}$$

Mortensen *et al.* [99] showed that l for n Poisson distributed photons is then given by:

$$l = \sum_i (-E_i + n_i \ln E_i - \ln(n_i!)) \tag{3.25}$$

with

$$E_i = \frac{n_i A^2}{2\pi\sigma^2} \mathrm{e}^{\frac{-(x_i-x_0)^2-(y_i-y_0)^2}{2\sigma^2}} \tag{3.26}$$

where A is the background noise intensity, x_0 and y_0 the centroid coordinates of the normal distribution and σ its standard deviation, which is assumed to be equal in the x- and y-direction.

Eq. 3.25 was solved using the Downhill Simplex or Nelder-Mead algorithm [100], which was used to calculate the minimum of Eq. 3.25 multiplied by -1. The Downhill Simplex algorithm has the advantage compared to the Levenberg-Marquardt algorithm that it does not require an approximation of the nonlinear problem by a Taylor series expansion: However, it tends to need more iterations to converge and is more sensitive to imprecise setting of the starting parameters. This means that the risk of converging to a local minimum instead of the global minimum is higher in this case. A detailed description of the algorithm can be found in Section A.4.

The method was tested on simulated data in order to evaluate its efficiency and to compare it to least squares fitting by means of localization accuracy and computation speed. The results are depicted in Figure 3.12, where Figure 3.12A shows the localization accuracy for MLE compared to least squares fitting at different signal-to-noise ratios. The start parameters for MLE localization were chosen as for least squares fitting, the average standard deviation σ was calculated as $\frac{\sigma_x+\sigma_y}{2}$. Apparently, the accuracy of MLE under these conditions considerably depended on the number of fit iterations. When a relatively large threshold of 3000 was set for the maximum number of iterations, the accuracy of MLE was comparable to that of a least squares

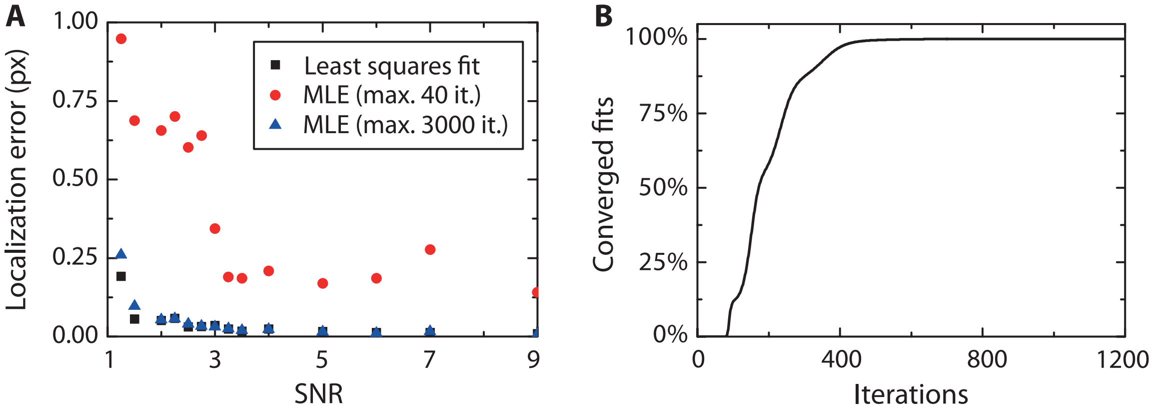

Figure 3.12: Performance of maximum likelihood based particle localization. (A) Localization accuracy of Gaussian least squares fit for varying SNR was compared to MLE with a maximal number of 40 and 3000 iterations, respectively. (B) The percentage of converged MLE localizations depended on the number of performed fit iterations using a maximal fitting accuracy of 0.01.

fit. When, however, a threshold of 40 iterations was selected, which had been the threshold for the least squares fit, the accuracy decreased significantly. This was confirmed by Figure 3.12B where the number of converged fits depending on the maximal number of iterations steps was plotted and it was revealed that a conversion rate of 90 % was not reached before approximately 300 iteration steps.

Comparing the calculation speed of MLE to least squares fitting (Table 3.2) revealed that again a considerable improvement can be achieved by running the algorithm on a Java-based script. Apart from that, MLE was about a factor 1.5 to 3 faster than least squares fitting when the maximum number of iterations was set to 3000 for MLE. When it was reduced to 40, the calculation speed increased, but, as shown in Figure 3.12, at the cost of localization accuracy. It also has to be mentioned here that the MLE was performed with one free fit parameter less as only the average standard deviation was used.

Table 3.2: Performance of MLE based particle localization compared to Gaussian least squares fit

Method	Localizations/second
MATLAB based fit	
Least squares fit, σ free	69.1
MLE ($\leq$ 40 iterations)	486.6
MLE ($\leq$ 3000 iterations)	51.2
Java based fit	
Least squares fit, σ free	237.0
MLE ($\leq$ 40 iterations)	1081.1
MLE ($\leq$ 3000 iterations)	691.0

In order to tap the full potential of maximum likelihood estimation, it would be necessary to use a model of the actual PSF instead of the current Gaussian approximation. The same consideration is true for the noise: instead of treating noise as a free fit parameter, application of a model of the actual noise seems suitable to optimize localization performance. Further, extension of the algorithm for 3D imaging is of interest, which means for PSF astigmatism, Eq. 3.26 has to be modified to account for elliptic PSF shapes. However, modeling PSF shape for obtaining the axial position is difficult to make compatible with a measured model of the PSF, which would be beneficial for increasing the accuracy of MLE.

Nevertheless, the relatively simple approach to MLE that was already applied here demonstrated the potential of this method although further optimization and tuning of the applied parameters is necessary. For this reason, especially under consideration of the requirements for astigmatism-based 3D imaging, least squares fitting was used in this work.

3.2.4 Image rendering

After successful localization of the single emitters, the final super-resolution image can be rendered using the obtained values in a next step. This includes a number of correction steps that are carried out in order to remove inaccurate and false localizations and thereby increase the quality of the final image. An image rendering routine that includes all these parameters and settings was implemented into the home-written STORM data analysis software.

In the first step of the image rendering process, the aim is to remove events that are obviously the result of unspecific blinking, which arises from other fluorescent sources than dye molecules attached to the respective structure, or multiple activations. Therefore, all events with less than 300 photons were discarded from further evaluation in order to increase localization accuracy and, as a consequence, image resolution. The same was done for PSFs with standard deviations larger than 4 pixel or 480 nm, which most likely arise from non-converging fits or several fluorophores close to each other that could not be separated by the localization algorithm. In the case of 2D imaging, the standard deviations can be used to further reduce the risk of evaluating multiple activations in a diffraction-limited area. For this purpose, all localized molecules with a PSF ellipticity larger than 15% were discarded from further evaluation as shown in [10]. In this context, ellipticity E was defined as

$$E = 2\left|\frac{\sigma_x - \sigma_y}{\sigma_x + \sigma_y}\right| \tag{3.27}$$

and should be 0 in theory for the PSF of a single emitter in a diffraction-limited area, which should be isotropic in absence of any optical aberrations or astigmatisms. Significant deviations from this value are therefore a clear sign for two or more overlapping PSFs. Figure 3.13 shows the distribution of ellipticity values calculated with Eq. 3.27 (Figure 3.13A) and the number of collected photons (Figure 3.13B) for a typical STORM measurement together with the applied thresholds. In the case of 3D imaging where an astigmatism is introduced on purpose to decode the axial position of the emitter (cf. Section 3.6), it is not possible to apply this threshold. Instead, a previously measured calibration curve is used in order to convert the standard deviation values into z-positions. Following these steps, drift can be corrected with a previously calculated drift data set if necessary. A detailed description how to quantify sample drift is given in the following section.

In the next step, events that appear within the range of 1 px (or 120 nm) in two or more consecutive frames were considered as originating from the same fluorescent molecule. The individual Gaussian centroid positions obtained from fits that were assigned to the same fluorescent molecule by this means were averaged and the average centroid position was taken for image rendering. The same was done for the PSF standard deviations whereas the photon counts of the contributing localizations were added up. All events that did not appear in at least

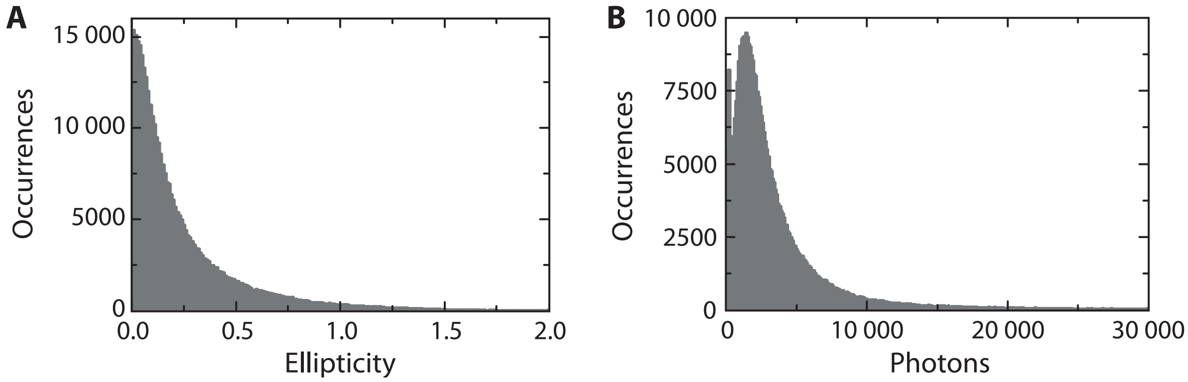

Figure 3.13: Example for photon and ellipticity statistics. The distribution of (A) ellipticity values and (B) number of collected photons per activated molecule are shown for an example of an analysis with 365 084 localizations in total.

two subsequent frames were discarded from further evaluation in order to eliminate unspecific blinking events most likely coming from background noise or freely diffusing dye molecules. Furthermore, if an activation color is used, which is mandatory for STORM and PALM but optional for dSTORM, it is optionally possible to exclude all events that are activated in other frames than frames directly following this activation pulse. By this means, it is possible to identify unspecific blinking. Objects that are active for longer than one activation cycle and do not show any blinking at all are also excluded because they most likely arise from dirt.

Following the selection of image data, the final high-resolution image was rendered using the obtained cleaned-up data set. Each event was represented by a two-dimensional Gaussian whose centroid coordinates are those of the localized event. Its standard deviation can be set to the localization uncertainty defined by Eq. 2.22 or to the actual image resolution (cf. Section 3.3) in order to represent the localization accuracy in the final image. The amplitude of the Gaussian distributions was set to a fixed value of 1000 counts in the case of 2D imaging or encodes the z-position in the case of 3D imaging.

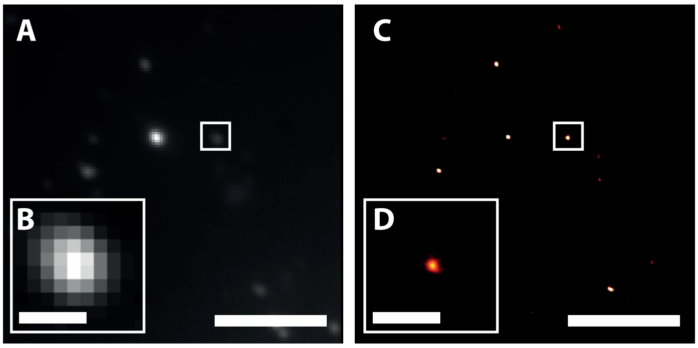

Figure 3.14: 2D dSTORM imaging of 200 nm sized polystyrene beads. (A) The diffraction-limited widefield image of a sample of Cy5-labeled 200 nm sized polystyrene beads attached to a glass slide demonstrates the resolution limit in conventional widefield microscopy. (B) A zoom-in into the region marked by the white rectangle in A is shown. (C) A super-resolution dSTORM image is rendered for the sample shown in A. (D) A zoom-in into the region marked by the white rectangle in C reveals the underlying structure of the bead. Scale bars: 5 μm (A and C), 600 nm (B and D).

Figure 3.14 demonstrates the applied analysis methods at the example of dSTORM imaging of a sample of 200 nm sized polystyrene beads, which were labeled with Cy5. In the left part of the figure, a diffraction-limited widefield image of the sample is shown (Figure 3.14A). A zoom-in into the region marked by the white rectangle (Figure 3.14B) demonstrates that the size of the bead could not be reproduced by conventional widefield imaging. These images can be compared to the dSTORM image on the right site (Figure 3.14C), which was acquired and rendered as described in the sections above. A zoom-in into the same region as shown for the diffraction-limited image reveals the underlying size and shape of the selected bead (Figure 3.14D).

3.2.5 Correction of lateral drift

STORM and PALM are localization-based methods, which require a high stability of the microscope setup in order to avoid interference by sample drift caused by e.g. vibrations, temperature fluctuations or air current. It is recommendable to reduce these and other sources of drift as far as possible in the first place as results of unbiased measurements are always superior to data sets whose flaws have to be corrected afterwards. For this reason, a large amount of effort was placed on mechanical stability throughout the assembly of the STORM microscope. However, as the number of potential interferences is considerable, it is not always possible to eliminate all of them. In the case of axial drift, upgrades like the perfect focus system, which was described above, are able to correct drift simultaneously during data acquisition. In order to transfer this method to lateral drift, it is necessary to introduce fiducial markers whose positions can subsequently used for correction. However, as lateral movement of the stage could only be performed by motors, this approach would not have provided the required accuracy. Here, analytical correction mechanisms have to be applied in order to reconstruct a reasonable image.

Several approaches are possible for drift correction, from which the following attracted interest for super-resolution microscopy in literature. One possibility is to add a fluorescent marker that does not blink and to localize and track its position over the entire acquired data stack [9, 10]. The second method, which was adapted for this study, can be applied without the use of an additional marker and is based on cross-correlation of the images of the respective raw data stack [60]: one reference frame m, which is typically the first frame of the image stack, is correlated with another frame n from the same image stack obtaining its cross-correlation function G_{mn}:

$$G_{mn}(x,y) = \frac{\sum_i \sum_j \left(I_m(i,j) I_n(i+x,j+y)\right)}{\sqrt{\sum_i \sum_j (I_m(i,j))^2 \sum_i \sum_j (I_n(i+x,j+y))^2}} \tag{3.28}$$

The intensities from each pixel (i,j) in m, $I_m(i,j)$, are compared to the intensities from each pixel $(i+x,j+y)$ in n, $I_n(i+x,j+y)$, where the variable pair x,y defines a spatial shift between m and n. The term in the denominator normalizes the function. For reasons of programming efficiency, the cross-correlations for x-drift, $G(x)$ and y-drift, $G(y)$ were calculated separately from each other in this context. Examples for such cross-correlation functions are shown in Figure 3.15A. For this purpose, 200 nm sized polystyrene beads labeled with Alexa Fluor 488 and Cy5 as activator-reporter dye pair (for a detailed sample preparation protocol, see Section A.1.3) were measured with STORM for 25 minutes under a constant air current in order to intentionally generate drift, and thereby test the efficiency of the correction algorithm. The functions are shown for the x- and y-dimensions both for the auto-correlation of the first frame of the stack with itself (Figure 3.15A, blue and green points) and for the cross-correlation of the last frame with the first frame (Figure 3.15A, red and black points). Two features of the functions are of importance: first, the amplitude of the maximum, which gives information about the general similarity of both images, and second, the position of the maximum, which states at which shift x, y the similarity between the respective images is maximal and which therefore corresponds to the drift between both frames. In order to obtain the exact position of the maximum on a sub-pixel scale, G_{mn} was subsequently fitted to a second order polynomial.

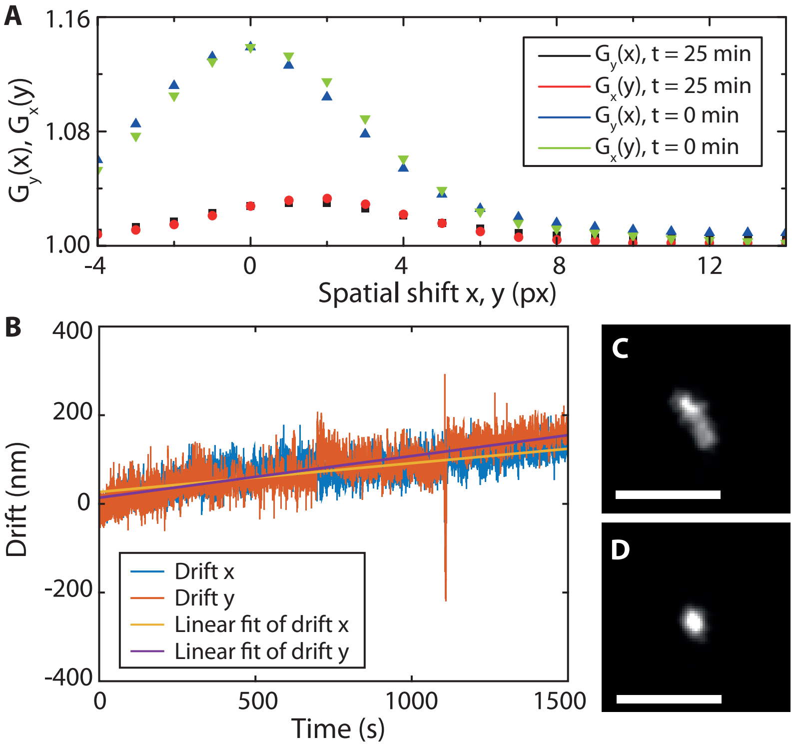

Figure 3.15: Principle of lateral drift correction at the example of the STORM image of a 200 nm sized bead. (A) The first frame of the image stack was cross-correlated with itself and with the last frame of the stack, separately calculated for x- and y-dimension. (B) A drift curve was obtained by plotting the maxima of all cross-correlation functions of each frame of the stack with the first frame calculated analogously to A. The raw data curve was subsequently fitted to a first order polynomial. (C) The STORM image of a single 200 nm sized bead is shown, which is biased by drift. (D) The drift visible in C was corrected applying the fitted curve from B. Scale bars: 500 nm.

This analysis was performed for the entire movie stack and the cross-correlation maxima of the correlation of each frame with the reference frame were plotted against data acquisition time. The result was a drift curve as shown in Figure 3.15B for the example of the bead measurement. In order to remove fluctuations, the raw drift curve was fitted to a polynomial function of first or higher order depending on the course of the drift. For example, a linear fit was sufficient in Figure 3.15B. The obtained fit could then be used to correct the localizations in the respective frames during the image rendering process (Section 3.2.4). In order to demonstrate the performance of this method, Figure 3.15C shows the uncorrected image of a 200 nm sized bead in comparison to the corrected image of the same bead in Figure 3.15D using the drift curve shown in Figure 3.15B. The quality of the image obviously improved and the round shape of the bead, which could not be derived from Figure 3.15C, became visible.

Despite the fact that this method also works without additional non-blinking or markers, which do not photobleach, as it is the case for the tracking approach, it is nevertheless important to select a region of the respective image stack where the signal density is high. Otherwise, the risk of comparing signals with background noise increases, which will result in a lower similarity, which will affect the cross-correlation function and distort the obtained drift value. In contrast, a too high signal density is again unfavorable for super-resolution imaging. This means that either a compromise between both conditions has to be found or that fiducial markers have to be used.

There are also some cases where drift correction by image cross-correlation is not possible. This applies especially to the correction of axial drift for 3D imaging when the information about the axial position is only indirectly derived from e.g. PSF astigmatism or similar approaches. It is possible to correlate the final localized particle coordinates instead of the raw data pixels but this method requires an even higher density of events to deliver accurate results coming along with the already described conflict with low activation density. In order to improve the results provided by this approach, it might be helpful to apply the algorithm only to a subregion of the image with a high event density arising, for example, from fiducial markers.

Alternatively, drift data can be emulated by linear or polynomial interpolation when magnitude and direction of the drift can be roughly estimated. If these conditions are given, image quality can still be enhanced considerably by careful selection of the respective parameters. This option was additionally implemented into the STORM data evaluation software. However, it has to be emphasized again that none of these correction methods can compete with data that was not biased by drift from the beginning.

3.3 Calculation of image resolution

Calculation of image resolution is mandatory to estimate image quality in a reliable way. It has already been discussed that the achievable resolution defines the smallest distance at which two signals can still be separated. In STORM, PALM and other related methods, this parameter strongly depends on the localization accuracy, which in turn is a result of the number of detected photons.

In order to transform this value into a resolution according to the definition given above, a displacement analysis was performed, which is depicted in Figure 3.16A. The underlying principle is based on the fact that each fluorescent molecule that is activated in a STORM measurement can usually be observed for a certain number of frames before it eventually switches back to the dark state or photobleaches. A position can be assigned to the fluorophore in each of these frames, which might vary slightly from frame to frame due to localization inaccuracies. Signals in two subsequent frames are assumed to arise from the same fluorescent molecule when their distance is not larger than 1 pixel as described in Section 3.2.4. Likewise, events that occur in only one frame are excluded from analysis. In the next step, the displacements for each of the obtained positions relative to the position of the respective molecule in the first frame where it is active are calculated and added to a displacement histogram. This principle is illustrated in the left part of Figure 3.16A for the example of the x-coordinate of a molecule that is active for three subsequent frames providing three slightly varying x-positions (x_1, x_2, x_3). This gives the respective displacements $x_1 - x_1$ for the first frame, $x_2 - x_1$ for the second frame and $x_3 - x_1$ for the third frame, which are plotted in the histogram shown in the left part of Figure 3.16A. When this analysis is performed for all molecules in the respective measurement, a displacement distribution plot can be created for each imaging dimension as shown in the right part of Figure 3.16A for the x-dimension, which does not include the values for $x_1 - x_1$. This distribution

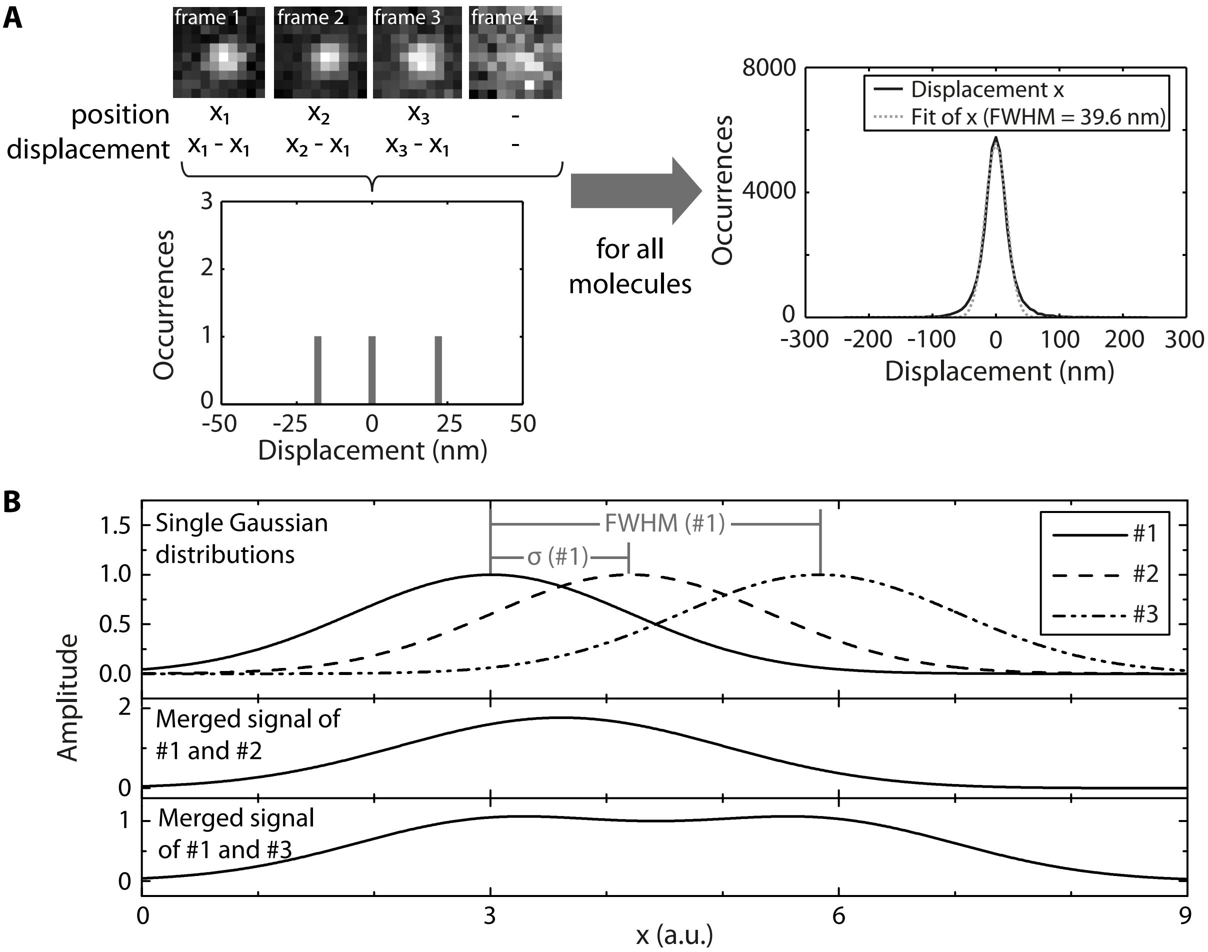

Figure 3.16: Calculation of STORM image resolution. (A) *Left panel.* The displacements for the localizations of a single fluorescent emitter are calculated and plotted into a histogram (separately for each dimension, here shown at the example of the x-dimension). *Right panel.* This analysis is repeated for all events of a measurement and the histogram containing all displacements of the respective measurement is fitted to a Gaussian function returning the FWHM as resolution criterion. (B) The preference of the FWHM from A as resolution criterion is shown for a simulated Gaussian distributions #1, #2 and #3 (top row). The distance between the centroid positions of #1 and #2 is equal to σ of #1 and the distance between the centroid positions of #1 and #3 is equal to the FWHM of #1. Whereas the distinct functions are not separable in the sum of #1 and #2 (middle row), this is the case for the sum of #1 and #3 (bottom row).

is subsequently fitted to a one-dimensional Gaussian function

$$I(x) = I_0 \cdot \mathrm{e}^{-\frac{(x-x_0)^2}{2\sigma^2}} \tag{3.29}$$

with amplitude I_0, centroid position x_0 and standard deviation σ. The FWHM of the obtained function is selected as resolution criterion, which can be calculated by means of σ as FWHM $= 2\sqrt{2\ln 2} \cdot \sigma$. Figure 3.16B illustrates the suitability of the FWHM as a meaningful resolution criterion in contrast to other options such as the standard deviation of the Gaussian function fitted to the displacement histogram. In the top row of Figure 3.16B, three Gaussian functions (#1, #2 and #3) are plotted, where the distance between the centroid positions of #1 and #2 is equal to the standard deviation of #1 and where the distance between the centroid positions of #1 and #3 is equal to the FWHM of #1. The middle row shows the merged signal of distributions #1 and #2, which does not allow the separation of the original distributions from the top row. In contrast, the merged signal of #1 and #3 (bottom row) can be resolved into the respective parts as the maxima of #1 and #3 remain visible. This means that the FWHM of the displacement histogram gives a reliable value for optical resolution in contrast to the standard deviations.

Although this approach does not directly include the number of collected photons per event to calculate the localization accuracy it is nevertheless strongly influenced by this number as it is shown in Figure 3.17A. Different photon thresholds were applied to a data set of localized molecules (the resulting image can be found in Section 3.5) whereas all other parameters were hold constant. As expected, the more events with low photon counts were included into the evaluation the worse was the obtained resolution. The calculated resolutions are compared to the localization accuracy given by $\sigma/\sqrt{N}$ (Eq. 2.21) for the respective photon thresholds and a standard deviation, $\sigma = 200\,\text{nm}$. Apparently, the values obtained by Eq. 2.21 yield a significant underestimation of the actual resolution, which is also influenced by other factors such as background noise. This result shows the need for a method as presented in Figure 3.16, which includes these factors and therefore provides a more reliable result.

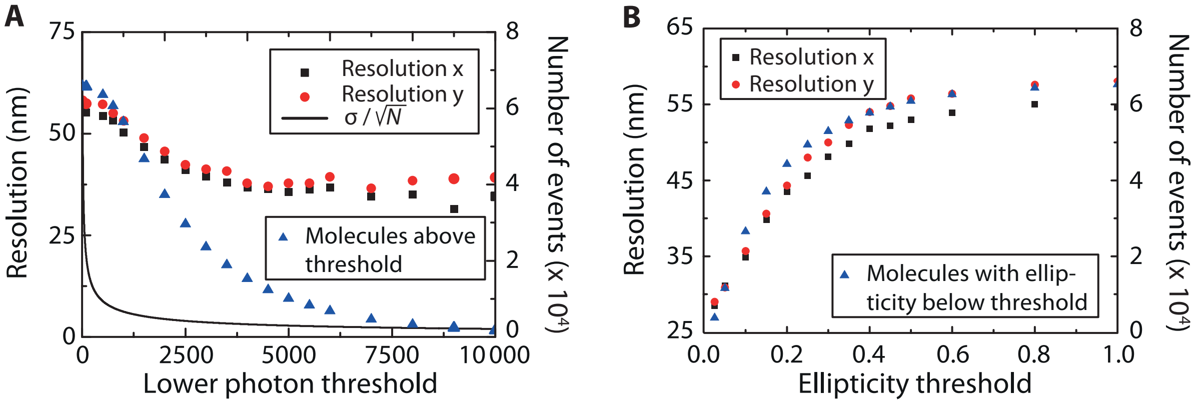

Figure 3.17: Effect of lower photon and ellipticity thresholds on resolution is shown at an exemplary acquisition with 668 908 detected events in total. (A) Optical resolution of a STORM or PALM image improves with raising of the lower photon threshold. The theoretical minimal localization accuracy calculated by $\sigma/\sqrt{N}$ underestimates the actual resolution. (B) Optical resolution decreases with increasing ellipticity threshold. Both thresholds come along with a diminishing number of molecules included into the evaluation.

Apart from photon statistics, multiple activations have negative impact on resolution in STORM and PALM as well. This is demonstrated in Figure 3.17B for the same data set as used in Figure 3.17A, where the ellipticity threshold defined by Eq. 3.27 was continuously increased from 0.0 to 1.0 whereas the lower photon threshold was kept constant at 300 photons. It is evident that higher ellipticity thresholds result in a worse resolution.

However, excluding events by redefining the thresholds also means that less points are available to render the high-resolution image. As a consequence, the apparent labeling density gets too low and the final result might be an image of bad quality despite a nominally good resolution. Therefore, a compromise must be found between reasonable thresholds and the number of discarded data points. Regarding ellipticity, a threshold value of 0.15 was chosen, which did not discard more than approximately half of the molecules. As imposing a similarly strict threshold on the photon counts as well would critically decrease the number of admitted molecules, the criterion was here set to the relatively low value of 300 photons. The combination of both thresholds however has been shown to provide reasonable resolutions. For example, the calculation shown in Figure 3.16A returned a resolution in the x-dimension of approximately 40 nm. This value lies about 20 nm above the lowest numbers presented in literature so far (Table 2.2). However, instead of reducing statistics below a critical point to reach these values, it is rather recommendable to improve photon detection efficiency of the used optics. The obtained resolutions have nevertheless been found to be sufficient for the studies presented here.

3.4 Calculation of cluster sizes in super-resolution images

Apart from the determination of image resolution, the quantitative analysis of super-resolution images further requires a comparable standard to measure sizes of observed structures. Two approaches were applied in this study. The first uses the FWHM of a Gaussian function that is fitted to the structure as shown previously [62]. The second is based on Ripley's cluster analysis, which also has already been used for super-resolution microscopy [101].

The first method is based on fitting a model function to the observed structures for quantification. Each event in the final super-resolution image is represented by a normal distribution defined by the localization uncertainty or the image resolution as discussed in Section 3.2.4. According to Cramér's theorem [102], the sum of normal Gaussian distributions is again a normal distribution and as complex structures in a super-resolution image are a sum of normal distributions, these structures can be described by a Gaussian distribution as well. As a consequence, a cross-section can be laid through the respective structure and fit to a Gaussian function. Depending on the sample, it might be either preferable to lay a cross-section through the sample and fit this cross-section to a one dimensional Gaussian function (e.g. for filamentous structures) or to a two-dimensional Gaussian function (e.g. for spherical objects). The FWHM of the obtained Gaussian function can then be taken as an estimate for the size of the structure.

The performance of this method is demonstrated on a simulated data set representing a hollow sphere with a diameter of 200 nm and a variable shell size. This system was chosen to simulate dye molecules attached to the surface of a sample. For example, Figure 3.18A shows, on the left, the simulated data points for a 200 nm sphere with a thin shell of diameter 12 nm and, on the right, the corresponding STORM image reconstructed from the simulated data set. In contrast, a compact sphere is shown in Figure 3.18B, which was emulated by setting the shell width to half of the diameter of the sphere.

Figure 3.18C shows the results of the FWHM analysis, on the one hand, for the one-dimensional fit of a vertical cross-section through the cluster (black points) and, on the other hand, for a two-dimensional Gaussian fit for the entire object (red points). The value provided by the FWHM was the closer to the actual size of the bead of 200 nm when the shell was thin. It delivered almost exact results for shell widths smaller than 12 nm when using a one-dimensional fit. As the size of typical chemical dyes lies in this order of magnitude, the FWHM can be considered as an appropriate approach to measure cluster sizes. Although a slight underestimation of the size cannot be excluded, the results are reliable. When the aim is not the determination of absolute values but to compare relative size differences as done in Chapter 4, the underestimation does not have negative impact on the results. Interestingly, the one-dimensional fit throughout delivered better results than the two-dimensional fit. For this reason, a fit to the one-dimensional cross-section was always performed in the course of this study for estimating cluster sizes by the FWHM if not stated otherwise.

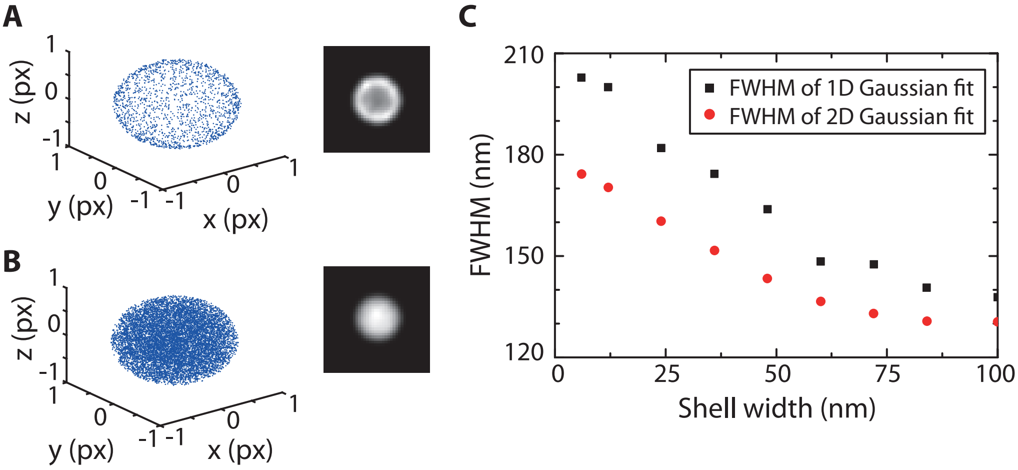

Figure 3.18: FWHM cluster size analysis. (A) Simulation of a hollow sphere with a diameter of 200 nm and a shell thickness of 12 nm (*left panel*) and the corresponding 2D STORM image (*right panel*). (B) Simulation of a compact bead with a diameter of 200 nm (*left panel*) and the corresponding STORM image (*right panel*). (C) Apparent size of simulated hollow spheres with varying shell thicknesses using the FWHM of a one- or two-dimensional Gaussian fit as estimate.

It is, however, not always possible to apply a fit-based analysis method, for example, when the number of localized molecules contributing to a structure is too small to allow an accurate fit. For these cases, Ripley's K-function [103, 104] and the related L-function [105] were used for estimating the cluster size. The K-function provides a statistical analysis of all possible distances d between distinct components that form a larger structure and is given by the following expression:

$$K(d) = \frac{\sum\limits_{i \neq j} I(d_{ij} < d)}{\lambda} \tag{3.30}$$

Here, d_{ij} is the distance between two points i and j and I an indicator function, which is 1 if d_{ij} is smaller than d and 0 otherwise. λ represents the density of points in the cluster. In other words, $K(d)$ sums up all events within distance d normalized to the density of events λ as shown in Figure 3.19A, which depicts the K-function of a 200 nm sized bead. Apparently, the K-function reaches its maximum at the size of the respective structure as obviously no distances d_{ij} exist within the structure that exceed this value.

The K-function is a test for spatial randomness and takes the value πd^2 for Poisson distributions (e.g. given by background noise) and detecting clusters by deviations thereof. The disadvantage of this kind of representation is that these deviations are difficult to distinguish from randomness due to the non-constant mean of $K(d)$. For this reason, the L-function was introduced [105], which is derived from Eq. 3.30 by

$$L(d) = \sqrt{\frac{K(d)}{\pi}} \tag{3.31}$$

Written in this form, the function is constant for strictly Poissonian distributions. Eq. 3.31 can be further modified to the following expression, which is 0 for random processes and which is sometimes referred to as H-function:

$$H(d) = L(d) - d = \sqrt{\frac{K(d)}{\pi}} - d \tag{3.32}$$

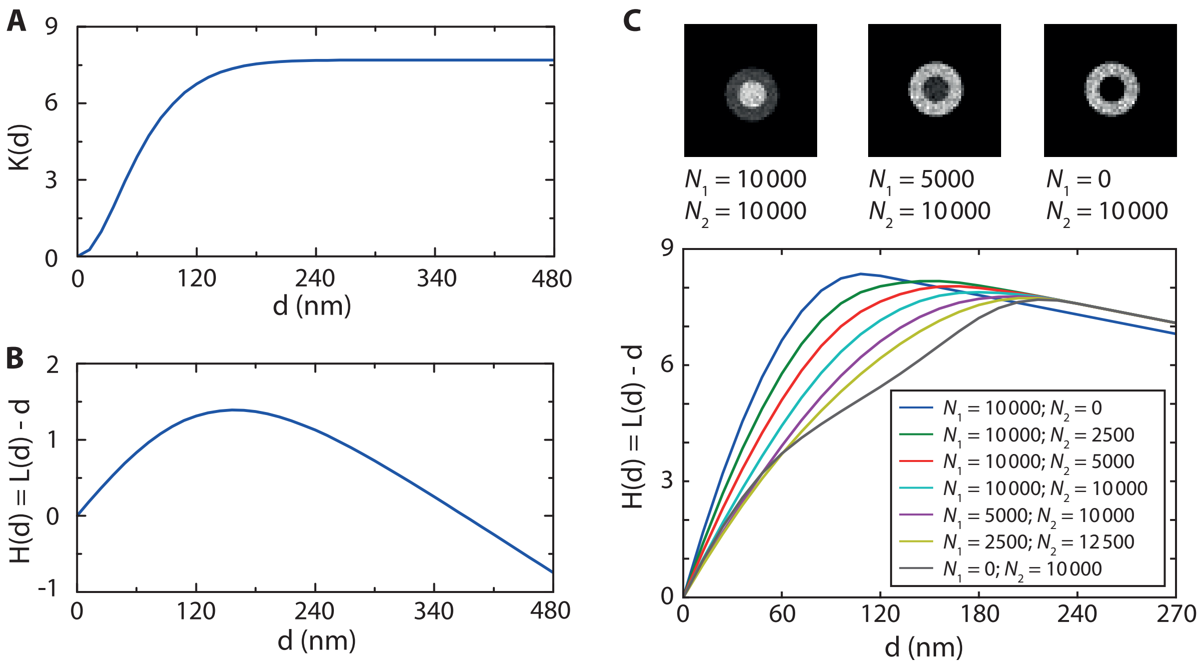

Figure 3.19: Ripley's cluster size analysis. Ripley's cluster functions were applied on a simulated 200 nm sized fluorescently labeled bead using (A) Ripley's K-function and (B) Ripley's L-function, which shows a maximum at 170 nm. (C) Ripley's L-function was applied on simulated structures of a circle with a diameter of 10 px containing N_1 points, which is surrounded by a ring with an inner radius of 10 px and an outer radius of 20 px, which contains N_2 points.

The H-Function for the bead, whose K-function is depicted in Figure 3.19A, is shown in Figure 3.19B revealing a maximum at $d = 170$ nm. This value is close to the nominal size of the bead although there is a certain underestimation. Kiskowski *et al.* [106] showed that the maximum of the combined H-function of two non-random clusters with the same radius r and the same point density λ lies between r and $2r$ depending on the distance S between the single clusters. When $S \to \infty$, the position of the maximum converges to $2r$. In order to further evaluate the dependence of the position of the maximum of Ripley's L function on the nature of the analyzed cluster, ring structures were simulated consisting of two rings. The inner structure with a point density N_1 had a radius of 10 px and the outer ring with point density N_2 an inner radius of 10 px and an outer radius of 20 px: analysis of the resulting L-functions showed that the size of inner structure was only reproduced correctly when the outer ring was not present ($N_2 = 0$). Otherwise, the maximum was shifted more and more towards higher values until it reached the other extrema when $N_1 = 0$. With respect to the evaluation of STORM images this means that a reliable result can only be expected when the respective cluster is isolated from other non-random structures and featuring a homogeneous point density distribution.

In contrast to the FWHM as size estimate, Ripley's cluster analysis strongly depends on environment conditions. Although the FWHM-based method involves an underestimation of the actual size, it appears to be more reliable as especially in densely populated images the requisite of isolated particles is not always given. As a consequence, structure sizes measured in the course of this studies are based on the one-dimensional FWHM, which gave better results than the two-dimensional FWHM, if not stated otherwise. Ripley's cluster analysis was primarily performed in cases where particle statistics were too low to allow an accurate fit for the FWHM analysis.

3.5 2D dSTORM imaging of HeLa cell microtubules

In order to test the capacity of the super-resolution microscope and the applied measurement and analysis protocols, microtubules of HeLa cells were imaged with dSTORM. Microtubules are a component of the cellular cytoskeleton and form a fine network of filaments that consist of dimers of the two proteins α- and β-tubulin. Microtubules fulfill a number of important functions in the cell such as building a scaffold for dynein and kinesin motor proteins or the formation of the spindle apparatus that organizes allocation of chromosomes during cell division [107].

For dSTORM imaging, α-tubulin was labeled by immunostaining with primary anti-α-tubulin and appropriate Cy5-labeled secondary antibodies. The detailed protocol can be found in Section A.1.5. Figure 3.20A shows a conventional widefield image of the microtubule network of a HeLa cell prepared in this way. It can be easily seen that, although the coarse orientations of the filaments are visible, detailed structures remain hidden especially in regions when filaments are crossing or running close to each other as e.g. in the region marked with the yellow rectangle. As a consequence, a dSTORM image was acquired. For this purpose, a stack of 15 000 frames was recorded at a frame rate of 20 Hz. A least squares Gaussian fit was performed and the resulting super-resolution image, which is shown in Figure 3.20B, was rendered as described in the sections above. Comparing the super-resolution image to the widefield image shown in Figure 3.20A reveals the gain in structural resolution obtained by dSTORM. Filaments that could not be separated before are now distinguishable. The difference can be even more pointed out when the widefield and the corresponding super-resolution image of a region of the image with a relatively dense structure are compared in higher magnification in Figure 3.20C.

Figure 3.20D shows a cross-section through a filament that is marked by the green rectangle in Figure 3.20B. A one-dimensional Gaussian function was fitted to the average cross-section profile and its FWHM was taken as a good estimate of the diameter of the filament (cf. Section 3.4). The measured FWHM of approximately 82 nm is considerably larger than literature values from EM measurements which state an average diameter of a single filament of about 25 nm [108]. The resolution of the dSTORM image in Figure 3.20B, which was calculated as described in Section 3.3, was found to be 40.4 nm and 41.7 nm in x- and y-direction, respectively (Figure 3.20E), which means that the measured size could not only be an artifact of suboptimal resolution. However, it has to be considered that both antibodies, which were attached to the structure, had a finite size of approximately 10 nm each [108]. When this size is added to the diameter of the filament, the resulting value lies in the same order of magnitude as the measured value. In order to increase structural resolution, the use of smaller labels is necessary. For example, nanobodies that only consist of the antigen binding region of the original antibody might be considered [109, 110]. If visualization of a modified protein instead of the endogenous protein is feasible, specific labeling of tubulin might also be achieved by using small self-labeling protein constructs (e.g. SNAP-tag [111]) in combination with appropriate dyes for STORM or dSTORM.

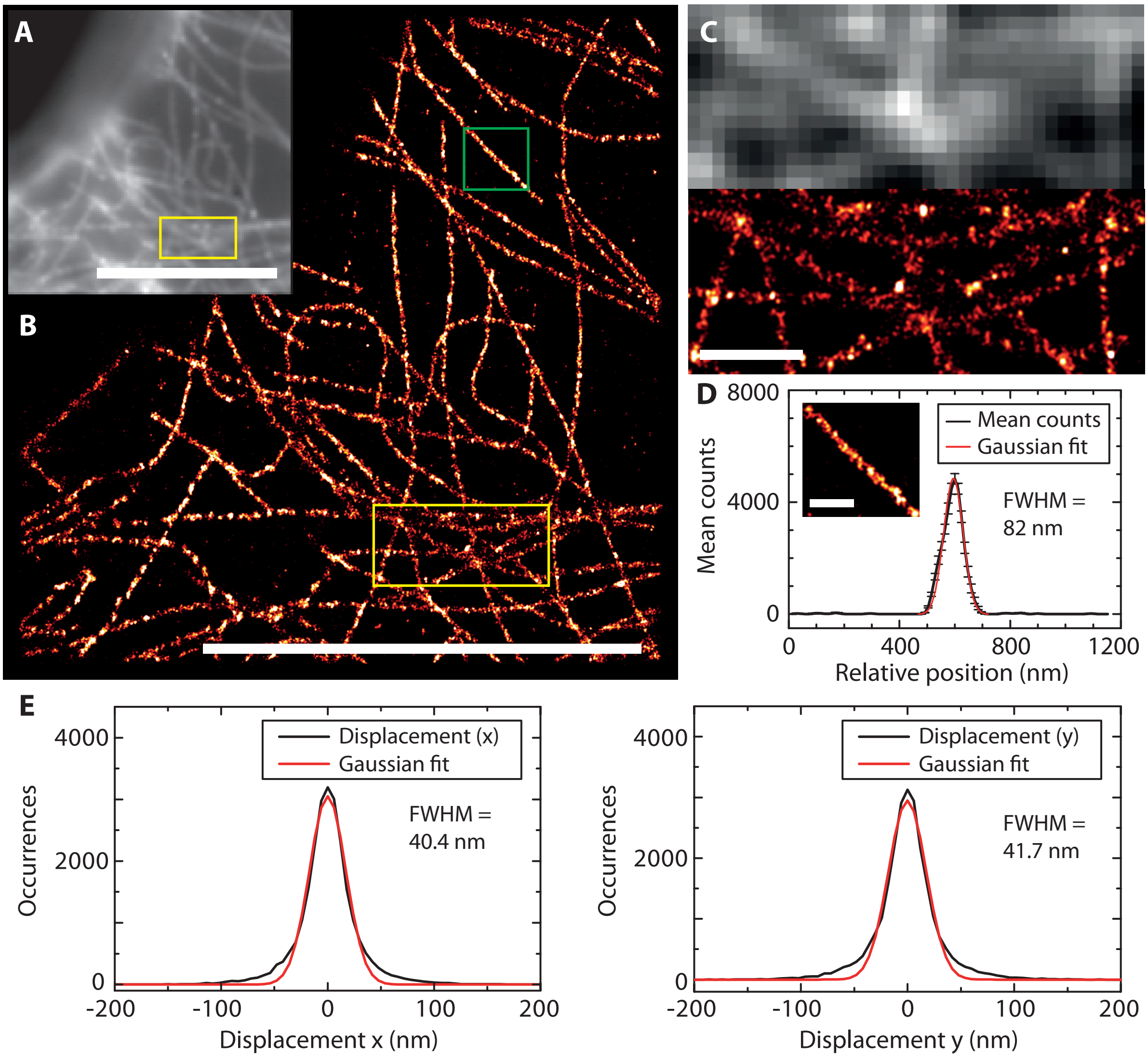

Figure 3.20: 2D dSTORM super-resolution imaging at the example of HeLa cell microtubules. (A) A conventional widefield image of immunostained microtubules of a HeLa cell is shown. (B) Resolution was significantly increased in the corresponding 2D dSTORM image. Scale bars: 10 µm. (C) Direct comparison of the widefield and the super-resolution image at a region with high tubulin density marked by yellow rectangles in A and B, respectively, demonstrates the gain in structural resolution. Scale bar: 1 µm. (D) The average cross-section (black line, error bars represent the standard error of the mean) through the filament marked by green rectangle in B and shown in the small inlay was fitted to a Gaussian function (red line) with a FWHM of 82 nm. Scale bar: 500 nm. (E) Displacement analysis returns resolutions of 40.4 nm in the x-direction (left panel) and of 41.7 nm in the y-direction (right panel), respectively, for the super-resolution image shown in B.

3.6 Implementation of three-dimensional STORM and dSTORM

After two-dimensional super-resolution microscopy was successfully established, the next step was the extension of the method to the third dimension. For this purpose, the astigmatism-based approach as presented by Huang *et al.* [72, 73] (see also Section 2.3.3) was chosen.

3.6.1 Astigmatism calibration for 3D STORM and dSTORM imaging

Although astigmatism-based 3D STORM or dSTORM offers a relatively straightforward approach for three-dimensional super-resolution imaging, careful selection of tools and parameters such as the cylindrical lens as well as conditions for calibration measurements is nevertheless crucial to obtain images of good quality. The first step here was the selection of a suitable cylindrical lens combined with the optimal distance to the detector, in which the lens is placed. The longer the focal length or the smaller the distance to the detector becomes, the weaker will be the astigmatism of the PSF. If the latter gets too small, as shown for example in Figure 3.21A, the sensitivity for accurate separation of z-coordinates is too low.

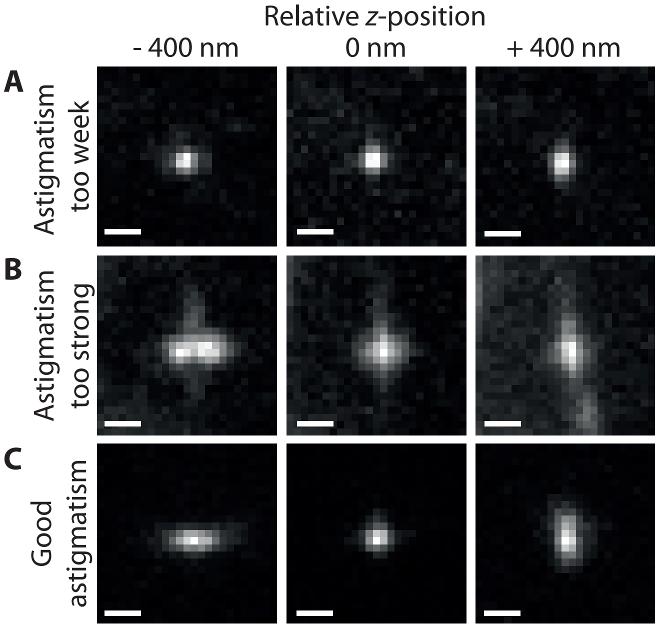

Figure 3.21: Criteria for selection and alignment of the cylindrical lens for 3D super-resolution imaging. The PSFs are shown for setups where (A) the astigmatism too weak and does not offer enough sensitivity for high-resolution imaging, (B) the astigmatism is too strong and (C) the astigmatism is suitable for 3D imaging. Scale bars: 600 nm.

In contrast, a too strong lens or a too large distance to the detector will result in a too strong astigmatism, which will distort the image as demonstrated in Figure 3.21B. Here, the PSF shows already an astigmatism when the system is in focus and accurate fitting of this PSF is hardly possible. For a good astigmatism, as depicted in Figure 3.21C, the PSF should still appear round in the focal plane with a detectable elongation of the PSF visible when defocussing. In this case, these conditions could be obtained when a cylindrical lens with a focal length of 3 m was placed in a distance of 24 cm in front of the camera.

In the next step, a calibration measurement had to be performed in order to be able to assign specific PSF shapes to the corresponding z-coordinates. In this context, both the sample and the environment in which the calibration measurement is performed are essential. For the selection of a good calibration sample, it is important that the sample is significantly smaller than the PSF of the system in a way that σ^2_{object} in Eq. 2.10 is negligible compared to σ^2_{PSF}. Here, 40 nm sized polystyrene or latex beads were labeled with Cy5 and embedded in a polymeric gel with a refraction index very close to that of water ($n_{Gel} = 1.32$). A detailed protocol for the preparation of the calibration sample can be found in Section A.1.4.

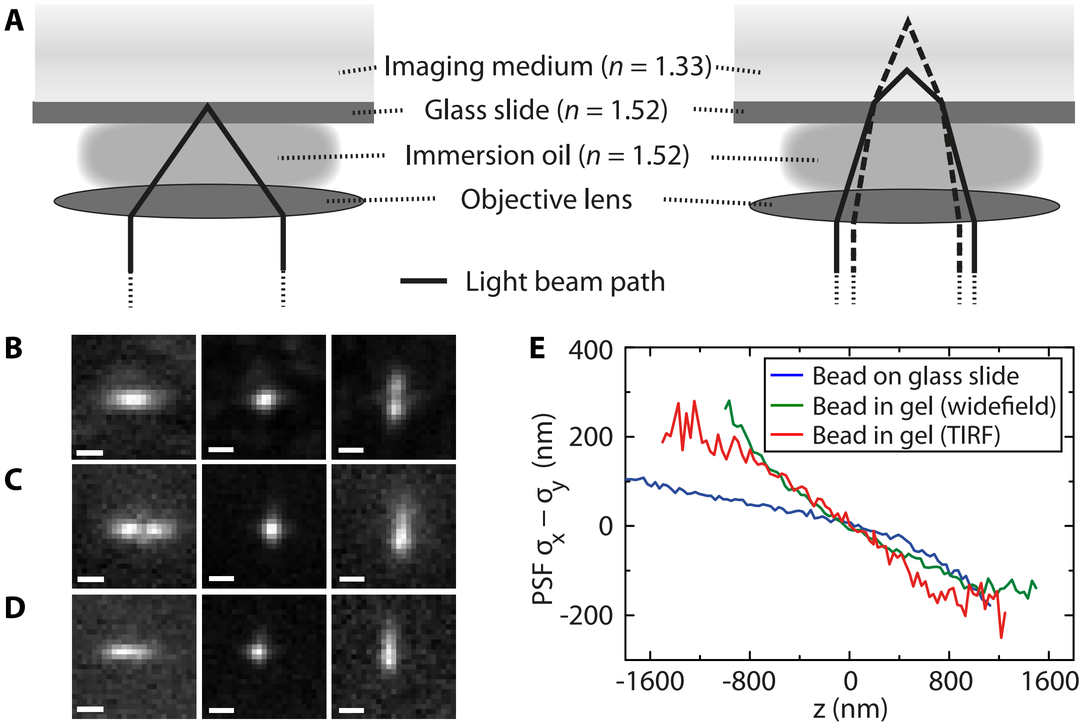

Figure 3.22: Dependence of 3D STORM astigmatism calibration on axial position of the calibration sample. (A) The fluorescence beampaths vary between objects touching the glass slide (left part) and objects in two different distances from the surface (right part, solid and dashed lines). (B-D) The PSFs for a 40 nm sized bead are shown above the focal plane (left), in focus (middle) and below (right) for (B) a bead touching the slide, (C) a bead in gel visualized in TIRF mode and (D) in widefield mode. Scale bars: 600 nm. (E) The calibration curves for the measurements shown in B-D deviate depending on the experimental conditions.

Embedding the sample in a gel was necessary as the calibration measurement depends on the axial position of the sample as explained in Figure 3.22A: on the left side, the detection optics for a fluorophore directly placed on the surface of a glass microscope slide are shown, whereas the sample on the right side is found in a certain distance from the slide in a medium whose diffraction index is smaller than that of the slide. This is of importance because the emitted fluorescence has to pass several phase interfaces and refraction will be observed at each of them according to Snell's law. First, refraction occurs at the interface between the sample medium and the glass of the slide. As usually $n_{Medium} < n_{Oil}$, the fluorescence will be refracted towards the perpendicular according to Snell's law. In the extreme case, which is shown in the left part of the figure, where the object is in direct contact with the surface, refraction does not occur at all. The following interfaces between the slide and the immersion medium as well as between the latter and the objective lens will also induce a small change in direction on the light. However, these changes can be neglected in general as the refraction indexes of common immersion oils (in this case: $n_{Oil} = 1.52$) are typically designed to match that of glass ($n_{Glas} \sim 1.5$). Depending on the distance of the emitter from the surface of the slide the angle of refraction changes as demonstrated in the example on the right part of Figure 3.22A. As a consequence, the remaining detection pathway and eventually the PSF will change as well.

The effect of these considerations is demonstrated in Figure 3.22B-E: Figure 3.22B shows the PSF for a bead placed directly on the glass slide and imaged with the implemented cylindrical lens. The middle image was taken when the bead was in focus, the left and the right image show the PSF for positions above and below the focal plane, respectively. The same measurement was performed for a bead embedded in a gel as described above. In Figure 3.22C, TIRF illumination was used in order to ensure that a bead relatively close to the slide was imaged, whereas the bead in Figure 3.22D was imaged with widefield illumination. Although the general shapes of the PSFs seemed to be relatively similar, the corresponding calibration curves in Figure 3.22E, where the differences of the PSF standard deviations, $\sigma_x - \sigma_y$, were plotted against the axial position z, revealed divergences. Especially the curve for the bead in contact with the glass slide (blue curve) showed a significant deviation from the curves for the beads in a gel using either TIRF (red curve) or widefield illumination (green curve). It has to be pointed out that these deviations were larger for positions measured below the focal plane, which were closer to the glass slide. The difference between the two curves for the beads in gel was not as large but nevertheless still visible. Another observation that should not be omitted can be found in the right image of panel B: the PSF acquired very close to the surface of the slide appeared to be split, which was probably the result of a reflection on the surface. This is supported by the fact that a similar pattern is visible in the left image of panel C, where reflection on the upper surface on the gel could be the reason. In contrast, the PSF of the bead in the middle of the gel (panel D) did not show such an artifact. All these observations underline the significance of the axial position at which the calibration curve for 3D STORM was measured.

Taking all of this into consideration, a calibration curve shown in Figure 3.23A and B could be acquired. Again, a 40 nm sized, labeled bead as described above was scanned in steps of 10 nm by moving the piezoelectric objective scanner. In panel A, the standard deviations of the fitted PSF in x and y-direction, σ_x and σ_y were plotted against the axial position. It has to be pointed out that the two curves should be symmetric to each other as it is the case in Figure 3.23A. If this is not the case, it is most likely a sign for a misaligned detection channel. A reason for this can, for example, be a tilted cylindrical lens. Such a misalignment will result in a tilted PSF shape and has to be corrected in order to achieve a good resolution in the axial dimension.

Another form of presentation of the calibration measurement, which was already used in Figure 3.22E, is shown in Figure 3.23A, where $\sigma_x - \sigma_y$ is plotted against z and subsequently subjected to a polynomial fit. In the case of well aligned detection optics including the cylindrical lens, this plot should give a straight line. The obtained parameters from this fit can be used afterwards to transform the PSF standard deviations of any sample into z-positions as long as the optics are not changed and imaging is performed in approximately the same height as the calibration before due to the reasons described above.

Another important aspect for 3D super-resolution imaging is the stability of the microscope system and applied correction mechanisms like the perfect focus system. In fact, the demands on stability are significantly higher than they are for 2D super-resolution imaging. This was tested for the described microscope by monitoring the z-position of a 40 nm sized bead from the calibration sample over time. The respective z-positions were subsequently obtained by applying the calibration curve shown in Figure 3.23B yielding the results that are depicted

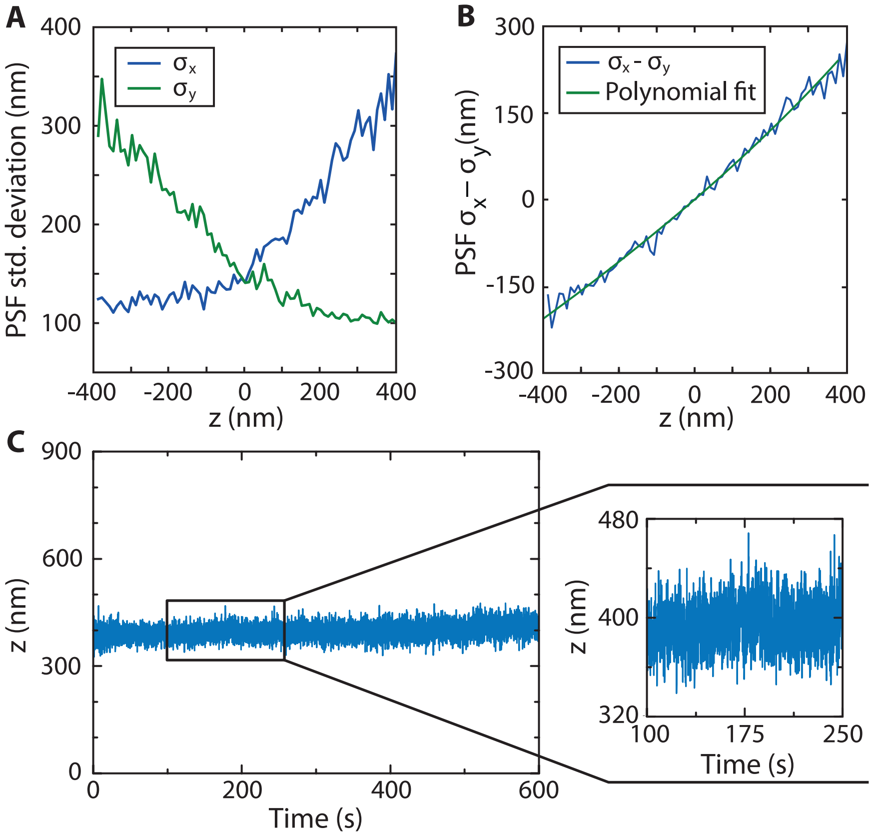

Figure 3.23: Optimized calibration curve and setup stability test for 3D STORM. (A) A calibration curve at optimized microscope alignment condition is shown either with standard deviations, σ_x and σ_y, directly plotted against the axial position z or (B) in the form of $\sigma_x - \sigma_y$ that allows a polynomial fit. (C) The stability of the 3D STORM setup was tested by monitoring the position of a 40 nm sized bead over 10 minutes.

in Figure 3.23C. It can be seen that the position of the sample was stable within a range of approximately 80 nm over a time period of 10 minutes. This value therefore defines the best achievable axial resolution under the given conditions.

3.6.2 3D dSTORM imaging of test samples and data analysis

After the optimization of the calibration process, test measurements with appropriate samples were performed in order to evaluate the resolution capacity of the microscope in the axial dimension. First experiments were performed with Cy5-labeled polystyrene beads with a nominal diameter of 200 nm (for a detailed sample preparation protocol, see Section A.1.3). Figure 3.24A shows the diffraction-limited image of such a bead sample, which was emulated from the average time projection of the widefield image stack that was acquired for dSTORM imaging. Figure 3.24B shows the x-y-projection of the reconstructed 3D dSTORM image of one selected bead. This image would correspond to the corresponding 2D dSTORM image. The lateral dimensions of the structure in terms of the FWHM of a Gaussian function fitted to the cross-sections were 214 nm in the x- and 225 nm in the y-dimension, respectively, which reproduced the nominal size of the bead accurately. Figure 3.24C depicts the x-z-projection of the same bead, revealing an apparent size of 247 nm in the axial dimension. These results showed that it was possible to reproduce the actual size of the bead in good proximity although the axial resolution (162 nm) was worse than the lateral resolution of 64 nm in the x- and of 40 nm in the y-dimension, respectively.

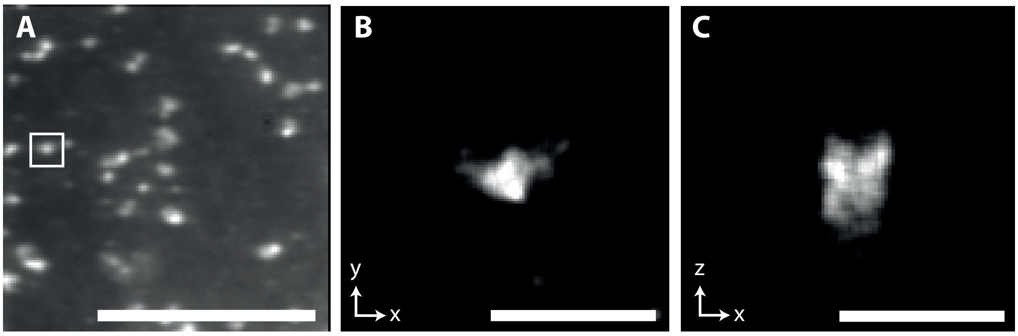

Figure 3.24: 3D dSTORM imaging of polystyrene beads. (A) The average time projection of an image stack acquired for dSTORM emulates the widefield image of 200 nm sized polystyrene beads. Scale bar: 10 µm. (B) The x-y-projection and (C) the x-z-projection of the 3D dSTORM image of the bead marked by the rectangle in panel A reveals the spherical shape of the bead. Scale bars: 600 nm.

Although imaging of the bead sample demonstrated the successful implementation of 3D dSTORM, a more complex and finer structure was required to determine the limits in resolution, which is achievable under the given conditions. For this purpose, immunostained microtubules in HeLa cells were imaged, which where prepared following the same protocol as for 2D dSTORM imaging. Figure 3.25A shows the diffraction-limited TIRF image of a cell with immunostained α-tubulin, which was generated by means of the average time projection of the image stack acquired for super-resolution imaging. Figure 3.25B depicts the corresponding 2D dSTORM image and Figure 3.25C the 3D dSTORM image (generated with rapidSTORM [97]), where the color code represents the axial position. In contrast to panels A and B, the axial course of the single microtubule filaments becomes clearly visible in the three-dimensional image. Different levels can be easily distinguished and the relative position of filaments at crossing points is revealed, which is information that is not accessible in conventional widefield fluorescence microscopy or TIRFM.

The resolution calculated for the image shown in Figure 3.25C was 51.4 nm in x-, 45.2 nm in y- and 161 nm in z-direction (Figure 3.25D). Whereas the resolution in the lateral dimensions lay approximately in the same range as found for the 2D image in Section 3.5, the axial resolution could not compete with this value. Although axial resolution cannot be expected to be as good as the lateral resolution, literature values for astigmatism-based 3D STORM report resolutions down to 50 nm (cf. Table 2.2, [72, 73]), which is considerably better than the resolution that was achieved here. Additionally, axial resolution was also worse than the position stability of 80 nm that was determined in the previous section. In order to improve axial resolution, it is necessary not only to increase the current photon yield but also to seek a further improvement of the mechanical stability of the microscope, which might be a reason for the larger discrepancy to literature values in the case of the axial resolution.

Optical resolution is not the only criterion that defines the quality of a super-resolution image. Structural features like the size of attached labels can also have a significant impact. In order to analyze structural resolution, a single filament, which is marked by the white rectangle in Figure 3.25C, was selected and 2D projections were calculated for the different dimensions. These projections are shown in the inlays in Figure 3.25E-G, where Figure 3.25E shows the x-y-projection, Figure 3.25F the x-z- and Figure 3.25G the y-z-projection of the selected filament.

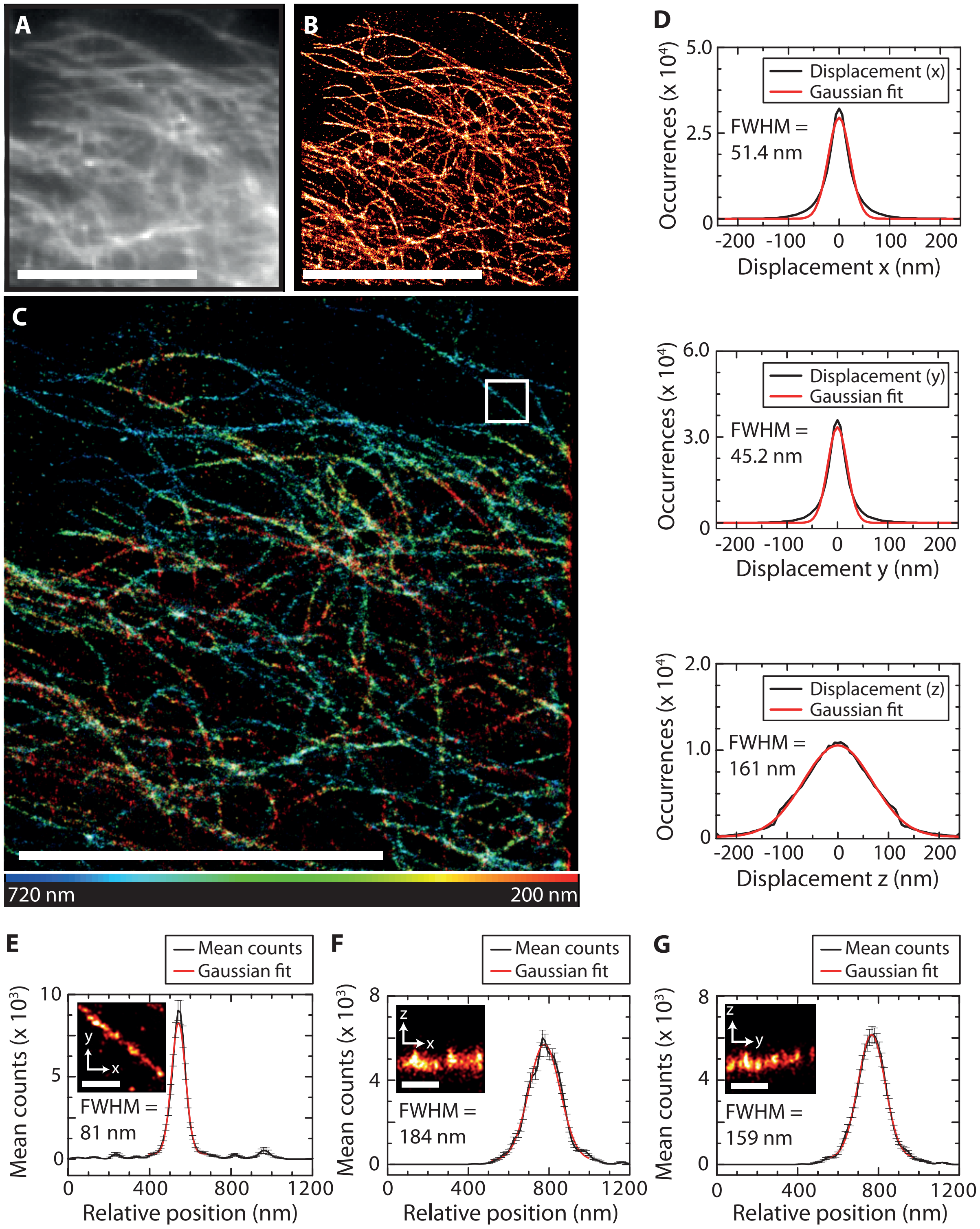
A
B
C
720 nm
200 nm
D
Occurrences (x 10⁴)
5.0
2.5
0
Displacement (x)
Gaussian fit
FWHM =
51.4 nm
-200 -100 0 100 200
Displacement x (nm)
Occurrences (x 10⁴)
6.0
3.0
0
Displacement (y)
Gaussian fit
FWHM =
45.2 nm
-200 -100 0 100 200
Displacement y (nm)
Occurrences (x 10⁴)
2.0
1.0
0
Displacement (z)
Gaussian fit
FWHM =
161 nm
-200 -100 0 100 200
Displacement z (nm)
E
Mean counts
Gaussian fit
Mean counts (x 10³)
10
5
0
y
x
FWHM =
81 nm
0 400 800 1200
Relative position (nm)
F
Mean counts
Gaussian fit
Mean counts (x 10³)
8
4
0
z
x
FWHM =
184 nm
0 400 800 1200
Relative position (nm)
G
Mean counts
Gaussian fit
Mean counts (x 10³)
8
4
0
z
y
FWHM =
159 nm
0 400 800 1200
Relative position (nm)

Cross-sections were taken for each projection and averaged over the entire length of the selected part of the filament (black curves, where the error bars represent the standard error of the mean). A one-dimensional Gaussian function was subsequently fitted to the respective cross-sections and the diameter of the filament estimated by the obtained FWHM. The diameter was found to be 81 nm in the x-y-projection, which was comparable to the value measured with 2D dSTORM. Again, the additional size of the attached antibodies has to be accounted for to explain the difference to the actual diameter of a microtubule filament. Measurements of the axial height of the filament yielded values of 184 nm (x-z-projection) and 159 nm (y-z-projection). These values match with the axial resolution calculated above, which therefore does not allow the determination of the actual diameter, which should, in theory, lie in the same range as for the lateral dimension.

Overall, the performed test measurements showed that three-dimensional super-resolution imaging could be successfully established on the constructed microscope applying the settings and parameters presented in Section 3.6.1. Although the resolution in the axial dimension can still be improved, it could be demonstrated that the present conditions have the capacity to provide meaningful insights into the three-dimensional organization and structure of biological samples.

3.7 Multi-color dSTORM

The vast majority of biological processes consists of an interaction of two or more different structures. Therefore, it is necessary to distinguish between distinct components using fluorescence microscopy in order to understand existing connections between them. This can be realized in the form of multi-color experiments where distinct structures are labeled with differently colored fluorescent labels. This approach can be combined with localization-based super-resolution techniques as was already introduced in Section 2.3.1.2.

In order to test the capability of the established super-resolution microscope to perform multi-color experiments, a multi-color dSTORM experiment was performed where Cy3 and Cy5 were used to label two different structures for imaging. This experimental approach was chosen as multi-color dSTORM is relatively easy to realize compared to other alternatives. Multi-color STORM experiments, for example, require labeling of different structures with different activator-reporter combinations as described in Section 2.3.1. As a consequence, crosstalk

---

Figure 3.25 *(preceding page)*: 3D dSTORM imaging of HeLa cell microtubules. (A) The TIRF image of immunostained microtubules of a HeLa cell was emulated by the average time projection of a TIRF image stack acquired for dSTORM imaging. (B) The 2D dSTORM image of the cell shown in A reveals fine structure of the microtubule network and (C) the corresponding 3D dSTORM image of A further gives insight into the axial course of the filaments, the color code corresponds to axial position in nanometers. Scale bars: 10 µm. (D) Displacement analysis returns resolutions of 51.4 nm in x-direction (top panel), 45.2 nm in y-direction (middle panel) and of 161 nm in z-direction (bottom panel) for the super-resolution image shown in C. (E-G) 2D projections (small inlays) of a single filament marked by the white rectangle in C and average cross-sections through these projections (black lines, error bars represent the standard error of the mean) were fitted to Gaussian functions (red). These reveal diameters of the filament by means of the respective FWHM of (E) 81 nm in the x-y-, (F) 184 nm in the x-z- and of (G) 159 nm in the y-z-projection. Scale bars: 500 nm.

caused by incorrect activations has to be corrected. Another alternative would be imaging one structure with PALM and a second structure with STORM. Different imaging conditions (cf. Section 3.2.2) hinder efficient imaging in this case as well as negative effects of cross-activations that can be hardly avoided (cf. Section 4.3.6.1 for details). In multi-color dSTORM, these problems do not occur although chromatic aberrations are a factor that has to be considered. However, it was shown in Section 3.1.3.2 that these can be effectively corrected for by high-resolution mapping.

The system that was selected for testing consisted of the secretory protein Cab45, which was immunostained with Cy3-labeled antibodies, and a second secretory protein, LysC, which was labeled with Cy5 and has been shown [112] to bind to Cab45. For this *in vitro* experiment, LysC was allowed to cluster on a glass slide and Cy3-labeled Cab45 was added subsequently. Figure 3.26A depicts the widefield image of a cluster of Cy5-labeled LysC agglomerating on the glass slide whereas Figure 3.26B shows the corresponding image of Cy3-labeled Cab45 taken at the same spot. An overlay of both images can be found in Figure 3.26C, which revealed that Cab45 is associating to the LysC structure.

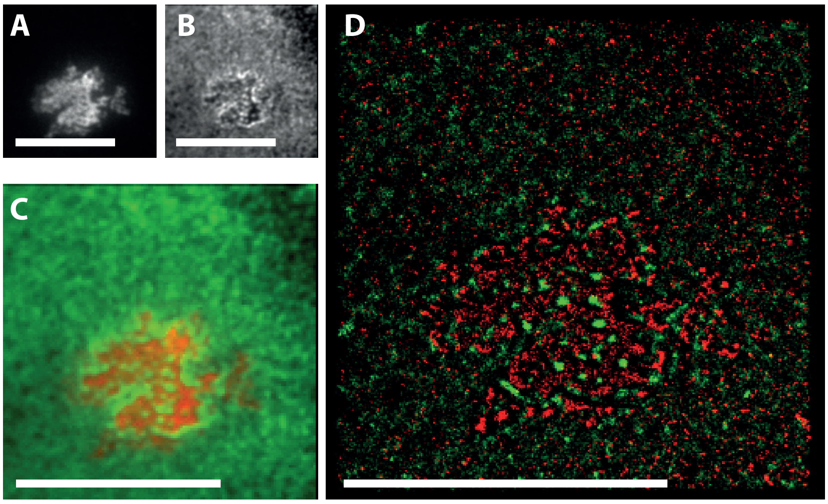

Figure 3.26: Demonstration of dual-color dSTORM. The diffraction-limited widefield images are shown of (A) Cy5-labeled LysC clustering on a glass slide and of (B) Cy3-labeled Cab45 that was added to the LysC cluster shown in A. (C) The overlay of the widefield images in panels A and B reveals attachment of Cab45 (green) to the LysC structure (red). (D) The corresponding dual-color super-resolution dSTORM image reveals the distribution of Cab45 and LysC on the nanoscale. Scale bars: 10 µm.

Subsequently, widefield image stacks were acquired in both colors for subsequent reconstruction of a dual-color dSTORM image. The Cy5-labeled structure was imaged first in order to avoid photobleaching of Cy5 molecules by excitation at 561 nm, which is required for dSTORM imaging of the Cy3-labeled structure. Drift was first calculated separately for both colors before the drift value that was obtained for the final frame of the first stack was added to the drift values calculated for the second stack. The overlay of the obtained super-resolution dSTORM images is depicted Figure 3.26D. It revealed that Cab45 formed distinct clusters around the LysC substrate. Calculated resolutions were 60.8 nm for Cy5-labeled structure and 87.6 nm for the Cy3-labeled structure. Although the resolutions in this case could not compete with resolutions shown in previous sections, they still lay clearly below the diffraction limit. The difference in resolution between Cy3 and Cy5 was expectable as Cy3 has a significantly lower survival time under the given conditions until photobleaching occurs than Cy5 as described by Dempsey *et al.* [54]. This means a lower number of detected photons and therefore also a lower localization accuracy and image resolution.

Although these first experiments presented in this section demonstrated that the microscope is capable of performing multi-color super-resolution experiments, further improvements and refinements are necessary. These include the establishment of multi-color STORM experiments with the corresponding correction algorithms as well as combined STORM and PALM experiments. Further, in order to avoid mutual photobleaching of the dyes, it would be beneficial to enable simultaneous data acquisition of the respective color instead of the sequential acquisition as was performed here. Again, multi-color STORM with different activator-reporter combinations would be the most convenient approach here as it can be performed without the switching of filters or installation of a second detector.

3.8 Summary & Outlook

In this chapter, it was shown that STORM could be successfully established using a self-built microscope setup. Experiments demonstrated that the system provides the required mechanical stability to perform super-resolution imaging with localiztaion accuracies below 10nm. Different analysis parameters and localization algorithms were tested for their performance and image rendering was implemented. The efficiency of the selected methods and analysis algorithms could be demonstrated for super-resolution imaging in two as well as in three dimensions.

Images shown in this chapter could provide resolutions down to 40 nm in the lateral and to 160 nm in the axial dimension although it was possible to improve these values to approximately 30 nm in the lateral and to 120 nm in the axial dimension in experiments that will be shown in Chapters 4 and 5. When these values are compared to literature values that were obtained by the same approach (Table 2.2), an improvement by a factor of 1.5 for the lateral and – when using astigmatism-based imaging – of approximately 2.5 for the axial dimension should be possible. A major factor, which limits the resolution in STORM and dSTORM, depends on localization accuracy, which is determined by the number of detectable photons. Reduction of background noise through improved shielding of the microscope or through a better selection of emission filters could bring some improvement here. Regarding axial resolution, focus stability plays an important role as well. For example, the implemented perfect focus system emerged to be an indispensable extension for 3D STORM or dSTORM. Furthermore, stability of optical settings is influenced by temperature and humidity conditions in the environment of the microscope. The room where the microscope was set up is regulated by a simple ventilation-based air-condition system. Apart from unstable temperature conditions, air current, which flowed over the setup, was a main cause for lateral and axial drift. Movement of the system to a room with a stable temperature control would very likely bring significant improvement as well as a more efficient shielding from external vibrations. In addition, it might be worth considering the removal of the AOTF from the setup and to choose different ways for laser line selection. By doing so, the distortion of the beam introduced by the AOTF would be omitted together with the need for an additional pinhole for beamshape clean-up. This would increase the available laser power at the objective, which would increase the speed and quality of data acquisition. Together with an incubation system that allows for maintaining living cells on the microscope stage, these modifications could open the door for live cell imaging. The latter would also require the introduction of alternate sample labeling techniques to immunostaining, which has been mainly used so far in this work, as it is not compatible with live cell imaging. Apart from PALM imaging, labeling approaches such as SNAP-tags [111] or related techniques can be used for STORM and dSTORM.

Initial experiments further confirmed the capacity of the super-resolution setup for multi-color experiments. However, although these first steps are promising, further efforts are required. These include implementation of additional approaches to multi-color STORM, dSTORM or PALM as described in Sections 2.3.1.2 and 3.7 as well as improvement of the image analysis for efficient correction of occurring errors such as STORM crosstalk. Additional modifications of the microscope in this context might include a second EMCCD camera to simplify dual-color imaging as this would allow parallel imaging instead of sequential acquisition of the data sets for the respective colors.

The applied analysis methods based on least squares Gaussian fitting have shown to provide the required accuracy for localization-based super-resolution imaging. The only drawback was the fact that data evaluation speed was relatively slow compared to values reported in literature (e.g. rapidSTORM by Wolter *et al.* [97]) although the accuracy of the algorithm is in the end more essential for super-resolution microscopy than speed. Still, faster evaluation would be convenient, for example, to be able to react faster to experimental results. An option for further speed improvement would be, for example, relocation of the fitting algorithm to the graphics processing unit (GPU) of the data analysis unit, which has been shown to bring an acceleration of a factor between 10 and 100 compared to conventional CPU computation [66].

Overall, although minor improvements should still be considered, the microscope and the analysis have proven their capabilities on established samples. For this reason, the method can now be applied to uncharacterized samples to provide answers to currently open biological questions.

Chapter 4

Super-resolution imaging of ESCRT proteins at HIV-1 assembly sites

In this chapter, super-resolution microscopy is applied to the study of the interaction between the human immunodeficiency virus type 1 (HIV-1) and the cellular endosomal sorting complex required for transport (ESCRT), which is recruited by the virus to complete release from an infected host cell in a late stage of the viral reproduction cycle. The contents of the following chapter were published in PLoS Pathogens under the title *'Super-Resolution Imaging of ESCRT Proteins at HIV-1 Assembly Sites'* [113] under the creative common license CC BY 4.0 [114].

4.1 Introduction

How HIV-1 exploits the host cell ESCRT machinery for budding is a complex process. In this section, an introduction including general information about HIV and its reproduction cycle is given and then special focus is put on ESCRT-mediated budding from the host cell.

4.1.1 Acquired immunodeficiency syndrome (AIDS) and HIV

Since the first reports of an at that stage unknown disease appeared in 1981 [115] that has become known as the acquired immunodeficiency syndrome (AIDS), it has turned into a pandemic, which has claimed more than 35 million victims worldwide [12]. AIDS is characterized by a gradual collapse of the human immune system that makes AIDS patients defenseless against opportunistic infections that eventually lead to the death of the infected persons. Because of its fatality combined with its pandemic character, AIDS has become one of the most studied diseases of all times. However, despite all the efforts, no cure or vaccine has been found so far although several drugs are available that can in combination suppress the outbreak of AIDS in the case of infection and significantly prolong the lifespan of the patient.

A first breakthrough in AIDS research was achieved in 1983 when two research groups were able to isolate and characterize the pathogen that is responsible for AIDS [116, 117]. In the beginning, it was assumed that the virus behind AIDS, which was named human immunodeficiency virus (HIV), was a variation of the already known human T-lymphotropic virus (HTLV) [118]. However, it soon emerged that the newly discovered virus must belong to a different genus. HIV belongs to the genus of lentiviruses, which are part of the family of retroviruses. The name lentivirus refers to the fact that diseases caused by these viruses stand out by their relatively slow progress [119, 120]. For example, a latency period of more than 10 years can easily lie between an infection with HIV and the outbreak of AIDS [121].

It has to be noted in this context that two different types of HIV are known, which are termed HIV-1 and HIV-2, respectively. HIV-2 was discovered several years after HIV-1 [122]. Although both types are very similar in most of the aspects and both cause AIDS, certain differences exist. Infectivity of HIV-2 is significantly lower than of HIV-1 and HIV-2 infections are further characterized by an even longer latency period than typically found for HIV-1. As a consequence, only about 4-5 % of all registered HIV infections worldwide are attributed to HIV-2 and these infections are mostly restricted to regions in western Africa [123]. Therefore, most research including this study focuses exclusively on HIV-1. Many results and derived therapies might be transferable to HIV-2 but this cannot be taken for granted.

As all viruses, HIV-1 cannot be considered as a living organism because it is mainly a carrier of genetic material consisting of structural proteins and lipids. For reproduction, viruses depend on infection of living organisms and on exploitation of host cell factors for reproduction of their genetic material and viral proteins. In general, viruses are grouped depending on the genome they carry, which can be either DNA or RNA. In this context, HIV-1 has like all members of the retrovirus family a single-stranded RNA genome [116, 124]. In contrast to other RNA virus families, this genome is transcribed into a DNA intermediate by the viral reverse transcriptase enzyme during replication [116, 125, 126], which will be described in detail in the next section.

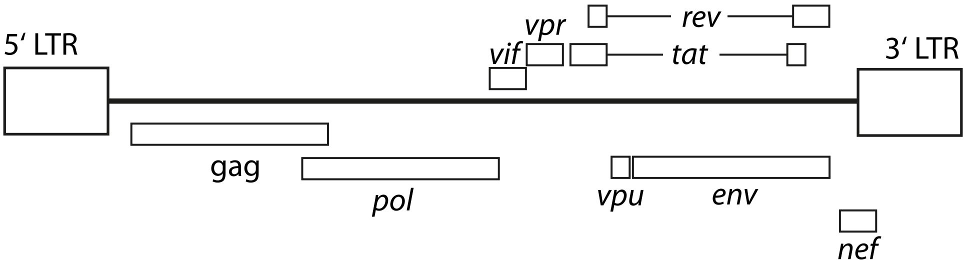

Figure 4.1: HIV-1 genome. A simplified scheme of the HIV-1 genome shows the relative position of all 9 HIV-1 genes and the two long-terminal repeat (LTR) sequences on the RNA genome.

The RNA genome of retroviruses, which encodes all viral proteins, is characterized by a relatively small number of genes and is framed on both ends by a long terminal repeat (LTR) sequence. The LTR of HIV-1 is a 640 bp long repetitive sequence [127–129] that, after transcription into proviral DNA by reverse transcriptase, allows integration of the viral genome into the genome of the host cell by viral integrase (reviewed in [130]). Furthermore, the LTR serves as a promoter for transcription of the entire viral genome. All retroviruses have three structural genes in common: *env*, *pol* and *gag*, which also can be found in a scheme of the HIV-1 genome shown in Figure 4.1. These genes encode the envelope protein (Env), the structural group-specific antigen protein (Gag) and polymerase (Pol), which are cleaved into fully processed viral proteins at a late stage of the viral reproduction cycle (for details, see next section). In this context, Env comprises glycoproteins gp120 and gp41, which are integrated into the viral envelope as depicted in Figure 4.2A and which recognize host cell receptors during virus entry [131–133].The viral envelope depicted in Figure 4.2A, which is present in all retroviruses, is a lipid bilayer taken from the host-cell membrane. The second structural protein, Gag, which is depicted in Figure 4.2B, is a multiple domain protein that contains a matrix domain (MA), which can attach to the lipid membrane and fulfills additional regulatory functions (reviewed in [134]) and a capsid (CA) domain that builds a protecting hexagonic surface lattice around the RNA genome [135, 136]. Further protection of the genome is provided by the nucleocapsid (NC) domain. The C-terminal p6 domain finally plays an important role during release of a newly formed virion from the host cell (for details, see Section 4.1.3). Unprocessed Gag occurs together with GagProPol in a ratio of 20:1. The latter is a result of a ribosomal frameshift [137] and includes, in addition to Gag, viral integrase, protease and reverse transcriptase. Maintaining this ratio between GagProPol and Gag emerged to be critical for virus reproduction [138].

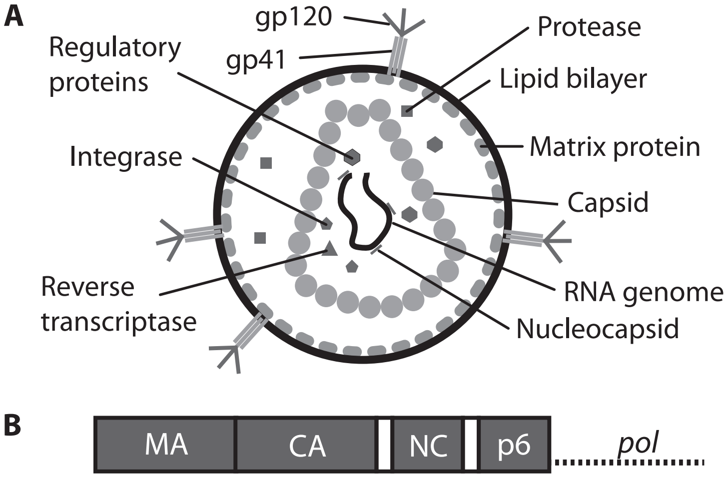

Figure 4.2: Structure of the HIV-1 virion and the structural protein Gag. (A) The structure of a mature HIV-1 virion particle is shown where viral proteins are labeled in gray and the bilipid membrane and the viral genome are shown in black. (B) The HIV-1 Gag molecule contains the matrix (MA), capsid (CA), nucleocapsid (NC) and p6 domains. Gag occurs together with GagProPol in a ratio of 20:1.

In contrast to other retroviruses, the genome of lentiviruses comprises additional regulatory genes for controlling the expression of the viral genes. In the case of HIV-1, these include, on the one hand, the regulatory genes *tat* and *rev*, which encode the proteins Tat and Rev that support transcription and transport of the structural proteins Gag, Pol and Env (reviewed in [139]). On the other hand, HIV-1 features accessory genes *vpr*, *nef*, *vif* and *vpu*. The corresponding accessory proteins fulfill various functions in the life cycle of the virus, for example, helping to circumvent defense systems of the host cells (reviewed in [140]).

4.1.2 HIV-1 life cycle

The effectiveness of HIV-1 is mainly attributed to the fact that it directly attacks the human immune system by infecting cells with CD4 receptors, such as T-cells, macrophages or dendritic cells. T-cells are regarded as their main host [141] although HIV-1 also infects the early immune response system, which consists of macrophages or dendritic cells [142, 143]. These cells play a key role in the immune response as they recognize and bind foreign antigens that are presented by major histocompatibility complexes (MHC) on the surface of infected cells. Subsequently, they either activate macrophages that destroy the infected cells or recruit B-lymphocytes that, in turn, produce specific antibodies that mask those antigen surface proteins on the pathogen. Cells decorated by antibodies are later recognized by phagocytes and destroyed [144]. Removal of T-cells from this pathway through HIV-1 therefore inflicts critical damage on the human immune system.

Recognition of CD4 molecules on the surface of a potential host cell is therefore the first step in the reproduction cycle of HIV-1, which is depicted in Figure 4.3. The viral membrane

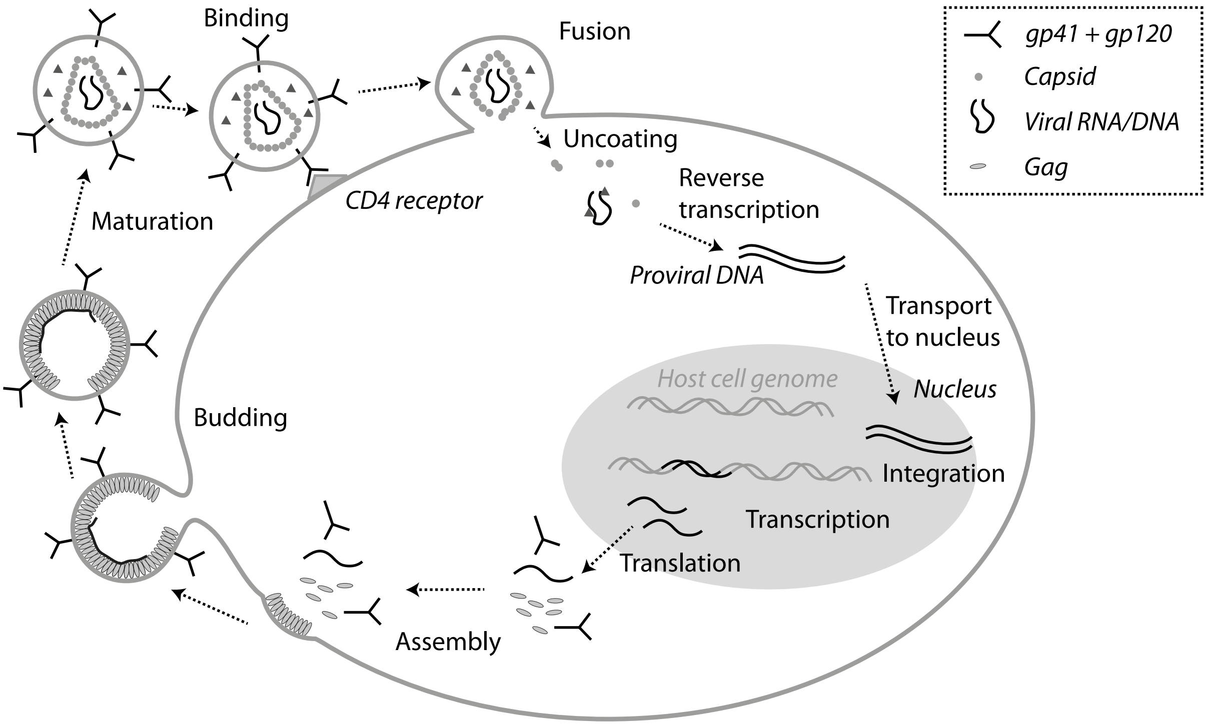

Figure 4.3: HIV-1 life cycle. A scheme of the life cycle of HIV-1 is shown beginning with fusion of a virion with a target cell (a minor entry pathway using endocytosis is not depicted) and continuing with reproduction of the viral genome and proteins before completing the cycle with assembly, budding and maturation of a new virion.

protein gp120, which is encoded in *env*, binds to CD4 receptors at the host cell membrane [141]. Following this first anchoring, at least one additional chemokine coreceptor (CCR5 or CXCR4) at the host cell membrane is targeted. They induce a structural change in gp120 that allows gp41, which is an additional viral membrane protein derived from *env*, to induce the fission process, which results in fusion of the membranes [145]. Fusion is the main entry pathway for HIV-1, although the virus particle can also be taken up by endocytosis. This alternative occurs in lower quantity than fusion but it nevertheless can lead to viral reproduction [146].

Entry is followed by the formation of a reverse transcription complex (RTC) where reverse transcriptase starts to convert the RNA genome into proviral DNA. Along with transcription, the viral capsid, which protects the viral genome, starts to disassemble. It is assumed that this uncoating is a gradual process although it is not fully understood at which time point it starts relative to reverse transcription (reviewed in [147]). RTC is transported towards the nucleus exploiting the cytoskeleton of the host cell. Upon completion of reverse transcription and uncoating, RTC is converted into a pre-integration complex (PIC), which, apart from the proviral DNA, also comprises viral integrase and the viral protein R (Vpr, encoded by *vpr*). The PIC is required to recruit nuclear import factors that mediate transport through nuclear pore complexes to overcome the nuclear membrane. In the nucleus, viral integrase mediates integration of the proviral DNA intro the host cell genome. In contrast to many other viruses that are not able to overcome the nuclear membrane, this represents a considerable evolutionary advantage and allows HIV-1 to infect non-dividing cells with an intact nuclear membrane. Integration can be followed by a latency period, where the virus remains dormant, making it temporarily undetectable by the immune system (reviewed in [148]). Eventually, however, the viral genome is transcribed into mRNA where the LTR (Figure 4.1) serves as promoter for the cellular RNA polymerase and transcription elongation is additionally promoted and regulated by viral Tat protein. Subsequently, some of the produced mRNA strands are spliced for translation. Alternative splicing leads to different mRNA strands, which are translated into the regulatory, accessory and structural viral proteins (reviewed in [139]). Unspliced copies of the full RNA genome are exported from the nucleus by the regulatory protein Rev and are later packed into the newly formed virus.

Subsequent assembly of new viral particles is mainly orchestrated by the structural protein Gag, which can be seen by the fact that already the expression of Gag alone leads to formation of virus-like particles (VLP) in cells [149]. With its lipophilic MA domain (Figure 4.2B), Gag is able to bind to lipid membranes where the cellular phospholipid PI(4,5)P_2 seems to play an important role for specific targeting of the cell membrane [150]. When Gag accumulates at the cell membrane, multiple Gag molecules form a hexagonal lattice, which induces membrane curvature by introduction of irregular lattice defects [151, 152]. The assembly process can be grouped into three different phases as described by Ivanchenko *et al.* [153]. In experiments where fluorescently labeled Gag.eGFP was expressed in the context of the full HIV genome, a first phase was observed that is characterized by successive recruitment of Gag molecules to the membrane, which was detected by an increasing fluorescence intensity. The duration of this phase is approximately 8-9 minutes but might be faster when Gag.eGFP is expressed alone [154]. The recruitment comes to a halt in a second phase before the fluorescence intensity decreases again in the third phase when the newly formed particle detaches from the cell. Gag further binds remaining components of the virus such as the viral RNA genome by the NC domain [151] and other viral proteins. Assembly is closely connected to budding where the newly formed, immature virion is released from the host cell assisted by the cellular ESCRT machinery. This process will be discussed in detail in the following section.

The very last step in the HIV-1 replication cycle is called maturation. Here, the large structural proteins Gag and GagProPol are cleaved into their subcomponents and a conical capsid protecting the RNA genome is formed. The newly formed virion is infectious only after maturation is complete and is able to infect new host cells, which starts the cycle again.

4.1.3 ESCRT-mediated budding of nascent HIV-1 particles

The budding of HIV-1 at the plasma membrane of a host cell and the subsequent release of a newly formed immature HIV-1 virus particle is a process containing multiple steps, from which many depend on recruitment and exploitation of a number of host cell factors by the virus. The initial formation of the viral bud is primarily induced by membrane associated Gag molecules as described before. Whereas their assembly and membrane deformation steps do not essentially need support from host cell factors [155], the final steps leading to membrane fission and the release of the viral particle depend on recruitment of the cellular ESCRT machinery [156–158]. The latter plays a key role in various membrane bending and fission processes in the cell, for example cytokinesis (reviewed in [159]), formation of multivesicular bodies (MVB) ([160] and reviewed in [161, 162]) or nuclear envelope reformation [163]. ESCRT is a multiprotein complex whose components can be categorized into four subcomplexes (ESCRT-0, ESCRT-I, ESCRT-II and ESCRT-III) and an additional number of associated proteins such as VPS4 and the ALG-2 interacting protein X (ALIX) (reviewed in [164, 165]). Each of these subcomplexes fulfills different tasks in the host cell: these include recognition and sorting of cargo for MVBs, proteins that actually mediate membrane fission and factors that are responsible for the disassembly of the ESCRT complex. HIV-1 does not employ all components of ESCRT but mainly certain components of ESCRT-I and ESCRT-III as well as the AAA ATPase VPS4 and the ESCRT associated ALIX protein [158, 166–173]. There are also studies that show a dependency of HIV-1 reproduction on ESCRT-II [174] as well as on ESCRT-0 [175].

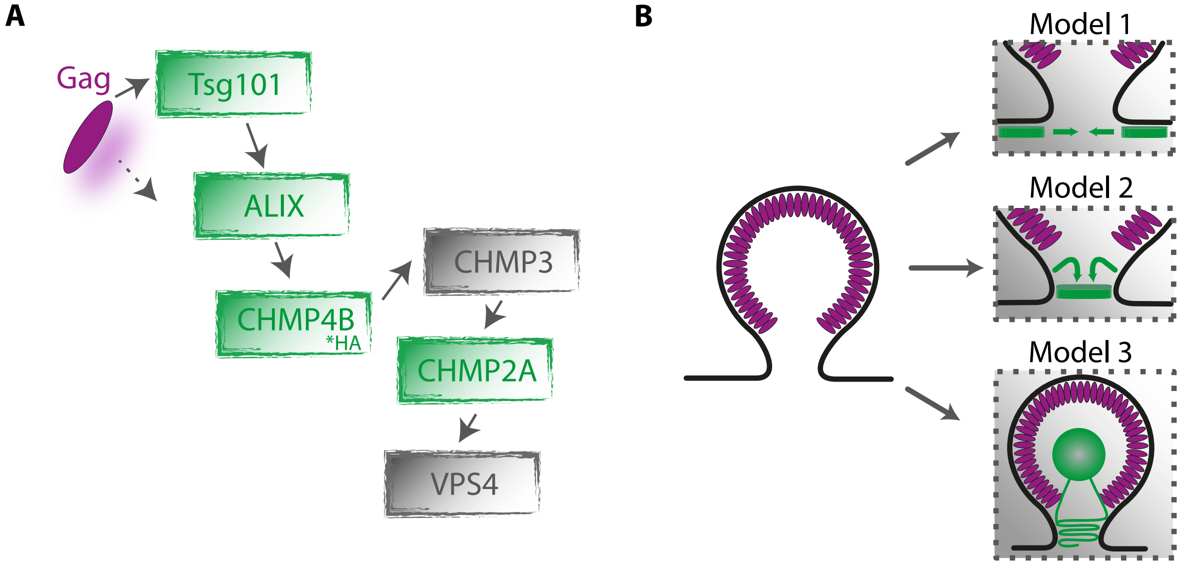

Figure 4.4: Gag-ESCRT interactions. (A) A simplified schematic of the interaction scheme between HIV-1 assembly sites and the ESCRT recruitment pathway. The constructs analyzed in this study are highlighted in green, *HA indicates the use of an HA-tagged mutant. (B) An overview of the proposed models of membrane scission where ESCRT factors (green) that are recruited by HIV-1 Gag (magenta) at the plasma membrane (black) interact either via external constriction from the cytosol (cytosolic model, Model 1), via internal constriction of the budding virus in the neck region (neck model, Model 2) or from within the bud (bud model, Model 3).

The ESCRT recruitment process, which is depicted in Figure 4.4A, is initiated by the C-terminal p6-domain of HIV-1 Gag. p6 contains several motifs, from which two late domain motifs are of particular interest for this step. The term late domain or L-domain in this context refers to the function of these sequences in a late step of the virus release process (reviewed in [176]). Mutations at these L-domain motifs are therefore suitable to arrest viral release at a very late stage. One of these L-domains found in the p6-domain of HIV-1 Gag is the so called PT/SAP motif that is able to interact with a component of ESCRT-I, the tumor susceptibility gene 101 (Tsg101) [171, 177–179]. Experiments have shown that mutations in the PT/SAP motif lead to an arrest of virus budding [171, 180, 181]. An ESCRT-recruiting PT/SAP domain can be found in all lentiviruses except for the equine infectious anemia virus (EIAV). Here, a L-domain YPXL motif triggers virus release [182]. This is also possible in the case of HIV-1 Gag, which can use its own YPXL motif to recruit ALIX, exploiting a second pathway [166, 172, 183]. However, this alternative plays only a minor role for ESCRT recruitment compared to PT/SAP [173]. This is in agreement with the observation that mutations of the ALIX binding site in YPXL have less effect on HIV-1 release than it is the case for the Tsg101 binding site in PT/SAP [184, 185]. However, in cases where Tsg101 recruitment is blocked due to a non-functioning PT/SAP motif, HIV-1 particle release can be rescued by overexpression of ALIX [184, 186]. Overexpression means that the quantity of a certain protein in a cell is enhanced compared to the original amount, which happens, for example, upon transient transfection of an organism with a plasmid that encodes the respective protein. Changes in protein function including trafficking or protein-protein interactions are however a phenomenon that is often observed upon overexpression, which can be even more critical when a mutant of the original protein is expressed. In this case, the number of molecules of the mutated version will outnumber the endogenous protein molecules. For example, when a version of ALIX is overexpressed where the binding site to p6 is removed or replaced by other proteins, virus production is disrupted [172, 187]. This mutant is an example for a dominant-negative effect, which means that the function of the protein is completely abolished [188]. Dominant-negative effects do not only occur as a consequence of mutations but can also occur when fusion proteins are expressed, for example, when a fluorescent protein is tagged to the original protein for visualization. In extreme cases, when the function of the disrupted protein is vital for the cell, this can lead to cell death.

ESCRT-I and ALIX are mainly responsible for initiation of the fission process and deliver additional support for membrane bending and remodeling by ESCRT-III [189]. The latter is regarded as the key component for membrane remodeling necessary for catalyzing fission. ESCRT-III consists of several proteins, which are summarized under the name charged multivesicular body proteins (CHMP) comprising the proteins CHMP2, CHMP3, CHMP4 and CHMP6. In the first step of ESCRT-III mediated membrane remodeling, CHMP4 is recruited by ALIX [172, 184, 190] through interaction of its Bro1-domain with CHMP4 [190]. Three isoforms are known for CHMP4, which are termed CHMP4A, B and C, respectively. Although they fulfill similar functions, CHMP4B has been shown to be the major binding partner of ALIX. First of all, the expression level of CHMP4B has been shown to be significantly higher than for the other isoforms [191]. Secondly, siRNA based depletion of CHMP4B has – in contrast to CHMP4A or CHMP4C – a clear effect on viral infectivity and almost completely arrested virus release [169]. Depletion experiments by Morita *et al.* have further shown [169] that at least one CHMP4 isoform is required for the release of virus particles as well as one of the isoforms of CHMP2, CHMP2A or B. Depletion of CHMP3 on the contrary causes only a moderate reduction of particle release. CHMP4 has been found to build polymeric filamentous structures that effectively constrict budding necks and drive membrane fission. This process has not only been observed for HIV-1 release [157, 158, 192] but also for the cellular functions of ESCRT such as cytokinesis [159, 193] or MVB formation [194]. CHMP4 is further able to interact with CHMP3, which then recruits CHMP2A as shown by Morita *et al.* [169]. Alternatively, CHMP4 can also interact directly with CHMP2B although the first pathway seems to be preferred. Regardless of its recruitment, CHMP2 serves as a bridge to activate VPS4, which is responsible for disassembly of the complex after fission is complete. VPS4 is predominantly recruited to the budding site at the second phase of viral assembly (see above) as shown by Baumgärtel *et al.* [195]. Further results however suggest that VPS4 may have additional roles in membrane remodeling apart from ESCRT disassembly [168, 195].

Jouvenet *et al.* [168] further investigated the dynamics of certain ESCRT recruitment by HIV-1 and EIAV using fluorescent protein tagged (FP-tagged) versions of the respective proteins. They found that the assembly of ESCRT proteins CHMP1B, CHMP4B/C and VPS4 is a transient process that takes place in the range of a few minutes. The only exception was ALIX, which seemed to accumulate at EIAV budding sites.

Whereas the recruitment pathway that HIV-1 exploits for budding is relatively clear, the actual mechanism and geometry of this fission process has still not been fully understand. Different models have been proposed regarding how ESCRT and especially ESCRT-III might drive membrane fission.

One model (Figure 4.4B, Model 1) was presented by Hanson *et al.* [196] who performed cryo-EM experiments with COS-7 cells over-expressing tagged ESCRT components. They observed large, lasso-like spirals of ESCRT filaments surrounding a central hole. It was speculated [197] based on *in vitro* experiments with liposomes that CHMP4 oligomers encircle the cargo and then actively support membrane deformation and subsequently constrict the neck [198].

The second model postulates, in contrast to Model 1, that ESCRT-III filaments rather assemble within the neck of the bud (Figure 4.4B, Model 2, reviewed in [194]) and form there either dome- [199, 200], whorl- [201], circular- or spiral-shaped structures [193, 197, 202–206]. CHMP4 filaments here drive narrowing and constriction of the neck assisted in the case of HIV-1 by VPS4 ATP-hydrolysis until its radius goes below 3 nm whereupon spontaneous fission occurs [199, 207]. ESCRT-III proteins CHMP3 and CHMP2 are suggested to form a cap for CHMP4 filaments [208] and stabilize the neck from within together with CHMP2A and B by forming a dome-structure [199, 200, 202, 205]. This is supported by electron micrograph images [169], which showed CHMP2 striations in the neck at cells where budding was arrested in a late stage. Lata *et al.* [200] further found tubular structures formed by CHMP2-CHMP3 heteromeric complexes in a dome-like assembly using *in vitro* cryo-EM imaging. Additional support for Model 2 was given by *in vitro* experiments with giant unilamellar vesicles and purified ESCRT-III, which further showed involvement of other ESCRT-III components such as CHMP6 in the initial membrane neck formation during HIV-1 assembly [160, 197]. Bleck *et al.* [209] further detected ESCRT-III fusion constructs in the context of labeled Gag assemblies rather at the edge of the Gag assembly using dual-color super-resolution microscopy, which is also consistent with a within-neck-model. Cashikar *et al.* [203] performed deep-etch electron microscopy and observed ESCRT-III in VPS4 depleted cells forming spirals with an approximate diameter of 110 nm encircling nascent virus buds. This additionally suggests that VPS4 might be required for the disassembly of ESCRT-III structures.

The third model (Figure 4.4B, Model 3) was proposed by van Engelenburg *et al.* [210] who performed three-dimensional iPALM imaging of Gag assemblies in the context of FP-tagged versions of Tsg101, CHMP2A and CHMP4B and VPS4. Probability density maps showed all analyzed ESCRT components assembling within the head of the virus bud rather than in the neck. This model has been very controversial as so far. In particular, only negligible amounts of ESCRT proteins apart from ALIX could be found in biochemical analysis of released viral particles [166, 172, 211]. It is in this context difficult to understand how ESCRT proteins in the bud should be removed from the virus after completing membrane fission.

4.2 Experimental design

Previous experiments for the study of interactions between HIV-1 and ESCRT proteins have mostly focused on *in vitro* experiments or systems with certain modifications. These include, for example, arrested budding by VPS4 depletion in order to increase buddings statistics or tagging of ESCRT proteins with fluorescent marker proteins. The differences between the models that have been proposed might therefore be a consequence of the experimental conditions. For these reasons, the aim of this study was to observe the respective structures using super-resolution fluorescence microscopy under more physiological conditions in order to obtain results that are not biased by sample modifications. Super-resolution microscopy offers an elegant method to distinguish between the proposed models as the sizes and distributions of the ESCRT proteins should vary significantly depending on the respective model. Furthermore, expected sizes lie in an optimal range for methods such as STORM and PALM. TIRFM imaging further ensures that only processes occurring at the cell membrane were imaged and to avoid bias through cellular autofluorescence background.

One compromise that had to be made was to use HeLa cells for the experiments, which represent an immortal cell line of human cervical cancer cells ([212], reviewed in [213]). Theoretically, it would be preferable to use T-cells or other natural host cells of HIV-1 such as macrophages or dendritic cells for these experiments. However, imaging of T-cells with fluorescence microscopy is often challenging as they grow in suspension in contrast to HeLa cells, which makes it difficult to achieve adhesion to the surface required for imaging. Cultivation of dendritic cells and macrophages is also challenging and in the case of macrophages, membrane invaginations could be problematic for imaging of surface structures. For these reasons, HeLa cells were chosen as an alternative, which has been previously used for studies of ESCRT in the context of virus budding (e.g. [168, 172]) and which has been shown to be a good model system for this purpose.

The lack of CD4-receptors in HeLa cells did not affect the experiment as the cells were transiently transfected with plasmids coding the required viral proteins. For this purpose, experiments were performed using the full viral construct pCHIV, which was presented by Lampe *et al.* [214]: it encodes the entire HIV-1 genome except of the LTR and the accessory *nef* gene, which overlaps with LTR (cf. Figure 4.1). As a consequence, virus particles produced by pCHIV support the majority of viral functions including all processes involved in assembly and budding but are not able to reproduce. For visualization of the particles in fluorescence microscopy, fluorescent marker proteins such as RFP-derivate mCherry [215] for TIRFM imaging or the photoconvertible protein mEos for PALM [53] were introduced between the matrix and the capsid domain of the viral Gag protein (cf. Figure 4.2B). The obtained constructs are termed pCHIV$^{\mathrm{mCherry}}$ [214] and pCHIV$^{\mathrm{mEos}}$ [153], respectively, producing the viral particles with the fluorescently labeled Gag molecules Gag.mCherry or Gag.mEos. Insertion at that position has been shown to be compatible with production of virus-like particles [214, 216]. However, a 1:1 mixture of labeled and untagged plasmid was used for transient transfection experiments. Adding of unlabeled plasmids is necessary to avoid the formation of malformed particles caused by spatial hindrance between adjacent fluorescent proteins. The entirety of expressed proteins of both labeled and untagged plasmids was termed HIV$^{\mathrm{mCherry}}$ and HIV$^{\mathrm{mEos}}$, respectively. This spiking approach of using fluorescently tagged proteins was chosen as other techniques like, for example, immunostaining of the viral Gag shell were not applicable. Super-resolution imaging requires a highly dense labeling to achieve good resolutions. No anti-Gag antibodies were available that provided the required specificity for STORM or dSTORM imaging. This can be due to the fact that the relatively dense packing of Gag proteins in the curved shell matrix makes it difficult for the relatively large antibody molecules to bind.

For control experiments with arrested budding, a mutant of pCHIV was used where the late PT/SAP motif is disrupted thereby blocking the predominant ESCRT recruitment pathway exploited by HIV-1. This mutant is termed pCHIV (late-) and were either used in wildtype form or tagged with a fluorescent protein at the same position as in pCHIV$^{\mathrm{mCherry}}$. Expression of a 1:1 mixture of tagged and untagged late- constructs gave HIV$^{\mathrm{mCherry}}$ (late-) particles.

In the case of the ESCRT proteins Tsg101, CHMP2A and the ESCRT-related protein ALIX, the endogenous proteins were immunostained with commercially available antibodies, which were fluorescently labeled for STORM and dSTORM imaging (see Section A.2). Only in the case of CHMP4B, an epitope tagged version had to be used as no anti-CHMP4B antibodies featuring the required specificity were available. An epitope-tagged version of CHMP4B was expressed in HeLa cells where the human isoform of the protein was tagged with a hemagglutinin (HA) label (CHMP4B-HA). This relatively small HA-tag was chosen to minimize any dominant-negative effect on ESCRT recruitment that significantly reduces virus release and infectivity [166], as has been known for CHMP4 isoforms fused to fluorescent proteins [166, 196].

As immunostaining was not possible for imaging of HIV-1 assembly sites, PALM was used in this case whereas STORM or dSTORM were used for imaging of ESCRT proteins. STORM instead of dSTORM was used for experiments performed chronologically first (CHMP4B-HA and ALIX) when the required laser power for dSTORM (cf. Section 3.2.2) was not yet available. Immunostaining further requires fixation and permeabilization of the cells, which, on the one hand, does not allow for the study of dynamics but, on the other hand, conserves the transient ESCRT structures ensuring that also long data acquisition times needed for STORM do not affect the quality of the results. As the acquisition of dual-color super-resolution images did not bring enough statistics under the given conditions (cf. Section 4.3.6.1), identification of HIV-1 assembly sites was performed by searching for colocalizations of ESCRT and HIV-1 structures in the overlay of the respective TIRF images and the sizes of viral clusters and ESCRT protein assemblies were determined in separate super-resolution experiments. Size determination was performed as described in Section 3.4 by fitting a Gaussian function to the vertical and horizontal cross-section through the respective structure. The average FWHM of both fits was then taken as an estimate for the cluster size. Detailed protocols regarding sample preparation and data evaluation can be found in Section A.2.

4.3 Results

4.3.1 Characterization of HIV-1 assembly sites using PALM

In order to be able to compare the sizes of ESCRT components with the size of HIV-1 particles, super-resolution PALM imaging of the HIV-1 Gag shell was performed in a first step according to the protocol described in Section 3.2.2. For this purpose, HeLa cells were transfected with pCHIV$^{\mathrm{mEos}}$ and untagged pCHIV in a 1:1 mixture. HeLa cells displaying HIV$^{\mathrm{mEos}}$ in TIRF images (Figure 4.5A, left panel) were subsequently imaged with PALM in TIRFM mode.

The comparison between the TIRF image (Figure 4.5A, middle panel) of a single virus bud and the respective super-resolution PALM image (Figure 4.5A, right panel) underlines the need of super-resolution microscopy techniques for analysis: only the PALM image is able to reveal round, dense structure of the HIV-1 buddings site. It has to be noted that this cluster consists of many precisely localized Gag.mEos molecules at the membrane whose overlaid positions render the structure of the assembly site.

The average of the FWHM of the Gaussian functions fitted to the horizontal and vertical cross-sections of 159 HIV$^{\mathrm{mEos}}$ clusters was used to determine the sizes of the underlying HIV-1 budding sites as described in Section 3.4. Under the given conditions, the diameter size distribution of an individual budding site ranged from 70 to 220 nm (Figure 4.5B) with a mean value of 116 ± 36 nm. When the cluster size was estimated by means of the Ripley's L-function, the result for the mean HIV-1 particle size was 141 ± 41 nm. This is in good agreement with sizes determined from super-resolution fluorescence images with Ripley's L-function by Lehmann *et al.* (94 ± 37 nm) [101], with FWHM analysis by Eckhardt *et al.* (~ 140 nm) [217] and with a cluster analysis of Gunzenhäuser *et al.*, which gave a cluster radius of 53 ± 12 nm [218]. They agree also with cryo-EM measurements of the virion particle size of 169 ± 25 nm [219], 145 ± 25 nm [220] and 125 ± 14 nm [221].

However, in order to ensure that the obtained value is not biased by artifacts, which might arise from fixation or permeabilization, an analogous PALM experiment was performed using living, non-fixed cells that expressed HIV$^{\mathrm{mEos}}$. The size distribution of 54 HIV-1 assembly sites in living cells is shown in Figure 4.5C. Measuring of the cluster size with the same methods as for the fixed cells gave average diameters of 108 ± 35 nm by means of the FWHM and of 152 ± 37 nm using Ripley's L-function. No significant differences could therefore be found compared to the fixed and permeabilized cells, which proves that this particular treatment required for immunostaining, does not create artifacts, but gives a reliable reference value for super-resolution imaging of ESCRT and ALIX structures.

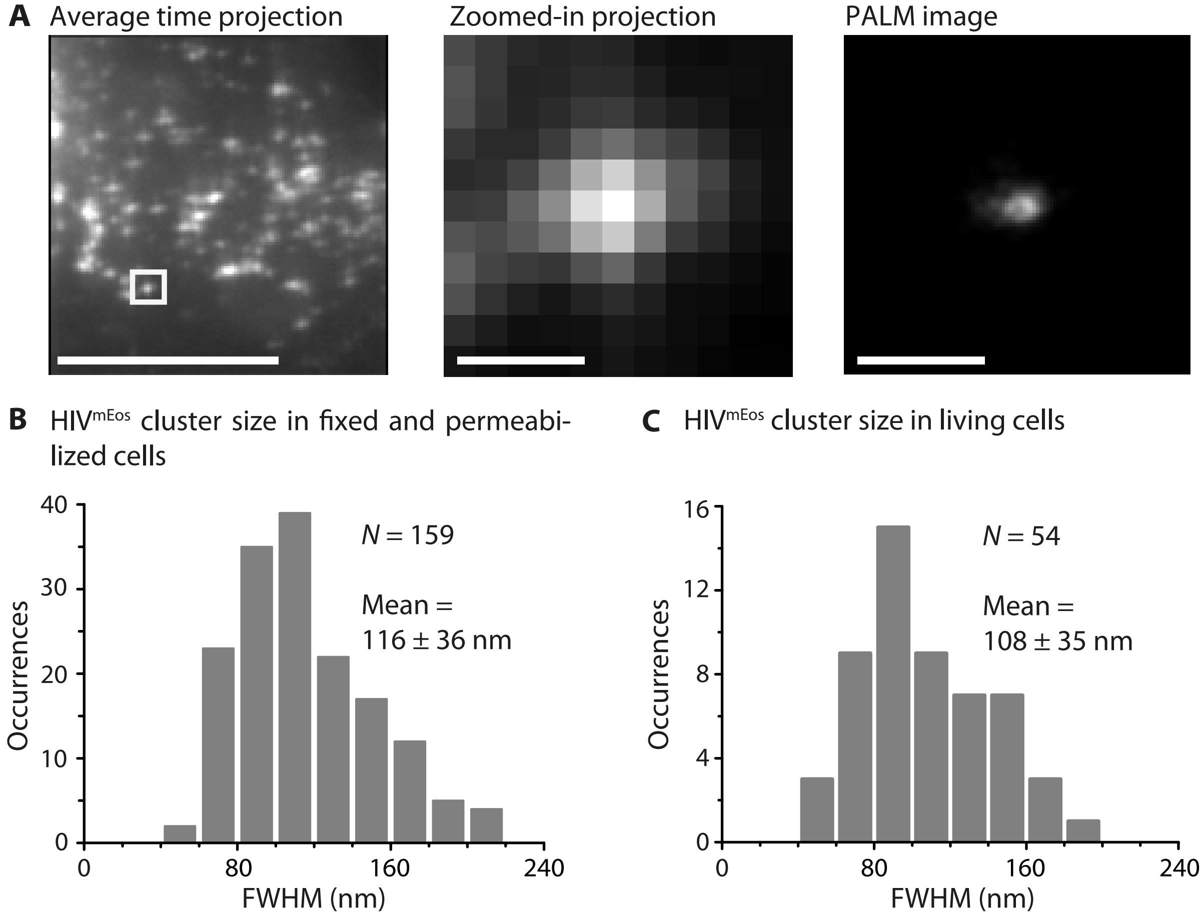

Figure 4.5: Super-resolution imaging of HIV-1 assembly sites. Cells were transfected with equimolar amounts of pCHIV$^{\mathrm{mEos}}$ and untagged pCHIV. (A) *Left panel.* The average, drift-corrected time projection of a TIRF image stack acquired for PALM of a cell expressing HIV$^{\mathrm{mEos}}$ emulates the corresponding TIRF image and shows various HIV-1 assembly sites. Scale bar: 10 µm. *Middle panel.* A zoomed-in TIRF image of a single HIV-1 assembly site highlighted by the white box in the left panel is shown. Scale bar: 500 nm. *Right panel.* The drift-corrected super-resolution PALM image of the HIV-1 assembly site shown in the middle panel is rendered. Scale bar: 500 nm. (B) The size distribution of 159 HIV$^{\mathrm{mEos}}$ clusters determined from the FWHM of the Gaussian fit of the super-resolution images yields an average size (FWHM) of 116 ± 36 nm. (C) The size distribution of 54 HIV$^{\mathrm{mEos}}$ clusters in non-fixed cells is show with an average size (FWHM) of 108 ± 35 nm. *N* represents the number of analyzed colocalizing clusters.

4.3.2 Verification of efficient immunostaining inside nascent HIV-1 buds

Although PALM successfully allowed super-resolution imaging of HIV-1 budding sites, this approach was discarded for imaging of ESCRT proteins. PALM requires a FP-tagged version of the respective proteins and previous works showed that fusing ESCRT proteins to large tags such as fluorescent proteins often affects its functionality [167, 183, 222, 223]. For this reason, all ESCRT proteins analyzed in this study were labeled by immunostaining using appropriate commercially available antibodies and were subsequently imaged with STORM or dSTORM. The accuracy and resolution of STORM and dSTORM images, however, depends considerably on the achievable labeling efficiency and effectivity of immunostaining. Although it could be shown that fixation and permeabilization of the cells did not have any effect on the observed structures, additional aspects have to be considered. Apart from the required specificity of the antibodies, which has to be tested for each experimental setting, it is also important to take into account the finite size of the antibody molecules of approximately 10 nm [108]. For this reason, it has to be ensured that these proteins are able to diffuse through the neck of a nascent virus bud. Otherwise, it would not be possible to differentiate between Models 2 and 3.

The efficiency of labeling protein structures within the bud was determined by a control experiment using an eGFP-tagged version of the viral accessory protein Vpr. Interaction with the C-terminal p6 domain of the polyprotein precursor Pr55Gag recruits Vpr into the bud [224–226]. In contrast to other proteins that are in the immature state of the HIV-1 particle parts of Gag or GagProPol polyproteins, Vpr is already present in its fully processed form at this point. As no reliable anti-Vpr antibody was available, an eGFP-tagged version (eGFP.Vpr) was used for this experiment, which was labeled with anti-GFP antibodies. eGFP.Vpr was co-expressed with HIV-1 Gag alone instead of the full viral construct $\text{HIV}^{\text{mCherry}}$, which would also comprise wildtype Vpr, which is not detectable by the anti-GFP antibodies. A previously described Rev-independent Gag expression construct [227], which can be expressed without the viral regulatory Rev protein, was used for this purpose. Similar to the pCHIV constructs, a 1:1 mixture of unlabeled and labeled Gag is used for transfection in order to allow visualization in fluorescence microscopy. In contrast to $\text{HIV}^{\text{mCherry}}$, the FP tag is fused to the C-terminus of Gag.mCherry.

In order to avoid artifacts in the form of malformed buds caused by steric hindrance between adjacent FP tags, HeLa cells were transiently co-transfected with an equimolar ratio of plasmids encoding untagged HIV-1 Gag (synGag) and a mCherry-tagged derivative (Gag.mCherry), respectively, together with peGFP.Vpr, which encodes eGFP.Vpr. Cells were fixed at 18-20 hours after transfection and eGFP.Vpr was stained for dSTORM imaging using primary polyclonal anti-GFP antibodies and corresponding secondary antibodies labeled with Cy5. TIRF images of cells expressing all three constructs showed characteristic fluorescence signals for eGFP.Vpr (Figure 4.6A, left panel), Gag:Gag.mCherry (1:1) (Figure 4.6A, middle panel) and anti-GFP immunostaining (Figure 4.6A, right panel). A high number of eGFP.Vpr protein assemblies strongly colocalized with Gag.mCherry budding sites (Figure 4.6B), giving evidence that the Vpr version is functionally recruited by Gag during the assembly process. The majority of eGFP.Vpr clusters (53 %) could also be detected by the introduced antibodies (Figure 4.6C) attesting to the accessibility of proteins inside the nascent bud to immunostaining.

The size of all 49 eGFP.Vpr clusters colocalizing with Gag.mCherry that were detected in dSTORM images of immunostained Vpr were estimated analogously to the size of HIV-1 assembly sites. The fits gave an average FWHM of 56 ± 12 nm (Figure 4.6D), which is smaller than the average diameter that was calculated for a virus bud before. This difference is expectable when eGFP.Vpr has a central localization in the virus bud as assumed. Analysis of the cluster size by Ripley's L-function with a diameter of 95 ± 53 nm gave a larger average value

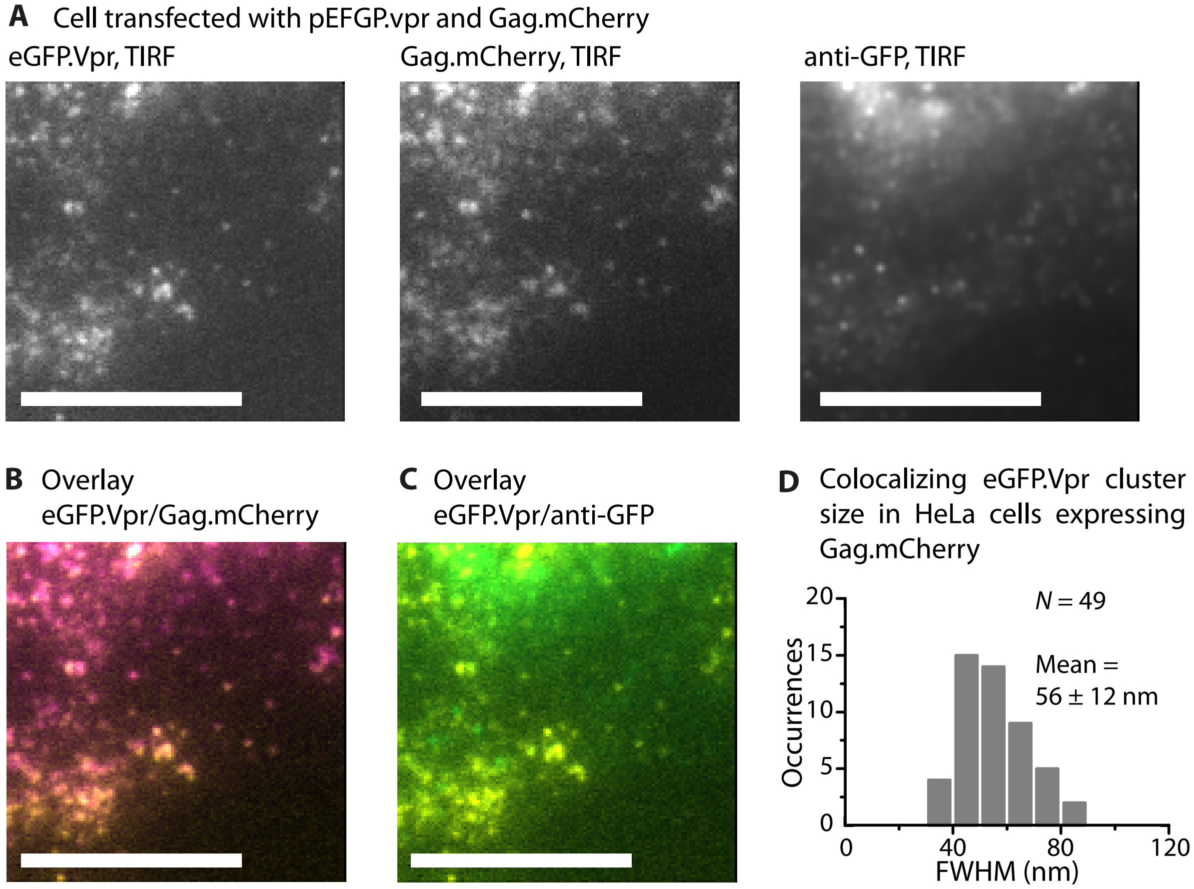

Figure 4.6: Immunostaining efficiency control experiment. In all images, eGFP.Vpr expressed in HeLa cells was detected by immunostaining or directly via the eGFP fluorescence by TIRFM. (A) TIRF images of a HeLa cell expressing both eGFP.Vpr and Gag.mCherry that was immunostained using antibodies against GFP is visualized in the eGFP channel (*left panel*), the mCherry channel (*middle panel*) and the anti-GFP (*right panel*) channel. Overlays of images demonstrate (B) the colocalizations of eGFP.Vpr and $\text{HIV}^{\text{mCherry}}$ and (C) the colocalizations of eGFP.Vpr and anti-GFP (magenta: Gag.mCherry, yellow: eGFP.Vpr, green: anti-GFP). Scale bars: 10 µm. (D) The size distribution of eGFP.Vpr clusters colocalizing with Gag.mCherry is determined from the average FWHM obtained by fitting Gaussian functions to the horizontal and vertical cross-sections through the respective eGFP.Vpr cluster. The average cluster size (FWHM) is 56 ± 12 nm. N represents the number of analyzed colocalizing clusters.

but this is to be expected as demonstrated in Section 3.4. Furthermore, this result is in good agreement with experiments performed by Lehman *et al.* [101] who obtained a similar diameter of 94 ± 17 nm using Ripley's analysis at PALM images of Dronpa-Vpr.

4.3.3 Characterization of ESCRT proteins and ALIX at HIV-1 budding sites

With the prerequisites laid in the previous sections, the structure and size of ESCRT proteins Tsg101, CHMP4B, CHMP2A and the ESCRT-associated protein ALIX assembling at nascent buds could now be analyzed. The control experiments performed provided the apparent diam-

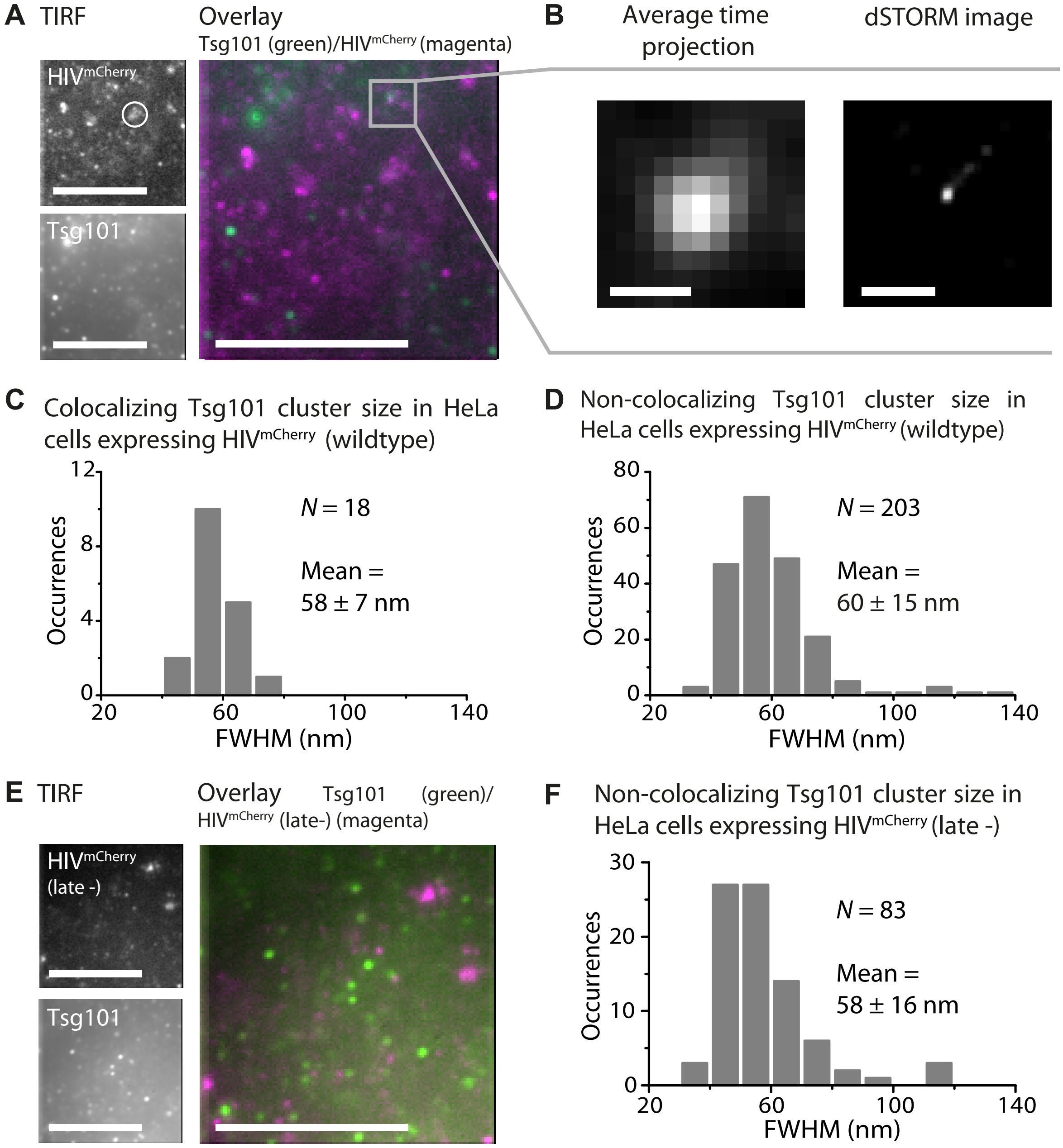
A
TIRF
Overlay
Tsg101 (green)/HIVmCherry (magenta)
HIVmCherry
Tsg101
B
Average time projection
dSTORM image
C
Colocalizing Tsg101 cluster size in HeLa cells expressing HIVmCherry (wildtype)
N = 18
Mean = 58 ± 7 nm
Occurrences
0
4
8
12
20
60
100
140
FWHM (nm)
D
Non-colocalizing Tsg101 cluster size in HeLa cells expressing HIVmCherry (wildtype)
N = 203
Mean = 60 ± 15 nm
Occurrences
0
20
40
60
80
20
60
100
140
FWHM (nm)
E
TIRF
Overlay Tsg101 (green)/ HIVmCherry (late-) (magenta)
HIVmCherry (late -)
Tsg101
F
Non-colocalizing Tsg101 cluster size in HeLa cells expressing HIVmCherry (late -)
N = 83
Mean = 58 ± 16 nm
Occurrences
0
10
20
30
20
60
100
140
FWHM (nm)

eter of HIV-1 budding sites in the context of the applied experimental settings and protocols. It could be further demonstrated that immunostaining could be successfully performed inside the virus bud. The endogenous version of the listed proteins or a version with a small epitope were labeled by immunostaining. For this reason, super-resolution imaging was performed using either STORM or dSTORM.

4.3.3.1 Super-resolution imaging of endogenous of Tsg101

As described above, Tsg101 is the first ESCRT protein that is recruited by HIV-1 during virus budding. Tsg101 was imaged by dSTORM, where the endogenous protein was directly stained by adding primary anti-Tsg101 antibodies and appropriate secondary antibodies that were labeled with Cy5. Virus budding was induced by transient transfection of HeLa cells with an equimolar ratio of pCHIV and the pCHIV$^{\text{mCherry}}$. This allowed the identification of Tsg101 assembly sites colocalizing with HIV-1 that are most likely involved in budding and to separate them from other signals, which might be detectable at the cell membrane. Cells were fixed and immunostained 14-15 h after transfection and TIRF images revealed several HIV-1 budding sites (Figure 4.7A, top-left panel). Large fluorescent assembly sites such as the example marked by the white circle were excluded from further evaluation as they most likely did not represent single viruses. This can occur, for example, when the ratio of labeled to unlabeled Gag is high. It has been shown that particles that contain only labeled Gag show a significantly decreased infectivity [216]. TIRFM imaging further revealed a high number of immunostained Tsg101 protein assemblies at the membrane (Figure 4.7A, bottom-left panel). An overlay of this image with HIV-1 budding sites showed that Tsg101 assemblies could be categorized into colocalizing and non-colocalizing structures, where the number of the latter was significantly higher than of colocalizing structures (Figure 4.7A, right panel). From 1052 Gag assembly sites in 14 analyzed cells, only 18 (1.8 %) colocalized with Tsg101. This apparently low number of colocalizations, however, has to be seen in the context of the transient, dynamic nature of ESCRT recruitment during HIV-1 budding [168, 211]. When using fixed-cell samples, only

---

Figure 4.7 ***(preceding page)*****:** Super-resolution imaging of endogenous Tsg101 at HIV-1 assembly sites. (A) *Top-left panel.* A TIRF image of HIV$^{\text{mCherry}}$ in a HeLa transfected with pCHIV:pCHIV$^{\text{mCherry}}$ (1:1) is shown, the white circle indicates a large Gag aggregate, which is most likely a budding artifact. *Bottom-left panel.* The average, drift-corrected time projection of a TIRF image stack acquired for dSTORM imaging of immunostained Tsg101 emulates the corresponding TIRF image. *Right panel.* The overlay of both panels reveals colocalizing and non-colocalizing Tsg101 clusters (magenta: HIV$^{\text{mCherry}}$, green: Tsg101). Scale bars: 10 µm. (B) *Left panel.* A zoomed image of the individual colocalizing Tsg101 cluster highlighted in panel A. *Right panel.* The corresponding drift-corrected dSTORM image. Scale bars: 500 nm. (C) In cells expressing HIV$^{\text{mCherry}}$, a size distribution with an average cluster size (FWHM) of 58 ± 7 nm is revealed for Tsg101 structures colocalizing with HIV$^{\text{mCherry}}$ and (D) of 60 ± 15 nm for all non-colocalizing Tsg101 clusters, respectively. (E) *Top-left panel.* TIRF image of HIV$^{\text{mCherry}}$ (late-) assembly sites. *Bottom-left panel.* The average, drift-corrected time projection of an immunostained Tsg101 TIRF image series in pCHIV (late-):pCHIV$^{\text{mCherry}}$ (late-) (1:1) transfected cells is shown. *Right panel.* The overlay of both panels (magenta: HIV$^{\text{mCherry}}$ (late-), green: Tsg101) shows no colocalizing Tsg101 structures. Scale bars: 10 µm. (F) The size distribution of all non-colocalizing Tsg101 clusters in cells expressing HIV$^{\text{mCherry}}$ (late-) reveals an average cluster size of 58 ± 16 nm. N represents the number of events contributing to the respective histogram.

snapshots of such processes be observed. Super-resolution dSTORM images of these colocalizing Tsg101 assemblies characterized all these structures as small, condensed, circular clusters as shown at the example in Figure 4.7B. Analysis of cluster sizes based on the FWHM (Figure 4.7C) revealed sizes between 40 and 75 nm with a mean value of 58 ± 7 nm, which was significantly smaller than the value obtained for the HIV-1 bud size in the previous section.

In order to get further insight into the function of the remaining, non-colocalizing Tsg101 structures assembling at the membrane of transfected cells, the size distribution of these protein assemblies was analyzed analogously. Despite the fact that the visual appearance, which showed circular, condensed structures as well, was similar to the results found for actual budding sites, the size distribution of all 141 detected non-colocalizing Tsg101 clusters (Figure 4.7D) revealed a larger distribution ranging from 35 up to 135 nm although the average diameter of 60 ± 15 nm by means of the FWHM was comparable to that of the colocalizing structures.

In order to be able to establish this similarity as significant, it is necessary to verify that the observed Tsg101 assemblies were actual specifically labeled by anti-Tsg101 antibodies. Only if this assumption holds true, a separation between Tsg101 involved in HIV-1 budding and other processes at the membrane is valid. Therefore, experiments were repeated with HeLa cells transfected with an equimolar ratio of pCHIV$^{\mathrm{mCherry}}$ (late-) and pCHIV (late-) where the PT/SAP motif of Gag is disrupted. Imaging with this mutant brought a drastic decrease of colocalizations compared to the experiments with wildtype HIV. Thus, from more than 210 analyzed HIV-1 assembly sites, not a single one was found to colocalize with Tsg101 (Figure 4.7E). The size distribution that was obtained for the analysis of the 83 Tsg101 clusters detected on the cell membrane of four analyzed HIV$^{\mathrm{mCherry}}$ (late-) expressing cells ranged from 40 to 120 nm with a mean value of 58 ± 16 nm. Although the mean values of all three distributions shown in Figure 4.7C,D and E did not vary significantly, the distributions of non-colocalizing Tsg101 (Figure 4.7D and E) included a considerably higher amount of larger protein clusters than observed for colocalizing structures (Figure 4.7C).

One possible explanation is that the size of colocalizing structures was confined by a surrounding structure, which could be either the neck of the virus bud or the nascent virus bud itself. This observation gave further evidence that the observed colocalizations in the diffraction-limited images are indeed a result of a functional interaction between the virus and the ESCRT structures and are not only a result of arbitrary superpositions.

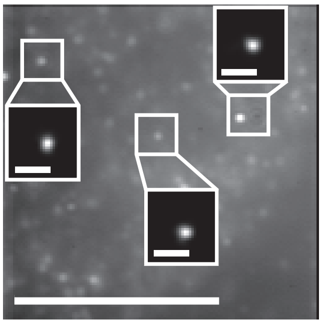

Figure 4.8: Tsg101 negative control. An untransfected HeLa cell was immunostained with anti-Tsg101 primary plus labeled secondary antibodies binding to the primary antibodies. Zoomed-in insets show drift-corrected super-resolution dSTORM images of the respective clusters highlighted in the TIRF image. Scale bars: 10 μm (large image), 200 nm (insets).

The presence of Tsg101 assemblies that are not related to HIV-1 budding would agree with previous work by Welsch *et al.* [228] where quantitative immuno-EM measurements showed that ∼ 15 % of all Tsg101 proteins are present at the plasma membrane of untransfected immune cells and that the distribution of Tsg101 between plasma and intracellular membranes do not significantly change upon HIV-1 infection.

The fact that Tsg101 immunostaining depends on the presence of the Tsg101 binding motif provided the required evidence for specific binding of the antibody. As a further control, untransfected HeLa cells were immunostained with the same set of primary and secondary antibodies. This would ensure that the observed distribution of Tsg101 is not influenced by the transfection itself. TIRFM imaging of untransfected also showed Tsg101 structures at the cell membrane and super-resolution dSTORM imaging (Figure 4.8) revealed condensed, circular structures with an average size of 59 ± 14 nm. These structures were similar to non-colocalizing Tsg101 clusters found at the membrane of cells expressing HIV$^{\mathrm{mCherry}}$.

4.3.3.2 Distribution of membrane-bound ALIX and association to HIV-1 budding

Apart from Tsg101, the ESCRT-related protein ALIX, another early-acting factor in HIV-1 budding, plays a key role in the ESCRT recruitment process. As described in Section 4.1.3, ALIX is not only able to replace Tsg101 in ESCRT recruitment by HIV-1 when the latter is not available but plays also an important role in the recruitment of further downstream ESCRT factors after initiation of the budding process. Thus, HeLa cells were transiently transfected with the full viral constructs pCHIV and pCHIV$^{\mathrm{mCherry}}$ (1:1) to analyze the size and structure of membrane-associated ALIX protein assemblies in the context of HIV-1 recruitment and to identify colocalizing and non-colocalizing ALIX protein clusters. Endogenous ALIX was directly stained 14-15 h after transfection with primary anti-ALIX antibodies that were labeled with the activator-reporter dye pair Alexa Fluor 488-Cy5. Direct labeling of the primary antibody is favorable when measuring cluster sizes as the absence of an additional secondary antibody reduces the size artifacts introduced by the size of the antibody molecules. However, direct staining of the primary antibody is often problematic compared to the use of an additional labeled secondary antibody as primary antibodies appear to be more sensible to chemical modifications. In the case of the primary anti-ALIX antibodies that were used here, attempts to find a compatible secondary antibody turned out to be unsuccessful.

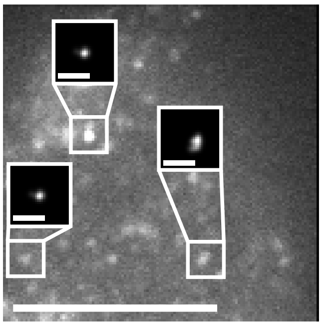

Figure 4.9: ALIX negative control. An untransfected HeLa cell was immunostained with labeled anti-ALIX primary antibodies. Zoomed-in insets show drift-corrected super-resolution STORM images of the respective clusters highlighted in the TIRF image. Scale bars: 10 µm (large image), 200 nm (insets).

In order to evaluate the specificity of the anti-ALIX antibodies after labeling and in the context of the applied immunofluorescence staining procedure, super-resolution imaging of membrane-associated ALIX structures in non-transfected HeLa cells was performed (Figure 4.9). High-resolution STORM reconstructions of membrane associated ALIX structures exclusively exhibited condensed spots of ALIX, similar to those found for membrane-associated Tsg101.

This is in agreement with the previously cited quantitative EM-study from Welsch *et al.* [228], where similar to Tsg101, 6 to 19 % of all ALIX proteins could be observed in the absence of HIV-1 at the plasma membrane of non-transfected immune cells. ALIX is known to associate with so called exosomes [156, 229], intraluminal vesicles of MVBs, which fuse with the plasma membrane to release their content for cell-cell communication [230]. Thus, the spot-like assemblies of ALIX in cells not expressing HIV$^{\mathrm{mCherry}}$ could potentially be attributed to exosome-related ALIX structures captured during the process of membrane secretion.

These results could show that labeling did not affect the anti-ALIX primary antibody. This made it possible to perform subsequent experiments with transfected cells as shown in Figure 4.10A. Apart from several individual HIV-1 budding sites at the cell membrane, immune-detected ALIX protein assemblies could be identified. Similar to Tsg101, ALIX clusters at the cell membrane could be categorized into protein assemblies that colocalize with HIV-1 budding sites and others that did not. After performing super-resolution STORM reconstructions, three distinct classes of colocalizing ALIX structures could be identified and were categorized into condensed spots (Figure 4.10A, crop 1), condensed spots with surrounding, diffuse cloud-like structures (Figure 4.10A, crop 2) and diffuse cloud-like structures without a central spot (Figure 4.10A, crop 3). Non-colocalizing clusters were, in contrast, only observed in the form of condensed spots similar to the negative control (Figure 4.9).

The cloud-like ALIX structures with a central spot were clearly different from all Tsg101 protein assemblies observed. The fact that these structures did not appear in untransfected cells further indicated that any cloud-like spreading of ALIX proteins can be regarded as a Gag specific and recruitment induced effect that is only present in cells expressing HIV$^{\mathrm{mCherry}}$. Any non-colocalizing round ALIX structures in cells expressing HIV$^{\mathrm{mCherry}}$ (Figure 4.10A, circles) were not correlated to Gag specific recruitment. Thus, they represent individual ALIX protein assemblies that were most likely retained at the membrane in the course of other cellular processes, which is in agreement with the negative control and the previous studies of ALIX that were cited above. In contrast, ALIX clusters colocalizing with HIV$^{\mathrm{mCherry}}$ but not showing the cloud-like structure could still be connected to HIV-1 budding as it is possible that the number of molecules forming the cloud-like structure was below the detection limit in these cases. Structures that only showed a diffuse, cloud-like structure without a central spot were discarded from further analysis as it could not be ensured that they represent specific ALIX clusters.

As non-colocalizing ALIX clusters at the membrane can be linked to cellular structures and thus to processes unaffected by HIV-1 infection, analysis was categorized in ALIX clusters colocalizing with virus buds and clusters that did not colocalize. In 10 cells expressing HIV$^{\mathrm{mCherry}}$, 3.4 % of all virus buds colocalized with ALIX. 17 ALIX clusters colocalizing with HIV$^{\mathrm{mCherry}}$ could be detected in total and 13 out of these 17 clusters (76 %) showed an additional cloud around the central cluster. Again, Gaussian functions were fitted to the cross-section profiles of all 17 colocalizing spot-like ALIX clusters with and without cloud. The spot diameter ranged from 30 to 90 nm (Figure 4.10B) with an average value of 64 ± 18 nm, which again was significantly smaller than the mean HIV-1 bud size of 116 ± 36 nm. Analysis of ALIX clusters that did not colocalize with HIV$^{\mathrm{mCherry}}$ showed a broader size distribution analogously to Tsg101 ranging from 30 to 130 nm with an average size of 74 ± 26 nm (Figure 4.10C). Thus, similar to Tsg101, ALIX appears to form compact protein assemblies inside a confined structure, which might either be the virus bud or the neck of the bud, after specific recruitment by HIV-1 Gag. Localization of ALIX proteins inside the budding neck would be in agreement with any kind of neck stabilizing mechanism during HIV-1 budding or membrane scission, which stands in good agreement with a proposed stabilizing function of ALIX besides its involvement in recruitment of downstream ESCRT factors [189].

The conventional Gaussian fitting method for size determination as done for the condensed

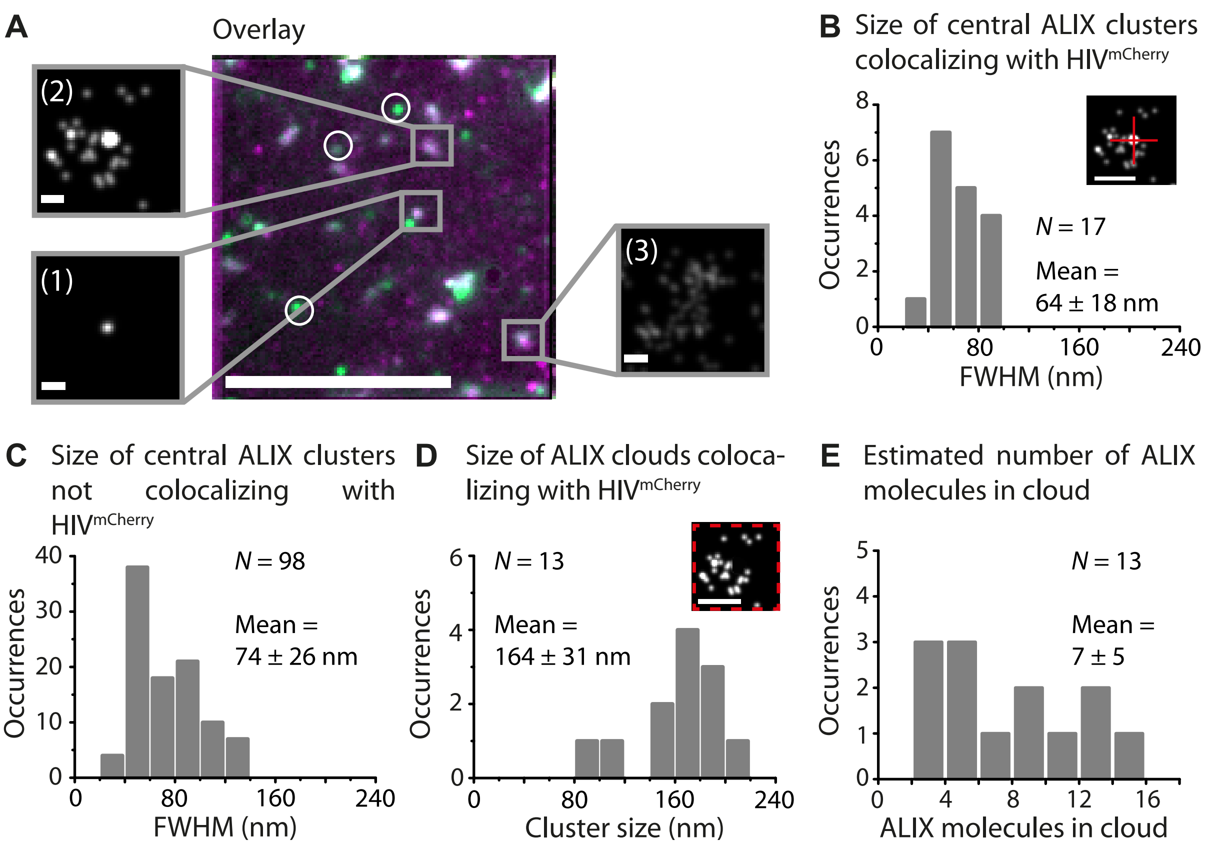

Figure 4.10: Super-resolution imaging of endogenous ALIX at HIV-1 assembly sites. HeLa cells were transfected with pCHIV:pCHIV$^{\mathrm{mCherry}}$ (1:1) and endogenous ALIX was immunostained. (A) An average, drift-corrected time- projected TIRF image of ALIX (green) is overlaid with the corresponding TIRF image of HIV$^{\mathrm{mCherry}}$ assembly sites (magenta). Circles indicate non-colocalizing ALIX clusters and the rectangles highlight different colocalizing ALIX classes. The crops show drift-corrected super-resolution STORM images of the three identified object classes: condensed ALIX structures without a surrounding cloud (1), ALIX structures with a central, condensed spot surrounded by a cloud-like structure (2) and diffuse ALIX membrane assemblies without a central spot (3). Scale bars: 10 µm (large image), 100 nm (crops). (B) The size distribution of all central spots of colocalizing ALIX protein clusters reveals an average cluster size (FWHM, small inset) of 64 ± 18 nm. Scale bar: 200 nm. (C) The size distribution of all central spots of non-colocalizing ALIX protein clusters is shown with an average cluster size (FWHM) of 74 ± 26 nm. (D) Cloud cluster size characterization for all cloud structures of ALIX colocalizing with HIV$^{\mathrm{mCherry}}$ was obtained by Ripley's cluster analysis with an average diameter of 164 ± 31 nm where the central spot was masked for analysis (small inset). Scale bar: 200 nm. (E) The distribution of the minimum number of ALIX proteins detected per cloud was estimated from the super-resolution data with a mean value of 7 ± 5 molecules. N represents the number of events contributing to the respective histogram.

spots of ALIX however could not be applied in the case of the cloud-like assemblies due to the low number of ALIX proteins. Thus, cluster sizes were calculated using the Ripley's L-function (see Section 3.4). As the Ripley's L-function requires uniformly distributed point distributions to provide unbiased results about the cluster size as shown before, the central ALIX cluster was masked for the calculations. In detail, the centroid position of the central cluster was determined and all points within a distance smaller than the radius of the central cluster were discarded from the analysis. The Ripley's L-function analysis of the cloud-like structures alone (Figure 4.10D, small inset) gave an estimate for the diffuse spreading of ALIX proteins with a diameter ranging from 95 to 210 nm (Figure 4.10D) and a mean value of 164 ± 31 nm. The size distribution was certainly slightly shifted to larger values when compared to the distribution of HIV-1 bud diameters ranging from 70 to 220 nm and a mean value of 116 ± 36 nm. However, the size determination of HIV-1 buds based on the FWHM of the Gaussian function fitted to the spot-like assemblies (Figure 4.10B, small inset) slightly underestimates the true size of the cluster (Section 3.4). This is in agreement with a slightly larger average size of HIV-1 buds of 141 ± 41 nm that was determined by Ripley's L-function (cf. Sections 4.3.1 and 3.4). Hence, the size of the HIV-1 buds and the diameter of the ALIX clouds were in the same range. In addition, the size of the cloud structure showed a relatively narrow size distribution with no strong outliers, which would indicate a random membrane association. Hence, all ALIX proteins inside the cloud colocalizing with an HIV-1 assembly site are very likely restricted by the HIV-1 bud. This gave evidence that ALIX was incorporated into nascent buds remaining there over the whole process from assembly to membrane scission. Based on western plot and biochemical analysis [166, 172, 231–234], ALIX molecules are known to be found in released virus-like particles indicating that they are already incorporated during the HIV-1 budding process. ALIX molecules potentially incorporated into the bud by direct interaction with the $\mathrm{LYPX_nL}$ or $\mathrm{LX_nLF}$ L-domains motifs of the NC domain of Gag [172, 235] would very likely appear as a diffuse cloud of single ALIX proteins spread around the condensed spot-like assemblies inside the budding neck in super-resolution images. Any random membrane association of ALIX molecules can be excluded due to the presence of the auto-inhibitory domain in ALIX [236–238], preventing any unspecific membrane binding. Furthermore, when individual ALIX proteins are incorporated into the formed bud, their spatial distribution on the membrane should be limited to the size of the bud. However, if the spatial limitations of the bud are not present and the Gag induced release of autoinhibition is not necessary, individual ALIX proteins should be able to freely associate with the membrane and eventually spread over an unlimited large area.

In a next step, a rough estimation was done for the minimum number of ALIX molecules incorporated into the virus Gag shell. For this purpose, the masked image of the cloud (without the central cluster) that was already used for Ripley's L-function was analyzed. In order to consider the fact that dye molecules may be activated more than once during STORM imaging, a threshold of 40 nm, which was based on the achievable resolution of the STORM microscope, was set and all signals occurring within this threshold were regarded as a single molecule. The analysis yielded a number of 2 up to 15 molecules per cloud (Figure 4.10E) with a mean value of 7 ± 5 molecules. It has to be emphasized however, that this is only a very rough estimate of the total number of molecules as it cannot be excluded that more than one ALIX molecule exist within the selected threshold that could not be resolved. Therefore, the given value can only be regarded as a minimum.

4.3.3.3 CHMP4B-HA lattices colocalizing with HIV-1 assembly sites

In HIV-1, the recruitment of downstream ESCRT factors that are directly involved in the membrane scission process such as the ESCRT-III component CHMP4 significantly relies on

A Overlay of $HIV^{mCherry}$ (magenta) and CHMP4B-HA (green)

B CHMP4B-HA average time projection CHMP4B-HA STORM image

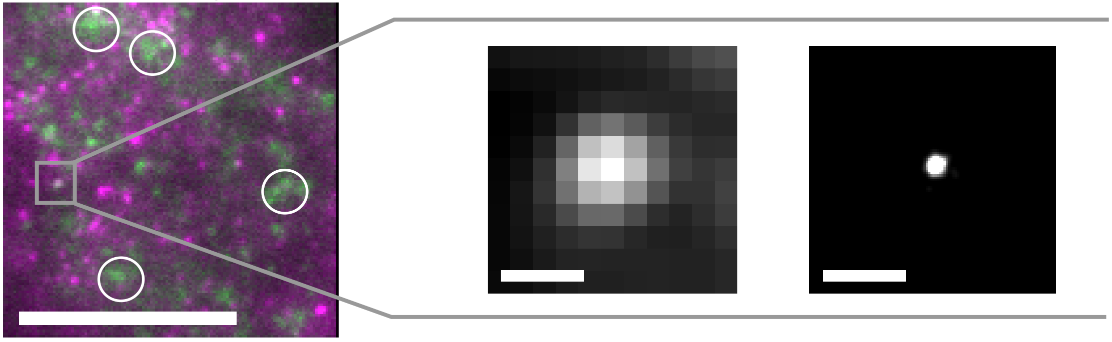

C Colocalizing CHMP4B-HA cluster size in HeLa cells expressing $HIV^{mCherry}$ (wildtype)

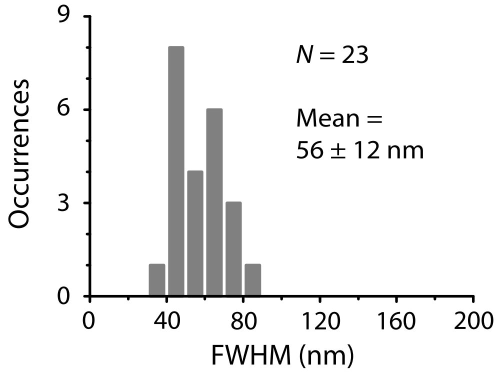

D Non-colocalizing CHMP4B-HA cluster size in HeLa cells expressing $HIV^{mCherry}$ (wildtype)

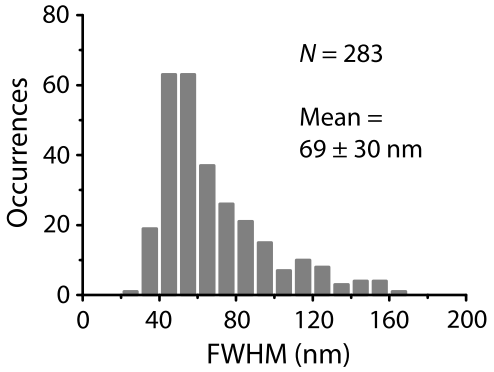

E Overlay of $HIV^{mCherry}$ (late-) (magenta) and CHMP4B-HA (green)

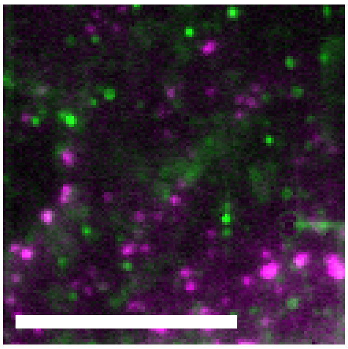

F Non-colocalizing CHMP4B-HA cluster size in HeLa cells expressing $HIV^{mCherry}$ (late-)

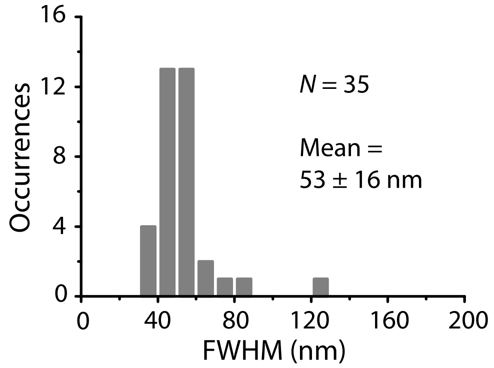

the interaction with the early-acting protein factors ALIX and Tsg101, which directly bind to the bud-forming structural protein Gag. Among all human CHMP4 isoforms, CHMP4B is the major component involved in membrane scission by forming large membrane-associated protein assemblies of different geometries [169]. Hence, experiments for this study focused on CHMP4B for investigation of structure and size of membrane-associated CHMP4 clusters during HIV-1 assembly and budding. As described previously (Section 4.2), a relatively small hemagglutinin (HA) tagged version of CHMP4B was expressed because reliable commercial anti-CHMP4B antibodies were not available. Expressed CHMP4B-HA protein clusters were detected by immunofluorescence staining using primary monoclonal anti-HA antibodies, which were directly labeled by Alexa Fluor 488 and Cy5 as activator-reporter dye pair for STORM imaging.

In HeLa cells displaying both HIV$^{\mathrm{mCherry}}$ assembly sites and immunostained CHMP4B-HA, colocalizing as well as non-colocalizing CHMP4B-HA protein clusters were observed 14-15 h post transfection (Figure 4.11A). Considering the relatively high number of detected CHMP4B-HA protein clusters, the overall number of colocalizations between CHMP4B-HA and HIV-1 budding sites seemed low, but was again attributable to the transient nature of membrane-associated ESCRT-III protein assemblies [168]. Some CHMP4B-HA proteins, primarily non-colocalizing ones, not only formed condensed spots but also diffuse clusters at the membrane, which were significantly larger than the optical resolution (Figure 4.11A, left panel, circles) and might represent overexpression artifacts that were excluded from further evaluation.

STORM imaging was performed on 23 colocalizing CHMP4B-HA clusters such as shown in Figure 4.11B. In contrast to the diffraction-limited images, (Figure 4.11B, left panel), STORM image reconstructions revealed round, condensed structures in all cases (Figure 4.11B, right panel). The average diameter of all colocalizing spot-like CHMP4B-HA clusters was determined as done before for Tsg101 and ALIX. This resulted in a relatively narrow CHMP4B-HA cluster size distribution ranging from 35 to 85 nm with a mean value of 56 ± 12 nm (Figure 4.11C). Thus, recruited CHMP4B-HA proteins assembled at the membrane into significantly smaller structures than the average size of a HIV-1 bud of 116 ± 36 nm. Furthermore, the 283 non-colocalizing CHMP4B-HA clusters showed a much broader size distribution ranging from 20

Figure 4.11 ***(preceding page)*****:** Super-resolution imaging of CHMP4B-HA at HIV-1 assembly sites. HeLa cells were transfected with pCHMP4B-HA and an equimolar ratio of pCHIV and pCHIV$^{\mathrm{mCherry}}$ and expressed CHMP4B-HA was detected by immunostaining. (A) An overlay of TIRF images of a HeLa cell expressing both HIV$^{\mathrm{mCherry}}$ (magenta) and CHMP4B-HA (green). The circles indicate partially diffuse CHMP4B-HA clusters at the membrane, which were ignored in further analyses. Scale bar: 10 µm. (B) *Left panel.* A zoomed-in TIRF image of the selected CHMP4B-HA cluster colocalizing with HIV$^{\mathrm{mCherry}}$ emulated by the average, drift-corrected time projection of TIRF images of immunostained CHMP4B-HA. *Right panel.* The corresponding drift-corrected STORM image. Scale bars: 500 nm. (C) The size distribution of all CHMP4B-HA structures colocalizing with HIV$^{\mathrm{mCherry}}$ is shown with an average cluster size (FWHM) of 56 ± 12 nm. (D) The size distribution of all non-colocalizing CHMP4B-HA clusters in cells co-expressing HIV$^{\mathrm{mCherry}}$ wildtype is shown with an average cluster size (FWHM) of 69 ± 30 nm. (E) HeLa cells were transfected with pCHIV:pCHIV$^{\mathrm{mCherry}}$ (late-) and pCHMP4B-HA. An overlay of TIRF images of a HeLa cell expressing both HIV$^{\mathrm{mCherry}}$ (late-) (magenta) and CHMP4B-HA is shown (green). The latter was emulated by average, drift-corrected time projection. Scale bar: 10 µm. (F) The corresponding size distribution of all non-colocalizing CHMP4B-HA clusters in HIV$^{\mathrm{mCherry}}$ (late -) expressing cells is shown with an average cluster size (FWHM) of 53 ± 16 nm. N represents the number of events contributing to the respective histogram.

up to 160 nm with an average size of 69 ± 30 nm (Figure 4.11D) and were more spread than CHMP4B-HA clusters colocalizing with HIV-1 budding sites. This strongly suggests that colocalizing CHMP4B-HA protein assemblies form inside a restricting structure such as the budding neck or the bud whereas non-colocalizing CHMP4B-HA clusters, which did not correspond to nascent HIV-1 buds, have larger freedom in spatial spreading.

In HeLa cells co-expressing CHMP4B-HA and the HIV$^{\mathrm{mCherry}}$ (late-) mutant (Figure 4.11E), the number of Gag clusters colocalizing with CHMP4B-HA reduced significantly from 1.5 % to only 0.4 %, which corresponded to only 1 colocalization in more than 200 CHMP4B-HA clusters. This observation could be expected for a partially recruitment defective Gag variant containing a disrupted PT/SAP motif. This result indicated that, under the given experimental conditions, the relatively small HA-Tag did not significantly alter the CHMP4B binding abilities and functionality. However, in order to gain further evidence for the wildtype-like behavior of an overexpressed tagged version of CHMP4B, the diameter of all non-colocalizing CHMP4B-HA spot-like clusters in HIV$^{\mathrm{mCherry}}$ (late-) control cells was analyzed (Figure 4.11F) and compared to the distributions for cells expressing wildtype HIV$^{\mathrm{mCherry}}$ (Figure 4.11D). The measured size distribution with an average of 53 ± 16 nm showed a similar broadness as observed for non-colocalizing CHMP4B-HA in cells expressing wildtype HIV$^{\mathrm{mCherry}}$. It was also broader than for colocalizing CHMP4B-HA, which is a similar behavior as was observed before for Tsg101 before.

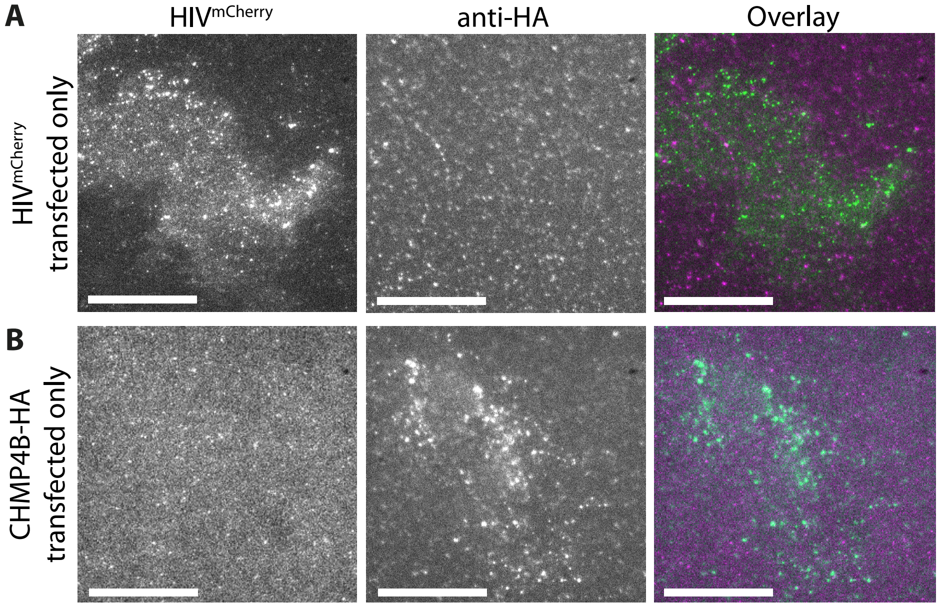

Figure 4.12: CHMP4B-HA control experiments. HeLa cells were transfected with (A) only pCHIV:pCHIV$^{\mathrm{mCherry}}$ (1:1) or (B) only pCHMP4B-HA and immunostained with anti-HA primary antibodies. TIRF images of the HIV$^{\mathrm{mCherry}}$ channel and the CHMP4B-HA channel are shown in the left and middle panels, respectively. Right panels show overlays of the HIV$^{\mathrm{mCherry}}$ channel (magenta) with the CHMP4B-HA channel (green). The images shown in this figure were acquired at a combined TIRF/widefield setup described in [153]. Scale bars: 20 µm.

In control experiments, HeLa cells that were not transfected with CHMP4B-HA were immunostained using anti-HA antibodies labeled with Alexa Fluor 488-Cy5 (Figure 4.12A). In this case, very few spots were visible, which do not colocalize with virus budding sites, confirming the specificity of the labeled antibodies. HeLa cells expressing CHMP4B-HA and in the absence of HIV-1 were imaged under identical staining and imaging conditions as before in order to confirm that any non-colocalizing CHMP4B-HA clusters in previous experiments were related to other cellular functions. No virus assemblies were detected and existing signals, which are not confined to the shape of the cell visible in the middle panel, are most likely results of dirt on the surface of the glass slide and do not colocalize with CHMP4B-HA clusters. Similar CHMP4B-HA protein assemblies at the membrane (Figure 4.12B) could be identified as in the case of cells expressing CHMP4B-HA in the presence of HIV$^{\mathrm{mCherry}}$, confirming that non-colocalizing CHMP4B-HA clusters at the membrane are most likely not related to HIV-1 budding.

4.3.3.4 Super-resolution imaging of CHMP2A lattices

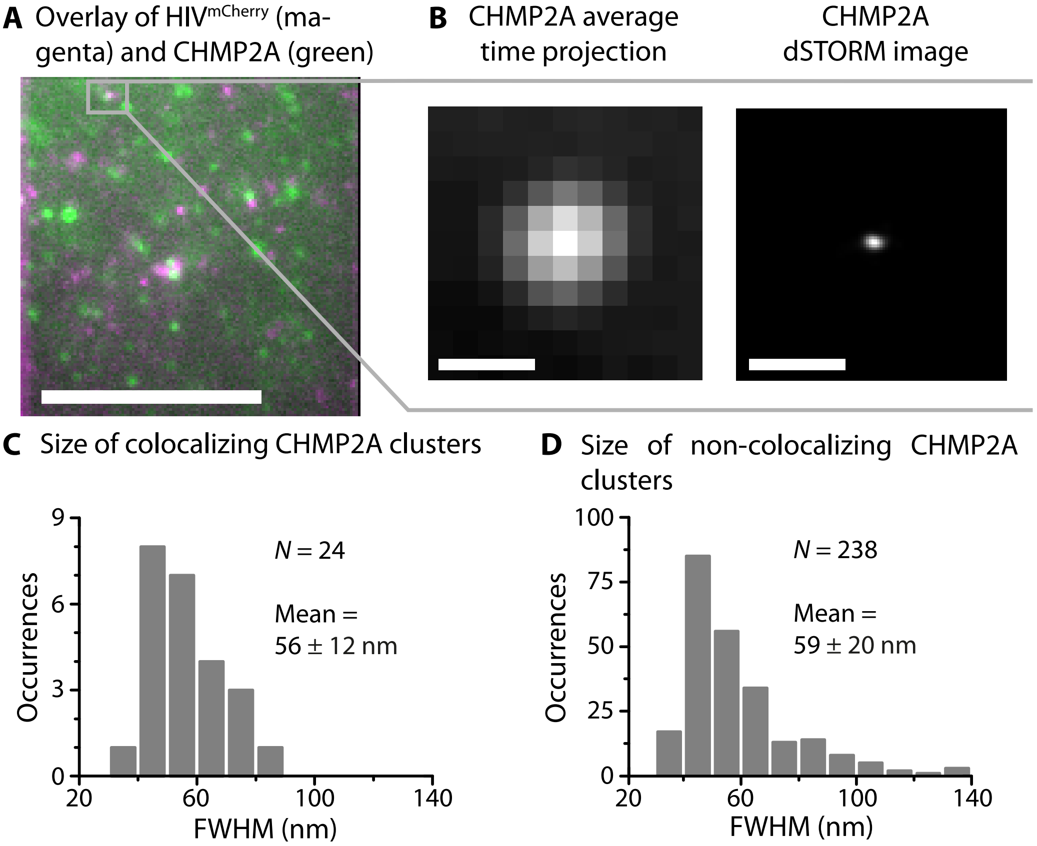

Figure 4.13: Super-resolution imaging of endogenous CHMP2A at HIV-1 assembly sites. HeLa cells were transfected with pCHIV:pCHIV$^{\mathrm{mCherry}}$ (1:1) and endogenous CHMP2A was detected by immunostaining. (A) An overlay of the corresponding TIRF images of HIV$^{\mathrm{mCherry}}$ (magenta) and of CHMP2A (green) prior to dSTORM analysis. Scale bar: 10 µm. (B) *Left panel.* A zoomed-in TIRF image of the selected CHMP2A cluster highlighted in gray in the left panel colocalizing with an HIV-1 assembly site is emulated by the average, drift-corrected time projection of TIRF images of immunostained CHMP2A acquired for dSTORM imaging. *Right panel.* The corresponding drift-corrected dSTORM image of the colocalizing CHMP2A cluster. Scale bars: 500 nm. (B) The size distribution of all CHMP2A structures colocalizing with HIV$^{\mathrm{mCherry}}$ is shown with an average cluster size (FWHM) of 56 ± 12 nm. (C) The size distribution of all non-colocalizing CHMP2A clusters in cells expressing HIV$^{\mathrm{mCherry}}$ is shown with an average cluster size (FWHM) of 59 ± 20 nm. *N* represents the number of events contributing to the respective histogram.

Following the ESCRT recruitment pathway, CHMP4 recruits CHMP3, which in turn recruits the CHMP2-isoform CHMP2A [169]. In the final step of the budding process, CHMP2A eventually recruits VPS4A. As reliable antibodies against CHMP3 as well as a functioning epitope-tagged version were not available, focus was turned to CHMP2A.

In contrast to CHMP4B and CHMP3, appropriate antibodies against endogenous CHMP2A were available. Therefore, overexpression by transient transfection of a tagged variant, which might lead to artifacts or changes in protein localization, could be avoided and endogenous CHMP2A protein could be imaged. HeLa cells were therefore transfected with an equimolar ratio of plasmids encoding $\mathrm{HIV}^{\mathrm{mCherry}}$ as described before. Endogenous CHMP2A proteins were visualized using primary polyclonal anti-CHMP2A antibodies and appropriate secondary antibodies labeled with Cy5 for dSTORM imaging. Similar to the previous experiments, distinct single HIV-1 budding sites and compact CHMP2A protein assemblies were detected at the membrane by TIRFM imaging. The latter could again be categorized into clusters that colocalized with the virus buds and those that did not (Figure 4.13A). Overall, 2.0 % of all HIV-1 assembly sited colocalized with CHMP2A. This value is comparable to the colocalization rate found for Tsg101 (1.8 %) and CHMP4B-HA (1.5 %) but slightly smaller than for ALIX (3.4 %). As illustrated with the example shown in Figure 4.13B, 24 CHMP2A clusters colocalizing with HIV-1 assembly sites (Figure 4.13B, left panel) appeared as circular, condensed spots in super-resolution dSTORM images (Figure 4.13B, right panel). Their size distribution (FWHM) ranged from 38 to 82 nm with an average value of 56 ± 12 nm (Figure 4.13C). These values are in good agreement with the size of CHMP2 structures found in *in vitro* EM images by Effantin *et al.* [239], who measured an average diameter of approximately 50 nm. Analysis of non-colocalizing CHMP2A clusters revealed a broader size distribution than determined from the colocalizing structures ranging from 36 nm up to 138 nm (Figure 4.13D) with a mean size of 59 ± 20 nm. As observed before, the disappearance of the cluster size limit in the case of non-colocalizing CHMP2A suggests that the size of colocalizing clusters is potentially restricted by the dimensions of a surrounding structure.

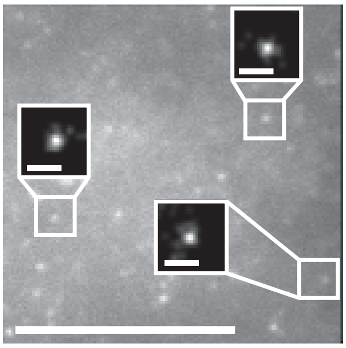

Figure 4.14: Negative control for CHMP2A super-resolution imaging. An untransfected HeLa cell was immunostained with anti-CHMP2A primary antibodies plus labeled secondary antibodies binding to the anti-CHMP2A primary antibodies and imaged using TIRFM. Zoomed-in insets show drift-corrected super-resolution dSTORM images of the respective clusters highlighted in the TIRF image. Scale bars: 10 µm (large image), 200 nm (insets).

dSTORM images of CHMP2A in a control experiment, where untransfected HeLa cells were immunostained as described above, showed condensed, circular structures at the cell membrane (Figure 4.14). They resembled those found at the plasma membrane of transfected cells and suggest that CHMP2A, similar to the other analyzed proteins, fulfills functions at the cell membrane that go beyond support of viral budding.

4.3.4 Super-resolution imaging of YFP-tagged Tsg101 at HIV-1 assembly sites

The diameters that were found for ESCRT clusters colocalizing with HIV-1 assembly sites differ significantly from the results presented by van Engelenburg *et al.* [210]. They are also smaller than diameters of approximately 100 nm, which were measured by Bleck *et al.* for different ESCRT protein assemblies at HIV-1 budding sites [209]. Although the deviations to the latter can also be explained by the fact that Bleck *et al.* used Ripley's analysis for cluster size estimation, the differences might also be a result of the respective experimental conditions especially when they are compared to the results of van Engelenburg *et al.*: whereas (with the exception of CHMP4B-HA) endogenous proteins were analyzed in this study, the studies cited above employed ESCRT protein variants that were tagged with fluorescent proteins. In order to set the experiments performed in this work in context to other works using FP-tagged versions, a control experiment was performed where a FP-tagged variant of Tsg101 was expressed together with the full viral construct ($\mathrm{HIV^{mCherry}}$) or labeled Gag alone (Gag:Gag.mCherry). The latter was necessary as other works did not use the full viral construct as done here but fluorescently labeled Gag molecules alone. Therefore, experiments with Gag alone were also performed to make the results as comparable as possible.

TIRFM imaging of HeLa cells co-transfected with a YFP-Tsg101 fusion construct and pCHIV: $\mathrm{pCHIV^{mCherry}}$ (1:1) revealed single virus budding sites as well as YFP-Tsg101 assemblies that could be detected both by their YFP-tag as well as by anti-Tsg101 antibodies (Figure 4.15A), which were also used for super-resolution imaging of endogenous Tsg101 (Section 4.3.3.1). Over 60 % of the YFP-Tsg101 complexes were also detected by the antibody, giving further evidence for the specificity of the applied combination of primary and secondary antibody. However, a colocalization rate of 18 % between $\mathrm{HIV^{mCherry}}$ and YFP-Tsg101 was detected in the overlay of TIRF images of HIV-1 buds (magenta) and of Tsg101 clusters (green) in Figure 4.15B. This was an increase by a factor of 10 compared to a the colocalization rate of 1.8 % that had been found for $\mathrm{HIV^{mCherry}}$ clusters colocalizing with endogenous Tsg101. In contrast to this discrepancy, the super-resolution images of YFP-Tsg101 assemblies at HIV-1 budding sites revealed similar circular, condensed structures (Figure 4.15C) as found before. The size distribution did not vary significantly in comparison to endogenous Tsg101 assemblies with cluster sizes by means of the FWHM ranging from 35 to 100 nm and a mean diameter of 60 ± 19 nm (Figure 4.15D).

The increase in the number of colocalizing structures was even stronger when Gag and Gag.mCherry were used in an equimolar ratio instead of the full viral construct. In this case, up to 30 % of Gag assemblies colocalized with Tsg101, which means an increase by more than a factor of 10 (Figure 4.15E and F) compared to the percentage of $\mathrm{HIV^{mCherry}}$ colocalizing with endogenous Tsg101. As expected, the structures of Tsg101 at Gag-assembly sites revealed by dSTORM imaging (Figure 4.15G) as well as the size distribution (Figure 4.15H) resembles those found for the other experiments. Thus, 55 colocalizations were found with sizes ranging from 40 up to 100 nm with an average size of 60 ± 10 nm.

Although these results give reasonable evidence that changes in the dynamics of the ESCRT interaction caused by the protein tag induce the increase in colocalization, the possibility that the higher fraction of colocalizations is due to better accessibility of the antibody epitope in the FP-Tsg101 clusters cannot be totally ruled out. Although the protein might still be functional in this case, the FP tag would undeniably have an effect on structure and conformation of Tsg101 that does not conform to the endogenous protein. This system would therefore certainly not allow any significant statements about the behavior of endogenous Tsg101 at HIV-1 budding sites as well.

It might also be possible that the increase in colocalization is an artifact of the overexpression of Tsg101. In order to rule out this possibility, an analogue control experiment was performed, where HeLa cells were transiently transfected with pCHIV:$\mathrm{pCHIV^{mCherry}}$ (1:1) (Figure 4.16A,

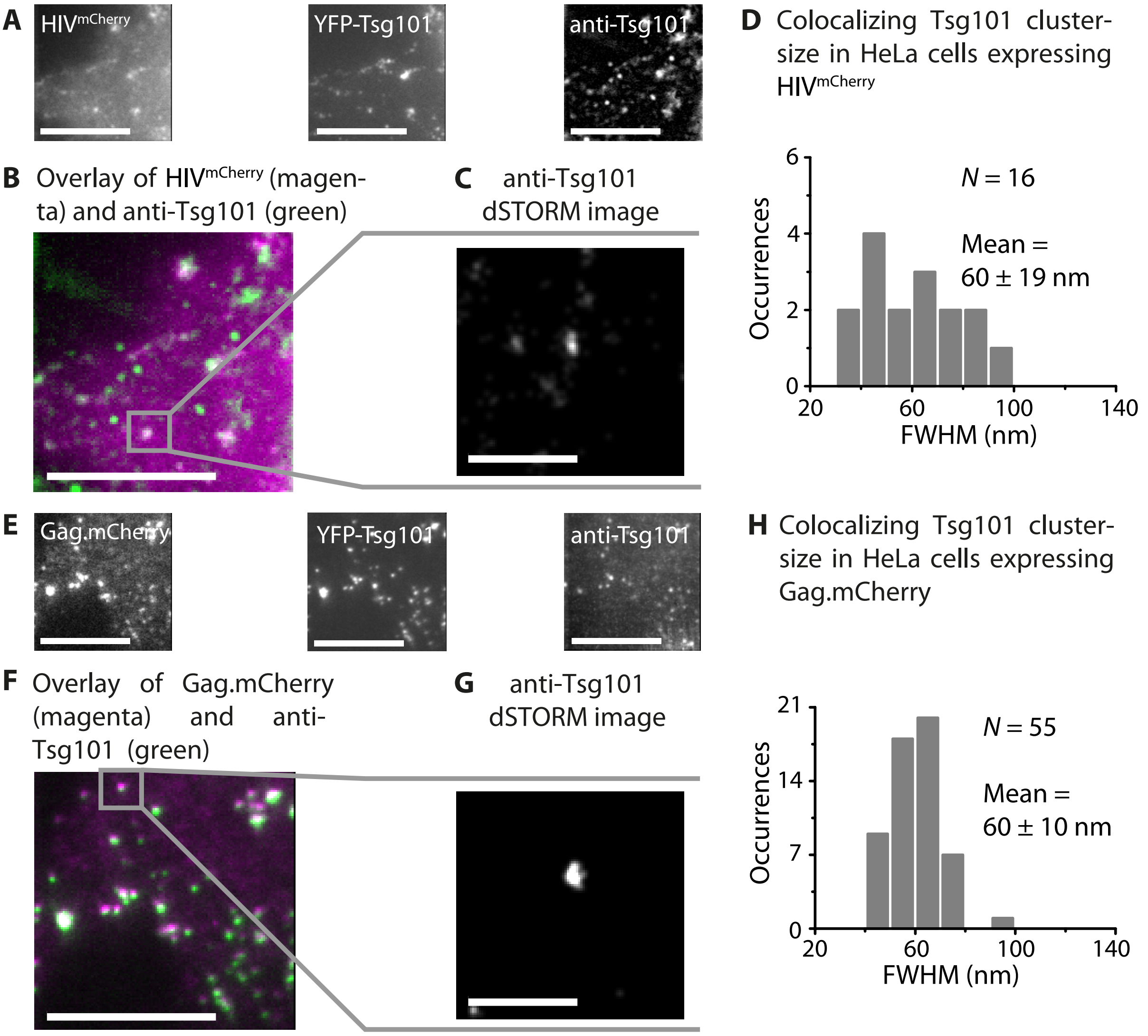

Figure 4.15: Effect of a FP tag on Tsg101 clustering during HIV-1 budding. (A) A HeLa cell expressing the ESCRT fusion protein YFP-Tsg101 and HIV$^{\text{mCherry}}$. Signals from the HIV$^{\text{mCherry}}$ channel (*left panel*), YFP channel (*middle panel*) and an average, drift-corrected time projection of the immunostained Tsg101 signal acquired for dSTORM imaging (*right panel*) are shown. Scale bars: 10 µm. (B) The overlay of the TIRF images of HIV$^{\text{mCherry}}$ (magenta) and immunostained YFP-Tsg101 (green) reveals colocalizing and non-colocalizing YFP-Tsg101 clusters. Scale bar: 10 µm. (C) A dSTORM image of the small, condensed YFP-Tsg101 structure highlighted in the left panel in gray. Scale bar: 500 nm. (D) The size distribution of immunostained YFP-Tsg101 clusters colocalizing with HIV$^{\text{mCherry}}$ with an average size (FWHM) of 60 ± 19 nm. (E) A HeLa cell expressing the ESCRT fusion protein YFP-Tsg101 and Gag:Gag.mCherry. Signals from the Gag:Gag.mCherry channel (*left panel*), YFP channel (*middle panel*) and a drift-corrected time projection of the immunostained Tsg101 signal (*right panel*) are shown. Scale bars: 10 µm. (F) The overlay of the TIRF images of Gag.mCherry (magenta) and immunostained YFP-Tsg101 (green) reveals colocalizing and non-colocalizing YFP-Tsg101 clusters. Scale bar: 10 µm. (G) A dSTORM image of the condensed, circular Tsg101 structure highlighted in the middle panel in gray. Scale bar: 500 nm. (H) The size distribution of immunostained YFP-Tsg101 clusters colocalizing with Gag.mCherry is shown with an average size (FWHM) of 60 ± 10 nm. N represents the number of events contributing to the respective histogram.

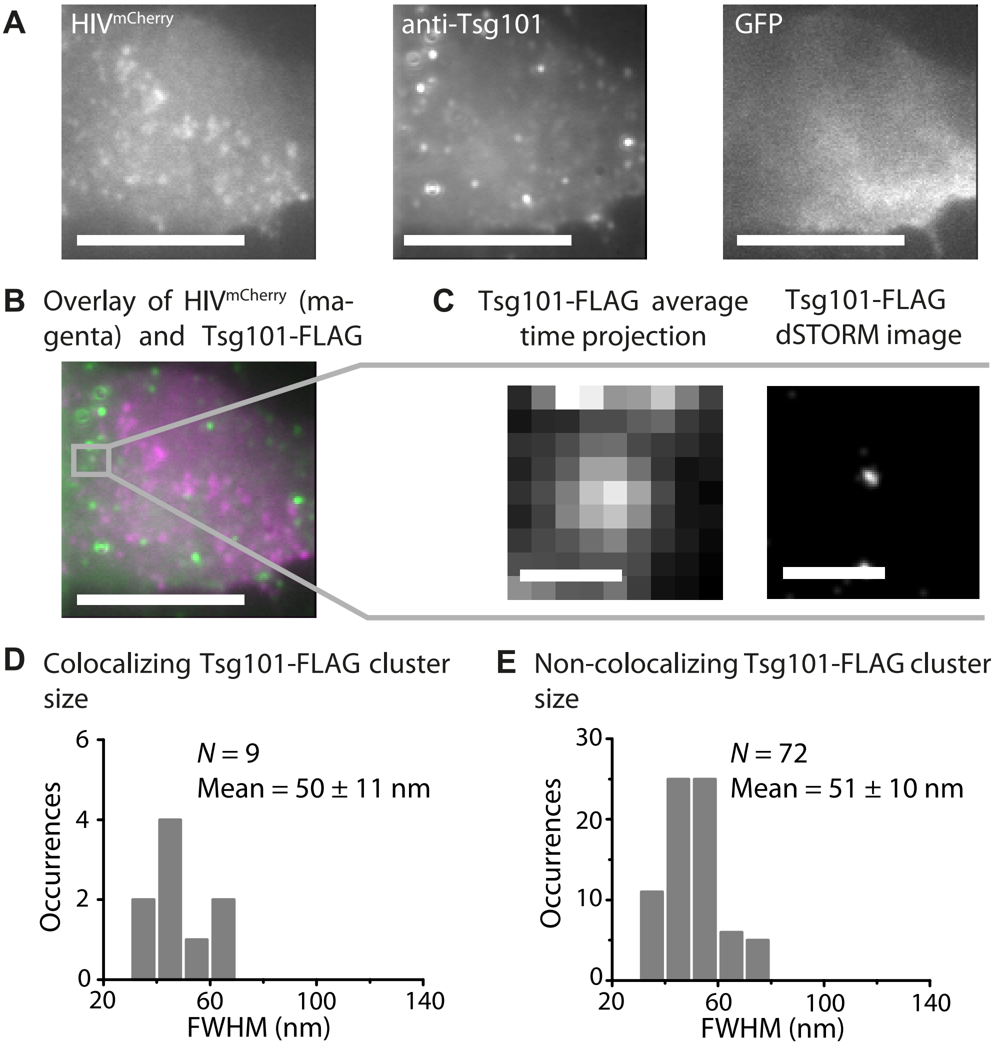

Figure 4.16: Effect of overexpression of Tsg101-FLAG-IRES-GFP on HIV-1 budding. (A) Imaging of a HeLa cell expressing both Tsg101-FLAG-IRES-GFP and $\mathrm{HIV}^{\mathrm{mCherry}}$ shows a TIRF image of $\mathrm{HIV}^{\mathrm{mCherry}}$ (*left panel*), a time-projected TIRF image of immunostained Tsg101-FLAG (*middle panel*) and a widefield image of GFP (*right panel*). Scale bars: 10 µm. (B) The overlay of the TIRF images of immunostained Tsg101-FLAG (green) and $\mathrm{HIV}^{\mathrm{mCherry}}$ (magenta). Scale bar: 10 µm. (C) *Left panel.* A zoomed-in image of the selected Tsg101-FLAG cluster highlighted in gray in the left panel colocalizing with $\mathrm{HIV}^{\mathrm{mCherry}}$. *Right panel.* The corresponding drift-corrected dSTORM image of the Tsg101-FLAG cluster. Scale bars: 500 nm. (D) The size distribution of all Tsg101-FLAG structures colocalizing with $\mathrm{HIV}^{\mathrm{mCherry}}$ with an average cluster size (FWHM) of 50 ± 11 nm. (E) The size distribution of all non-colocalizing Tsg101-FLAG clusters in cells co-expressing $\mathrm{HIV}^{\mathrm{mCherry}}$ (wildtype) with an average cluster size (FWHM) of 51 ± 10 nm. N represents the number of events contributing to the respective histogram.

left panel) and Tsg101-FLAG-IRES-GFP. It has been shown that – in contrast to FP – the relatively small FLAG-tag has only minor influence on HIV-1 budding [240]. In order to identify cells that express the construct, IRES-GFP was introduced, where IRES stands for internal ribosomal entry site. IRES describes a specific folding on the mRNA that allows the expression of two proteins using the same mRNA [241]. Thus, it was ensured that every cell that expresses unlabeled Tsg101-FLAG (Figure 4.16A, middle panel) also expresses GFP as a marker (Figure 4.16A, right panel). Figure 4.16B shows an overlay of the TIRF images of $\text{HIV}^{\text{mCherry}}$ and Tsg101-FLAG immunostained with anti-Tsg101 antibodies and appropriate secondary antibodies in a cell expressing all involved constructs. The colocalization rate appeared lower than for YFP-Tsg101. Super-resolution imaging of colocalizing Tsg101-FLAG clusters (as shown in the example in Figure 4.16C) revealed closed, condensed structures as observed before for endogenous Tsg101. In fact, after analysis of 4 cells, the obtained value was 2.9 % of HIV-1 buds colocalizing with the Tsg101-FLAG clusters similar to that of endogenous Tsg101 (1.8 %). The same observation was made for the size distributions of both colocalizing (Figure 4.16D) and non-colocalizing (Figure 4.16E) Tsg101 clusters, which also resembled those of endogenous Tsg101 with average cluster diameters of 50 ± 11 nm and 51 ± 10 nm, respectively.

In summary, overexpression did not have a considerable effect on Tsg101 functioning compared to the endogenous expression level. Therefore, it can be stated that the increased colocalization rate of HIV-1 assembly sites with YFP-Tsg101 compared to endogenous Tsg101 was indeed an effect of the FP tag.

4.3.5 Effect of a dominant-negative VPS4 mutant on ESCRT structures

As described before, Cashikar *et al.* [203] observed 110 nm broad ESCRT-III spirals encircling nascent virus buds in VPS4-depleted cells. These diameters were larger than those observed in this study. Therefore, in order to clarify whether this difference is a result of VPS4 depletion, an additional control experiment was performed. A dominant-negative mCherry-tagged mutant of VPS4 (VPS4A-E228Q-mCherry, Figure 4.17A, left panel) was co-expressed with Gag.eGFP (Figure 4.17A, middle panel) and unlabeled Gag. Expression of a dominant-negative form of VPS4 should effectively block virus budding and lead to an increase in colocalizations of ESCRT structures with Gag assemblies. For visualization of ESCRT, CHMP2A was immunostained (Figure 4.17A, right panel) as described in Section 4.3.3.4. CHMP4B-HA might have been an alternative option, especially with regard to the observation of the large filamentous structures by Cashikar *et al.* A successful reproduction of this experiment would give clear evidence for the effect of VPS4 depletion. However, this experiment required the co-expression of four different plasmids, which could not be achieved successfully.

Figure 4.17B shows the overlay of the TIRF images of HIV^{eGFP} (magenta) and of the average, drift-corrected time projection of immunostained CHMP2A (green) in a HeLa cell expressing also VPS4A-E228Q-mCherry. Again, colocalizing and non-colocalizing structures could be identified and colocalizing structures could be selected (Figure 4.17C, left panel). Super-resolution dSTORM images of these structures revealed circular, dense structures (Figure 4.17C, right panel). In contrast to the experiment without the VPS4 mutant however, the size of the CHMP2A structures by means of the FWHM (Figure 4.17D) was not limited to the expected size of the bud neck but could reach diameters up to $\sim$ 160 nm. A similar distribution was observed for non-colocalizing CHMP2A structures (Figure 4.17E). As expected, the amount of Gag assemblies colocalizing with CHMP2A increased from 2.0 % in the case of wildtype VPS4 up to 8.5 %. The increase is not as significant as it was observed for the FP-tagged ESCRT version. However, the expression rate of the respective plasmid has to be considered. If it is

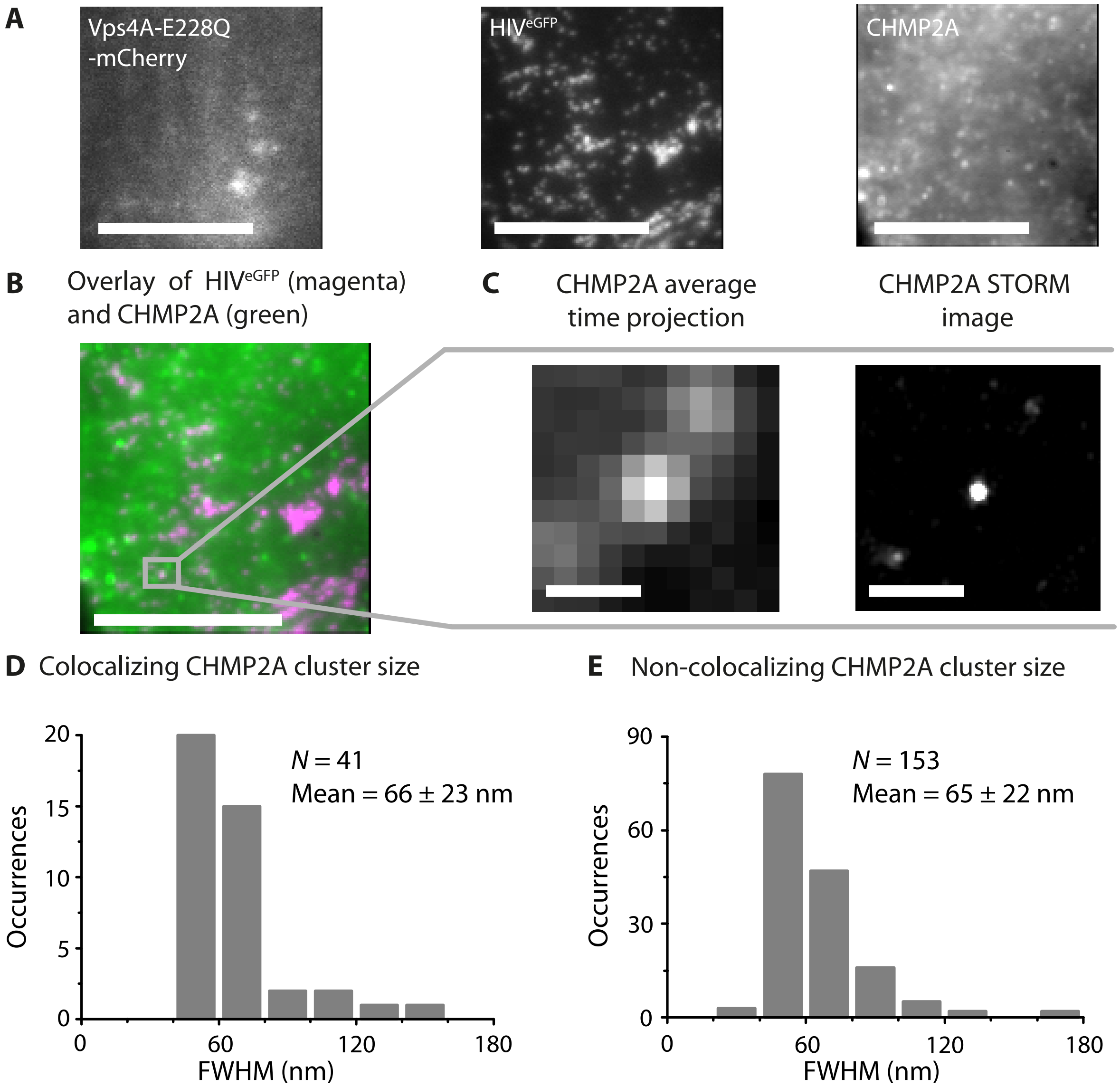

Figure 4.17: Super-resolution imaging of CHMP2A in HeLa cells expressing a dominant-negative VPS4 mutant and pCHIV$^{\text{eGFP}}$:pCHIV (1:1). (A) TIRF images of (*left panel*) the VPS4A mutant VPS4A-E228Q-mCherry, (*middle panel*) HIV$^{\text{eGFP}}$ and (*right panel*) the average, drift-corrected time projection of TIRF images of immunostained CHMP2A acquired for dSTORM imaging. Scale bars: 10 µm. (B) Overlay of TIRF images of immunostained CHMP2A (green) and HIV$^{\text{eGFP}}$ (magenta). Scale bar: 10 µm. (C) *Left panel.* A zoomed-in image of the selected CHMP2A cluster highlighted in gray in B colocalizing with an HIV-1 assembly site. *Right panel.* The corresponding drift-corrected dSTORM image of the CHMP2A cluster. Scale bars: 500 nm. (D) The size distribution of all CHMP2A structures in cells expressing the dominant-negative VPS4A-E228Q-mCherry mutant colocalizing with HIV$^{\text{mCherry}}$ is shown. The average cluster size (FWHM) is 66 ± 23 nm. (E) The size distribution of all non-colocalizing CHMP2A clusters in cells co-expressing HIV$^{\text{eGFP}}$ (wildtype) and VPS4A-E228Q-mCherry is plotted with an average cluster size (FWHM) of 65 ± 22 nm. *N* represents the number of events contributing to the respective histogram.

relatively low, endogenous VPS4 might still be active and reduce the effect of the dominant-negative mutant. Nevertheless, the observed change depending on the expression of the mutant was still significant and supported the results of Cashikar *et al.*.

4.3.6 Relative orientation of ESCRT with respect to HIV-1

So far, TIRF images of ESCRT structures were overlaid with TIRF images of HIV-1 assembly sites to identify colocalizing structures and active budding sites. Separate super-resolution experiments were performed for the determination of the average sizes of virus buds and ESCRT clusters, respectively. Although this approach was straightforward and allowed a comparison of the relative difference in sizes between the structures, it did not reveal the relative orientation of the ESCRT cluster with respect to the virus bud, which would give more detailed information about the geometry of the budding complex, which might help to differentiate between Models 2 and 3 (cf. Figure 4.4). Whereas Model 2 would not cause any restrictions regarding possible geometries, a central position of the ESCRT structure relative to the budding site should be expected in the case of Model 3 where ESCRT is assembling with an isotropic distribution within the bud.

4.3.6.1 Dual-color super-resolution imaging of ESCRT and HIV-1 budding sites

The most elegant approach to realize this would be a dual-color super-resolution experiment, which in this case meant a combination of STORM and PALM where the first method was used to image ESCRT and the second one for the HIV-1 assembly sites. HeLa cells were cotransfected with pCHMP4B-HA and pCHIV:pCHIV$^{\mathrm{mEos}}$ (1:1) for this purpose and subsequently imaged with the respective method.

These experiments have however emerged to be technically challenging due to the overlap of spectral parts that are required for activation or imaging of the involved fluorophores. For example, a laser pulse at a wavelength of 405 nm that would photoconvert mEosFP would at the same time also activate Cy5 [54]. The latter is furthermore excitable at 561 nm, which means that imaging of mEosFP at this wavelength would simultaneously bleach Cy5. STORM imaging before PALM creates a similar problem: wavelengths in the green part of the electromagnetic spectrum that are usually used for activation of Cy5 also excite the blue state of mEosFP and would therefore lead to unwanted photobleaching as well. Due to these reasons, only one colocalization was found in the overlay of the TIRF images (Figure 4.18A) in many analyzed cells expressing both HIV$^{\mathrm{mEos}}$ and CHMP4B-HA, where statistics allowed the reconstruction of super-resolution images for both constructs. The obtained images are shown in Figure 4.18B: whereas the overlay of the TIRF images obviously does not display any difference in size between both structures, the overlay of the STORM and PALM images in the lower part of the panel clearly reveals that the spot-like CHMP4B-HA cluster was situated on the rim of the larger HIV-1 bud, rather than in the center. Sizes estimated by means of the FWHM gave a diameter of 57 nm for the CHMP4B-HA cluster and of 133 nm for the virus bud, respectively (Figure 4.18C). These values were in agreement with the results obtained by the single-color experiments with HIV$^{\mathrm{mEos}}$ (116 ± 36 nm) and CHMP4B-HA (56 ± 12 nm).

Certainly, a single observation alone does not allow any significant statement to be made but it nevertheless demonstrated that combined STORM and PALM experiments are a promising method for further super-resolution studies of the ESCRT machinery under the premise that the efficiency of the dual-color experiments can be increased. One solution might be to use

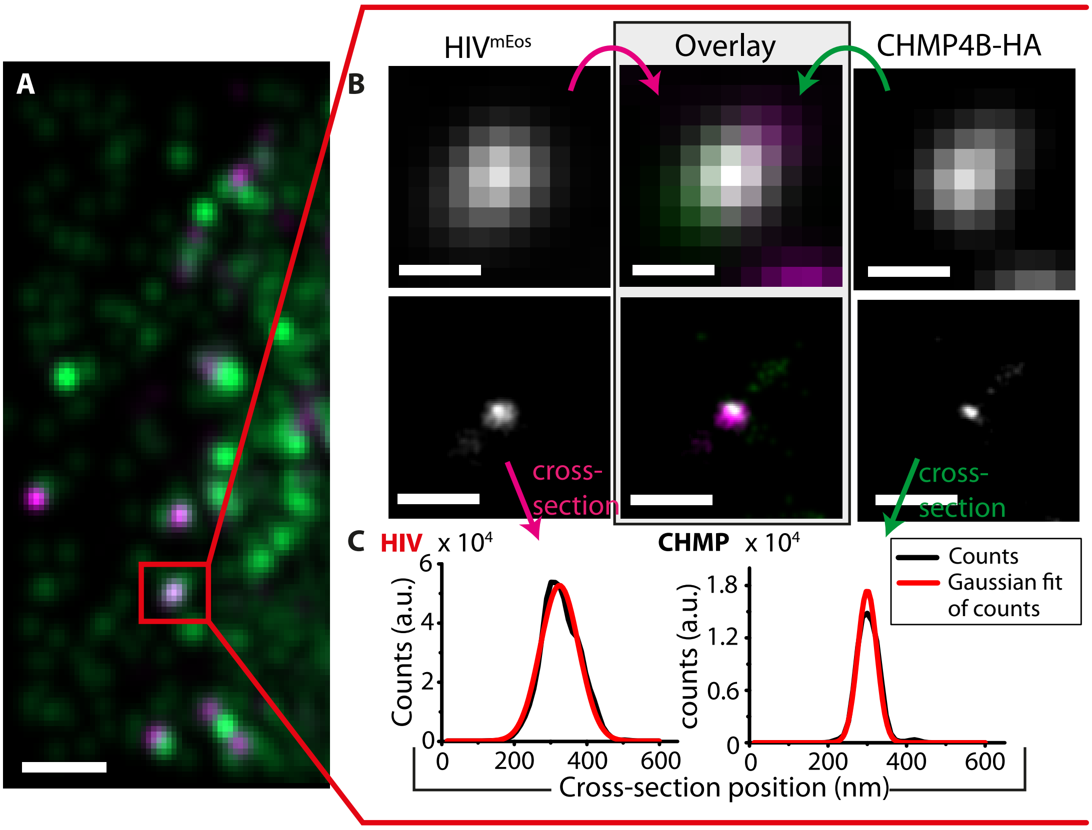

Figure 4.18: Dual-color super-resolution imaging of CHMP4B-HA and HIV-Gag. (A) Overlay of the drift-corrected, average time projections of independent TIRFM image series for HIV$^{\text{mEos}}$ and CHMP4B-HA (magenta: HIV$^{\text{mEos}}$, green: CHMP4B-HA). Scale bar: 2 µm. (B) A zoomed-in image of the single colocalizing structure (*upper panels*) and corresponding super-resolution PALM (HIV$^{\text{mEos}}$) or STORM (CHMP4B-HA) images, respectively (*lower panels*). Scale bars: 500 nm. (C) The Gaussian fit of cross-section profiles through the respective PALM/STORM images yielding a FWHM of 133 nm for HIV$^{\text{mEos}}$ (*left panel*) and 57 nm for CHMP4B-HA cluster (*right panel*).

other dyes where no such cross-interactions occur as described above. Alternatively, image acquisition could be modified in a way that allows simultaneous detection of both STORM and PALM signals, for example, in two separate detection pathways.

4.3.6.2 Determination of relative orientation by overlaying widefield and super-resolution images

As dual-color super-resolution experiments did not bring enough statistics, an alternative analysis was applied, where the super-resolution images of ESCRT clusters were overlaid with the diffraction-limited TIRF images of the virus bud (Figure 4.19). Although the size of the virus bud is below the resolution limit, its actual size is not that much smaller. For this reason, a rough estimate about the orientation of the ESCRT proteins and ALIX with respect to the viral particle by this method seems justifiable. The examples in Figure 4.19 showed that ESCRT and ALIX clusters were, in most cases, not located in the center of the viral bud but rather shifted towards the edge confirming the observation from the dual-color super-resolution experiment.

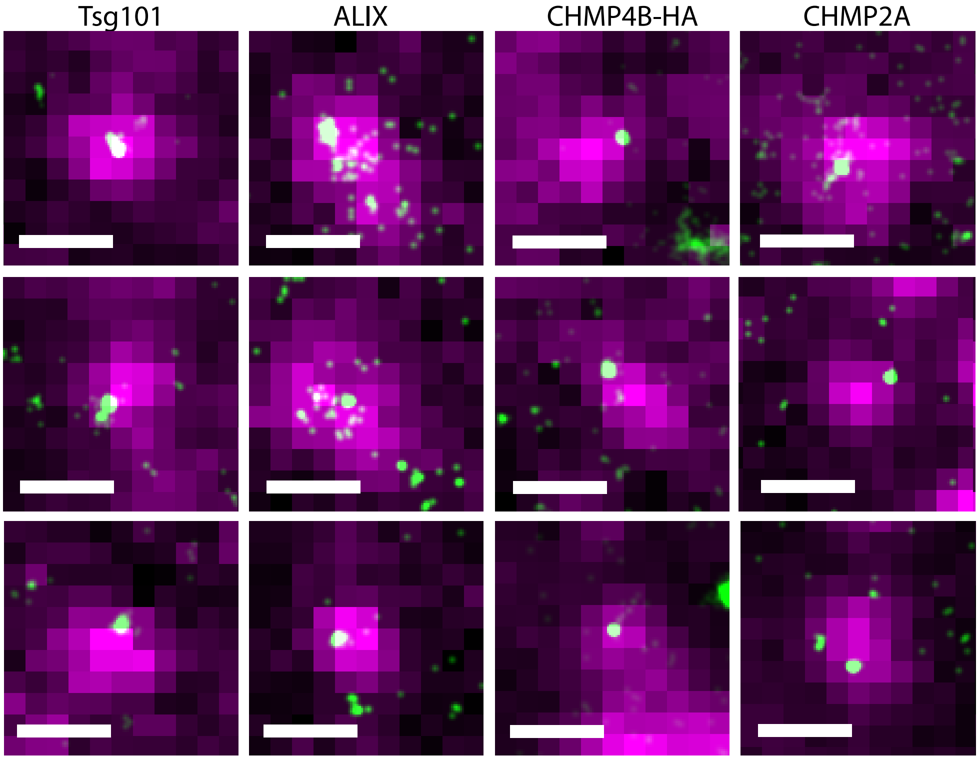

Figure 4.19: Position of ESCRT proteins relative to the bud. Overlays of super-resolution images of ALIX and ESCRT proteins Tsg101, CHMP4B-HA and CHMP2A (green) with the corresponding TIRF images of the respective evolving HIV-1 buds (magenta) reveal the relative position of the ESCRT protein cluster relative to the viral bud. Scale bars: 500 nm.

This is also in agreement with experiments by Bleck *et al.* [209] who co-expressed Gag alone with FP-tagged ESCRT proteins and observed that the latter were significantly shifted with respect to the Gag assembly site at the membrane. Furthermore, the orientation of the cloud-like structures in the case of ALIX showed an apparent overlap with the virus bud, which further supports ALIX being incorporated into the virus. However, as the virus bud images were diffraction-limited, one has to be careful with respect to a definitive statement in this particular case.

4.4 Discussion

The main aim of this study was to distinguish between the three different models for the ESCRT-mediated membrane constriction mechanism, which were presented in Figure 4.4B. For this purpose, super-resolution imaging of ESCRT proteins Tsg101, CHMP4B and CHMP2A as well as of the ESCRT-related protein ALIX at HIV-1 budding sites were performed together with super-resolution imaging of HIV-1 budding sites alone. The focus of the study was kept on keeping the environmental conditions of the experiments as close as possible to the endogenous conditions, which included immunostaining of the endogenous protein in contrast to FP-tagged versions as it was the case in previous studies. Only in the case of CHMP4B, a tagged version had to be used but it could be shown that this small HA-tag did not affect the protein in a critical way.

Major experimental support for an external restriction model (Model 1 in Figure 4.4B) was provided by Cashikar *et al.* [203] who analyzed endogenous ESCRT proteins in VPS4 depleted cells using deep-etch electron microscopy. Under these conditions, they found relatively large, flat rings or conical spirals with an average diameter of $108 \pm 30\,\text{nm}$. These structures surrounded either a central membrane protrusion of $\sim 50\,\text{nm}$ diameter or Gag assembly sites. In contrast to these results, none of the ESCRT or ALIX structures that were analyzed during the course of this study that colocalized with HIV-1 budding sites showed a diameter larger than 100 nm. Super-resolution imaging of ESCRT structures colocalizing with $\text{HIV}^{\text{mCherry}}$ budding sites, appeared throughout as small, condensed, circular structures whose sizes were significantly smaller than the value that was obtained for the average size of HIV-1 budding sites (Table 4.1). Larger sizes were only observed for non-colocalizing structures, which suggests that the size of colocalizing ESCRT structures might be restricted by a viral structure, which might either be the neck or the complete bud. In the latter case, one might also expect larger structure up to the size of the virus bud than the values that were measured here. However, eGFP.Vpr clusters detected in virus buds did not bring significantly larger sizes than measured for the ESCRT proteins at HIV-1 budding sites. The non-colocalizing structures were most likely linked to other cellular processes such as exosome activity. In order to test whether the differences compared to the results of Cashikar *et al.* were caused by VPS4 depletion, CHMP2A was measured in the presence of a dominant-negative VPS4-mutant as shown in Section 4.3.3.4 and Figure 4.17. As described before, the number of colocalizations increased slightly compared to experiments with wildtype VPS4 and some colocalizing clusters showed larger diameters than 100 nm in this case. This result indicates that VPS4 depletion indeed has an effect on the apparent size of ESCRT protein assemblies at HIV-1 budding sites although the measured structure sizes were not as large as those detected by Cashikar *et al.* This can contributed to the fact that they observed CHMP4 lattices in contrast to CHMP2A, which rather builds a cap to the ESCRT structure instead of the large filamentous structures observed for CHMP4. The fact that the increase in size was not as explicit as it was the case in Cashikar *et al.* might also be ascribed to the different sample preparation protocols for fluorescence and electron microscopy, respectively.

Overall, the fact that no larger ESCRT structures were observed in all experiments with non-arrested budding and endogenous ESCRT proteins or versions with a relatively small HA-tag, is another strong evidence that supports an internal constriction mechanism. This implicates that the majority of the components that form the ESCRT machinery are situated close to or within the HIV-1 budding neck [194, 201] or within the bud [210] rather then on the flat part of the cell membrane outside the neck. The remaining question was whether membrane constriction occurs from within the bud (Model 3 in Figure 4.4B) or whether ESCRT assembles within the neck of the bud (Model 2 in Figure 4.4B).

Model 3 was supported by a study from van Engelenburg *et al.* [210] who detected ESCRT protein clusters inside the Gag shell using three-dimensional iPALM imaging. The main differences in experimental design can be found in the use of Gag protein alone in contrast to a full virus construct and in the use of FP-tagged versions of ESCRT proteins instead of immunostaining of the endogenous proteins as done in this study most of the cases.

Experiments with a YFP-tagged version of Tsg101 in comparison with results obtained for endogenous Tsg101 showed a clear sensitivity of ESCRT proteins towards larger tags that manifested itself particularly in the deviating number of virus buds colocalizing with ESCRT. These results showed that ESCRT factors can react very sensitive to the attachment of large additional tags, which can have a significant influence on the structure of the assembled ESCRT complex [196, 203] and its functionality [166]. The significantly lower number of colocalizations in the case of endogenous Tsg101, which was on the same order of magnitude as for ALIX, CHMP4B-HA and CHMP2A, is in accordance with the transient interaction of ESCRT proteins

Table 4.1: Summary of results for analyzed ESCRT proteins Tsg101, CHMP4B and CHMP2A and ESCRT-related protein ALEX regarding number of analyzed cells, cluster and colocalization events and appearance of cloud-like structures. Sizes are given by means of the FWHM except for the size of cloud-like structures, which were obtained using the Ripley's L-function.

	Tsg101 + $HIV^{mCherry}$	ALIX + $HIV^{mCherry}$	CHMP4B-HA + $HIV^{mCherry}$	CHMP2A + $HIV^{mCherry}$	YFP-Tsg101 + $HIV^{mCherry}$	YFP-Tsg101 + Gag.mCherry	Tsg101 + $HIV^{mCherry}$ (late -)	CHMP4B-HA + $HIV^{mCherry}$ (late -)
Number of experiments	3	4	11	4	1	1	2	2
Number of analyzed cells	14	10	23	17	2	4	6	5
Number of detected HIV-1 buds	1052	529	1662	1128	87	194	210	235
HIV-1 buds colocalizing with ESCRT	1.8 %	3.4 %	1.5 %	2.0 %	18.3 %	29.5 %	0.0 %	0.4 %
Avg. colocalization cluster size (nm)	58 ± 7.1	64 ± 18	56 ± 12	56 ± 12	60 ± 19	60 ± 10	-	47
Protein clusters total	221	115	306	262	70	146	83	36
Protein clusters colocalizing with HIV-1 budding site	18	17	23	24	16	55	0	1
Protein clusters not colocalizing with HIV-1 budding site	203	98	283	238	54	91	83	35
Protein clusters enclosed by cloud	0	13	0	0	0	0	0	0
Size of cloud (nm)	-	164 ± 31	-	-	-	-	-	-

[168, 211] with nascent assembly sites. The process occurs on the time scale of a few minutes and is expected to lead to the low percentage of colocalizations. An increase is seen as an unnatural behavior induced by modifications of the proteins. Additional control experiments explicitly showed that this effect was not a result of overexpression but of the FP tag. Regarding the use of Gag alone instead of the full viral context, no significant difference between the cluster sizes of colocalizing YFP-Tsg101 with Gag.mCherry (60 ± 10 nm), $\mathrm{HIV}^{\mathrm{mCherry}}$ (60 ± 19 nm) and endogenous Tsg101 colocalizing with $\mathrm{HIV}^{\mathrm{mCherry}}$ (58 ± 7.1 nm) could be detected (Table 4.1). Therefore, the lack of the full viral context was apparently not as influential as the modification of the ESCRT proteins.

Although these results give evidence for an effect of the FP tag, which caused a deviation form physiological behavior, further clarification was necessary to distinguish between Models 2 and 3. For this purpose, the position of ESCRT complexes relative to the HIV-1 particle was analyzed (Section 4.3.6). Although the resolution in the case of HIV-1 budding sites was limited, ESCRT clusters were often observed rather on the edge of the virus bud instead of in the center. This observation is in agreement with experiments by Bleck *et al.* [209] who expressed Gag alone with FP-tagged ESCRT proteins and observed significant shifts of the ESCRT proteins with respect to the Gag assembly. These observations are difficult to harmonize with the results from van Engelenburg *et al.*. Assuming ESCRT assembling with an isotropic distribution within the bud as the probability distributions presented in the publication suggest, a central position of the ESCRT structure relative to the budding site should be expected. This observation therefore suggests a model of ESCRT proteins assembled within the neck of the nascent virus bud (Model 2). This is supported by the fact that all the sizes that were measured for colocalizing ESCRT structures were significantly smaller than the virus particle. Assuming the model presented by Engelenburg *et al.* with an integrated probability of up to 90 % for ESCRT being distributed within the entire bud, also larger structure sizes should be expected than those that were measured in this study.

Additionally, the model presented by van Engelenburg *et al.* is based on the detection of significant amounts of eGFP-Tsg101, eGFP-CHMP2A and eGFP-CHMP4B proteins inside released viral particles, which were quantified by their eGFP fluorescence intensity and by immune-gold staining of cryo-TEM images using anti-eGFP antibodies. However, other studies [166, 172] could – with the exception of ALIX [211] – only detect very low amounts of ESCRT proteins inside released viruses with western blot and mass spectrometry.

This was supported by analysis of super-resolution images of the ESCRT-related protein ALIX, which gave in some ways different results than obtained for the other proteins. In 76 % of the cases, the central ALIX cluster was surrounded by a diffuse, cloud-like structure, which were only found when colocalizing with HIV-1 buds and did not occur at all in cells that did not express HIV-1. In these cells, as well as on non-colocalizing ALIX clusters in transfected cells, only condensed spot-like clusters, similar to Tsg101, CHMP4B-HA and CHMP2A were found. The appearance of non-colocalizing clusters was expected as for all other ESCRT proteins, ALIX can assemble into clusters at the cell membrane to fulfill other cellular functions [228, 230].

The correlation of the clusters with HIV-1 budding sites suggests that ALIX molecules inside those cloud-like structures are recruited by the virus. Analysis of the cloud size using Ripley's L-function supported this interpretation by revealing a strong correlation between the diameter of the cloud and the size of nascent virus buds, which points to ALIX molecules being taken up into the evolving Gag shell. This is supported by previous reports that found evidence for ALIX molecules in released viral particles using Western Blot assays [166, 172]. Accumulation of ALIX has been further shown in live-cell experiments at the budding sites of EIAV [168]. In the case of HIV-1, results from Ku *et al.* [211] suggest, however, a lower tendency for accumulation as only 20 % of all recruited ALIX proteins were eventually found in the released viral particle. The estimate, which was performed in this study and which yielded an average number of seven

ALIX molecules in the cloud-like structure, is in agreement with a low number of incorporated particles. These results are contradictory to a model where ALIX continuously accumulates at the nascent viral particle [168]. One might expect that also Tsg101 would form these cloud-like structures as Tsg101 is recruited by the same p6-domain within Gag as ALIX [172, 177] and has also been reported to be found in virus particles released from macrophages [233]. It cannot be totally excluded that a potential Tsg101 cloud will not be visualized when the number of molecules forming it lies below the detection limit of the microscope. If both Tsg101 and ALIX were incorporated into the bud, it could be argued that the number of ALIX molecules in the bud would be relatively higher than for Tsg101, where only the number of ALIX molecules would lie above the detection threshold. The persistence of ALIX at the budding site may point to other functions of ALIX apart from recruitment of the ESCRT machinery as both are involved into recruitment of downstream ESCRT components but only ALIX showed the cloud-like structure. An additional function of ALIX is supported by *in vitro* experiments by Pires *et al.* [189] that found that ALIX can form a stabilizing scaffold for CHMP4 filaments, which assembled within the neck.

When comparing these results with the experiments performed for this study, it could be ruled out that the lack of any detected ESCRT structures in the bud apart from ALIX arose from insufficient immunostaining as the successful detection of immunostained eGFP-tagged Vpr inside the bud demonstrated (Section 4.3.2). Furthermore, the differences could not be ascribed to the achievable lateral resolution, which was approximately 40 nm (Table 4.2) and thus slightly worse than the values stated by van Engelenburg *et al.*, who report a resolution of 25 nm. However, if the ESCRT structures had a size comparable to the size of the virus bad, the achieved resolution would have been more than sufficient to measure these sizes.

In this context, it is important to state that the measured diameters of the ESCRT structures were not considerably larger than the calculated resolution of the STORM setup of about 40 nm. According to Eq. 2.10, the observed image in optical microscopy can be treated as a convolution of the object with the PSF of the system. The PSF is, in this case, represented by the localization uncertainty or resolution. As the sizes of both the PSF and the observed structures lay in the same order of magnitude, an influence of the PSF on the measured sizes had to be expected. This means that the actual size of the ESCRT structures is most likely smaller than the measured value and will therefore lie below the 60 nm and also below the 50 nm that Cashikar *et al.* calculated for the central membrane protrusions they observed [203]. A rough estimate using the achieved resolutions given in Table 4.2 and the average size of colocalizing ESCRT clusters given in Table 4.1 yielded ESCRT structure sizes of $\sim 29\,\text{nm}$ for Tsg101, $\sim 52\,\text{nm}$ for ALIX, $\sim 37\,\text{nm}$ for CHMP4B-HA and of $\sim 30\,\text{nm}$ for CHMP2A. This seems plausible as the size of the ESCRT structures would be closer to the late bud neck diameter. ALIX structures appear to be slightly larger than the other structures in this context. This effect might be due to ALIX molecules in the cloud-like structure that could not be separated from the central cluster but this very rough estimate does not allow any significant statement to be made here. In this context, it is also important to note that the size of the IgG antibodies attached to the structures will also increase the actual size of protein clusters as has already been shown at the example of dSTORM imaging of microtubules (Section 3.5). In the case of two antibodies, the additional size can go up to 20 nm (assuming a maximal length of 10 nm per IgG antibody [108]). Similar considerations have to be taken into account for PALM imaging of HIV-1 assembly sites. On the one hand, HIV-1 assemblies were significantly larger than the ESCRT structures but on the other hand, the resolution for PALM was slightly worse than for STORM (70 nm instead of 40 nm, Table 4.2) due to the lower photon yield of fluorescent proteins compared to organic dyes. A rough estimate using Eq. 2.10 yields that the actual FWHM of a HIV-1 assembly site is rather $\sim 95\,\text{nm}$ than 116 nm but this value is still significantly larger than those observed for ESCRT structures.

Overall, super-resolution imaging of ESCRT and ALIX structures at nascent HIV-1 buds gave strong evidence for a within-neck model (Model 2 in Figure 4.4) and pointed out that especially modifications such as tagging of ESCRT proteins to a large tag such as a fluorescent protein can lead to alternate budding geometries. Further evidence for Model 2 (in particular compared to Model 3) could be brought by optimization of dual-color super-resolution imaging that could give a more accurate picture of ESCRT orientation with respect to the HIV-1 bud as it was possible with the overlay of super-resolution ESCRT images with diffraction-limited images of the virus buds (Section 4.3.6.2). 3D super-resolution imaging could reveal further details about distribution of ESCRT proteins at the virus budding sites. However, this experiment remains technically challenging especially as it requires resolutions in the axial dimension better than 50 nm in order to discriminate between the neck and the bud itself. This value lies at the very edge of resolutions that have been so far achieved with astigmatism-based 3D imaging ([72, 73], Table 2.2). Other approaches, such as iPALM [70] or dual-objective STORM [68], might be alternatives worth considering as these techniques are able to provide axial resolutions below 20 nm (Table 2.2).

Table 4.2: Calculated image resolutions for different proteins measured at HIV-1 assembly sites

Protein	**STORM/PALM image resolution**		
	x **(nm)**	y **(nm)**	**Average (nm)**
Tsg101	48.1 ± 10.3	51.1 ± 11.9	49.6 ± 11.1
ALIX	36.1 ± 13.4	37.8 ± 10.3	36.9 ± 11.4
CHMP4B-HA	40.8 ± 8.4	43.6 ± 9.6	42.2 ± 9.0
CHMP2A	46.0 ± 14.2	46.9 ± 12.7	46.5 ± 13.3
HIV$^{\mathrm{mEos}}$	71.8 ± 11.7	76.6 ± 16.8	74.2 ± 14.2

Improvement in resolution in lateral dimension might be easier to realize and could help to answer the question whether the ESCRT-III filaments assemble in form of a dome or rather in a spiral-shaped structure. However, a resolution far below 40 nm is required to distinguish between these two models, which puts extremely high requirements on the stability of the super-resolution microscope, detection optics as well as on sample labeling.

Nevertheless, the results described in these chapter could demonstrate that localization-based super-resolution techniques are suitable methods to answer complex biological questions. Limitations mostly arise from sample preparation. Especially too low expression rates of plasmids or low specificity of antibodies used for immunostaining can decrease the quality of super-resolution images considerably. However, previous and future improvements and development of new labeling techniques might eventually open new possibilities to overcome these remaining challenges.

Chapter 5

Super-resolution imaging of endothelial lamellipodia structures

Reacting to changes in the environment is essential for the survival of cells no matter whether they are part of a metazoan or form a unicellular organism. In many cases, this includes the necessity to achieve active movement. As a consequence, cells have developed different mechanisms to move actively. For example, some cell types feature flagella, which allow them to perform a swimming movement. However, in the human body, only sperm cells exploit this mechanism while all other cells that are able to migrate rely on a crawling locomotion mechanism. The required force is mainly generated by different actin filament structures that have to be able to react to external stimuli to achieve directed motion, for example, toward a nutrient source. The aim of this study is to investigate changes of this actin network caused as a consequence of changes in the environment.

5.1 Introduction

Directed migration depends on many cellular and external factors. This section intends to give an introduction to cellular migration and to the factors that influence it. This includes, on the one hand, the actin cytoskeleton and its role in migration in general but, on the other hand, also the effects that environmental conditions impose on migration.

5.1.1 Actin

Together with microtubules (cf. Section 3.5) and intermediate filaments, actin filaments are a substantial part of the cellular cytoskeleton (reviewed in [242]). Actin monomers are able to build oligo- and polymeric filamentous structures that fulfill various functions in the cell from providing mechanical stability to active movement.

Actin occurs in two conformations, which are a monomeric globular form (G-actin) and a filamentous polymerized form (F-actin). The assembly and disassembly of actin filaments is a continuous functional interaction between both forms, which is regulated by a number of associated factors. The transition of G-actin to F-actin can be enhanced by binding of an adenosine nucleotide. Whereas bound adenosine diphosphate (ADP) molecules cause only minor effects, adenosine triphosphate (ATP) significantly enhances polymerization. The formation of actin-ATP can be enhanced by binding of nucleotide exchange factor profilin. Whereas profilin is able to reduce the pool of G-actin in the cell by favoring polymerization, thymosin proteins, which also bind to G-actin, have the opposite effect by holding actin monomers in a locked state that cannot associate with existing filaments. The combination of both proteins opens the possibility of a fine regulation of the G-actin pool available for filament assembly.

Initiation of filament growth is called nucleation, which depends on the interaction of monomeric actin with a variety of nucleation factors such as formin proteins or the ARP2/3 complex, which comprises the actin related proteins (ARP) 2 and 3. Actin filaments show an unidirectional growth. The end, where nucleation started is called the (-)-end or, according to its shape in SEM images, pointed end whereas the opposite end, where new actin monomers attach to the existing filament is referred to as the (+)- or barbed end. At the (-)-end, actin-ATP will eventually be hydrolyzed to actin-ADP and phosphate. Cofilin proteins are subsequently able to bind to ADP-actin and promote depolymerization in order to regain free G-actin. The simultaneous assembly of actin-filaments at the (+)-end and disassembly at the (-)-end can also be described by a treadmilling system.

Single actin filaments, which have an average diameter of about 10 nm [243] and can obtain lengths up to several micrometers, can combine and form larger structures with more complex geometries with the support of other proteins. One example is ARP2/3, which can attach to existing filaments and serve as a core for new polymerization. By this means, branched filaments can be generated, which can form dendritic networks.

Single filaments can further be incorporated into larger bundles or fibers. For this purpose, distinct filaments are interconnected by linker proteins, which determine the characteristics of the resulting bundle. Filaments might be, for example, either connected by relatively short fimbrin proteins, which results in a stiff bundle, or by α-actinin, which allows incorporation of myosin II motor proteins. These motor proteins give the fiber a high flexibility allowing active contraction or stretching. Other linker proteins such as filamin or spectrin allow the formation of dense three-dimensional networks or gels.

The huge versatility of the different organization forms of actin filaments allows actin to fulfill a number of various functions in the cell from which the following list intends to select only the most important ones. One aspect includes support of cellular migration, which will be discussed in detail in the next sections. Actin, however, further increases mechanical stability by building a fine meshwork of filaments below the lipid membrane, which is referred to as cellular cortex [244]. Like microtubules, actin can also support directed transport of cargo molecules through the cell using myosin motor proteins. Actin-mediated transport is typically used for short range transport whereas long-range transport is usually performed over microtubule structures [245]. Due to the high contractibility of actin-myosin complexes, they are not only involved in cell migration but also in other kinds of cellular movement such as the contraction of muscle cells [246, 247]. Furthermore, actin can also be found in the nucleus. Although this question was disputed for a long time, evidence has been found that actin monomers and short filaments play a role, for example, in chromatin-remodeling complexes and in the RNA polymerase machinery [248]. However, it is not clear whether actin also forms longer filaments in the nucleus [249, 250].

5.1.2 Cellular migration and lamellipodia

Cell migration is an indispensable mechanism in the life cycle of both uni- and multicellular organisms [251]. It is, for example, essential for unicellular organisms to move actively towards a nutrient source [252]. For multicellular species, the migration of single cells plays an important role in processes such as reproduction, tissue formation or organization of the immune response [253]. Cells can use different techniques to achieve locomotion. One option is flagella, which are long protrusions of cells formed by microtubule bundles that can be moved by dynesin motor proteins [254]. Other migrating cells show a crawling movement driven mainly by actin filaments. As reviewed in [251], this type of movement requires a substrate to which the respective cells can attach such as the extracellular matrix (ECM). In order to generate the necessary force to crawl over such a substrate, the migration process can be categorized into three different steps: first, protrusions have to be formed that push the membrane walls into the direction of migration. Second, new adhesions spots have to be formed in the front part of the cell. Third, traction has to be built up to pull the cell into the respective direction.

The focus of this chapter is on the first step comprising the development of membrane protrusions. The latter are formed by a dense network of actin filaments. This meshwork can either take one-dimensional forms, which are called filopodia, build two-dimensional flat networks called lamellipodia or three-dimensional blebs or pseudopodia.

The directed growth and coordinated motion of a cell requires fine regulation of cell polarity, which is controlled by a variety of proteins. Three GTPase proteins, which are members of the Rho protein family and are termed Rac, Cdc42 and Rho, stand in the center of interest [255–257]. Migration is usually stimulated by an external signal, which can be a nutrient source or other stimulants such as growth factors, which bind to a compatible G-coupled receptor protein (as, for example, an epidermal growth factor (EGF) that binds to an EGF receptor). As reviewed in [257], the activated G-protein is able to recruit phosphatidylinositol 3-kinase (PI3K) for the production of phosphatidylinositol-3,4,5-trisphosphate. This step is now followed by the activation of a Rho-family protein. This can be either Cdc42, which predominately leads to the formation of filopodia [255, 258]) or Rac, which triggers the growth of lamellipodia. In both cases, a part of the Wiskott-Alderich-Syndrome protein (WASp) family, notably the WASP verprolin-homologous protein complex (WAVE) is activated. Upon activation by Rac-GTP or Cdc42-GTP, WAVE is able to recruit ARP2/3 complexes, which are, as described above, able to act as nucleation cores for actin filaments and to trigger filament branching. Further regulation is provided by the lamellipodin protein. Lamellipodin is able to regulate the WAVE complex [259], which is not only involved in ARP2/3 recruitment (see above) but which can also control the length of lamellipodia actin filaments by recruitment of Ena/VASP proteins [260]. This protein complex, which was named after the two members identified at first, Ena and Vasodilator-stimulated phosphoprotein (VASP), is able to prevent capping of filaments (reviewed in [261]). The lamellipodium – similar to single actin filaments – can be seen as a treadmilling structure where new filaments assemble at the leading edge while cofilin-mediated disassembly occurs at the trailing edge at the same time. However, not all filaments are disassemble and the remaining filaments are bundled using myosin linkers and form a structure of parallel bundled filaments that is termed lamellum [262]. This structure is built to ensure a more persistent advancement of the cell.

In contrast to Cdc42 and Rac, Rho-GTP does not induce filaments of fine meshworks but rather triggers the assembly of thick, contractible actin bundles where contractibility is achieved by incorporation of myosin into the bundles (actomyosin). While the lamellipodium and the lamellum are responsible for moving the membrane forward, other mechanisms are required to generate the force necessary to pull the entire cell forward. For this purpose, thick actin bundles are formed. These are called stress fibers and are built of short actin filaments connected by α-actinin and myosin. They can be anchored to the substrate by so called focal adhesion spots. These are composed of transmembrane proteins (e.g. integrin) and other proteins that form a link to the actin filament bundles [263]. This type of stress fibers are also called dorsal stress fibers. In order to provide higher stability, additional fibers are formed. This includes transverse arcs, which are obtained by bundling of lamellum filaments into thicker bundles. Transverse arcs and dorsal fibers can also be combined to form ventral stress fibers, which show adhesion spots at both fiber ends. Contractibility of the anchored stress fibers through the incorporated myosin is able to generate tension. When this tension is released, the cell is able to achieve a directed motion of the entire cell body.

5.1.3 Micro-environment influence on cell motility

It is evident that large, multicellular organisms react to mechanical stimuli. For a long time, however, it was not clear whether this principle applies to single cells as well or whether they are driven only by chemotaxis, phototaxis or other non-mechanical effects. Bray *et al.* [264] showed that manipulation of a neuron by a repeatedly advancing and withdrawing microelectrode was suitable to stimulate axonal growth. An evidence that such forces also occur in cell-cell-interactions between two neurons was subsequently brought by Lamoureux *et al.* [265] who showed that axon growth cones can exert a pulling force.

Lamellipodia growth is primarily triggered by growth factors (see Section 5.1.2), nevertheless it has been shown that the mechanical micro-environment has an effect on the signaling pathway, which was described in the previous section, and therefore directly influences cell motility. Aznavoorian *et al.* [266], for example, showed that various ECM components such as fibronectin are able to stimulate the chemotactic and haptotactic motility of cancer cell lines. A study by Price *et al.* [267] further found evidence that integrin molecules found in focal adhesion points recruit Rac and Cdc42, which are the two main effectors for the growth of filopodia and lamellipodia. Verkhovsky *et al.* [268] applied mechanical stimuli in form of a medium stream at a certain pressure to stationary fish epidermal keratocytes. This provoked changes in cell polarization and, as a consequence, triggered migration in the absence of any other kind of stimuli. Lo *et al.* [269] further performed experiments with 3T3 cells that were grown on an ECM surface with varying stiffness. Under these conditions, cells turned to migrate into the direction of increasing stiffness.

In the previous section, it was shown that cell migration is strongly determined by the dynamics of the actin filament network. For this reason, Théry *et al.* tested the behavior of cells subjected to varying ECM geometry, which was defined by micropatterns applied by microcontact printing (cf. Section 5.2). They could show that ECM geometry influences both actin dynamics at the membrane and, as a consequence, also the cell division axis [270]. The mentioned growth of the actin stress fibers, which are considerably stronger in non-adhesive areas [271]. Further, the geometry of external adhesive conditions determines cell polarity and, as a consequence, also the direction of migration [272].

These studies showed how the micro-environment is able to control cell migration, which is important to gain further insight into the mechanisms that govern processes such as metastasis formation or wound healing. Many studies such as [270] so far focused on studying cell motility on two-dimensional surfaces. In addition, dualObjective STORM imaging [273] of lamellipodia structures of BSC-1 cells growing on glass slides [273] further delivered a detailed insight into the three-dimensional structure of the actin network involved in migration. However, migration in the body is in many cases a three-dimensional process. Therefore, it would be beneficial to study the involved structures in three dimensions, which is difficult to realize. However, Doyle *et al.* [274] found that cell motility on an approximately one-dimensional surface is more similar to three-dimensional movement than motility of cells on a two-dimensional structure. For these reasons, the aim of this study was to perform three-dimensional super-resolution imaging on endothelial cells that were grown on one-dimensional microstructures in order to reveal potential differences in the organization of the lamellipodia network compared to cells that were grown on a two-dimensional surface.

5.2 Experimental design

Microcontact printing (µCP) was used in order to provide the required micro-environment for the study of the lamellipodia network. This method has been previously shown to provide versatile and suitable systems to study the behavior of cells in artificial environments [275]. µCP is a micropatterning method that is highly compatible for printing of biological substances. Although first realizations focused on printing of gold nanostructures [276], it is applicable for efficient printing of proteins and nucleic acids onto substrate structures (see review article [277]).

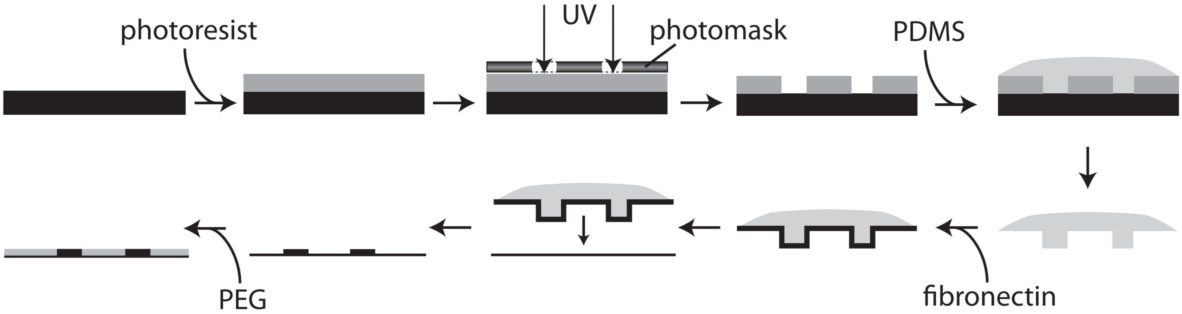

Figure 5.1: Micropattern preparation protocol. A negative mask of the stamp (light gray) was created by manipulation of a UV-sensitive photoresist (dark gray) that was spin-coated onto a silicon wafer (black) and developed. The obtained stamp was coated with fibronectin and the coating was transferred to a microscope slide. Non-adhesive areas were blocked with polyethylene glycol (PEG).

The sample preparation procedure is depicted in Figure 5.1. Briefly, a template wafer is created in the first step. For this purpose, a photoresist is spin-coated onto a silicon wafer and exposed to UV light through a photomask featuring the structure of the final micropattern. Where UV light can hit the photoresist, the latter polymerizes. The photoresist is subsequently developed in a developer solution that gradually dissolves out the photoresist that was not exposed to UV irradiation. This obtained template can then be used to create a polydimethylsiloxane (PDMS) stamp that embodies a negative form of the final microstructure. This stamp is subsequently coated with ECM proteins that are suitable for attachment and growth of the respective cell line. The final stamp can then be placed onto a microscope glass slide to which the protein on the stamp is transferred to providing that the affinity of the respective load to the glass slide is higher than to PDMS. Intermediate spaces between the obtained structures are filled with polyethylene glycol (PEG).

Micropatterns featuring stripes of fibronectin with a width of 3 µm were prepared for experiments as shown in Figure 5.2. Synthesis of the template wavers was performed by the group of Prof. Rädler (Ludwig-Maximilians-University Munich), preparation of the micropatterns by the group of Prof. Zahler (Ludwig-Maximilians-University Munich) following the protocol described by Théry *et al.* [278].

Experiments were performed with human umbilical vein endothelial cells (HUVEC). These cells are isolated from blood vessels taken from the umbilical cord. Due to their origin, they are commonly used as a model system for processes in the endothelium. This includes, for example, the formation of new blood vessels via angiogenesis [279], which is an important process in tissue regeneration processes and requires a high degree of cellular migration. This fact makes them an ideal system to study cellular migration. HUVEC were seeded into micropatterned chamber-slides (IBIDI) prepared as described above or on control slides without micropatterns, which were only coated with fibronectin. Actin filaments of fixed and permeabilized cells were

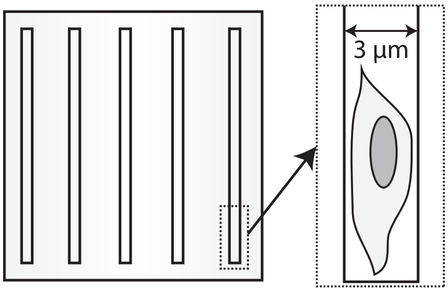

Figure 5.2: Micropattern design. HUVEC were grown on fibronectin-coated stripes with a width of 3 μm created by microcontact printing.

visualized using phalloidin labeled with Alexa Fluor 647 for dSTORM imaging (for a detailed protocol, see Section A.3). Phalloidin is a toxin that is found in *Amanita phalloides* (death cap mushroom) [280]. It specifically binds to F-actin and stabilizes its filamentous structures by inhibiting hydrolysis of actin-bound ATP and therefore blocking depolymerization [281].

5.3 Results

In a first step, the labeling efficiency of the Alexa Fluor 647 phalloidin reagent in combination with the applied fixation protocol was tested. As demonstrated in [282, 283], fixation conditions have a significant impact on the stability and subsequent staining of actin filaments. Wrong reagents can easily break smaller structures and reduce image quality significantly.

Figure 5.3A shows the super-resolution dSTORM image of a section of a HeLa cell that was grown on a conventional collagen-coated glass slide and prepared as described in Sections 5.2 and A.3. Continuous filaments with varying thicknesses are visible showing only a low number of fractures. Again, the superiority of super-resolution techniques is demonstrated when the dSTORM image is compared to the corresponding diffraction-limited TIRF image in Figure 5.3B, where many details of the structure cannot be resolved. However, the applied protocol still has limits that can be seen in Figure 5.3C, which shows a zoom-in into the fine structure of the actin network highlighted by the yellow rectangle in Figure 5.3A. Although the rough course of the filaments is visible, where the TIRF image only shows a more or less uniform background, the distinct filaments do not show continuous staining. This might either be caused by incomplete labeling or by mechanical raptures that are most likely to affect thin filaments easier than the thicker bundles. Figure 5.3D gives estimates of the thicknesses of the bundles marked by the green rectangles in Figure 5.3A. The size calculated by means of the FWHM of the Gaussian fitted to the cross-sections was 70 nm for filament 1 (left panel) and 125 nm for filament 2 (right panel). These values are in good agreement with literature values for actin stress fibers, which are bundles of 10-30 filaments [284], which each have a diameter of approximately 10 nm [243]. The resolution that was achieved in Figure 5.3A was 41.2 nm in x- and 37.6 nm in y-dimension. Interestingly, the cell did not show significant amount of lamellipodia structures. This was an additional reason for the use of HUVEC for the further study of cell migration.

With successful labeling of the actin cytoskeleton, experiments with HUVEC that were grown on micropatterns, as described in Section 5.2, were performed and compared to cells that grew on fibronectin coated surfaces without micropattern structure. An example for the latter is shown in Figure 5.4A and B. The first panel depicts the conventional widefield image and the

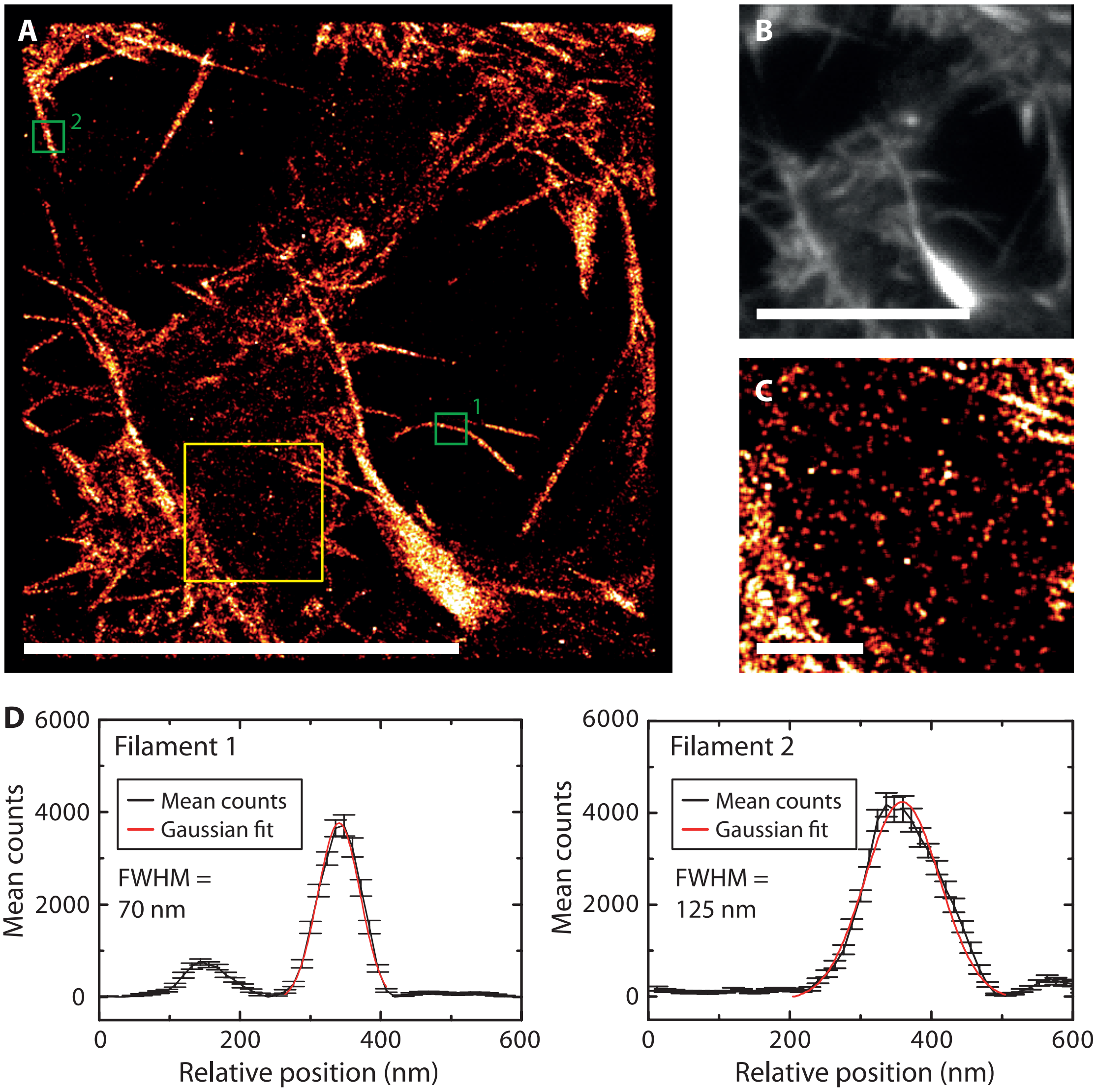

Figure 5.3: Demonstration of actin labeling efficiency. (A) A 2D dSTORM super-resolution image of HeLa cells stained with Alexa Fluor 647 phalloidin reveals thick actin bundles as well as thin filaments. Scale bar: 10 µm. (B) The corresponding diffraction-limited TIRF image. Scale bar: 10 µm. (C) A zoom-in into the region highlighted by the yellow rectangle in panel A reveals actin fine structure despite incomplete staining. Scale bar: 1 µm. (D) Gaussian fits to the average cross-sections of filaments and bundles marked by the green rectangles in panel A give FWHMs of 70 nm and 125 nm, respectively.

second panel the corresponding super-resolution three-dimensional dSTORM image of the protruding edge of a HUVEC growing on a conventional fibronectin coated glass surface. The super-resolution image (Figure 5.4B) clearly depicts the parallel orientation of the actin filaments growing towards the protrusion edge where the transition to the very fine structure of the lamellipodium occurs and where single filaments could no longer distinguished with the obtained resolution. As expected, the observed actin structures formed a flat structure with an estimated average thickness of only 118 nm (Figure 5.4C) by means of the FWHM of the Gaussian function fitted to the distribution of obtained z-positions. This value corresponds to the achieved axial resolution of 115.4 nm. Therefore, the actual distribution might even be smaller than observed. Calculated lateral resolutions were 50.4 nm in x- and 31.7 nm in y-dimension,

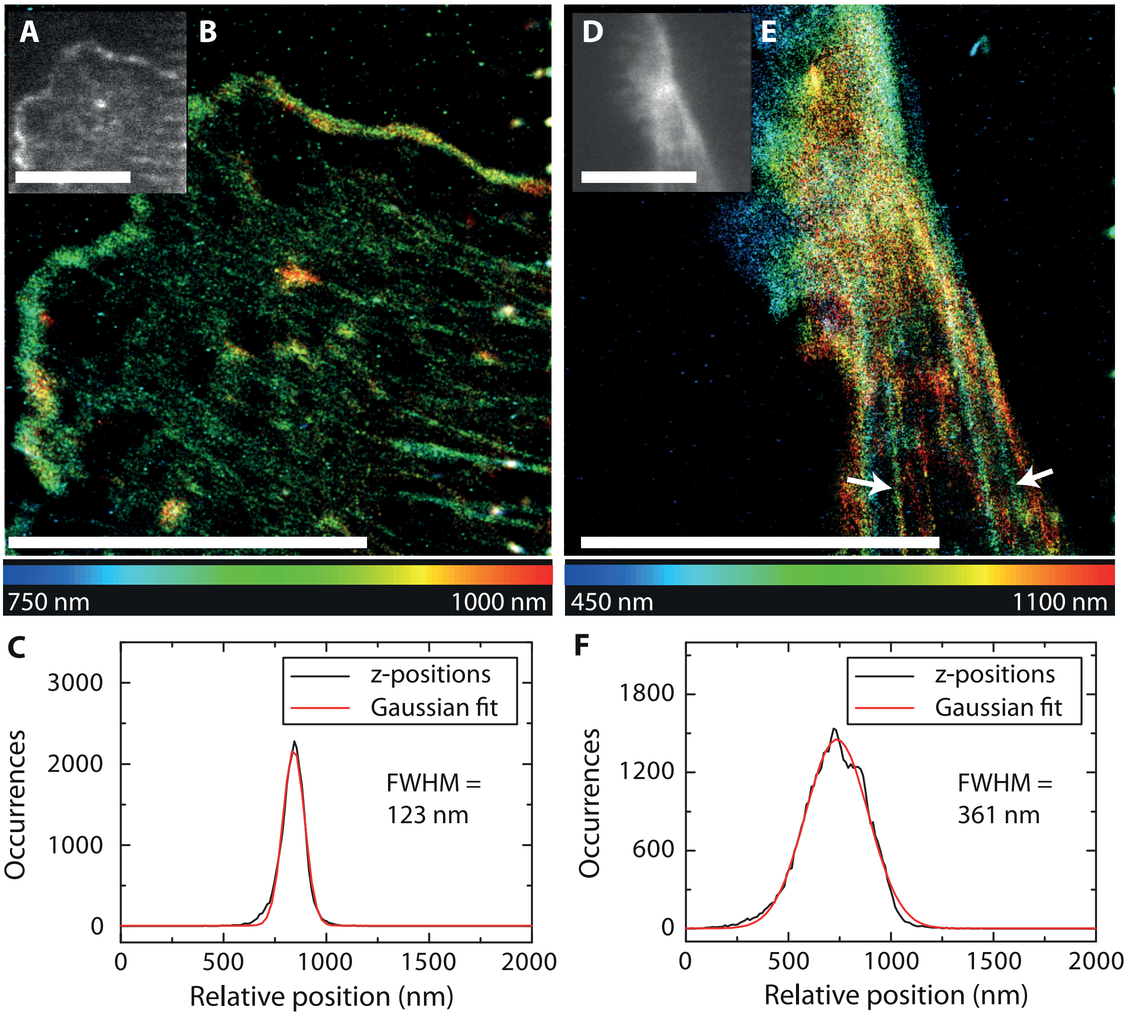

Figure 5.4: 3D dSTORM imaging of HUVEC lamellipodia. (A) Widefield image of the protruding edge of a HUVEC on a fibronectin coated surface without micropatterns. (B) The corresponding 3D dSTORM image reveals a flat structure of the protruding actin filaments and the lamellipodia under these conditions. (C) A Gaussian function fitted to the histogram containing all measured z-positions in B gives an averages thickness of the structure of 118 nm. (D) Widefield image of the protruding edge of a HUVEC growing on 3 µm broad micropatterns. (E) The corresponding 3D dSTORM image reveals a significantly broader expansion in the axial dimension than observed in panel B. The white arrows mark two stress fibers within a distance of 3 µm framing the micropattern. (F) A Gaussian function fitted to the histogram containing all measured z-positions in E gives an averages thickness of the structure of 361 nm. Color code: axial position. Scale bars: 10 µm.

respectively. Figure 5.4D shows the widefield image of a cell that grew on a micropattern bridge as depicted in Figure 5.2. Whereas no apparent differences are visible between the widefield images, the corresponding 3D dSTORM image (Figure 5.4E) reveals clear distinctions to the cells growing directly on the coated glass slide. First, two parallel stress fibers, which are marked by white arrows, are visible in the bottom of the image. The distance between the fibers of approximately 3 µm reproduces the width of the micropattern accurately. Further, the structure shows a much broader expansion in axial direction of 361 nm by means of the FWHM of the Gaussian function fitted to the distribution of obtained z-positions. (Figure 5.4F). Noticeable,

]

the attempts of the cell trying to overcome the artificial obstacle can be observed with lamellipodia structures hanging over the edge of the structure. Lateral resolutions were 53.8 nm and 43.7 nm, respectively and axial resolution was found to be 135.8 nm in this case. A second cell, which was grown under the same conditions on a microstructure, showed an axial diameter of the protruding edge of 428 nm, which was also significantly larger than the axial diameter of the cell grown on the flat surface. However, more statistics are required to obtain a meaningful distribution of the thickness of the lamellipodia in the one-dimensional environments.

5.4 Discussion

The main interest in this study was to analyze changes of the actin network in the protruding edge of a migrating cell upon changes of the micro-environment that deviate from the conventional two-dimensional environment that is present in conventional cell culture experiments. This was realized by restriction of the freedom to move of the cells by using micropatterns that provided an approximately one-dimensional environment. Widefield images showed that HUVEC could be successfully grown on these structures and did not appear to be affected in their viability compared to the control where cells where grown on a conventional two-dimensional surface. It was further confirmed that the limits of these structures could not be overcome by the cells therefore ensuring that the one-dimensional character of the sample could be maintained.

When comparing the respective three-dimensional super-resolution dSTORM images, the most striking difference is the larger axial expansion of the actin network in the presence of micropatterns proving clearly the effect of a changed substrate geometry. The lamellipodium of the cell on a two-dimensional surface had a thickness of 118 nm, which is in agreement with SEM measurements of fibroblast lamellipodia by Abercrombie *et al.* [285] (110 to 160 nm) although they are slightly smaller than values reported by Abraham *et al.* [286] (176 ± 14 nm) and from STORM measurements by Xu *et al.* [68] (up to 200 nm). The latter could further resolve two separated layer of actin filaments in the protruding edges of the cell using dualObjective STORM. This difference could not be detected in this case, which is most likely a result of the higher axial resolution Xu *et al.* could achieve by using dualObjective STORM.

The axial extension of the lamellipodia in the analyzed cells that were grown on one-dimensional structures was significantly broader. This observation gives evidence that the framing structure does not only stop the cell from moving but actively changes the organization of the actin filament network. It might be speculated that the increased axial expansion could be an evidence for the increased similarity between one- and three-dimensional systems in cell motility, which was shown by Doyle *et al.* [274]. Cells growing on the micropatterns also showed stress fibers that frame the micropattern structure. This is in agreement with Théry *et al.* [271] who observed stress fibers growing along the adhesive edges of cells on micropatterns. It is assumed that these fibers counteract the inward pulling caused by unattached membranes. Furthermore, in both cases, the ruffled outer shape of the lamellipodium is visible and the transition between the denser lamellipodia meshwork and the attaching lamellum could be visualized. However, in order to make a more significant statement it would be necessary to increase the statistics.

This example further represents an excellent demonstration of the ability of three-dimensional super-resolution microscopy to provide information that is not accessible by conventional optical microscopy. Comparison of the different actin structures also reveals the limit of the performed experiments. Whereas stress fibers and thicker filaments of the lamellum can be reproduced well with a measured diameter that corresponds to literature values, imaging of single filaments of the actin fine structures (cf. Figure 5.3) and especially of the dense meshwork of the lamellipodium (cf. Figure 5.4) proved to be highly challenging. Despite the fact that phalloidin labeling has been shown to be an efficient and specific agent for labeling of filamentous actin, a detailed analysis especially of thinner filaments reveals that the staining is not always continuous. The axial resolution that was achieved in these images is among the best values that have been reached with the presented STORM microscope so far, but further improvement of axial resolution as well as of labeling efficiency should be targeted to increase image quality. It should also be noted that the labeling efficiency appears to be slightly worse in the micropattern experiment shown in Figure 5.4 than in the control experiment depicted in Figure 5.3 although the same staining protocol was applied in both cases. Already early experiments that were performed to identify optimal sample preparation conditions revealed that already small changes in the fixation and staining protocol can have significant impact on the quality of the final super-resolution image. Therefore, a certain variation of image quality cannot be avoided. Additionally, differences between HUVEC and HeLa cells might play a role as well. Overall, the performed experiments have shown that super-resolution fluorescent microscopy is a highly suitable method to study these systems. Further insight into the arrangement of the stress fiber network is also impeded by the relatively small imaging area defined by the optical settings. Here, a larger field of view would be certainly beneficial to allow further insights.

Despite potential improvements in image quality and especially visualization of details of the fine structure, it nevertheless has to be emphasized again that the obtained images provide the necessary informations to answer the primary question of this study. It could be shown that manipulation of the environment has impact on the organization of the actin network involved in migration. This underlines the spectacular flexibility and adaptability these filaments are able to provide. For future experiments, it would be interesting to study the effect of different micropattern shapes on structural organization and behavior of lamellipodia network in three dimensions. Additionally, the effect of the environment on other cellular compartments such as microtubules is of interest as the latter have been shown to play a significant role in cell migration as well [287].

Chapter 6

Conclusion

Localization-based super-resolution microscopy demands special requirements compared to other fluorescence microscopy techniques regarding the technical setup and analysis methods but also to application and interpretation of the obtained results. These topics were addressed in this thesis, which focused on building and establishment of a super-resolution microscope together with providing the required analysis tools, for applying the methods to biological structures on the nanoscale. The super-resolution microscope was built for two- and three-dimensional STORM, dSTORM and PALM imaging and is currently able to provide optical resolutions down to 30 nm in the lateral and 115 nm in the axial dimension. Although this resolution might still be improvable, it nevertheless allows nanoscopic imaging of biological systems as it was successfully demonstrated by the two applications presented in this thesis.

Several features are essential for the layout of a localization-based super-resolution microscope. First, mechanical stability is one of the key features to provide good localization accuracies. Nanoscale imaging brings fluorescence microscopy to a new level of resolution where stability is more important than it is the case for conventional, diffraction-limited microscopy. This was achieved with a compact setup design and implementation of correction tools such as a perfect focus system with nanometer-precise feedback. Second, a sufficiently high laser power to enable dye switching is no less important. Apart from using high-performance instrumentation, the optical beampath was designed to keep photon loss at the respective optical elements as small as possible. This is a crucial factor as photon detection efficiency governs the localization accuracy and hence the obtainable resolution. The super-resolution microscope could additionally be easily switched from two- to three-dimensional, astigmatism-based super-resolution imaging by insertion of a weak cylindrical lens into the detection pathway. Self-written control software further provided the required accurate and synchronized control of the microscope stage as well as of the data acquisition process.

For precise and meaningful analysis of the obtained data, an analysis software was written. This software determined the localization of the single fluorescent emitters in the acquired raw data with different localization algorithms. The localized data could then be used for rendering of super-resolution images in two and three dimensions. Versatile applicable thresholds and correction mechanisms (e.g. correction of lateral drift) allowed the refinement of the results and increased image quality. Additionally, the software provided analysis tools for evaluating the goodness of the super-resolution image such as calculation of the image resolution, localization accuracy and goodness of the fit. The suitability of these tools was tested and evaluated in this study. The performance of the instrumental and analytical approach was demonstrated at two- and three-dimensional super-resolution imaging of appropriate test systems such as components of the cytoskeleton.

Over the course of this study, it further emerged that despite good optical stability and alignment, the labeling efficiency and quality of the respective sample is crucial for successful super-resolution imaging. The requirements are significantly more sensitive to imperfectness than it is the case for conventional widefield or TIRFM imaging. Therefore, it is inevitable to carefully monitor and evaluate sample preparation conditions and perform the required control experiments to exclude imaging artifacts.

The latter was also a main motivation for the experiments that were performed to study the interaction between HIV-1 and the cellular ESCRT machinery during viral budding. Three different models were discussed in literature describing the geometric structure of ESCRT assembly at the budding site. The complex was suggested to form either flat lattices outside of the neck, dome or spiral-shaped structures within the neck or to assemble within the virus bud itself. However, these studies relied on FP-fusion tags for visualization. Other studies as well as control experiments performed for this study have shown how sensitive ESCRT proteins react to labeling conditions and how easily a deviation from the endogenous behavior can occur as a consequence. For this reason, experiments for this study were performed on endogenous systems whenever possible. In some cases, minor modifications were necessary and also fixation and permeabilization of the cells could not be avoided. However, appropriate control experiments showed that these did not affect the results. The observed structures eventually gave clear evidence for ESCRT assembly within the neck of the virus bud and could rule out other previously assumed models. It was therefore possible to answer this for a long time highly disputed problem by using super-resolution methods.

The second application of localization-based super-resolution microscopy was focused on imaging of the lamellipodia network of migrating cells in the context of micropatterns that limit their freedom of movement. Information about the axial distribution of the lamellipodia network could be obtained by applying astigmatism-based three-dimensional dSTORM imaging. This technique revealed the influence of the restricting micropattern. In contrast to conventional diffraction-limited images of the same system, it was possible to visualize how lamellipodia deviate from their native, flat structure showing a much broader expansion.

Future work on the established super-resolution microscope will focus on the improvement of the resolution capacity and on refinement of multi-color experiments. Another labeling approach might be achievable with DNA-PAINT. This method has the same demands on the microscope setup regarding stability and uses the same analysis methods like STORM, dSTORM and PALM. The major difference is found in the labeling approach that makes this method especially suitable for multi-color applications.

The microscope that was established over the course of this thesis together with the analysis methods provide the required tools to apply super-resolution microscopy also to other samples than to the examples that were studied in this thesis. The system and the presented applications underline the significance of localization-based super-resolution microscopy techniques. In particular, STORM, dSTORM and PALM are highly suitable and versatile methods to image and analyze structures whose size lies below the diffraction limit and to provide answers to relevant biological questions that can not be obtained by other methods.

Appendix A

Materials and Methods

A.1 STORM sample preparation protocols

A.1.1 STORM imaging buffer

The STORM imaging buffer preparation protocol was adapted from the procedure described in [54]. Briefly, an oxygen scavenger buffer was prepared containing 5 mg of glucose oxidase (#C1233, Sigma-Aldrich, St. Louis, MO, USA) and 30 μL of an aqueous catalase suspension of a concentration of 20 to 50 mg/mL and 10 000 to 40 000 units/mg (#C30, Sigma-Aldrich) diluted in 100 μL phosphate buffered saline (PBS, #14190, pH = 7.0, Life Technologies, Carlsbad, CA, USA). For 1 mL STORM imaging buffer, 10 μL of this glucose oxidase solution was mixed with 100 μL of a 1 M aqueous β-mercaptoethylamine solution (#30070, Sigma-Aldrich) and 790 μL PBS. The obtained solution has a pH of ~ 9 and can be kept up to two weeks at 4 °C.

Immediately before starting STORM or dSTORM experiments, 100 μL of a 25 % (w/w) glucose (#G7528, Sigma-Aldrich) solution was added to the buffer and the final buffer added to the respective sample. Typically, imaging times up to 5-6 hours were possible (in the case of LabTek II chamber slides). This value can be increased up to 24 hours by sealing the sample chamber with paraffin in order to reduce permeation of oxygen.

A.1.2 Antibody labeling

For dSTORM imaging, the unconjugated antibody was mixed with the NHS-ester of the respective dye in a molar ratio of 1:4 (antibody : dye) in 150 mM $NaHCO_3$ buffer (pH = 8.2) and incubated for at least 4 hours at 4 °C. In the case of STORM imaging, a molar ratio of 1:4:1 (antibody : activator dye : reporter dye) was used. Unreacted dye molecules were subsequently removed by gel permeabilization chromatography columns (Performa DTR Gel Filtration Cartridges, Edge BioSystems, Gaithersburg, MD, USA) according to the manufacturer's instructions.

A.1.3 STORM bead sample preparation

a) Labeling of 200 nm sized beads with labeled streptavidin. A solution of streptavidin (#SNN1001, BioSource) was labeled with Cy5 bis-NHS ester (#PA25000, GE Healthcare Life Sciences, Little Chalfont, United Kingdom) for dSTORM imaging or with Alexa Fluor 488 carboxylic acid succinimidyl ester (#A-20000, Life Technologies) and Cy5 bis-NHS ester for STORM imaging in analogue to the protocol for antibody labeling (Section A.1.2).

In the next step, 20 µL of a stock of 200 nm sized biotin-coated latex beads (#L8780, Sigma-Aldrich) were suspended in 835 µL Tris-HCl (pH = 7.5). The prepared beads were given to 45 µL of a 1:10 mixture of labeled and unlabeled streptavidin. After 10 minutes, the beads were spun down, the supernatant liquid was discarded and the beads were resuspended in Tris-HCl buffer.

b) Direct labeling of 40 nm sized beads. 20 µL of a stock of 40 nm sized neutravidin-coated latex beads (#F-8772, Life Technologies) were suspended in 835 µL Tris-HCl (pH = 7.5). For STORM samples, 1.50 µL of a 50 mM solution of Alexa Fluor 488 carboxylic acid succinimidyl ester (#A-20000, Life Technologies) and 0.68 µL of a 50 mM solution of Cy5 bis-NHS ester (#PA25000, GE Healthcare Life Sciences) were added. For dSTORM samples, labeling was performed analogously but with Cy5 dye only. The mixture was stored for at least 4 hours at 4 °C before the beads are spun down at maximum speed (10 minutes). The supernatant liquid was discarded and the beads were resuspended in Tris-HCl buffer.

A.1.4 3D calibration sample preparation

Cy5-labeled 40 nm sized beads were prepared according to the protocol described above and 20 µL of the obtained stock were mixed with 20 µL water and 150 µL of a polymer substrate (#MY-132-MC, MY Polymers, Nes Ziona, Israel), which cures upon contact with water to a gel with a refraction index of 1.32. The mixture was allowed to stand for at least 2 hours to allow polymerization.

A.1.5 Microtubules sample preparation protocol

The following protocol is a slightly modified version of the routine described in [54]. HeLa cells (Japanese Collection of Research Bioresources Cell Bank, Osaka, Japan) were grown in Dulbeccos modified Eagles medium (DMEM, #21885, Life Technologies), supplemented with 10 % fetal calf serum (#10099-133, Thermo Fisher Scientific, Waltham, MA, USA) and seeded on collagen-coated LabTek II chamber slides (#155409, Thermo Fisher Scientific) with a density of approximately $2 \cdot 10^4$ cells per well and incubated over night at 37 °C and 5 % CO_2. Cells were subsequently washed with phosphate buffered saline (PBS, #14190, pH = 7.0, Life Technologies, Carlsbad, CA, USA) and fixed with a solution of 3 % (v/v) paraformaldehyde (#15710, Electron Microscopy Sciences, Hatfield, PA, USA) and 0.1 % (v/v) glutaraldehyde (#G5882, Sigma-Aldrich) in PBS. After 15 minutes, fixation was stopped by rinsing the cells two times with PBS. In order to reduce background fluorescence, a reduction step was performed by incubating the cells with a 0.1 % (w/v) aqueous solution of $NaBH_4$ (#198072, Sigma-Aldrich) for 7 minutes. After rinsing the cells three times with PBS to remove all remaining $NaBH_4$, cells were treated with a blocking buffer containing 3 % (v/v) bovine serum albumin (BSA, #B9000S, New England Biolabs, Ipswich, MA, USA), 0.2 % (v/v) Triton X-100 (#T8787, Sigma-Aldrich) in PBS for 30 to 60 minutes in order to reduce unspecific antibody binding. In the next step, the blocking buffer was replaced by 150 µL of a 1:500 dilution of primary monoclonal mouse anti-α-tubulin antibodies (clone GT114, #GTX628802, Genetex, Irvine, CA, USA) in blocking buffer and allowed to incubate for 60 minutes. The sample was then rinsed once with a washing buffer containing 0.2 % (v/v) BSA and 0.05 % (v/v) Triton X-100 in PBS and subsequently washed two times for 5 minutes with washing buffer. Secondary donkey anti-mouse IgG antibodies (#ABIN336468, purchased via antibodies-online.com) were labeled with Cy5 bis-NHS-ester (#PA25000, GE Healthcare) (Section A.1.2) and diluted in blocking buffer at a ratio of 1:150 and the cells were incubated with 150 µL of this solution for 45 minutes. Analogous to the first labeling step, immunostaining was followed by rinsing with washing buffer and two washing steps (each step 5 minutes) with PBS. Finally, a post-fixation step was performed by treating the cells for 5 minutes with the same dilution ratio of fixation reagents as before. After rinsing the sample again twice with PBS, STORM imaging buffer (Section A.1.1) was added for immediate imaging or the sample was stored at 4 °C using a storage buffer of 100 mM NaN_3 (#S2002, Sigma-Aldrich) in water.

A.2 Sample preparation and analysis of super-resolution imaging of ESCRT proteins at HIV-1 assembly sites

Plasmids. Plasmids encoding the non-infectious mutants of HIV-1, pCHIV and its labeled derivatives have been previously described [214, 216] as well as the VPS4A-E228Q-mCherry plasmid [195]. Construct pCHMP4B-HA, where CHMP4B is fused to an HA-tag, and the YFP-Tsg101 plasmid were kindly provided by H. Göttlinger [288] and W. Sundquist (University of Utah, Salt Lake City, USA), respectively.

The plasmid peGFP.Vpr for the FP-tagged Vpr fusion protein was previously described by T. Hope [289]. The synGag plasmid (Graf *et al.*, [290]) was provided by R. Wagner (University of Regensburg, Germany), and pGag.eGFP (Hermida-Matsumoto *et al.* [227]) was provided by M. Resh (Memorial Sloan-Kettering Cancer Center, New York, USA).

pGag.mCherry was created by H.-G. Kräusslich and B. Müller (University of Heidelberg, Germany) as a derivate of pGag.eGFP and was obtained by replacing a BamHI/BsrGI fragment comprising the eGFP coding sequence with a corresponding restriction fragment comprising the mCherry open reading frame generated using a polymerase chain reaction.

Cells and transfection. HeLa cells were grown and seeded according to the same conditions as described in the microtubules sample preparation protocol. Cells were transfected the day after seeding using X-tremeGENE 9 DNA transfection reagent (#06365787001, Roche, Risch, Switzerland) according to the manufacturer's instructions. Briefly, transfection agent and plasmid DNA were incubated at a molar ratio of 3:1 for 20 minutes at room temperature before the mixture was given to the cells. After transfection, cells were incubated for at least 14-15 hours at 37 °C and 5.0 % CO_2.

For PALM imaging of the HIV-1 assembly sites, 50 ng pCHIV and 50 ng pCHIV$^{\mathrm{mEos}}$ were used for transfection. For STORM or dSTORM experiments with endogenous proteins Tsg101, ALIX and CHMP2A and HIV$^{\mathrm{mCherry}}$, 50 ng pCHIV and 50 ng pCHIV$^{\mathrm{mCherry}}$ were used for transfection. In the case of CHMP4B-HA, an additional amount of 100 ng CHMP4B-HA encoding plasmid pCHMP4B-HA was added. Control experiments with late- mutants were performed by replacing pCHIV and pCHIV$^{\mathrm{mCherry}}$ by the same amount of the respective late- mutant.

For experiments with the Tsg101 fusion proteins, 50 ng of YFP-Tsg101 and 50 ng of each pCHIV$^{\mathrm{mCherry}}$ and pCHIV were used for transfection, respectively. In order to study the fusion protein in the context of Gag alone, 50 ng synGag and 50 ng of Gag.mCherry replaced the pCHIV plasmids. Further control experiments included immunostaining control using viral Vpr. Here, 75 ng of pEGFP.Vpr and 50 ng of synGag (wildtype) and 50 ng of Gag.mCherry or Gag.eGFP were used for transfection, respectively. VPS4A-depletion experiments in the context of CHMP2A comprise transfection with 70 ng pCHIV$^{\mathrm{eGFP}}$, 70 ng pCHIV and 35 ng VPS4A-E228Q-mCherry.

Sample preparation and data acquisition. After at least 14-15 h of incubation, transfected HeLa cells were fixed and subsequently immunostained analogously to the protocol described for microtubule staining (Section A.1.5) with the following antibodies: Primary mouse monoclonal anti-Tsg101 antibodies (clone 4A10, #GTX70255, Genetex) were used in combination with secondary donkey anti-mouse IgG antibodies (#ABIN336468, purchased via antibodies-online.com) that were labeled with Cy5 according to the protocol described in Section A.1.2. Monoclonal primary mouse anti-ALIX antibodies (clone 3A9, #634502, BioLegend) and monoclonal primary anti-HA antibodies (clone 3F10, #11867423001; Roche) were directly labeled with activator-reporter dye pair Alexa Fluor 488 and Cy5. Immunostaining of CHMP2A was performed with primary polyclonal rabbit anti-CHMP2A antibodies (#ab76335, abcam) combined with secondary donkey anti-rabbit IgG (#ABIN376979, purchased via antibodies-online.com) that were labeled with Cy5 according to the protocol above. eGFP.Vpr fusion protein was stained with anti-GFP primary polyclonal antibodies from rabbit (#ABIN121945, purchased via antibodies-online.com) that were used in combination with the same secondary anti-rabbit IgG antibodies that were also used for in combination with the anti-CHMP2A antibody.

Data acquisition and analysis. Data acquisition was performed according to the principles and criteria described in Section 3.2.2. Rendering of the final STORM and PALM images analogously followed the descriptions in Sections 3.2.4 and 3.2.5.

For identification of single virus particles and exclusion of large Gag clusters, an additional self-written image analysis algorithm was developed in ImageJ Macro language [291], which was provided by A. A. Torrano (LMU Munich, group of Prof. C. Bräuchle). Images were individually analyzed as follows: First, a convolution filter (Gaussian blur) followed by background subtraction ("rolling ball" algorithm [292]) were applied. Next, point objects were selected based on their intensities (local maxima) and a multipoint selection was created. Objects corresponding to either assembly sites or clusters were then segmented by a watershed approach. As a last step, the center of brightness, distribution of intensities and area of each object were measured and Gag assemblies with an area $> 0.860\,\mu\mathrm{m}^2$ were excluded from further evaluation.

Quantification of ESCRT clusters was performed by rendering an additional image from the STORM data set with a pixel size of 120 nm. In order to avoid incorporation of unspecific signals and of signals with low statistics, only clusters with a maximum intensity higher than a threshold set individually for each measurement (typically 5000 counts) were considered for further evaluation. In addition, only structures that were not within a distance of 4 px to the border of the widefield image were evaluated in order to avoid fit artifacts. In some cases, no distinct structure could be obtained in the final super-resolution STORM image. As a consequence, these structures were discarded. Object sizes were calculated from the final super-resolution image using the mean of the FWHMs of two 1D Gaussian functions fit to the horizontal and vertical cross-sections of the respective cluster (Section 3.4). Determination of the size of the cloud-like structures in the case of ALIX was performed using the Ripley's L-function. ALIX structures often consisted of two distinct populations with different sample densities (a central cluster and the surrounding cloud). As demonstrated in Section 3.4, cluster size estimation by the Ripley's L-function does not give accurate results in these cases. Therefore, the central spot in the center of the cloud was masked to obtain more accurate results. The mask radius corresponded to the size of the central cluster that was measured before.

A.3 Sample preparation protocols for super-resolution imaging of endothelial lamellipodia

Microstructure sample preparation. Microcontact printing and seeding of HUVEC was performed in the laboratory of Prof. S. Zahler (LMU Munich). Template wafers for microcontact printing were obtained from the laboratory of Prof. J. Rädler (LMU Munich) [293].

Actin filaments staining protocol. The following procedure that was used to stain cellular actin filaments was derived from the protocol described in [68]. Cultivated cells were washed briefly with PBS (37 °C) before they were fixed and permeabilized by treatment for 2 minutes with a solution containing 0.3 % (v/v) glutaraldehyde (#G5882, Sigma-Aldrich) and 0.25 % (v/v) Triton X-100 (#T8787, Sigma-Aldrich) in a cytoskeleton buffer that contained 150 mM NaCl (#27810.295, VWR, Radnor, PA, USA), 5 mM $MgCl_2$ (#M2670, Sigma-Aldrich), 5 mM glucose (#G7528, Sigma-Aldrich), 5 mM ethylene glycol tetraacetic acid (EGTA, #E3889, Sigma-Aldrich) and 10 mM 2-(*N*-morpholino)ethanesulfonic acid (MES, #M2933, Sigma-Aldrich) at $pH = 6.1$. This was followed by a second fixation step, which comprised incubation with 2 % glutaraldehyde diluted in cytoskeleton buffer for 10 minutes. Subsequently, an optional reduction step could be performed to reduce background fluorescence by treating the cells with a 0.1 % (w/v) $NaBH_4$ (#198072, Sigma-Aldrich) solution in cytoskeleton buffer for 7 minutes. The cells were then washed three times with PBS with a 10 minute incubation period at each step before labeling was performed. For this purpose, a 0.06 µM solution of Alexa Fluor 647-Phalloidin (#8940S, New England Biolabs) was added to the sample and allowed to incubate at 4 °C for at least 24 hours. The labeled cells were then briefly washed once with PBS before the STORM imaging buffer was added and the sample was ready for imaging. In this context, it should be noted that the binding of Alexa Fluor 647-phalloidin to the actin filaments is reversible and the reagent will gradually dissolve from the sample once the labeling solution is removed. Therefore, unnecessary washing steps and buffer replacements should be avoided and the sample has to be imaged immediately after staining.

A.4 Optimization algorithms

In order to fit the measured PSF to a model system, two different optimization algorithms were applied that are both able to solve nonlinear optimization problems. These are the widely used Levenberg-Marquardt algorithm and the Downhill Simplex algorithm.

A.4.1 Levenberg-Marquardt algorithm

One commonly used method to solve nonlinear optimization problems is the Levenberg-Marquardt algorithm [95, 96]. It solves the following equation with the aim to minimize the squared error $\chi^2(p)$ depending on a set of parameters p for a data set with N data points:

$$\chi^2(p) = \sum_{i=1}^{N} [y_i - f(x_i, p)]^2 \tag{A.1}$$

y_i in Eq. A.1 is the observed data (e.g. measurement results) and $f(x_i, p)$ data points that were calculated for the variable set x_i and set of parameters p. The sum of Eq. A.1 can also be written in form of vectors as

$$\chi^2(p) = \parallel y - f(p) \parallel \tag{A.2}$$

In Eq. A.2, y is a vector containing the observed data points and $f(p)$ is a vector with values calculated by means of function f and parameter set p. In the next step, a Taylor series expansion is used to calculate a linear estimate f for small changes δp inflicted on p

$$f(p + \delta p) \approx f(p) + \frac{\partial f(p)}{\partial p} \cdot \delta p \tag{A.3}$$

where $\frac{\partial f(p)}{\partial p}$ is also called the Jacobi-Matrix J. Eq. A.2 can now be written as

$$\chi^2(p) = \parallel y - f(p + \delta p) \parallel \approx \parallel y - f(p) - J\delta p \parallel \tag{A.4}$$

Eq. A.4 is minimal when

$$J^T(J\delta p - y - f(p)) = 0 \tag{A.5}$$

Eq. A.5 can then be solved for δp:

$$\delta p = (J^T J)^{-1} J^T (y - f(p)) \tag{A.6}$$

In order to get a good solution, a so called damping parameter μ is introduced and Eq. A.6 replaced by Eq. A.7 where I is the identity matrix.

$$\delta p = (\mu I + J^T J)^{-1} J^T (y - f(p)) \tag{A.7}$$

This damping parameter also ensures the existence of a unique solution for δp. Otherwise, it is possible that J is not full rank. In this case, Eq. A.6 would have more than one solution. $\chi^2(p + \delta p)$ is now calculated in an iterative process. In each step, $\chi^2(p + \delta p)$ is compared to the value from the previous iteration step. When the new error is worse than the old error, the damping parameter is increased and the procedure is repeated. If the squared error, however, decreases, the new parameter set replaces the old values, the damping parameter is decreased and these values are used for the following iteration step. This procedure is repeated until χ^2 drops below a predefined threshold. In addition, a maximum number of allowed iterations can be defined in order to avoid endless calculations for optimizations where no conversion can be reached.

A.4.2 Downhill Simplex algorithm

The Downhill Simplex algorithms, which is also referred to as Nelder-Mead algorithm after the authors of the original publication [100], offers an approach to find the minimum of linear and nonlinear functions without the need of linearization. On the one hand, this eliminates one approximation that is, for example, necessary for algorithms such as the Levenberg-Marquardt algorithm. On the other hand, the Downhill Simplex algorithm usually requires a larger number of iterations to converge and has got a higher risk to converge at a local minimum if the initial parameters are too far off the actual solution.

As the name Downhill Simplex suggests, the algorithm seeks to minimize a function by taking advantage of the geometric form of a simplex, which is defined as an object with $n+1$ edges in an n-dimensional space (e.g. a triangle in a two-dimensional space). Assuming now a function f with n parameters P, a $n+1$ simplex can be formed in a n-dimensional space. For the initial simplex, start parameters are required that lie as close as possible to the unknown values. This set forms the first point of the initial simplex. The remaining parameter sets are usually obtained by varying one of the parameters in each set (e.g. by adding a fixed value). Subsequently, an iterative process can be started to localize the minimum of the function.

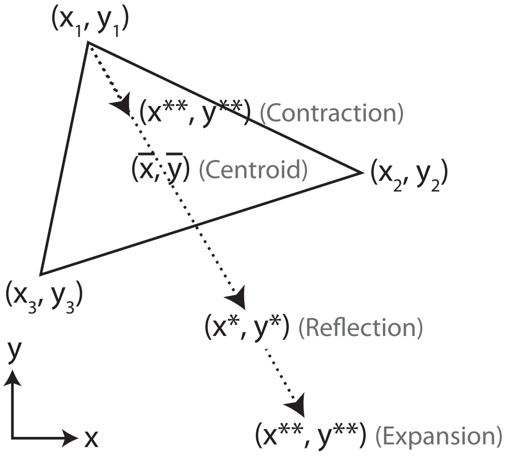

Figure A.1: Illustration of the Downhill Simplex algorithm at the example of a system with two fit parameters, x and y. The three different correction steps during one iteration step of the Downhill Simplex algorithm are illustrated for $n = 2$ where three parameter sets form a triangle on which the reflection, expansion and contraction steps are applied.

Figure A.1 illustrates the different geometrical transformations that constitute a single iteration step for the example of a two-dimensional simplex with two fit parameters (x and y). At the beginning of each step, the centroid $\overline{P}$ of the respective simplex is calculated. The parameter set P_{max}, returning the highest function value, which represents the parameter set with the largest fit error, is reflected on this point according to the following equation to calculate the reflected point P^*, where α is called reflection parameter:

$$P^* = (1+\alpha)\overline{P} - \alpha P_h \tag{A.8}$$

If P^* emerges to be a better solution for the problem than the best solution obtained so far, P_{min}, an expansion step is performed, which is tuned by the elongation parameter γ, in order to test whether going further in the respective direction might give an even better solution P^{**}:

$$P^{**} = \gamma P^* + (1-\gamma)\overline{P} \tag{A.9}$$

If P^{**} is better than P^* and P_{min}, P_{max} is replaced by P^{**}. If only P^* is better than P_{min}, P_{max} is substituted by that value. If neither the reflected nor the expanded value brought any improvement compared to P_{min}, it is checked whether one of the two values is at least better than any other parameter set except for P_{max}. If this is true, P_{max} is replaced by P^* nevertheless.

Otherwise, it is checked if P^* is at least better than P_{max} but worse than any other P. P_{max} is then also replaced by P^* but regardless of this question, a third transformation is performed at this point, which is a contraction, tuned by parameter β that moves f_{max} closer to the centroid:

$$P^{**} = \beta P_h + (1 - \beta)\overline{P} \tag{A.10}$$

If the contracted value now brings an improvement compared to P_{max}, the latter is replaced by this value. However, when also this last adjustment step failed to come closer to the actual minimum, a contraction of all points P_i around P_{min} is performed:

$$P_i = \frac{P_i + P_{min}}{2} \tag{A.11}$$

After each iteration step, it is checked whether P_{min} fulfills the convergence criteria that were defined for the respective optimization problem. If this is the case, the process is complete; otherwise a new iteration step is performed starting again with the calculation of the centroid of the simplex.

Appendix B

Abbreviations

ADP/ATP	adenosine di-/triphosphate
AIDS	acquired immunodeficiency syndrome
ALIX	ALG-2 interacting protein X
AOTF	acousto-optical tunable filter
ARP	actin-related protein
bp	base pair
BSA	bovine serum albumin
CA	capsid protein
CHMP	charged multivesicular body protein
CMOS	complementary metal-oxide semiconductor
CRLB	Cramér-Rao lower bound
cw	continuous wave
DNA/RNA	deoxyribonucleic acid/ribonucleic acid
EGF	epidermal growth factor
Eq.	equation
EIAV	equine infectious anemia virus
ECM	extracellular matrix
EM	electron microscopy
(EM)CCD	(electron multiplying) charge coupled device
ESCRT	endosomal sorting complex required for transport
FP	fluorescent protein
fPALM	fluorescence photoactivation localization microscopy
FPGA	field programmable gate array
FWHM	full width at half maximum
Gag	group specific antigen
GDP/GTP	guanosine di-/triphosphate
GFP/RFP/YFP	green-, red-, yellow fluorescing protein
GPU/CPU	graphics/central processing unit
HA	hemagglutinin
HIV	human immunodeficiency virus
HUVEC	human umbilical vein endothelial cell
IR	infrared
IRES	internal ribosomal entry site
L-domain	late domain
LTR	long-terminal repeat
MA	matrix protein
MLE	maximum likelihood estimation
MVB	multivesicular body
µCP	microcontact printing

NA	numerical aperture
NC	nucleocapsid
NHS	*N*-Hydroxysuccinimide
PALM (iPLAM)	Photoactivated Localization Microscopy (interferometric PALM)
PAINT	Point Accumulation for Imaging in Nanoscale Topography
PBS	phosphate buffered saline
PDMS	polydimethylsiloxane
PEG	polyethylene glycol
PIC	pre-integration complex
PID	proportional-integral-derivative feedback
PSF	point spread function
RTC	reverse transcription complex
SEM	Scanning Electron Microscopy
SNR	signal-to-noise ratio
SOFI	Super-Resolution Optical Fluctuation Imaging
STED	stimulated emission depletion
(d)STORM	(direct) Stochastic Optical Reconstruction Microscopy
TEM	Transmission Electron Microscopy
TIRF(M)	total internal reflection fluorescence (microscopy)
Tsg101	tumor susceptibility gene 101
UV	ultraviolet
VLP	virus-like particle
Vpr	viral protein R
VPS4(A)	vacuolar protein sorting 4 (homolog A)

List of Figures

List of Tables

Bibliography

[1] Albert Van Helden, Sven Dupré, Rob van Gent, and Huib Zuidervaart. *The Origins of the Telescope*. History of Science and Scholarship in the Netherlands. The Royal Netherlands Academy of Arts and Sciences, Amsterdam, 2011.

[2] Robert Hooke. *Micrographia*. J. Martyn and J. Allestr, London, 1st edition, 1665.

[3] Antoni van Leewenhoeck. Little Animals. *Philosophical Transactions*, 12:821–831, 1677.

[4] Ernst Abbe. Beiträge zur Theorie des Mikroskops und der mikroskopischen Wahrnehmung. *Archiv für mikroskopische Anatomie*, 9(1):413–468, 1873.

[5] John William Strutt. Investigations in optics, with special reference to the spectroscope. *Philosophical Magazine, Series 6*, 8(49):261–274, 1879.

[6] Stefan W. Hell and Jan Wichmann. Breaking the diffraction resolution limit by stimulated emission: stimulated-emission-depletion fluorescence microscopy. *Optics Letters*, 19(11):780–782, 1994.

[7] Eric Betzig. Proposed method for molecular optical imaging. *Optics Letters*, 20(3):237–239, 1995.

[8] Thomas A. Klar and Stefan W. Hell. Subdiffraction resolution in far-field fluorescence microscopy. *Optics Letters*, 24(14):954–956, 1999.

[9] Eric Betzig, George H. Patterson, Rachid Sougrat, O. Wolf Lindwasser, Scott Olenych, Juan S. Bonifacino, Michael W. Davidson, Jennifer Lippincott-Schwartz, and Harald F. Hess. Imaging intracellular fluorescent proteins at nanometer resolution. *Science*, 313(5793):1642–1645, 2006.

[10] Michael J. Rust, Mark Bates, and Xiaowei Zhuang. Sub-diffraction-limit imaging by stochastic optical reconstruction microscopy (STORM). *Nature Methods*, 3(10):793–795, 2006.

[11] W. E. Moerner and L. Kador. Optical detection and spectroscopy of single molecules in a solid. *Physical Review Letters*, 62(21):2535–2538, 1989.

[12] UNAIDS. 2013 Global fact sheet, 2013. Accessed: 12 January 2016, available from: `http://www.unaids.org/sites/default/files/en/media/unaids/contentassets/documents/epidemiology/2013/gr2013/20130923_FactSheet_Global_en.pdf`.

[13] P. A. M. Dirac. The quantum theory of the emission and absorption of radiation. *Proceedings of the Royal Society of London A: Mathematical, Physical and Engineering Sciences*, 114(767):243–265, 1927.

[14] Max Born and Julius Robert Oppenheimer. Zur Quantentheorie der Molekeln. *Annalen der Physik*, 389(20):457–484, 1927.

[15] J. Franck and E. G. Dymond. Elementary processes of photochemical reactions. *Transactions of the Faraday Society*, 21:536–542, 1926.

[16] Edward U. Condon. Nuclear motions associated with electron transitions in diatomic molecules. *Physical Review*, 32(6):858–872, 1928.

[17] George G. Stokes. On the change of refrangibility of light. *Philosophical Transactions*, 142:463–562, 1852.

[18] A. Jaboski. Efficiency of anti-Stokes fluorescence in dyes. *Nature*, 131(3319):839–840, 1933.

[19] Joseph R. Lakowicz. *Fluorescence Spectroscopy*, book section Quenching of Fluorescence, pages 278–330. Springer, New York, 3rd edition, 2006.

[20] Joseph R. Lakowicz. *Fluorescence Spectroscopy*, book section Energy Transfer, pages 443–475. Springer, New York, 3rd edition, 2006.

[21] Oskar Heimstädt. Das Fluoreszenzmikroskop. *Zeitschrift für wissenschaftliche Mikroskopie*, 28(1):330–337, 1911.

[22] Nikolaus Naredi-Rainer, Jens Prescher, Achim Hartschuh, and Don C. Lamb. *Fluorescence Microscopy*, book section Confocal Microscopy, pages 175–213. Wiley-VCH, Weinheim, Germany, 1st edition, 2013.

[23] J. S. Ploem. The use of a vertical illuminator with interchangeable dichroic mirrors for fluorescence microscopy with incident light. *Zeitschrift für wissenschaftliche Mikroskopie*, 68:129–142, 1967.

[24] David Dussault and Paul Hoess. Noise performance comparison of ICCD with CCD and EMCCD cameras. *Proceedings of the SPIE*, 5563:195–204, 2004.

[25] Mark Stanford Robbins and Benjamin James Hadwen. The noise performance of Electron Multiplying Charge-Coupled Devices. *IEEE Transactions on Electron Devices*, 50(5):1227–1232, 2003.

[26] Fang Huang, Tobias M. P. Hartwich, Felix E. Rivera-Molina, Yu Lin, Whitney C Duim, Jane J. Long, Pradeep D. Uchil, Jordan R. Myers, Michelle A. Baird, Walther Mothes, Michael W. Davidson, Derek Toomre, and Joerg Bewersdorf. Video-rate nanoscopy using sCMOS camera-specific single-molecule localization algorithms. *Nature Methods*, 10(7):653–658, 2013.

[27] George B. Airy. On the diffraction of an object-glass with circular aperture. *Transactions of the Cambridge Philosophical Society*, 5:283–291, 1835.

[28] Michiel Müller. *Introduction to Confocal Fluorescence Microscopy*, book section Confocal Fluorescence Microscopy, pages 1–28. The International Society for Optical Engineering, Washington, 2nd edition, 2006.

[29] C. E. Shannon. Communication in the presence of noise. *Proceedings of the IRE*, 37(1):10–21, 1949.

[30] C. M. Sparrow. On spectroscopic resolving power. *The Astrophyical Journal*, 44(2):76–86, 1916.

[31] E. J. Ambrose. The movements of fibrocytes. *Experimental Cell Research*, 8:54–73, 1961.

[32] Nancy L. Thompson, Thomas P. Burghardt, and Daniel Axelrod. Measuring surface dynamics of biomolecules by total internal reflection fluorescence with photobleaching recovery or correlation spectroscopy. *Biophysical Joumal*, 33(3):435–454, 1981.

[33] Daniel Axelrod. Cell-substrate contacts illuminated by total internal reflection fluorescence. *The Journal of Cell Biology*, 89(1):141–145, 1981.

[34] Rainer Heintzmann. *Fluorescence Microscopy*, book section Introduction to Optics and Photophysics, pages 175–213. Wiley-VCH, Weinheim, Germany, 1st edition, 2013.

[35] Srinivasan Ramachandran, Daniel A. Cohen, Arjan P. Quist, and Ratnesh Lal. High performance, LED powered, waveguide based total internal reflection microscopy. *Scientific Reports*, 3:2133, 2013.

[36] Andrea L. Stout and Daniel Axelrod. Evanescent field excitation of fluorescence by epi-illumination microscopy. *Applied Optics*, 28(24):5237–5242, 1989.

[37] E. H. Synge. A suggested method for extending microscopic resolution into the ultra-microscopic region. *Philosophical Magazine, Series 7*, 6(35):356–362, 1928.

[38] D. W. Pohl, W. Denk, and M. Lanz. Optical stethoscopy: Image recording with resolution λ/20 . *Applied Physics Letters*, 44(7):651–653, 1984.

[39] A. Lewis, M. Isaacson, A. Harootunian, and A. Muray. Development of a 500 Å spatial resolution light microscope: I. Light is efficiently transmitted through λ/16 diameter apertures. *Ultramicroscopy*, 13(3):227–231, 1984.

[40] A. Schropp, R. Hoppe, J. Patommel, D. Samberg, F. Seiboth, S. Stephan, G. Wellenreuther, G. Falkenberg, and C. G. Schroer. Hard X-ray scanning microscopy with coherent radiation: Beyond the resolution of conventional X-ray microscopes. *Appl. Phys. Lett.*, 100(25):253112, 2012.

[41] H. Jaksch and J. P. Martin. High-resolution, low-voltage SEM for true surface imaging and analysis. *Fresenius' Journal of Analytical Chemistry*, 353(3):378–382, 1995.

[42] Rolf Erni, Marta D. Rossell, Christian Kisielowski, and Ulrich Dahmen. Atomic-resolution imaging with a sub-50-pm electron probe. *Physical Review Letters*, 102(9):096101, 2009.

[43] Russell E. Thompson, Daniel R. Larson, and Watt W. Webb. Precise nanometer localization analysis for individual fluorescent probes. *Biophysical Journal*, 82(5):2775–2783, 2002.

[44] Ahmet Yildiz, Joseph N. Forkey, Sean A. McKinney, Taekjip Ha, Yale E. Goldman, and Paul R. Selvin. Myosin V walks hand-over-hand: Single fluorophore imaging with 1.5-nm localization. *Science*, 300(5628):2061–2065, 2003.

[45] Aurelie Dupont and Don C. Lamb. Nanoscale three-dimensional single particle tracking. *Nanoscale*, 3(11):4532–4541, 2011.

[46] W. Schottky. Über spontane Stromschwankungen in verschiedenen Elektrizitätsleitern. *Annalen der Physik*, 362(23):541–567, 1918.

[47] E. Schrödinger. Are there quantum jumps? *British Journal for the Philosophy of Science*, 3(11):233–242, 1952.

[48] M. Orrit and J. Bernard. Single pentacene molecules detected by fluorescence excitation in a p-terphenyl crystal. *Physical Review Letters*, 65(21):2716–2719, 1990.

[49] E. Brooks Shera, Newton K. Seitzinger, Lloyd M. Davis, Richard A. Keller, and Steven A. Soper. Detection of single fluorescent molecules. *Chemical Physics Letters*, 174(6):553–557, 1990.

[50] Samuel T. Hess, Thanu P.K. Girirajan, and Michael D. Mason. Ultra-high resolution imaging by fluorescence photoactivation localization microscopy. *Biophysical Joumal*, 91(11):4258–4272, 2006.

[51] Osamu Shimomura, Frank H. Johnson, and Yo Saiga. Extraction, purification and properties of Aequorin, a bioluminescent protein from the Luminous Hydromedusan, Aequorea. *Journal of Cellular and Comparative Physiology*, 59(3):223–239, 1962.

[52] Robert M. Dickson, Andrew B. Cubitt, Roger Y. Tsien, and W. E. Moerner. On/off blinking and switching behaviour of single molecules of green fluorescent protein. *Nature*, 338(6640):355–358, 1997.

[53] Jörg Wiedenmann, Sergey Ivanchenko, Franz Oswald, Florian Schmitt, Carlheinz Röcker, Anya Salih, Klaus-Dieter Spindler, and G. Ulrich Nienhaus. EosFP, a fluorescent marker protein with UV-inducible green-to-red fluorescence conversion. *PNAS*, 101(45):15905–15910, 2004.

[54] Graham T. Dempsey, Joshua C. Vaughan, Kok Hao Chen, Mark Bates, and Xiaowei Zhuang. Evaluation of fluorophores for optimal performance in localization-based super-resolution imaging. *Nature Methods*, 8(12):1027–1036, 2011.

[55] Jonas Fölling, V. Belov, R. Kunetsky, R. Medda, A. Schönle, A. Egner, Christian Eggeling, Mariano Bossi, and StefanW. Hell. Photochromic rhodamines provide nanoscopy with optical sectioning. *Angewandte Chemie Int. Ed.*, 46(33):6266–6270, 2007.

[56] Joan C. Politz. Use of caged fluorochromes to track macromolecular movement in living cells. *Trends in Cell Biology*, 9(7):284–287, 1999.

[57] Jonas Fölling, Mariano Bossi, Hannes Bock, Rebecca Medda, Christian A Wurm, Birka Hein, Stefan Jakobs, Christian Eggeling, and Stefan W. Hell. Fluorescence nanoscopy by ground-state depletion and single-molecule return. *Nature Methods*, 5(11):943–945, 2008.

[58] Graham T. Dempsey, Mark Bates, Walter E. Kowtoniuk, David R. Liu, Roger Y. Tsien, and Xiaowei Zhuang. Photoswitching mechanism of cyanine dyes. *Journal of the American Chemical Society*, 131(51):18192–18193, 2009.

[59] Sebastian van de Linde, Anna Löschberger, Teresa Klein, Meike Heidbreder, Steve Wolter, Mike Heilemann, and Markus Sauer. Direct stochastic optical reconstruction microscopy with standard fluorescent probes. *Nature Protocols*, 6(7):991–1009, 2011.

[60] Mark Bates, Bo Huang, Graham T. Dempsey, and Xiaowei Zhuang. Multicolor super-resolution imaging with photo-switchable fluorescent probes. *Science*, 317(5845):1749–1753, 2007.

[61] Mark Bates, Timothy R. Blosser, and Xiaowei Zhuang. Short-range spectroscopic ruler based on a single-molecule optical switch. *Physical Review Letters*, 94(10):108101, 2005.

[62] Mike Heilemann, Sebastian van de Linde, Mark Schüttpelz, Robert Kasper, Britta Seefeldt, Anindita Mukherjee, Philip Tinnefeld, and Markus Sauer. Subdiffraction-resolution fluorescence imaging with conventional fluorescent probes. *Angewandte Chemie Int. Ed.*, 47(33):6172–6176, 2008.

[63] Joerg Enderlein, Erdal Toprak, and Paul R. Selvin. Polarization effect on position accuracy of fluorophore localization. *Optics Express*, 14(18):8111–8120, 2006.

[64] Sjoerd Stallinga and Bernd Rieger. Accuracy of the Gaussian point spread function model in 2D localization microscopy. *Optics Express*, 18(24):24461–24476, 2010.

[65] Hendrik Deschout, Francesca Cella Zanacchi, Michael Mlodzianoski, Alberto Diaspro, Joerg Bewersdorf, Samuel T. Hess, and Kevin Braeckmans. Precisely and accurately localizing single emitters in fluorescence microscopy. *Nature Methods*, 11(3):253–266, 2014.

[66] Carlas S. Smith, Nikolai Joseph, Bernd Rieger, and Keith A. Lidke. Fast, single-molecule localization that achieves theoretically minimum uncertainty. *Nature Methods*, 7(5):373–375, 2010.

[67] Seamus J. Holden, Stephan Uphoff, and Achillefs N. Kapanidis. DAOSTORM: an algorithm for highdensity super-resolution microscopy. *Nature Methods*, 8(4):279–280, 2011.

[68] Ke Xu, Hazen P. Babcock, and Xiaowei Zhuang. Dual-objective STORM reveals three-dimensional filament organization in the actin cytoskeleton. *Nature Methods*, 9(2):185–188, 2012.

[69] Stefan W. Hell and Ernst H. K. Stelzer. Properties of a 4Pi confocal fluorescence microscope. *Journal of the Optical Society of America A*, 9(12):2159–2166, 1992.

[70] Gleb Shtengel, James A. Galbraith, Catherine G. Galbraith, Jennifer Lippincott-Schwartz, Jennifer M. Gillette, Suliana Manley, Rachid Sougrat, Clare M. Waterman, Pakorn Kanchanawong, Michael W. Davidson, Richard D. Fetter, and Harald F. Hess. Interferometric fluorescent super-resolution microscopy resolves 3D cellular ultrastructure. *PNAS*, 106(9):3125–3130, 2008.

[71] Manuel F. Juette, Travis J. Gould, Mark D. Lessard, Michael J. Mlodzianoski, Bhupendra S. Nagpure, Brian T. Bennett, Samuel T. Hess, and Joerg Bewersdorf. Three-dimensional sub-100 nm resolution fluorescence microscopy of thick samples. *Nature Methods*, 5(6):527–529, 2008.

[72] Bo Huang, Wenqin Wang, Mark Bates, and Xiaowei Zhuang. Three-dimensional super-resolution imaging by stochastic optical reconstruction microscopy. *Science*, 319(5864):810–813, 2008.

[73] Bo Huang, Sara A. Jones, Boerries Brandenburg, and Xiaowei Zhuang. Whole-cell 3D STORM reveals interactions between cellular structures with nanometer-scale resolution. *Nature Methods*, 5(12):1047–1052, 2008.

[74] H. Pin Kao and A. S. Verkman. Tracking of single fluorescent particles in three dimensions: use of cylindrical optics to encode particle position. *Biophysical Joumal*, 67:1291–1300, 1994.

[75] T. Dertinger, R. Colyer, G. Iyer, S. Weiss, and J. Enderlein. Fast, background-free, 3D super-resolution optical fluctuation imaging (SOFI). *PNAS*, 106(52):22287–22292, 2009.

[76] Stefan Geissbuehler, Claudio Dellagiacoma, and Theo Lasser. Comparison between SOFI and STORM. *Biomedical Optics Express*, 2(3):408–420, 2011.

[77] Thomas Dertinger, Jianmin Xu, Omeed Naini, Robert Vogel, and Shimon Weiss. SOFI-based 3D superresolution sectioning with a widefield microscope. *Optical Nanoscopy*, 1:2, 2012.

[78] Alexey Sharonov and Robin M. Hochstrasser. Wide-field subdiffraction imaging by accumulated binding of diffusing probes. *PNAS*, 103(50):18911–18916, 2006.

[79] Ralf Jungmann, Christian Steinhauer, Max Scheible, Anton Kuzyk, Philip Tinnefeld, and Friedrich C. Simmel. Single-molecule kinetics and super-resolution microscopy by fluorescence imaging of transient binding on DNA origami. *Nano Letters*, 10(11):4756–4761, 2010.

[80] Ralf Jungmann, Maier S. Avendano, Johannes B. Woehrstein, Mingjie Dai, William M. Shih, and Peng Yin. Multiplexed 3D cellular super-resolution imaging with DNA-PAINT and Exchange-PAINT. *Nature Methods*, 11(3):313–318, 2014.

[81] D. Wildanger, R. Medda, L. Kastrup, and S. W. Hell. A compact STED microscope providing 3D nanoscale resolution. *Journal of Microscopy*, 236(1):35–43, 2009.

[82] Marcus Dyba and Stefan W. Hell. Focal spots of size $\lambda/23$ open up far-field florescence microscopy at 33 nm axial resolution. *Physical Review Letters*, 88(16):163901, 2002.

[83] Charles-È. Guillaume. *Nobel Lectures, Physics: 1901-1921*, book section Invar and elinvar, pages 444–473. Elsevier Pubishing Group, Amsterdam, 1967.

[84] N. Minorsky. Directional stability Of automatically steered bodies. *Journal of the American Society for Naval Engineers*, 34(2):280–309, 1922.

[85] J. G. Ziegler and N. B. Nichols. Optimum settings for automatic controllers. *Transactions of the ASME*, 64:759–768, 1942.

[86] Kiam Heong Ang, Gregory Chong, and Yun Li. PID control system analysis, design, and technology. *IEEE Transactions on Control Systems Technology*, 13(4):559–576, 2005.

[87] Remi L. Boulineau and Mark A. Osborne. Direct object resolution by image subtraction: a new molecular ruler for nanometric measurements on complexed fluorophores. *Chemical Communications*, 49(49):5559–5561, 2013.

[88] Sebastian van de Linde, Ivan Krstic, Thomas Prisner, Soren Doose, Mike Heilemann, and Markus Sauer. Photoinduced formation of reversible dye radicals and their impact on super-resolution imaging. *Photochemical & Photobiological Sciences*, 10(4):499–506, 2011.

[89] Ricardo Henriques, Mickael Lelek, Eugenio F. Fornasiero, Flavia Valtorta, Christophe Zimmer, and Musa M. Mhlanga. QuickPALM: 3D real-time photoactivation nanoscopy image processing in ImageJ. *Nature Methods*, 7(5):339–340, 2010.

[90] Per Niklas Hedde, Jochen Fuchs, Franz Oswald, Jörg Wiedenmann, and Gerd Ulrich Nienhaus. Online image analysis software for photoactivation localization microscopy. *Nature Methods*, 6(10):689–690, 2009.

[91] Sean B. Andersson. Localization of a fluorescent source without numerical fitting. *Optics Express*, 16(23):18714–18724, 2008.

[92] Raghuveer Parthasarathy. Rapid, accurate particle tracking by calculation of radial symmetry centers. *Nature Methods*, 9(7):724–726, 2012.

[93] Daniel Sage, Hagai Kirshner, Thomas Pengo, Nico Stuurman, Junhong Min, Suliana Manley, and Michael Unser. Quantitative evaluation of software packages for single-molecule localization microscopy. *Nature Methods*, 12(8):717–724, 2015.

[94] Hazen Babcock, Yaron M Sigal, and Xiaowei Zhuang. A high-density 3D localization algorithm for stochastic optical reconstruction microscopy. *Optical Nanoscopy*, 1(1):1–10, 2012.

[95] Kenneth Levenberg. A method for the solution of certain non-linear problems in least squares. *Quarterly of Applied Mathematics*, 2:164–168, 1944.

[96] Donald W. Marquardt. An Algorithm for least-squares estimation of nonlinear parameters. *Journal of the Society for Industrial and Applied Mathematics*, 11(2):431–441, 1963.

[97] Steve Wolter, Anna Löschberger, Thorge Holm, Sarah Aufmkolk, Marie-Christine Dabauvalle, Sebastian van de Linde, and Markus Sauer. rapidSTORM: accurate, fast open-source software for localization microscopy. *Nature Methods*, 9(11):1040–1041, 2012.

[98] Janne Holopainen. Levenberg-Marquardt Algorithm (LMA) fit for non-linear, multidimensional parameter space for any multidimensional fit function, 2007. Accessed: 12 January 2016, available from: `http://virtualrisk.cvs.sourceforge.net/viewvc/virtualrisk/util/lma/`.

[99] Kim I. Mortensen, L. Stirling Churchman, James A. Spudich, and Henrik Flyvbjerg. Optimized localization analysis for single-molecule tracking and super-resolution microscopy. *Nature Methods*, 7(5):377–381, 2010.

[100] J. A. Nelder and R. Mead. A simplex method for function minimization. *The Computer Journal*, 7(4):308–313, 1965.

[101] Martin Lehmann, Susana Rocha, Bastien Mangeat, Fabien Blanchet, Hiroshi Uji-i, Johan Hofkens, and Vincent Piguet. Quantitative multicolor super-resolution microscopy reveals tetherin HIV-1 interaction. *PLoS Pathogens*, 7(12):e1002456, 2011.

[102] Harald Cramér. Über eine Eigenschaft der normalen Verteilungsfunktion. *Mathematische Zeitschrift*, 41(1):405–414, 1936.

[103] Brian D. Ripley. Modelling spatial patterns. *Journal of the Royal Statistical Society. Series B (Methodological)*, 39(2):172–212, 1977.

[104] Brian D. Ripley. Tests of 'randomness' for spatial point patterns. *Journal of the Royal Statistical Society. Series B (Methodological)*, 41(3):368–374, 1979.

[105] J. E. Besag. Comments on Ripley's paper. *Journal of the Royal Statistical Society. Series B (Methodological)*, 39(2):193–195, 1977.

[106] Maria A. Kiskowski, John F. Hancock, and Anne K. Kenworthy. On the use of Ripley's K-Function and its derivatives to analyze domain size. *Biophysical Joumal*, 97(4):1095–1103, 2009.

[107] Georg Löffler and Petro E. Petrides. *Biochemie und Pathobiochemie.* Springer-Verlag, Berlin, Heidelberg, 1998.

[108] Klaus Weber, Peter C. Rathke, and Mary Osborn. Cytoplasmic microtubular images in glutaraldehyde-fixed tissue culture cells by electron microscopy and by immunofluorescence microscopy. *PNAS*, 75(4):1820–1824, 1978.

[109] Ulrich Rothbauer, Kourosh Zolghadr, Sergei Tillib, Danny Nowak, Lothar Schermelleh, Anja Gahl, Natalija Backmann, Katja Conrath, Serge Muyldermans, M Cristina Cardoso, and Heinrich Leonhard. Targeting and tracing antigens in live cells with fluorescent nanobodies. *Nature Methods*, 3(11):887–889, 2006.

[110] Jonas Ries, Charlotte Kaplan, Evgenia Platonova, Hadi Eghlidi, and Helge Ewers. A simple, versatile method for GFP-based super-resolution microscopy via nanobodies. *Nature Methods*, 9(6):582–584, 2012.

[111] Alexandre Juillerat, Thomas Gronemeyer, Antje Keppler, Susanne Gendreizig, Horst Pick, Horst Vogel, and Kai Johnsson. Directed evolution of O^6-alkylguanine-DNA alkyltransferase for efficient labeling of fusion proteins with small molecules in vivo. *Chemistry & Biology*, 10(4):313–317, 2003.

[112] Julia von Blume, Anne-Marie Alleaume, Christine Kienzle, Amado Carreras-Sureda, Miguel Valverde, and Vivek Malhotra. Cab45 is required for Ca^{2+}-dependent secretory cargo sorting at the trans-Golgi network. *The Journal of Cell Biology*, 199(7):1057–1066, 2012.

[113] Jens Prescher, Viola Baumgärtel, Sergey Ivanchenko, Adriano A. Torrano, Christoph Bräuchle, Barbara Müller, and Don C. Lamb. Super-resolution imaging of ESCRT-proteins at HIV-1 assembly sites. *PLoS Pathogens*, 10(2):e1004677, 2015.

[114] Creative Commons. Creative commons Attribution 4.0 International, 2013. Accessed: 12 January 2016, available from: `https://creativecommons.org/licenses/by/4.0/legalcode`.

[115] Centers for Disease Control. Pneumocystis Pneumonia – Los Angeles. *Morbidity and Mortality Weekly Report*, 30(21):250–252, 1981.

[116] F. Barre-Sinoussi, J.C. Chermann, F. Rey, M.T. Nugeyre, S. Chamaret, J. Gruest, C. Dauguet, C. Axler-Blin Vezinet-Brun, C. Rouzioux, W. Rozenbaum, and L. Montagnier. Isolation of a T-Lymphotropic retrovirus from patient at risk for acquired immune deficiency syndrome (AIDS). *Science*, 220(4599):868–871, 1983.

[117] R. C. Gallo, P. S. Sarin, E. P. Gelmann, M. Robert-Guroff, E. Richardson, V. S. Kalyanaraman, D. Mann, G. D. Sidhu, R. E. Stahl, S. Zolla-Pazner, J. Leibowitch, and M. Popovic. Isolation of human T-cell leukemia virus in acquired immune deficiency syndrome (AIDS). *Science*, 220(4599):865–867, 1983.

[118] Bernard J. Poiesz, Francis W. Ruscetti, Adi F. Gazdar, Paul A. Bunn, John D. Minna, and Robert C. Gallo. Detection and isolation of type C retrovirus particles from fresh and cultured lymphocytes of a patient with cutaneous T-cell lymphoma. *PNAS*, 77(12):7415–7419, 1980.

[119] Ashley T. Haase. Pathogenesis of lentivirus infections. *Nature*, 322(6075):130–136, 1986.

[120] Hengli Tang, Kelli L. Kuhen, and Flossie Wong-Staal. Lentivirus Replication and Regulation. *Annual Review of Genetics*, 33(1):133–170, 1999.

[121] Anthony S. Fauci. Immunopathogenesis of HIV infection. *Annals of the New York Academy of Sciences*, 685(1):409–419, 1993.

[122] F. Clavel, D. Guetard, F. Brun-Vezinet, S. Chamaret, M. A. Rey, M. O. Santos-Ferreira, A. G. Laurent, C. Dauguet, C. Katlama, C. Rouzioux, and et al. Isolation of a new human retrovirus from West African patients with AIDS. *Science*, 233(4761):343–346, 1986.

[123] Jacqueline D. Reeves and Robert W. Doms. Human immunodeficiency virus type 2. *Journal of General Virology*, 83(6):1253–1265, 2002.

[124] Joseph M. Watts, Kristen K. Dang, Robert J. Gorelick, Christopher W. Leonard, Julian W. Bess Jr, Ronald Swanstrom, Christina L. Burch, and Kevin M. Weeks. Architecture and secondary structure of an entire HIV-1 RNA genome. *Nature*, 460(7256):711–716, 2009.

[125] Inder M. Verma. The reverse transcriptase. *Biochimica et Biophysica Acta (BBA) - Reviews on Cancer*, 473(1):1–38, 1977.

[126] Anthony D. Hoffman, Babak Banapour, and Jay A. Levy. Characterization of the AIDS-associated retrovirus reverse transcriptase and optimal conditions for its detection in virions. *Virology*, 147(2):326–335, 1985.

[127] Lee Ratner, William Haseltine, Roberto Patarca, Kenneth J. Livak, Bruno Starcich, Steven F. Josephs, Ellen R. Doran, J. Antoni Rafalski, Erik A. Whitehorn, Kirk Baumeister, Lucinda Ivanoff, Stephen R. Petteway, Mark L. Pearson, James A. Lautenberger, Takis S. Papas, John Ghrayeb, Nancy T. Chang, Robert C. Gallo, and Flossie Wong-Staal. Complete nucleotide sequence of the AIDS virus, HTLV-III. *Nature*, 313(6000):277–284, 1985.

[128] R. Sanchez-Pescador, M. D. Power, P. J. Barr, K. S. Steimer, M. M. Stempien, S. L. Brown-Shimer, W. W. Gee, A. Renard, A. Randolph, J. A. Levy, D. Dina, and A. Luciw, P. Nucleotide sequence and expression of an AIDS-associated retrovirus (ARV-2). *Science*, 227(4686):484–492, 1985.

[129] Simon Wain-Hobson, Pierre Sonigo, Olivier Danos, Stewart Cole, and Marc Alizon. Nucleotide sequence of the AIDS virus, LAV. *Cell*, 40(1):9–17, 1985.

[130] Robert Craigie. HIV integrase, a brief overview from chemistry to therapeutics. *Journal of Biological Chemistry*, 276(26):23213–23216, 2001.

[131] J. S. Allan, J. E. Coligan, F. Barin, M. F. McLane, J. G. Sodroski, C. A. Rosen, W. A. Haseltine, T. H. Lee, and M. Essex. Major glycoprotein antigens that induce antibodies in AIDS patients are encoded by HTLV-III. *Science*, 228(4703):1091–1094, 1985.

[132] Richard Wyatt and Joseph Sodroski. The HIV-1 envelope glycoproteins: fusogens, antigens, and immunogens. *Science*, 280(5371):1884–1888, 1998.

[133] Viola Baumgärtel, Sergey Ivanchenko, Barbara Müller, and Don C. Lamb. *Fluorescent Proteins II*, volume 12 of *Springer Series on Fluorescence*, book section Investigating the Life Cycle of HIV with Fluorescent Proteins, pages 249–277. Springer Berlin Heidelberg, 2012.

[134] Ruba H. Ghanam, Alexandra B. Samal, Timothy .F Fernandez, and Jamil S. Saad. Role of the HIV-1 matrix protein in Gag intracellular trafficking and targeting to the plasma membrane for virus assembly. *Frontiers in Microbiology*, 3, 2012.

[135] Su Li, Christopher P. Hill, Wesley I. Sundquist, and John T. Finch. Image reconstructions of helical assemblies of the HIV-1 CA protein. *Nature*, 407(6802):409–413, 2000.

[136] Gongpu Zhao, Juan R. Perilla, Ernest L. Yufenyuy, Xin Meng, Bo Chen, Jiying Ning, Jinwoo Ahn, Angela M. Gronenborn, Klaus Schulten, Christopher Aiken, and Peijun Zhang. Mature HIV-1 capsid structure by cryo-electron microscopy and all-atom molecular dynamics. *Nature*, 497(7451):643–646, 2013.

[137] Tyler Jacks, Michael D. Power, Frank R. Masiarz, Paul A. Luciw, Philip J. Barr, and Harold E. Varmus. Characterization of ribosomal frameshifting in HIV-1 gag-pol expression. *Nature*, 331(6153):280–283, 1988.

[138] Miranda Shehu-Xhilaga, Suzanne M. Crowe, and Johnson Mak. Maintenance of the Gag/Gag-Pol ratio is important for human immunodeficiency virus type 1 RNA dimerization and viral infectivity. *Journal of Virology*, 75(4):1834–1841, 2001.

[139] Jonathan Karn and C. Martin Stoltzfus. Transcriptional and posttranscriptional regulation of HIV-1 gene expression. *Cold Spring Harbor Perspectives in Medicine*, 2(2), 2012.

[140] David R. Collins and Kathleen L. Collins. HIV-1 accessory proteins adapt cellular adaptors to facilitate immune evasion. *PLoS Pathogens*, 10(1):e1003851, 2014.

[141] Angus G. Dalgleish, Peter C. L. Beverley, Paul R. Clapham, Dorothy H. Crawford, Melvyn F. Greaves, and Robin A. Weiss. The CD4 (T4) antigen is an essential component of the receptor for the AIDS retrovirus. *Nature*, 312(5996):763–767, 1984.

[142] Gretja Schnell, Sarah Joseph, Serena Spudich, Richard W. Price, and Ronald Swanstrom. HIV-1 replication in the central nervous system occurs in two distinct cell types. *PLoS Pathogens*, 7(10):e1002286, 2011.

[143] Olivier Manches, Davor Frleta, and Nina Bhardwaj. Dendritic cells in progression and pathology of HIV infection. *Trends in Immunology*, 35(3):114–122, 2014.

[144] Charles A. Janeway and Paul Travers. *Immunologie*. Spektrum Akademischer Verlag, Heidelberg, 1997.

[145] Ghalib Alkhatib and Edward A. Berger. HIV coreceptors: from discovery and designation to new paradigms and promise. *European journal of medical research*, 12(9):375–384, 2007.

[146] Jessica Daecke, Oliver T. Fackler, Matthias T. Dittmar, and Hans-Georg Kräusslich. Involvement of clathrin-mediated endocytosis in human immunodeficiency virus type 1 entry. *Journal of Virology*, 79(3):1581–1594, 2005.

[147] Edward M. Campbell and Thomas J. Hope. HIV-1 capsid: the multifaceted key player in HIV-1 infection. *Nat. Rev. Microbiol.*, 13(8):471–483, 2015.

[148] Debbie S. Ruelas and Warner C. Greene. An integrated overview of HIV-1 latency. *Cell*, 155(3):519–529, 2013.

[149] Dirk Gheysen, Eric Jacobs, Franoise de Foresta, Clotilde Thiriart, Myriam Francotte, Denise Thines, and Michel De Wilde. Assembly and release of HIV-1 precursor Pr55gag virus-like particles from recombinant baculovirus-infected insect cells. *Cell*, 59(1):103–112, 1989.

[150] Akira Ono, Sherimay D. Ablan, Stephen J. Lockett, Kunio Nagashima, and Eric O. Freed. Phosphatidylinositol (4,5) bisphosphate regulates HIV-1 Gag targeting to the plasma membrane. *PNAS*, 101(41):14889–14894, 2004.

[151] Wesley I. Sundquist and Hans-Georg Kräusslich. HIV-1 assembly, budding, and maturation. *Cold Spring Harbor Perspectives in Medicine*, 2(7):a007823, 2012.

[152] John A.G. Briggs and Hans-Georg Kräusslich. The molecular architecture of HIV. *Journal of Molecular Biology*, 410(4):491–500, 2011.

[153] Sergey Ivanchenko, William J. Godinez, Marko Lampe, Hans-Georg Kräusslich, Roland Eils, Karl Rohr, Christoph Bräuchle, Barbara Müller, and Don C. Lamb. Dynamics of HIV-1 assembly and release. *PLoS Pathogens*, 5(11):e1000652, 2009.

[154] Nolwenn Jouvenet, Paul D. Bieniasz, and Sanford M. Simon. Imaging the biogenesis of individual HIV-1 virions in live cells. *Nature*, 454(7201):236–240, 2008.

[155] Barbie K. Ganser-Pornillos, Mark Yeager, and Wesley I. Sundquist. The structural biology of HIV assembly. *Current Opinion in Structural Biology*, 18(2):203–217, 2008.

[156] Jörg Votteler and Wesley I. Sundquist. Virus budding and the ESCRT pathway. *Cell Host & Microbe*, 14(3):232–241, 2013.

[157] Eric R. Weiss and Heinrich G. Göttlinger. The role of cellular factors in promoting HIV budding. *Journal of Molecular Biology*, 410(4):525–533, 2011.

[158] Juan Martin-Serrano and Stuart J. D. Neil. Host factors involved in retroviral budding and release. *Nature Reviews Microbiology*, 9(7):519–531, 2011.

[159] Anna Caballe and Juan Martin-Serrano. ESCRT machinery and cytokinesis: the road to daughter cell separation. *Traffic*, 12(10):1318–1326, 2011.

[160] Thomas Wollert and James H. Hurley. Molecular mechanism of multivesicular body biogenesis by ESCRT complexes. *Nature*, 464:864–869, 2010.

[161] Camilla Raiborg and Harald Stenmark. The ESCRT machinery in endosomal sorting of ubiquitylated membrane proteins. *Nature*, 458(7237):445–452, 2009.

[162] Markus Babst. MVB vesicle formation: ESCRT-dependent, ESCRT-independent and everything in between. *Current Opinion in Cell Biology*, 23:1–6, 2011.

[163] Yolanda Olmos, Lorna Hodgson, Judith Mantell, Paul Verkade, and Jeremy G. Carlton. ESCRT-III controls nuclear envelope reformation. *Nature*, 522(7555):236–239, 2015.

[164] David Teis, Suraj Saksena, and Scott D. Emr. The ESCRT machinery. *Cell*, 137:182–183, 2009.

[165] John McCullough, Leremy A. Colf, and Wesley I. Sundquist. Membrane fission reactions of the mammalian ESCRT pathway. *Annual Review of Biochemistry*, 82:663–692, 2013.

[166] Uta K. von Schwedler, Melissa Stuchell, Barbara Müller, Diane M. Ward, Hyo-Young Chung, Eiji Morita, Hubert E. Wang, Thaylon Davis, Gong-Ping He, Daniel M. Cimbora, Anna Scott, Hans-Georg Kräusslich, Jerry Kaplan, Scott G. Morham, and Wesley I. Sundquist. The protein network of HIV budding. *Cell*, 114(6):701–713, 2003.

[167] Melissa D. Stuchell, Jennifer E. Garrus, Barbara Müller, Kirsten M. Stray, Sanaz Ghaffarian, Rena McKinnon, Hans-Georg Kräusslich, Scott G. Morham, and Wesley I. Sundquist. The human endosomal sorting complex required for transport (ESCRT-I) and its role in HIV-1 budding. *The Journal of Biological Chemistry*, 279(34):36059–36071, 2004.

[168] Nolwenn Jouvenet, Maria Zhadina, Paul D. Bieniasz, and Sanford M. Simon. Dynamics of ESCRT protein recruitment during retroviral assembly. *Nature Cell Biology*, 13(4):394–401, 2011.

[169] Eiji Morita, Virginie Sandrin, John McCullough, Angela Katsuyama, Ira Baci Hamilton, and Wesley I. Sundquist. ESCRT-III protein requirements for HIV-1 budding. *Cell Host & Microbe*, 9(3):235–242, 2011.

[170] Ivana De Domenico, Diane McVey Ward, Charles Langelier, Michael B. Vaughn, Elizabeta Nemeth, Wesley I. Sundquist, Tomas Ganz, Giovanni Musci, and Jerry Kaplan. The molecular mechanism of hepcidin-mediated ferroportin down-regulation. *Cell*, 18(7):2569–2578, 2007.

[171] Dimiter G. Demirov, Jan M. Orenstein, and Eric O. Freed. The late domain of human immunodeficiency virus type 1 p6 promotes virus release in a cell type-dependent manner. *Journal of Virology*, 76(1):105–117, 2002.

[172] Bettina Strack, Arianna Calistri, Stewart Craig, Elena Popova, and Heinrich G. Göttlinger. AIP1/ALIX is a binding partner for HIV-1 p6 and EIAV p9 functioning in virus budding. *Cell*, 114(6):689–699, 2003.

[173] Juan Martin-Serrano, Trinity Zang, and Paul D. Bieniasz. Role of ESCRT-I in retroviral budding. *Journal of Virology*, 77(8):4794–4804, 2003.

[174] Bo Meng, Natasha Ip, Liam Prestwood, Truus Abbink, and Andrew Lever. Evidence that the endosomal sorting complex required for transport-II (ESCRT-II) is required for efficient human immunodeficiency virus-1 (HIV-1) production. *Retrovirology*, 12(1):72, 2015.

[175] Katy Janvier, Annegret Pelchen-Matthews, Jean-Baptiste Renaud, Marina Caillet, Mark Marsh, and Clarisse Berlioz-Torrent. The ESCRT-0 component HRS is required for HIV-1 Vpu-mediated BST-2/tetherin down-regulation. *PLoS Pathogens*, 7(2):e1001265, 2011.

[176] Eric O. Freed. Viral late domains. *Journal of Virology*, 76(10):4679–4687, 2002.

[177] Jennifer E. Garrus, Uta K. von Schwedler, Owen W. Pornillos, Scott G. Morham, Kenton H. Zavitz, Hubert E. Wang, Daniel A. Wettstein, Kirsten M. Stray, Mélanie Côté, Rebecca L. Rich, David G. Myszka, and Wesley I. Sundquist. Tsg101 and the vacuolar protein sorting pathway are essential for HIV-1 budding. *Cell*, 107(1):55–65, 2001.

[178] Juan Martin-Serrano, Trinity Zang, and Paul D. Bieniasz. HIV-1 and Ebola virus encode small peptide motifs that recruit Tsg101 to sites of particle assembly to facilitate egress. *Nature Medicine*, 7(12):1313–1319, 2001.

[179] Lynn VerPlank, Fadila Bouamr, Tracy J. LaGrassa, Beth Agresta, Alexandra Kikonyogo, Jonathan Leis, and Carol A. Carter. Tsg101, a homologue of ubiquitin-conjugating (E2) enzymes, binds the L domain in HIV type 1 Pr55Gag. *PNAS*, 98(14):7724–7729, 2001.

[180] Heinrich G. Göttlinger, T. Dorfman, J. G. Sodroski, and W. A. Haseltine. Effect of mutations affecting the p6 gag protein on human immunodeficiency virus particle release. *PNAS*, 88(8):3195–3199, 1991.

[181] M. Huang, J. M. Orenstein, M. A. Martin, and E. O. Freed. p6$^{\mathrm{Gag}}$ is required for particle production from full-length human immunodeficiency virus type 1 molecular clones expressing protease. *Jorunal of Virology*, 69(11):6810–6818, 1995.

[182] B. A. Puffer, L. J. Parent, J. W. Wills, and R. C. Montelaro. Equine infectious anemia virus utilizes a YXXL motif within the late assembly domain of the Gag p9 protein. *Journal of Virology*, 71(9):6541–6546, 1997.

[183] Juan Martin-Serrano, Anton Yarovoy, David Perez-Caballero, and Paul D. Bieniasz. Divergent retroviral late-budding domains recruit vacuolar protein sorting factors by using alternative adaptor proteins. *PNAS*, 100(21):12414–12419, 2003.

[184] Robert D. Fisher, Hyo-Young Chung, Qianting Zhai, Howard Robinson, Wesley I. Sundquist, and Christopher P. Hill. Structural and biochemical studies of ALIX/AIP1 and its role in retrovirus budding. *Cell*, 128:841–852, 2007.

[185] Ken Fujii, Utpal M. Munshi, Sherimay D. Ablan, Dimiter G. Demirov, Ferri Soheilian, Kunio Nagashima, Andrew G. Stephen, Robert J. Fisher, and Eric O. Freed. Functional role of Alix in HIV-1 replication. *Virology*, 391(2):284–292, 2009.

[186] Yoshiko Usami, Sergei Popov, and Heinrich G. Göttlinger. Potent rescue of human immunodeficiency virus type 1 late domain mutants by ALIX/AIP1 depends on its CHMP4 binding site. *Journal of Virology*, 81(12):6614–6622, 2007.

[187] Utpal M. Munshi, Jaewon Kim, Kunio Nagashima, James H. Hurley, and Eric O. Freed. An Alix fragment potently inhibits HIV-1 budding – Characterization of binding to retroviral YPXL late domains. *The Journal of Biological Chemistry*, 282(6):3847–3855, 2007.

[188] Ira Herskowitz. Functional inactivation of genes by dominant negative mutations. *Nature*, 329(6136):219–222, 1987.

[189] Ricardo Pires, Bettina Hartlieb, Luca Signor, Guy Schoehn, Suman Lata, Manfred Roessle, Christine Moriscot, Sergei Popov, Andreas Hinz, Marc Jamin, Veronique Boyer, Remy Sadoul, Eric Forest, Dmitri I. Svergun, Heinrich G. Göttlinger, and Winfried Weissenhorn. A crescent-shaped ALIX dimer targets ESCRT-III CHMP4 filaments. *Structure*, 17(6):843–856, 2009.

[190] John McCullough, Robert D. Fisher, Frank G. Whitby, Wesley I. Sundquist, and Christopher P. Hill. ALIX-CHMP4 interactions in the human ESCRT pathway. *PNAS*, 105(22):7687–7691, 2008.

[191] Keiichi Katoh, Hideki Shibata, Kazumi Hatta, and Masatoshi Maki. CHMP4b is a major binding partner of the ALG-2-interacting protein Alix among the three CHMP4 isoforms. *Archives of Biochemistry and Biophysics*, 421(1):159–165, 2004.

[192] Winfried Weissenhorn and Heinrich G. Göttlinger. Essential Ingredients for HIV-1 Budding. *Cell Host & Microbe*, 9(3):172–174, 2011.

[193] Julien Guizetti and Daniel W. Gerlich. ESCRT-III polymers in membrane neck constriction. *Trends in Cell Biology*, 22(3):133–140, 2012.

[194] James H. Hurley and Phyllis I. Hanson. Membrane budding and scission by the ESCRT machinery: it's all in the neck. *Nature Reviews Molecular Cell Biology*, 11(8):556–566, 2010.

[195] Viola Baumgärtel, Sergey Ivanchenko, Aurélie Dupont, Mikhail Sergeev, Paul W. Wiseman, Hans-Georg Kräusslich, Christoph Bräuchle, Barbara Müller, and Don C. Lamb. Live-cell visualization of dynamics of HIV budding site interactions with an ESCRT component. *Nature Cell Biology*, 13(4):469–474, 2011.

[196] Phyllis I. Hanson, Robyn Roth, Yuan Lin, and John E. Heuser. Plasma membrane deformation by circular arrays of ESCRT-III protein filaments. *JCB*, 180(2):389–402, 2008.

[197] Suraj Saksena, Judit Wahlman, David Teis, Arthur E. Johnson, and Scott D. Emr. Functional reconstitution of ESCRT-III assembly and disassembly. *Cell*, 136(1):97–109, 2009.

[198] Natalie Elia, Rachid Sougrat, Tighe A. Spurlin, James H. Hurley, and Jennifer Lippincott-Schwartz. Dynamics of endosomal sorting complex required for transport (ESCRT) machinery during cytokinesis and its role in abscission. *PNAS*, 108(12):4846–4851, 2011.

[199] Gur Fabrikant, Suman Lata, James D. Riches, John A. G. Briggs, Winfried Weissenhorn, and Michael M. Kozlov. Computational model of membrane fission catalyzed by ESCRT-III. *PLoS Computational Biology*, 5(11):e1000575, 2009.

[200] Suman Lata, Guy Schoehn, Ankur Jain, Ricardo Pires, Jacob Piehle, Heinrich G. Göttlinger, and Winfried Weissenhorn. Helical structures of ESCRT-III are disassembled by VPS4. *Science*, 321(5894):1354–1357, 2008.

[201] Evzen Boura, Bartosz Różycki, Hoi Sung Chung, Dawn Z. Herrick, Bertram Canagarajah, David S. Cafiso, William A. Eaton, Gerhard Hummer, and James H. Hurley. Solution structure of the ESCRT-I and -II supercomplex: Implications for membrane budding and scission. *Structure*, 20(5):874–886, 2012.

[202] Gilles Bodon, Romain Chassefeyre, Karin Pernet-Gallay, Nicolas Martinelli, Grégory Effantin, David Lutje Hulsik, Agnès Belly, Yves Goldberg, Christine Chatellard-Causse, Béatrice Blot, Guy Schoehn, Winfried Weissenhorn, and Rémy Sadoul. Charged multivesicular body protein 2B (CHMP2B) of the endosomal sorting complex required for transport-III (ESCRT-III) polymerizes into helical structures deforming the plasma membrane. *The Journal of Biological Chemistry*, 286(46):40276–40286, 2011.

[203] Anil G. Cashikar, Soomin Shim, Robyn Roth, Michael R. Maldazys, John E. Heuser, and Phyllis I. Hanson. Structure of cellular ESCRT-III spirals and their relationship to HIV budding. *eLife*, page e02184, 2014.

[204] Megan J. Dobro, Rachel Y. Samson, Zhiheng Yu, John McCullough, H. Jane Ding, Parkson Lee-Gau Chong, Stephen D. Bell, and Grant J. Jensen. Electron cryotomography of ESCRT assemblies and dividing Sulfolobus cells suggests that spiraling filaments are involved in membrane scission. *Mol. Biol. Cell*, 24(15):2319–2327, 2013.

[205] Phyllis I. Hanson, Soomin Shim, and Samuel A Merrill. Cell biology of the ESCRT machinery. *Current Opinion in Cell Biology*, 21(4):568–574, 2009.

[206] Thomas Wollert, Christian Wunder, Jennifer Lippincott-Schwartz, and James H. Hurley. Membrane scission by the ESCRT-III complex. *Nature*, 458:172–177, 2009.

[207] Yonathan Kozlovsky and Michael M. Kozlov. Membrane Fission: Model for Intermediate Structures. *Biophysical Journal*, 85(1):85–96, 2003.

[208] David Teis, Suraj Saksena, and Scott D. Emr. Ordered assembly of the ESCRT-III complex on endosomes is required to sequester cargo during MVB formation. *Developmental Cell*, 15(4):578–589, 2008.

[209] Marina Bleck, Michelle S. Itano, Daniel S. Johnson, V. Kaye Thomas, Alison J. North, Paul D. Bieniasz, and Sanford M. Simon. Temporal and spatial organization of ESCRT protein recruitment during HIV-1 budding. *PNAS*, 111(33):12211–12216, 2014.

[210] Schuyler B. Van Engelenburg, Gleb Shtengel, Prabuddha Sengupta, Kayoko Waki, Michal Jarnik, Sherimay D. Ablan, Eric O. Freed, Harald F. Hess, and Jennifer Lippincott-Schwartz. Distribution of ESCRT machinery at HIV assembly sites reveals virus scaffolding of ESCRT subunits. *Science*, 343(6171):653–656, 2014.

[211] Pei-I Ku, Mourad Bendjennat, Jeff Ballew, Michael B. Landesman, and Saveez Saffarian. ALIX is recruited temporarily into HIV-1 budding sites at the end of Gag assembly. *PLoS ONE*, 9(5):e96950, 2014.

[212] George O. Gey, Ward D. Coffman, and Mart T. Kubicek. Tissue culture studies of the proliferative capacity of cervical carcinoma and normal epithelium. *Cancer Research*, 12(4):264–265, 1952.

[213] John R. Masters. HeLa cells 50 years on: the good, the bad and the ugly. *Nat Rev Cancer*, 2(4):315–319, 2002.

[214] Marko Lampe, John A.G. Briggs, Thomas Endress, Bärbel Glass, Stefan Riegelsberger, Hans-Georg Kräusslich, Don C. Lamb, Christoph Bräuchle, and Barbara Müller. Double-labelled HIV-1 particles for study of virus-cell interaction. *Virology*, 360(1):92–104, 2007.

[215] Nathan C. Shaner, Robert E. Campbell, Paul A. Steinbach, Ben N. G. Giepmans, Amy E. Palmer, and Roger Y. Tsien. Improved monomeric red, orange and yellow fluorescent proteins derived from Discosoma sp. red fluorescent protein. *Nature Biotechnology*, 22(12):1567–1572, 2004.

[216] Barbara Müller, Jessica Daecke, Oliver T. Fackler, Matthias T. Dittmar, Hanswalter Zentgraf, and Hans-Georg Kräusslich. Construction and characterization of a fluorescently labeled infectious human immunodeficiency virus type 1 derivative. *Journal of Virology*, 78(19):10803–10813, 2004.

[217] Manon Eckhardt, Maria Anders, Walter Muranyi, Mike Heilemann, Jacomine Krijnse-Locker, and Barbara Müller. A SNAP-tagged derivative of HIV-1 – A versatile tool to study virus-cell interactions. *PLoS ONE*, 6(7):e22007, 2011.

[218] Julia Gunzenhäuser, Nicolas Olivier, Thomas Pengo, and Suliana Manley. Quantitative super-resolution imaging reveals protein stoichiometry and nanoscale morphology of assembling HIV-Gag virions. *Nano Letters*, 12(9):4705–4710, 2012.

[219] Thomas Wilk, Ingolf Gross, Brent E. Gowen, Twan Rutten, Felix de Haas, Reinhold Welker, Hans-Georg Kräusslich, Pierre Boulanger, and Stephen D. Fuller. Organization of immature human immunodeficiency virus type 1. *Journal of Virology*, 75(2):759–771, 2001.

[220] John A. G. Briggs, Thomas Wilk, Reinhold Welker, HansGeorg Kräusslich, and Stephen D. Fuller. Structural organization of authentic, mature HIV-1 virions and cores. *The EMBO Journal*, 22(7):1707–1715, 2003.

[221] John A.G. Briggs, Kay Grünewald, Bärbel Glass, Friedrich Förster, Hans-Georg Kräusslich, and Stephen D. Fuller. The mechanism of HIV-1 core assembly: Insights from three-dimensional reconstructions of authentic virions. *Structure*, 14(1):15–20, 2006.

[222] Yuan Lin, Lisa A. Kimpler, Teresa V. Naismith, Joshua M. Lauer, and Phyllis I. Hanson. Interaction of the mammalian endosomal sorting complex required for transport (ESCRT) III protein hSnf7-1 with itself, membranes, and the AAA+ ATPase SKD1. *Journal of Biological Chemistry*, 280(13):12799–12809, 2005.

[223] Tiffani L. Howard, Daniel R. Stauffer, Catherine R. Degnin, and Stanley M. Hollenberg. CHMP1 functions as a member of a newly defined family of vesicle trafficking proteins. *Journal of Cell Science*, 114(13):2395–2404, 2001.

[224] C. Lavallée, X. J. Yao, A. Ladha, H. Göttlinger, W. A. Haseltine, and E. A. Cohen. Requirement of the Pr55gag precursor for incorporation of the Vpr product into human immunodeficiency virus type 1 viral particles. *Jorunal of Virology*, 68(3):1926–1934, 1994.

[225] Franois Bachand, Xian-Jian Yao, Mohammed Hrimech, Nicole Rougeau, and Éric A. Cohen. Incorporation of Vpr into human immunodeficiency virus type 1 requires a direct interaction with the p6 domain of the p55 Gag precursor. *The Journal of Biological Chemistry*, 274(13):9083–9091, 1999.

[226] Barbara Müller, Uwe Tessmer, Ulrich Schubert, and Hans-Georg Kräusslich. Human immunodeficiency virus type 1 Vpr protein is incorporated into the virion in significantly smaller amounts than Gag and is phosphorylated in infected cells. *Journal of Virology*, 74(20):9727–9731, 2000.

[227] Luz Hermida-Matsumoto and Marilyn D. Resh. Localization of human immunodeficiency virus type 1 Gag and Env at the plasma membrane by confocal imaging. *Journal of Virology*, 74(18):8670–8679, 2000.

[228] Sonja Welsch, Anja Habermann, Stefanie Jäger, Barbara Müller, Jacomine Krijnse-Locker, and Hans-Georg Kräusslich. Ultrastructural analysis of ESCRT proteins suggests a role for endosome-associated tubular-vesicular membranes in ESCRT function. *Taffic*, 7(11):1551–1566, 2006.

[229] Maria Francesca Baietti, Zhe Zhang, Eva Mortier, Aurélie Melchior, Gisèle Degeest, Annelies Geeraerts, Ylva Ivarsson, Fabienne Depoortere, Christien Coomans, Elke Vermeiren, Pascale Zimmermann, and Guido David. Syndecan-syntenin-ALIX regulates the biogenesis of exosomes. *Nature Cell Biology*, 14(7):677–685, 2012.

[230] James H. Hurley and Greg Odorizzi. Get on the exosome bus with ALIX. *Nature Cell Biology*, 14(7):654–655, 2012.

[231] Qianting Zhai, Robert D. Fisher, Hyo-Young Chung, David G. Myszka, Wesley I. Sundquist, and Christopher P. Hill. Structural and functional studies of ALIX interactions with YPXnL late domains of HIV-1 and EIAV. *Nat. Struct. Mol. Biol.*, 15(1):43–49, 2008.

[232] Sergei Popov, Elena Popova, Michio Inoue, and Heinrich G. Göttlinger. Human immunodeficiency virus type 1 Gag engages the Bro1 domain of ALIX/AIP1 through the nucleocapsid. *Journal of Virology*, 82(3):1389–1398, 2008.

[233] Elena Chertova, Oleg Chertov, Lori V. Coren, James D. Roser, Charles M. Trubey, Julian W. Bess, Raymond C. Sowder, Eugene Barsov, Brian L. Hood, Robert J. Fisher, Kunio Nagashima, Thomas P. Conrads, Timothy D. Veenstra, Jeffrey D. Lifson, and David E. Ott. Proteomic and biochemical analysis of purified human immunodeficiency virus type 1 produced from infected monocyte-derived macrophages. *Journal of Virology*, 80(18):9039–9052, 2006.

[234] Fengwen Zhang, Trinity Zang, Sam J. Wilson, Marc C. Johnson, and Paul D. Bieniasz. Clathrin facilitates the morphogenesis of retrovirus particles. *PLoS Pathogens*, 7(6):e1002119, 2011.

[235] Vincent Dussupt, Melodi P. Javid, Georges Abou-Jaoudé, Joshua A. Jadwin, Jason de La Cruz, Kunio Nagashima, and Fadila Bouamr. The nucleocapsid region of HIV-1 Gag cooperates with the PTAP and $\mathrm{LYPX_nL}$ late domains to recruit the cellular machinery necessary for viral budding. *PLoS Pathogens*, 5(3):e1000339, 2009.

[236] Xi Zhou, Jiali Si, Joe Corvera, Gary E. Gallick, and Jian Kuang. Decoding the intrinsic mechanism that prohibits ALIX interaction with ESCRT and viral proteins. *Biochemical Journal*, 432(3):525–534, 2010.

[237] Xi Zhou, Shujuan Pan, Le Sun, Joe Corvera, Yu-Chen Lee, Sue-Hwa Lin, and Jian Kuang. The CHMP4b- and Src-docking sites in the Bro1 domain are autoinhibited in the native state of Alix. *Biochemical Journal*, 418(2):277–284, 2009.

[238] Qianting Zhai, Michael B. Landesman, Hyo-Young Chung, Adam Dierkers, Cy M. Jeffries, Jill Trewhella, Christopher P. Hill, and Wesley I. Sundquist. Activation of the Retroviral Budding Factor ALIX. *Jorunal of Virology*, 85(17):9222–9226, 2011.

[239] Grégory Effantin, Aurélien Dordor, Virginie Sandrin, Nicolas Martinelli, Wesley I. Sundquist, Guy Schoehn, and Winfried Weissenhorn. ESCRT-III CHMP2A and CHMP3 form variable helical polymers in vitro and act synergistically during HIV-1 budding. *Cellular Microbiology*, 15(2):213–226, 2013.

[240] Alessia Zamborlini, Yoshiko Usami, Sheli R. Radoshitzky, Elena Popova, Giorgio Palu, and Heinrich Göttlinger. Release of autoinhibition converts ESCRT-III components into potent inhibitors of HIV-1 budding. *PNAS*, 103(50):19140–19145, 2006.

[241] Christian M. T. Spahn, Jeffrey S. Kieft, Robert A. Grassucci, Pawel A. Penczek, Kaihong Zhou, Jennifer A. Doudna, and Joachim Frank. Hepatitis C virus IRES RNA-induced changes in the conformation of the 40S ribosomal subunit. *Science*, 291(5510):1959–1962, 2001.

[242] Bruce Alberts, Alexander Johnson, Julian Lewis, Martin Raff, Keith Roberts, and Peter Walter. *Molecular Biology of the Cell*, book section The Cytoskeleton, pages 965–1052. Garland Science, New York, 5 edition, 2007.

[243] Enrico Grazi. What is the diameter of the actin filament? *FEBS Letters*, 405(3):249–252, 1997.

[244] Guillaume Salbreux, Guillaume Charras, and Ewa Paluch. Actin cortex mechanics and cellular morphogenesis. *Trends in Cell Biology*, 22(10):536–545, 2012.

[245] Jennifer L. Ross, M. Yusuf Ali, and David M. Warshaw. Cargo transport: molecular motors navigate a complex cytoskeleton. *Current Opinion in Cell Biology*, 20(1):41–47, 2008.

[246] H. E. Huxley. The mechanism of muscular contraction. *Science*, 164(3886):1356–1366, 1969.

[247] I. Rayment, H. M. Holden, M. Whittaker, C. B. Yohn, M. Lorenz, K. C. Holmes, and R. A. Milligan. Structure of the actin-myosin complex and its implications for muscle contraction. *Science*, 261(5117):58–65, 1993.

[248] Blaine T. Bettinger, David M. Gilbert, and David C. Amberg. Actin up in the nucleus. *Nature Reviews*, 5:410–415, 2004.

[249] Robert Grosse and Maria K. Vartiainen. To be or not to be assembled: progressing into nuclear actin filaments. *Nature Reviews Molecular Cell Biology*, 14(11):693–697, 2013.

[250] Christian Baarlink, Haicui Wang, and Robert Grosse. Nuclear actin network assembly by formins regulates the SRF coactivator MAL. *Science*, 349(6134):864–867, 2013.

[251] Miguel Vicente-Manzanares, Donna J. Webb, and A. Rick Horwitz. Cell migration at a glance. *Journal of Cell Science*, 118(21):4917–4919, 2005.

[252] Carol L. Manahan, Pablo A. Iglesias, Yu Long, and Peter N. Devreotes. Chemoattractant signaling in Dictyostelium Discoideum. *Annual Review of Cell and Developmental Biology*, 20(1):223–253, 2004.

[253] Anne J. Ridley, Martin A. Schwartz, Keith Burridge, Richard A. Firtel, Mark H. Ginsberg, Gary Borisy, J. Thomas Parsons, and Alan Rick Horwitz. Cell migration: Integrating signals from front to back. *Science*, 302(5651):1704–1709, 2003.

[254] YusukeS Kato, Toshiki Yagi, SarahA Harris, Shin-ya Ohki, Kei Yura, Yousk Shimizu, Shinya Honda, Ritsu Kamiya, StanA Burgess, and Masaru Tanokura. Structure of the Microtubule-Binding Domain of Flagellar Dynein. *Structure*, 22(11):1628–1638, 2014.

[255] Catherine D. Nobes and Alan Hall. Rho, Rac, and Cdc42 GTPases regulate the assembly of multimolecular focal complexes associated with actin stress fibers, lamellipodia, and filopodia. *Cell*, 81(1):53–62, 1995.

[256] Nicolas Tapon and Alan Hall. Rho, Rac and Cdc42 GTPases regulate the organization of the actin cytoskeleton. *Current Opinion in Cell Biology*, 9(1):86–92, 1997.

[257] Matthias Krause and Alexis Gautreau. Steering cell migration: lamellipodium dynamics and the regulation of directional persistence. *Nature Reviews Molecular Cell Biology*, 15(9):577–590, 2014.

[258] Aron B. Jaffe and Alan Hall. Rho GTPases: Biochemistry and Biology. *Annual Review of Cell and Developmental Biology*, 21(1):247–269, 2005.

[259] Ah-Lai Law, Anne Vehlow, Maria Kotini, Lauren Dodgson, Daniel Soong, Eric Theveneau, Cristian Bodo, Eleanor Taylor, Christel Navarro, Upamali Perera, Magdalene Michael, Graham A. Dunn, Daimark Bennett, Roberto Mayor, and Matthias Krause. Lamellipodin and the Scar/WAVE complex cooperate to promote cell migration in vivo. *The Journal of Cell Biology*, 203(4):673–689, 2013.

[260] Matthias Krause, Jonathan D. Leslie, Mary Stewart, Esther M. Lafuente, Ferran Valderrama, Radhika Jagannathan, Geraldine A. Strasser, Douglas A. Rubinson, Hui Liu, Michael Way, Michael B. Yaffe, Vassiliki A. Boussiotis, and Frank B. Gertler. Lamellipodin, an Ena/VASP ligand, is implicated in the regulation of lamellipodial dynamics. *Developmental Cell*, 7(4):571–583, 2004.

[261] Matthias Krause, Erik W. Dent, James E. Bear, Joseph J. Loureiro, and Frank B. Gertler. Ena/VASP proteins: Regulators of the actin cytoskeleton and cell migration. *Annual Review of Cell and Developmental Biology*, 19(1):541–564, 2003.

[262] A. Ponti, M. Machacek, S. L. Gupton, C. M. Waterman-Storer, and G. Danuser. Two distinct actin networks drive the protrusion of migrating cells. *Science*, 305(5691):1782–1786, 2004.

[263] Pirta Hotulainen and Pekka Lappalainen. Stress fibers are generated by two distinct actin assembly mechanisms in motile cells. *The Journal of Cell Biology*, 173(3):383–394, 2006.

[264] D. Bray. Axonal growth in response to experimentally applied mechanical tension. *Developmental Biology*, 102(2):379–389, 1984.

[265] Philip Lamoureux, Robert E. Buxbaum, and Steven R. Heidemann. Direct evidence that growth cones pull. *Nature*, 340(6229):159–162, 1989.

[266] S. Aznavoorian, M. L. Stracke, H. Krutzsch, E. Schiffmann, and L. A. Liotta. Signal transduction for chemotaxis and haptotaxis by matrix molecules in tumor cells. *The Journal of Cell Biology*, 110(4):1427–1438, 1990.

[267] Leo S. Price, Jie Leng, Martin Alexander Schwartz, and Gary M. Bokoch. Activation of Rac and Cdc42 by integrins mediates cell spreading. *Molecular Biology of the Cell*, 9(7):1863–1871, 1998.

[268] Alexander B. Verkhovsky, Tatyana M. Svitkina, and Gary G. Borisy. Self-polarization and directional motility of cytoplasm. *Current Biology*, 9(1):11–S1, 1999.

[269] Chun-Min Lo, Hong-Bei Wang, Micah Dembo, and Yu-li Wang. Cell movement is guided by the rigidity of the substrate. *Biophysical Journal*, 79(1):144–152, 2000.

[270] Manuel Thery, Victor Racine, Anne Pepin, Matthieu Piel, Yong Chen, Jean-Baptiste Sibarita, and Michel Bornens. The extracellular matrix guides the orientation of the cell division axis. *Nature Cell Biology*, 7(10):947–953, 2005.

[271] Manuel Théry, Anne Pépin, Emilie Dressaire, Yong Chen, and Michel Bornens. Cell distribution of stress fibres in response to the geometry of the adhesive environment. *Cell Motility and the Cytoskeleton*, 63(6):341–355, 2006.

[272] Manuel Théry, Victor Racine, Matthieu Piel, Anne Pépin, Ariane Dimitrov, Yong Chen, Jean-Baptiste Sibarita, and Michel Bornens. Anisotropy of cell adhesive microenvironment governs cell internal organization and orientation of polarity. *PNAS*, 103(52):19771–19776, 2006.

[273] Xiaowei Zhuang. Nano-imaging with STORM. *Nature Photonics*, 3(7):365–367, 2009.

[274] Andrew D. Doyle, Francis W. Wang, Kazue Matsumoto, and Kenneth M. Yamada. One-dimensional topography underlies three-dimensional fibrillar cell migration. *The Journal of Cell Biology*, 184(4):481–490, 2009.

[275] Manuel Théry. Micropatterning as a tool to decipher cell morphogenesis and functions. *Journal of Cell Science*, 123(24):4201–4213, 2010.

[276] Amit Kumar and George M. Whitesides. Features of gold having micrometer to centimeter dimensions can be formed through a combination of stamping with an elastomeric stamp and an alkanethiol 'ink' followed by chemical etching. *Applied Physics Letters*, 63(14):2002–2004, 1993.

[277] Sami Alom Ruiz and Christopher S. Chen. Microcontact printing: A tool to pattern. *Soft Matter*, 3(2):168–177, 2007.

[278] Manuel Théry and Matthieu Piel. Adhesive micropatterns for cells: A microcontact printing protocol. *Cold Spring Harbor Protocols*, 4(7):pdb.prot5255, 2009.

[279] Ho-Jin Park, Yali Zhang, Serban P. Georgescu, Kristin L. Johnson, Dequon Kong, and Jonas B. Galper. Human umbilical vein endothelial cells and human dermal microvascular endothelial cells offer new insights into the relationship between lipid metabolism and angiogenesis. *Stem Cell Reviews*, 2(2):93–101, 2006.

[280] Feodor Lynen and Ulrich Wieland. Über die Giftstoffe des Knollenblätterpilzes. IV. *Justus Liebigs Annalen der Chemie*, 533(1):93–117, 1938.

[281] P. Dancker, I. Löw, W. Hasselbach, and Th. Wieland. Interaction of actin with phalloidin. *Biochimica et Biophysica Acta (BBA) - Protein Structure*, 400(2):407–414, 1975.

[282] Rollin W. Robinson and Judith A. Snyder. An innovative fixative for cytoskeletal components allows high resolution in colocalization studies using immunofluorescence techniques. *Histochemistry and Cell Biology*, 122(1):1–5, 2004.

[283] J. V. Small, M. Herzog, and K. Anderson. Actin filament organization in the fish keratocyte lamellipodium. *The Journal of Cell Biology*, 129(5):1275–1286, 1995.

[284] Sari Tojkander, Gergana Gateva, and Pekka Lappalainen. Actin stress fibers – assembly, dynamics and biological roles. *Journal of Cell Science*, 125(8):1855–1864, 2012.

[285] M. Abercrombie, Joan E. M. Heaysman, and Susan M. Pegrum. The locomotion of fibroblasts in culture: IV. Electron microscopy of the leading lamella. *Experimental Cell Research*, 67(2):359–367, 1971.

[286] Vivek C. Abraham, Vijaykumar Krishnamurthi, D. Lansing Taylor, and Frederick Lanni. The actin-based nanomachine at the leading edge of migrating cells. *Biophysical Journal*, 77(3):1721–1732, 1999.

[287] Sandrine Etienne-Manneville. Microtubules in cell migration. *Annual Review of Cell and Developmental Biology*, 29(1):471–499, 2013.

[288] Yoshiko Usami, Sergei Popov, Eric R. Weiss, Christie Vriesema-Magnuson, Arianna Calistri, and Heinrich G. Göttlinger. Regulation of CHMP4/ESCRT-III function in human immunodeficiency virus type 1 budding by CC2D1A. *Journal of Virology*, 86(7):3746–3756, 2012.

[289] Megan G. Waldhuber, Michael Bateson, Judith Tan, Alison L. Greenway, and Dale A. McPhee. Studies with GFP-Vpr fusion proteins: induction of apoptosis but ablation of cell-cycle arrest despite nuclear membrane or nuclear localization. *Virology*, 313(1):91–104, 2003.

[290] Marcus Graf, Alexandra Bojak, Ludwig Deml, Kurt Bieler, Hans Wolf, and Ralf Wagner. Concerted action of multiple cis-acting sequences is required for Rev dependence of late human immunodeficiency virus type 1 gene expression. *Journal of Virology*, 74(22):10822–10826, 2000.

[291] Johannes Schindelin, Ignacio Arganda-Carreras, Erwin Frise, Verena Kaynig, Mark Longair, Tobias Pietzsch, Stephan Preibisch, Curtis Rueden, Stephan Saalfeld, Benjamin Schmid, Jean-Yves Tinevez, Daniel James White, Volker Hartenstein, Kevin Eliceiri, Pavel Tomancak, and Albert Cardona. Fiji: an open-source platform for biological-image analysis. *Nature Methods*, 9(7):676–682, 2012.

[292] S. R. Sternberg. Biomedical image processing. *Computer*, 16(1):22–34, 1983.

[293] F. J. Segerer, P. J. F. Röttgermann, S. Schuster, A. Piera Alberola, S. Zahler, and J. O. Rädler. A versatile method to generate multiple types of micropatterns. page arXiv:1510.08295, 2015. Accessed: 12 January 2016, available from `http://arxiv.org/abs/1510.08295`.

Acknowledgments

First of all, I would like to thank my adviser, Prof. Don C. Lamb for giving me the opportunity to do my PhD thesis in this highly exciting and relevant field. Thank you, Don, for always having an open door and for supporting my work in every way that you could. It has been a privilege to work in such a productive environment.

I am also grateful to my co-adviser, Prof. Christoph Bräuchle, for his continuous support of my work and for believing in the success of the HIV project especially in times when experiments were stuck.

I am also thankful for having such wonderful cooperation partners like Prof. Barbara Müller and Prof. Hans-Georg Kräusslich. Without their continuous efforts to provide all the samples on time, the advice and the fruitful discussions, the success of the HIV project would not have been possible. I also want to thank Barbara for spontaneously agreeing to be a member of my thesis committee.

These thanks are extended to Prof. Achim Hartschuh, Prof. Regina de Vivie-Riedle and Prof. Stefan Zahler for reviewing my thesis.

I further thank Prof. Stefan Zahler as well as Florian Gegenfurther for collaborating on the lamellipodia project that showed the capacity of 3D super-resolution microscopy. Thank you also, Florian, for proofreading of the lamellipodia chapter.

I also thank Dr. Alvaro Crevenna and Dr. Julia von Blume for the cooperation on the Cab45 project (although it did not become part of the thesis) providing me with various samples and thereby opening meaningful new applications for the STORM microscope.

Science does not work without money. Therefore, I acknowledge all the various and alternating money sources that funded my work, especially the excellence clusters NIM and CIPS, not to forget the SFBs 1032 and 1035.

However, none of this would have been possible without the continuous help and support from my fantastic colleagues from FabLab and from AK Bräuchle. I am glad that I had the chance to do my PhD in a group with such a great atmosphere and strong support system.

This includes firstly Viola, who taught me how to plan, design and interpret biological experiments and who jumped in for doing the cell culture when other sources became unavailable. Thank you also for your energy, your addictive enthusiasm for science, for the great discussions and all kinds of help and advice you gave me. And of course for proofreading my thesis!

Daniela, thank you for showing me science from a physicists' perspective and especially for telling me all those little tricks that are required to perform 3D STORM successfully but cannot be found in the papers. Thank you also for always motivating me, for all the tea and coffee breaks, which have always been great opportunities for discussions that more than once helped to solve various problems. And also, thank you for proofreading my thesis!

Sergey owns the credit for being the one who introduced me to the fascinating world of fluorescence microscopy a long time ago. Thank you for sharing your deep and profound knowledge that apparently covers every potential field there might be!

Thanks also to Vova for setting up the first version of the drift correction program and showing me by this way what things can be done with LabView (and also things that one should not do). I thank Adriano for finding out how one can count single viruses and demonstrating me

that ImageJ can do much more than just displaying images. Thank you also for the continuous supply of coffee! Although she has probably been enjoying her well-earned retirement for a couple of years now, it is impossible not to thank Monika for introducing me to the work in the cell culture and for the countless HeLa cell samples she seeded for me. In this context, I also have to thank Jaroslava Obel who took over as lab technician showing a quite different approach to the cell culture work.

I am thankful that I could rely on you, Moritz, for taking care of all the paper work that is necessary to keep research running. Thank you also for the various discussions and advice on every topic in the world, be it scientific or not.

I thank Silke Steger for all the help with administrative stuff and especially for her efforts to get back my travel costs for my Boston trip after the documents got lost somewhere in the bureaucratic labyrinth of the university travel-reimbursement system.

I further thank my student Ieva for helping me with my wok on the ESCRT/HIV project and for her creative cake recipes. Also, a special mention to Alvaro's student Derya, for her fascination and interest for super-resolution microscopy and for performing many of the Cab45 experiments.

I thank my office mates over the last five years, Martin, Gregor, Aurélie, Niko, Daniela, Sushi, Ivo and Chen for the productive atmosphere and also for our almost traditional morning tea break. Thank you, Lena, for always being there when I needed help for anything. Thank you for all the great discussions, your ideas and for everything you did and organized for the group! Thank you, Waldi for your suggestions and ideas, which have always been a great help. Thank you, Sushi, for introduction into Indian culture and for continuous English proofreading. Thank you, Vroni, for being the voice of common sense whenever necessary. Wehne, thank you for the LabView support and all the things you organized for the group! And of course many thanks to all the other people from the lab – Anders, Ellen, Philipp, Maria, Bässem, Ganesh, Evelyn, Kira and Leonhard – for every kind of help and support you provided!

I thank the FabLab Alumni Martin, Gregor, Niko, Matthias, Doro, Giulia and Jelle for everything that I could learn from them and together with all the other members of the original group from 2010 for giving me the warm welcome that I received when I joined the group.

Special thanks finally go to my fellow students Claudia, Lydia, Konstantin, Francisco, Amelie, Anna, Desiree and Sarah for making my time on campus, in undergraduate studies and later, the best times ever! Thank you for being the friends that you have been and thank you for all the great time that we spent together and that you showed me that there is still a life outside of the university.